UNIVERSIDADE DE SÃO PAULO
INSTITUTO DE GEOCIÊNCIAS

Petrochronology applied into evaluating the tectono-metamorphic context from rocks of the Turvo-Cajati Formation, Curitiba Terrane, and its influence in the Ribeira Belt Evolution, Cajati, SP

BRUNA DA SILVA RICARDO

Orientador: Prof. Dr. Renato de Moraes

Dissertação de Mestrado

Nº 872

COMISSÃO JULGADORA

Dr. Renato de Moraes

Dr. Maurício Pavan Silva

Dra. Kathryn Ann Cutts

SÃO PAULO
2021

UNIVERSIDADE DE SÃO PAULO

INSTITUTO DE GEOCIÊNCIAS

Petrochronology applied into evaluating the tectono-metamorphic context from rocks of the Turvo-Cajati Formation, Curitiba Terrane, and its influence in the Ribeira Belt Evolution, Cajati, SP

BRUNA DA SILVA RICARDO

Dissertação apresentada ao Programa Geociências (Mineralogia e Petrologia) para obtenção de título de Mestre em Ciências

Área de concentração: Petrologia Ígnea e Metamórfica

Orientador: Prof. Dr. Renato de Moraes

Coorientador: Prof. Dr. Frederico Meira Faleiros

São Paulo

2021

À Mª Estela,

(in memoriam)

você é a luz que me guia e protege

ACKNOWLEDGEMENTS

Esse trabalho não seria possível sem a contribuição direta e indireta de inúmeras pessoas. Espero fazer jus a todas nesse pequeno espaço.

À Fundação de Amparo à Pesquisa do Estado de São Paulo (FAPESP) pelos financiamentos investidos em mim (2016/12986-6, 2018/01572-1 e 2019/19651-8) e no nosso grupo de pesquisa (2015/04487-7 e 2018/10012-0). As opiniões, hipóteses, conclusões ou recomendações expressas nesse material são de total responsabilidade da autora e não necessariamente refletem à visão da FAPESP. Agradeço também à CAPES por apoio financeiro no desenvolvimento do projeto.

Ao meu orientador Dr. Renato de Moraes que acreditou no meu potencial desde quando eu o procurei em 2016, o contrariando querendo trabalhar com xistos. São muitos anos de muita paciência comigo e ensinamentos de geologia e vida nessa parceria e amizade que desenvolvemos.

Ao meu co-orientador e parceiro de campo Dr. Frederico Meira Faleiros. Muito obrigada pela disposição em tirar minhas inúmeras dúvidas em respeito da regional, petrologia, estrutural (...). Também agradeço ao Dr. Maurício Pavan e à CPRM (Serviço Geológico Brasileiro) pelo material cedido para essa pesquisa.

Aos funcionários do IGc-USP, representados aqui por Leandro e Marcos, da microssonda, Samuca, Bira, Antônio, Katherine e Alexandre. Aos professores do IGC-USP, representados pelos Profs Miguel Basei, Gergely Szabó, Eliane Del Lama e Sílvio Vlach. Agradeço também aos professores e pesquisadores do IG-UNICAMP que me receberam muito bem em uma parceria de um futuro trabalho. Em especial, Prof. Ticiano Saraiva, ao Robert e à Rep. Grão-Pará.

Aos meus amigos de Pós-Graduação, Grega, Dana, Yaki, Lê, Dina, Débora, Francy,e Fio entre outros pelos bons momentos de descontração. Ao digníssimo Dr. Caio A. Santos (ou Fofis), muito obrigada por toda ajuda profissional, pessoal, por me alimentar com broa e café. Faltam palavras para agradecer você.

Aos meus amigos de colégio, graduação, atlética, vôlei, vida. Ao João por não desistir de mim, mesmo que tenha tentado. À Che, faltam palavras, obrigada por tanto. À Baia, Fê, Welzin, Aninha, ao NOIS e tantos outros que a USP me trouxe. As relações mudam, o carinho fica. Aos inúmeros vôleis que me juntei nesses anos de USP, Geo, GeoPsico, EEFE, Nutri. Longas histórias de imenso aprendizado e evolução. Obrigada aos funcionários do CEPE e ao Portuga pela paciência (mútua!)

An important part of this research was developed abroad during the beginning of the COVID-19 pandemic. Therefore, I would like to thank the SEGG, University of Portsmouth, UK and especially the Crustal Group for welcoming me in the UK. It was totally unexpected and challenging but due to their support, we made it. Special thanks to my co-supervisor Dr Catherine M. Mottram for all the patience in teaching me how to use the LA-ICP-MS, dating my tiny monazites in only 15 days and showing me the best routes to cycle the Isle of Wight. Joe and Glenn for technical support with good talks in between. It was an adventure, and I am very grateful for all the people I met in Portsmouth. Nevertheless, without Sheila and Vivi none of this would happen. Sheila and Ricardo, I will never be able to return everything you did to me. To Clem and Miles thanks for our partnership in sharing a house. Everything was easier because of you and our movie sessions. Thanks to Scott, who joined me in our 'south-UK cycling exploration' adventure. I reckon we made it more than 1000 km together with lots of flat tires.

Finalmente, agradeço todo o suporte que recebo diariamente de minha família, especialmente do meu pai. No mundo onde vivemos, ter um pai tão carinhoso, presente e apoiador é exceção. Sou infinitamente grata por me permitir trilhar meus próprios caminhos. Obrigada à minha mãezinha, que segue me guiando onde quer que esteja. Obrigada também à família de sangue e coração: Pedrokas, Tia Vera, Beatriz Bessornia (!!!), Henriete e família, Noriko, Sisan (*in memorian*), Débora, Fábio, meus primos, primas, tias e tios mais distantes, mas cujo carinho se mantém. No final do dia, isso é o que mais importa. A história da nossa família é longa e vem desde a pequena Riacho das Almas, no interior de PE e eu fico feliz em conseguir trilhar caminhos que muitos de nós não puderam. A educação, o trabalho e o esforço mudaram a história de nossa família. Sou muito grata por adicionar mais uma página na história dos *da Silva* e dos *Ricardo*. Sem vocês, eu não teria conseguido.

“It is a journey of evolution, adaptation. The journey we all take. The journey that unites each and every one of us”

Charlie Kaufman, Adaptation

ABSTRACT

Ancient accretionary orogens occur all over the globe and their reconstruction present challenges once a great part of information is missing. The Ribeira Belt, SE Brazil, is an example of an accretionary orogen formed during the amalgamation of Gondwana in the Neoproterozoic. The current understanding of its tectonometamorphic history is a work-in-progress. In this study, we focus on its southernmost part, more specifically in the Curitiba Terrane. It uses different techniques to understand the sedimentation and metamorphic settings to a metasedimentary unit, the Turvo-Cajati Formation (TCF). To evaluate the sedimentation setting, detrital zircon and probability density plots are presented. To understand the metamorphism, high precision in-situ geochronology coupled with systematic thermodynamic modelling to provide new constraints for the *P-T*-t paths that some metasedimentary rocks have experienced. An isograd map distribution is also presented based on field work and petrography. In this unit, schists and paragneiss in distinct metamorphic conditions crop out and they are all assumed to belong to same unit (TCF). The unit is divided in three sub-units based on their metamorphic grade, the Low-TCF in the garnet zone, the Medium-TCF in the sillimanite zone and the High-TCF in the K-feldspar-kyanite/sillimanite zones with partial melting. Detrital zircon data indicates that samples from Low/Medium-TCF record signatures of a back-arc basin and the High-TCF of an accretionary wedge. It also indicates a maximum depositional age between 650-630 Ma. The metamorphism was constrained using petrography, pseudosection modelling in the MnNCKFMASHTO and NCKFMASHTO chemical systems with Perple_X software and the age of metamorphism using isotopic and chemical monazite dating. *P-T* phase diagrams are modelled to a broad set of samples either considering fractionation of different stages of garnet growth and conventional bulk composition. Each sample was modelled to obtain the *P-T* conditions from different metamorphic stages and *P-T*-t paths were obtained. They indicate complex evolution, even within rocks from the same metamorphic zone. Monazite ages indicate shared metamorphism in the High-TCF and Medium-TCF yielding monazite growth between 620-580 Ma, but two sample record older ages (~640 Ma). This period between 640-600 Ma anticipates our understanding of the timing of metamorphic events and that it was partially coeval with final stages of deposition. By comparing the metamorphic field gradients and *P-T*-t paths in High-TCF and Low and Medium-TCF, we can better understand the relation of the metamorphic events. Bimodal thermobaric ratios and pressure regime are observed by interpreting a large set of samples. Therefore, we propose a Japan-like microcontinent where the Low/Medium-TCF would be in the back-arc basin and the High-TCF would be in the accretionary wedge. This microcontinent also involves a Rhyacian orthogneisses from the Atuba

Complex as basement and the Piên Magmatic Arc as a result of a subduction-to-collision setting. This scenario evolved during at least 60 Ma (640-580 Ma) where the collision with the Luis Alves Microcontinent would cause most of the metamorphism and the exhumation of those rocks. Finally, somewhere around 580 Ma, the instauration of large-scale shear zones and A-type granites from the Graciosa Province mark the end of those events.

Keywords: accretionary orogen; metamorphic evolution; monazite dating; petrochronology; Ribeira Belt

RESUMO

Orógenos acrescionários antigos occrem em todo o globo e sua reconstrução apresenta desafios uma vez que grande parte de informação foi perdida. A Faixa Ribeira, SE do Brasil, é um exemplo de um orógeno acrescionário formado durante a amalgamação do Gondwana, no neoproterozoico. O entendimento da sua evolução tectonometamórfica é um trabalho em contínuo progresso. Nesse estudo, nós focamos em sua porção sul, especificamente no Terreno Curitiba. Diferentes técnicas são usadas para entender os ambientes de sedimentação e metamorfismo para uma unidade metassedimentar, a Formação Turvo-Cajati (TCF). Para avaliar o ambiente de sedimentação, zircão detrítico e gráficos de densidade de probabilidade são apresentados. Para entender o metamorfismo, geocronologia de alta resolução *in-situ* acoplada com modelagem termodinâmica sistemática para obter as trajetórias *P-T*-t que algumas rochas experimentaram. Um mapa de distribuição de isógradas também é apresentado baseado em trabalho de campo e petrografia. Nessa unidade, xistos e paragneisses de diferentes condições metamórficas afloram e assume-se que pertencem à mesma unidade (TCF). A unidade é dividida em três sub-unidades baseadas no seu grau metamórfico, a Low-TCF na zona da granada, a Medium-TCF na zona da sillimanita e a High-TCF na zona do feldspato potássico-cianita/sillimanita com fusão parcial. Zircão detrítico indica que as amostras da Low/Medium-TCF guarda assinaturas de uma bacia de retroarco e a High-TCF de prisma acrescionário. Ele também indica idade máxima de deposição entre 650-630 Ma. O metamorfismo foi delimitado usando petrografia, modelagem de pseudosseções nos sistemas MnKCKFMASHTO e NCKFMASHTO com o software Perplex. A idade do metamorfismo foi obtida através de datação isotópica e química. Diagramas de fase *P-T* são modelados para um grande conjunto de amostras tanto considerando fracionamento de diferentes estágios de crescimento de granada quanto composição de rocha total convencional. Cada amostra foi modelada para obter as condições *P-T* de diferentes estágios metamórficos e trajetórias *P-T*-t foram obtidas. Elas indicam uma evolução complexa, mesmo em rochas da mesma zona metamórfica. As idades de monazita indicam metamorfismo compartilhado na High-TCF e na Medium-TCF com crescimento de monazita entre 620-580 Ma, mas duas amostras recordam idades mais velhas (~640 Ma). Esse período entre 640-600 Ma antecipa o entendimento atual da duração do metamorfismo, que se sobrepõe parcialmente com os estágios finais de deposição. Comparando os gradientes metamórficos de campo e as trajetórias *P-T*-t na High-TCF e na Low/Medium-TCF, a relação dos eventos metamórficos pode ser melhor entendida. Razões termobáricas e regimes de pressão bimodais são observados ao interpretar um conjunto extenso de amostras. Portanto, é proposto um microcontinente tipo-Japão onde a Low/Medium-TCF estaria na bacia de retroarco e o

a High-TCF no prisma acrescionário. Esse microcontinente também envolve os ortognaisses riacianos do Complexo Atuba como embasamento e o Arco Magmático Piên como resultado de um ambiente de subducção-a-colisão. Esse cenário evoluiu surante pelo menos 60 Ma (640-580 Ma) onde a colisão com o microcontinente Luis Alves causaria a maior parte do metamorfismo e a exumação dessas rochas. Finalmente, em algum momento por volta de 580 Ma, a instauração de zonas de cisalhamento de larga escala e granitos tipo A da Província Graciosa marca o fim desses eventos.

Palavras-chave: orógeno acrescionário, evolução metamórfica, datação de monazita, petrocronologia, Faixa Ribeira

SUMMARY

LIST OF FIGURES

Figures and Tables are listed per chapter:

CHAPTER 2

CHAPTER 3

LIST OF TABLES

Figures and Tables are listed per chapter:

CHAPTER 2

CHAPTER 3

CHAPTER 1 - INTRODUCTION

The Ribeira Belt is a major tectonic segment in SE-Brazil. It occurs between Brazilians states of Espírito Santo and Santa Catarina. It is composed of units with different tectonic origins such as Archean-Paleoproterozoic basement, Proterozoic metasedimentary units and late-Ediacaran igneous provinces (e.g., Heilbron et al., 2000, 2017, Meira et al., 2019). It can be divided in Northern, Central and Southern parts and several studies have been made on the last decades on all of them from different research groups in Brazil and abroad (e.g. Cordani et al., 1973, Almeida et al., 1981, Heilbron et al., 2017 and references there in, and more recently Campanha et al., 2019, Malta et al., 2020, Ribeiro et al., 2019, Meira et al., 2015, Cavalcante et al., 2018; Ricardo et al., 2020).

This study is focused on the Southern Ribeira Belt that comprises four tectonic domains: the Embu, Apiaí, Curitiba and Costeiro/Paranaguá Terranes (Basei et al., 1992; Faleiros et al., 2011; Passarelli et al., 2018). They have been interpreted as tectonic segments with distinct evolutionary histories that collided in the Neoproterozoic. This collision involved the São-Francisco, Paranapanema, Luís Alves and Rio de la Plata Plates with the closure of the Adamastor Ocean and resulted in the formation of Western Gondwana (Brito Neves et al., 1999).

This theory was recently questioned. Recent studies suggest another context where the Ribeira Belt would be an intracontinental orogen, formed at ~620 Ma, when metamorphic events of intermediate *P* happened (Meira et al., 2019). According to the authors, this event was followed by an extensional and wrench tectonics low-P event associated with orogenic collapse. This event occurred ~575 Ma and can be related to strike-slip shear zones and voluminous peraluminous magmatism (Meira et al., 2019). This study is made on the Embu Terrane, Central Ribeira belt but the authors suggest the tectonic context can be expanded to the Southern Ribeira Belt as a whole.

Even though lots of studies are being conducted on the Southern Ribeira Belt (e.g. Faleiros et al., 2011, 2016, Passarelli et al., 2018, 2019, Campanha & Sadowiski, 1999, Campanha et al., 2015) just a few of them had the Curitiba Terrane as the main object of study. This lack of recent studies is even greater in the metasedimentary units that composes the terrane, the Turvo-Cajati (TCF) and Capiru Formations. From the first we highlight Faleiros et al., (2011, 2016) and from Capiru Formation, Guimarães et al., (2002) and Santos et al., (2018). Nevertheless, the studies conducted on the TCF only focus on gneiss and migmatitic rocks, even though lower *P-T* conditions rocks were already described on literature for this unit (e.g. Faleiros & Pavan, 2013).

The Curitiba Terrain occurs between a Mesoproterozoic Terrane (Apiaí Terrane) and an Archean/Paleoproterozoic craton (Luis Alves Terrane). This makes the understanding of the Curitiba Terrane an important piece on the Ribeira Belt tectonic puzzle. Therefore, this study is focused on the never studied metapelitic schists and phyllites from the TCF. It aims to have a better picture on both the metamorphic and sedimentary events that affected the unit and correlate them with other units forming the Curitiba Terrane.

1. Methods

The main goal of this study is to obtain more detailed information about the metamorphic events that affected the Turvo-Cajati Formation. The methodology is based on field work, detailed and extensive petrography, chemical and isotopic analysis based on U-Pb method. The field work is used to understand the isograd distribution, structural geological control and sample collection. Petrography was performed not only on samples collected on field work, but also in material from the Brazilian Geological Survey (CPRM). Some samples were selected for more detailed studies such as mineral chemistry on EPMA (electron probe micro-analyzer), thermodynamic modeling and U-Pb/trace element on monazite dating.

The study then is divided in 2 complementary approaches. The first one aimed to have a broad understanding on the metamorphism and to complement this information, the sedimentary provenance from the TCF is also studied. Samples were selected to chemical studies on the EPMA, followed by a classical, less detailed approach on thermodynamic modeling. It was complemented with detrital zircon information to produce a preliminary tectonic model. This part of the study was published in May 2020 in *Precambrian Research.* The paper is entitled '*Tectonic implications of juxtaposed high- and low-pressure metamorphic field gradient rocks in the Turvo-Cajati Formation, Curitiba Terrane, Ribeira Belt, Brazil*' and can be found on **CHAPTER 2** of this dissertation.

The second part of the study aimed to detail the metamorphic *P-T*-t paths that different rocks from the TCF passed through and its tectonic implications to the TCF evolution. To obtain this, systematic thermodynamic modeling was implemented considering both local equilibrium and how it is affected by process such as elements imprisoned during garnet growth. Therefore, more than one pseudosection is modeled to garnet-bearing samples considering the best *P-T* estimative for each stage of garnet growth. The timing-scale is obtained by monazite U-Pb dating. Two methods were implemented: chemical dating on EPMA and isotopic dating and trace element composition obtained with LA-ICP-MS technique. A paper for this part of the research is

being developed and will be submitted to acceptance in a petrological journal such as the *Journal of Metamorphic Geology*, *Lithos* or similar. A draft of the article containing the results and preliminary interpretation can be found on this dissertation on **CHAPTER 3**.

Combining all the information collected during the MSc research, discussions about the evolution of the TCF are also presented in **CHAPTER 4**. A discussion of the implications of this study on the Curitiba Terrane picture is also presented. Finally, it is expected that this MSc can contribute not only to the Ribeira Belt research, but also to evaluate the importance of using detailed studies and petrochronology to evaluate *P*-*T*-t evolution of metapelites even though some challenges may appear while applying such techniques. More detailed information about each methodology can be found in each article's respective Material and Methods sections.

CHAPTER 2 – RESULTS - ARTICLE APPROVED ON PRECAMBRIAN RESEARCH PUBLISHED IN MAY 2020

Tectonic implications of juxtaposed high- and low-pressure metamorphic field gradient rocks in the Turvo-Cajati Formation, Curitiba Terrane, Ribeira Belt, Brazil

B.S. Ricardo[1]*, F.M. Faleiros[1], R. Moraes[1], O. Siga Júnior[1], G.A.C. Campanha[1]

[1] Instituto de Geociências, Universidade de São Paulo, Rua do Lago, 562, CEP 05508-080, São Paulo, SP, Brazil

*Corresponding author at: IGc-USP (Instituto de Geociências, Universidade de São Paulo), Rua do Lago, 562, CEP 05508-080, São Paulo, São Paulo, Brazil. Tel.: +55 11 3091-3958

E-mail addresses: bruna.ricardo@usp.br (B.S. Ricardo), ffalei@usp.br (F.M. Faleiros), rmoraes@usp.br (R. Moraes), osigajr@usp.br (O. Siga Júnior), ginaldo@usp.br (G.A.C. Campanha)

Keywords: detrital zircon U-Pb ages; metamorphic field gradients; paired metamorphic belts; pseudosection modeling; Ribeira Belt; Neoproterozoic

Abstract

The Turvo-Cajati Formation (TCF) is an important unit forming the Curitiba Terrane, a major segment of the southern Ribeira Belt, SE Brazil. It is composed of rocks of greenschist (LTCF), amphibolite (MTCF) and granulite (HTCF) facies conditions. Previous studies in the HTCF indicate that the unit underwent extensive partial melting under high-pressure conditions (670-810 ºC and 9.5-12 kbar), within the kyanite stability field. In this paper, a study of the metamorphic zoning within the LTCF MTCF is undertaken using pseudosection modeling in the NCKFMASHTO and MnNCKFMASHTO model systems coupled with detrital zircon U-Pb geochronology. Four metamorphic zones are recognized for the LTCF and MTCF: biotite, garnet, staurolite and sillimanite zones, with predominance of sillimanite zone and pressures lower than 8 kbar, as staurolite breaks down straight to sillimanite, without formation of a kyanite zone. Pseudosections yielded metamorphic peak conditions of ~530-560 °C and ~6-7.5 kbar (garnet zone) and ~660-690 °C and ~6-7.5 kbar (sillimanite zone). The metamorphic field gradient is flat and of low to medium pressure, below the typical Barrovian-type baric regime, and different from the HTCF. Available petrological and geochronological data suggest that the TCF comprises a paired low-*P* and high-*P* metamorphic belt, associated with a major Ediacaran suture zone in the southern Ribeira Belt. Probability density plots from detrital zircon U-Pb ages indicate late-Cryogenian-Ediacaran arc-related and Rhyacian sources for all TCF sub-units. This scenario suggests that the TCF is made up of a collisional juxtaposition of an accretionary wedge (HTCF) and a back-arc basin (LTCF and MTCF) on the border of a microplate, which includes a Rhyacian basement microcontinent, the Atuba Complex. It is inferred the high metamorphic gradient recorded in the LTCF and MTCF was related with asthenospheric upwelling in the back-arc region, which also produced extensive partial melting in the Atuba Complex basement.

1. Introduction

The Barrovian-type metamorphism has been described in multiple places all over the World since it was characterized in the Scottish Highlands by George Barrow (1912), such as in Iberian Massif (Catalán *et al*., 2003), between Canada and EUA (Brown and Walker, 1993), in Andes (García *et al*., 2005), in Alps (Burg and Gerya, 2005), among others. Now, it is known to represent a common type of orogenic regional metamorphism (e.g. England & Thompson, 1984). In recent decades, advances in Metamorphic Petrology, such as geothermobarometry, pseudosection modeling and development of software such as THERMOCALC (Powell & Holland, 1988), PERPLEX (Connoly, 2005), Theriak/Domino (de Capitani & Brown 1987; de Capitani 1994) and Gibbs (Spear *et al*.,

2001), allowed the increase of knowledge in mechanisms and processes operating during metamorphism. Also, the relationship with large-scale tectonic processes is better understood with these advances. One interesting tool that allows comparing tectonic regimes of different metamorphic terranes is the metamorphic field gradient (Turner, 1981), a line defined by the metamorphic peak conditions of a rock pile that underwent the same metamorphic event, but with rocks at different depths. Its inclination defines the metamorphic facies series, as well as the d*T*/d*P* regime of the terrane and has a direct connection with the tectonic setting of metamorphism (Turner, 1981; Philpotts & Ague, 2009).

The Southern Ribeira Belt, in southeast Brazil, is formed by several different metamorphic terranes (Basei *et al*., 1992; Faleiros *et al*., 2011), including the Curitiba Terrane, in which the Turvo-Cajati Formation (TCF) is part of (Fig. 1a,b). The TCF is primarily made of metasedimentary rocks, with maximum deposition ages on the Cryogenian-Ediacaran transition, at 650-630 Ma (Faleiros *et al*., 2016), and metamorphism followed closely after its deposition, ca. 590-585 Ma (Faleiros *et al*., 2011, 2016). The TCF consists of several distinct segments that underwent metamorphism under quite different *P-T* conditions, varying from lower greenschist to granulite facies conditions (Faleiros, 2008). One of these segments (Figs. 1, 2), the HTCF, presents a metamorphic peak mineral assemblage of kyanite + K-feldspar + garnet + rutile + quartz + melt, attesting the rock underwent partial melting, under 670-810 ºC and 9.5-12 kbar (Faleiros *et al*., 2011) at 589±12 Ma (Faleiros *et al*., 2011) and 584±4 Ma (Faleiros *et al*., 2016). On the other hand, the greenschist to amphibolite facies rocks (LTCF and MTCF; Fig. 1b) were never subjected to detailed and quantitative petrological and geochronological studies.

The present work investigates the greenschist to amphibolite facies metapelites (LTCF and MTCF) from the TCF to understand its depositional and metamorphic settings. For this, detrital zircon geochronology is presented, as well as mapping of the regional metamorphic zones, mineral chemistry and *P-T* pseudosection modeling. Coupling the results of all data, a model for the sedimentation and metamorphism of the Turvo-Cajati Formation and its tectonic regime is envisaged.

2. Geological setting

The Southern Ribeira Belt is divided into four tectonic domains: Apiaí, Curitiba, Embu and Costeiro/Paranaguá Terranes (Basei *et al*., 1992; Faleiros *et al*., 2011; Passarelli *et al*., 2018, Fig. 1a). They are interpreted as tectonic segments with distinct evolutionary histories that were amalgamed as the result of the collision of the São Francisco-Congo, Paranapanema, Luís Alves and Rio de la Plata Plates in

Neoproterozoic, during the formation of Western Gondwana (Brito Neves *et al*., 1999).

The Turvo-Cajati Formation is a major unit of the Curitiba Terrane, which also includes the Atuba Complex and Capiru Formation. This terrane is located between two strike-slip shear zones with opposite movements: the dextral Lancinha-Cubatão Shear Zone, in the north, and the sinistral Serra do Azeite Shear Zone, in the south (*et al*Fig.1b). The Lancinha-Cubatão Shear Zone is an orogen-parallel structure that presents an average N65E/subvertical orientation and extends for approximately 2100 km (800 km exposed and 1300 km covered by the Paraná Basin; Sadowski, 1991) in southeastern Brazil (Fig. 1a). In the study area (Fig. 2) it comprises a greenschist facies mylonite-cataclasite zone with a width of approximately 200 m. The Lancinha-Cubatão Shear Zone represents an important boundary between regional geochronological domains, separating terranes dominated by Mesoproterozoic metasedimentary units in the north (Apiaí Terrane) and Neoproterozoic metasedimentary units in the south (Curitiba Terrane). It has been interpreted as a reworked Ediacaran suture zone (e.g., Basei *et al*., 2008; Faleiros *et al*., 2011, 2016; Passarelli *et al*., 2011, 2018).

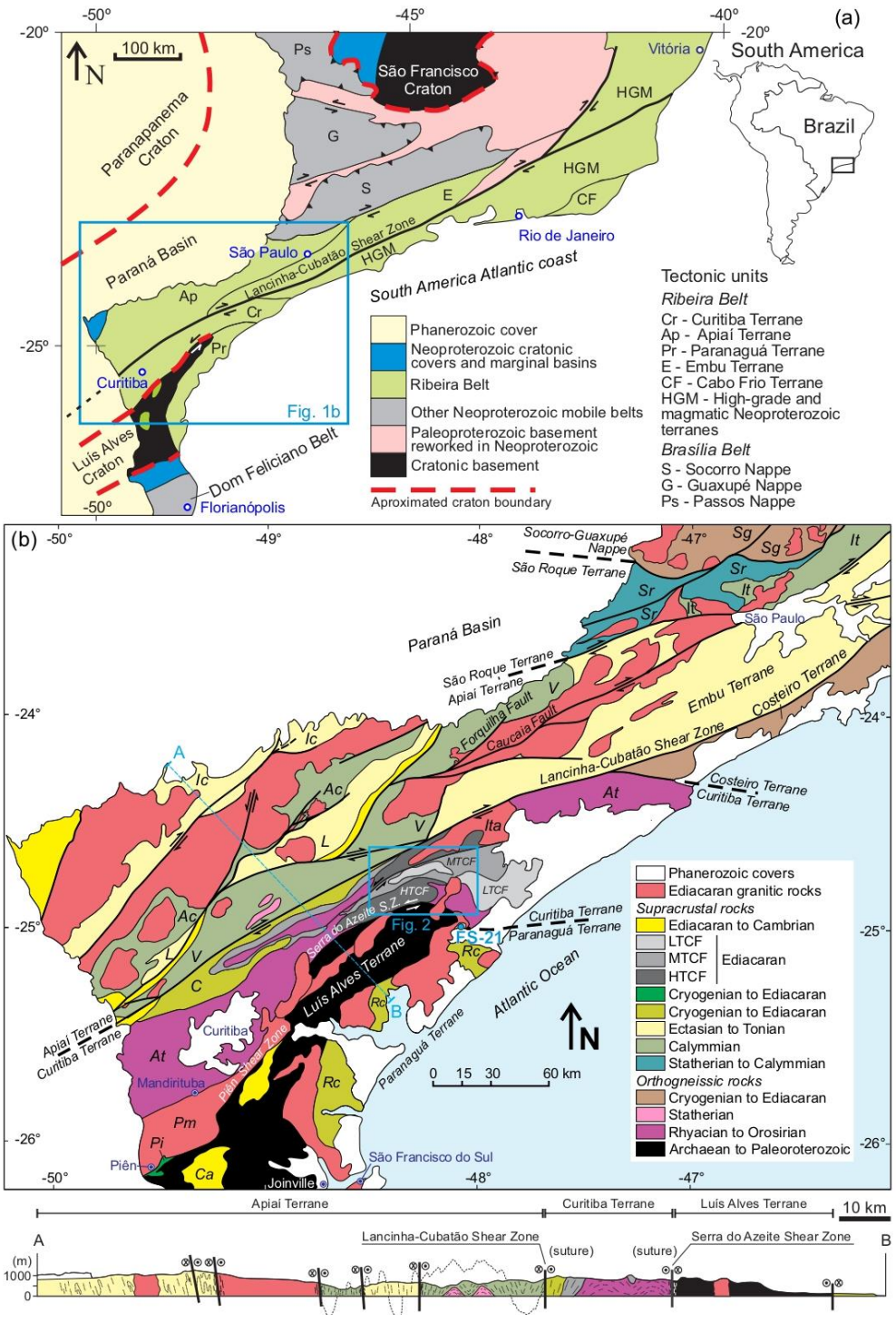

Figure 1(a) Regional geological context of southeastern and south Brazil (adapted from Faleiros et al., 2016). (b) Simplified geotectonic map of the southern and central portions of the Ribeira Belt with location of the study area (modified from Malta et al., 2020). Geological units: Itaiacoca Group (Ic), Água Clara Formation (Ac), Lajeado Group (L), Votuverava Group (V), São Roque Group (Sr), Serra do Itaberaba Group (It), Socorro-Guaxupé Nappe (Sg), Capiru Formation (C), Low, Medium and High Turvo-Cajati Formation (LTCF, MTCF, HTCF), Piên-Mandirituba Suite (Pm), Piên Mafic-Ultramafic Suite (Pi), Rio das Cobras Formation (Rc), Atuba Complex (At) and Campo Alegre Basin (CA). The maps use geographical coordinates in degrees (WGS-84 datum).The Serra do Azeite Shear Zone and its southwest continuation, the Piên Shear Zone, represent the tectonic contact between the Curitiba and Luís Alves Terranes (Fig. 1b; Faleiros *et al*., 2011, 2016; Passarelli *et al*., 2018). The Luís Alves Terrane (Fig. 1b) is a small cratonic remnant composed of Archaean–Paleoproterozoic (ca. 2.7–2.0 Ga.) mafic and leucocratic granulitic gneisses (Hartmann *et*

_al_., 2000; Basei _et al_., 2009; Passarelli _et al_., 2018). K-Ar cooling ages on biotite and amphibole between 2100 and 1700 Ma indicate the Luís Alves Terrane has been stable since the Palaeoproterozoic, with Ediacaran deformation and metamorphism being restricted to shear zones at its margins (Basei _et al_., 2009). Two important tectonic units occur along the southwestern contact between the Curitiba and Luís Alves Terranes: the Piên-Mandirituba granite suite (Fig. 1b), composed of 620-595 Ma arc-related granitoids, and the Piên mafic-ultramafic suite (ca. 650-630 Ma), interpreted as an ophiolite melange (Harara, 2001; Passarelli _et al_., 2018). These units have been interpreted as evidence of a suture zone between the Curitiba and Luís Alves Terranes, and a record of northwestward subduction (Passarelli _et al_., 2018).

The Atuba Complex is a fragment of an Archean crust reworked during the Rhyacian (ca. 2100-2200 Ma, Statherian (~1700 Ma) and Ediacaran (630-590 Ma, Sato *et al*., 2003, 2009). It is mainly composed by TTG-type migmatitic orthogneisses (Sato *et al*., 2003, 2009; Siga Júnior *et al*., 2007; Faleiros & Pavan, 2013). There is no consensus in literature about the interaction between the Atuba Complex and TCF once their contacts are always tectonic. Some authors interpret that the TCF was deposited over the Atuba Complex (e.g., Basei *et al*., 2008), whereas others interpret that the TCF is completely allochthonous (e.g., Faleiros *et al*., 2011). But a detailed provenance study to support any of these interpretations was never conducted. The structural relationships indicate that in most of the Curitiba Terrane the TCF overlays the Atuba Complex (Fig. 1b; C-D cross section in Fig. 2). Nevertheless, the TCF is overthrusted by the Atuba Complex in some regions (A-B cross section in Fig. 2).

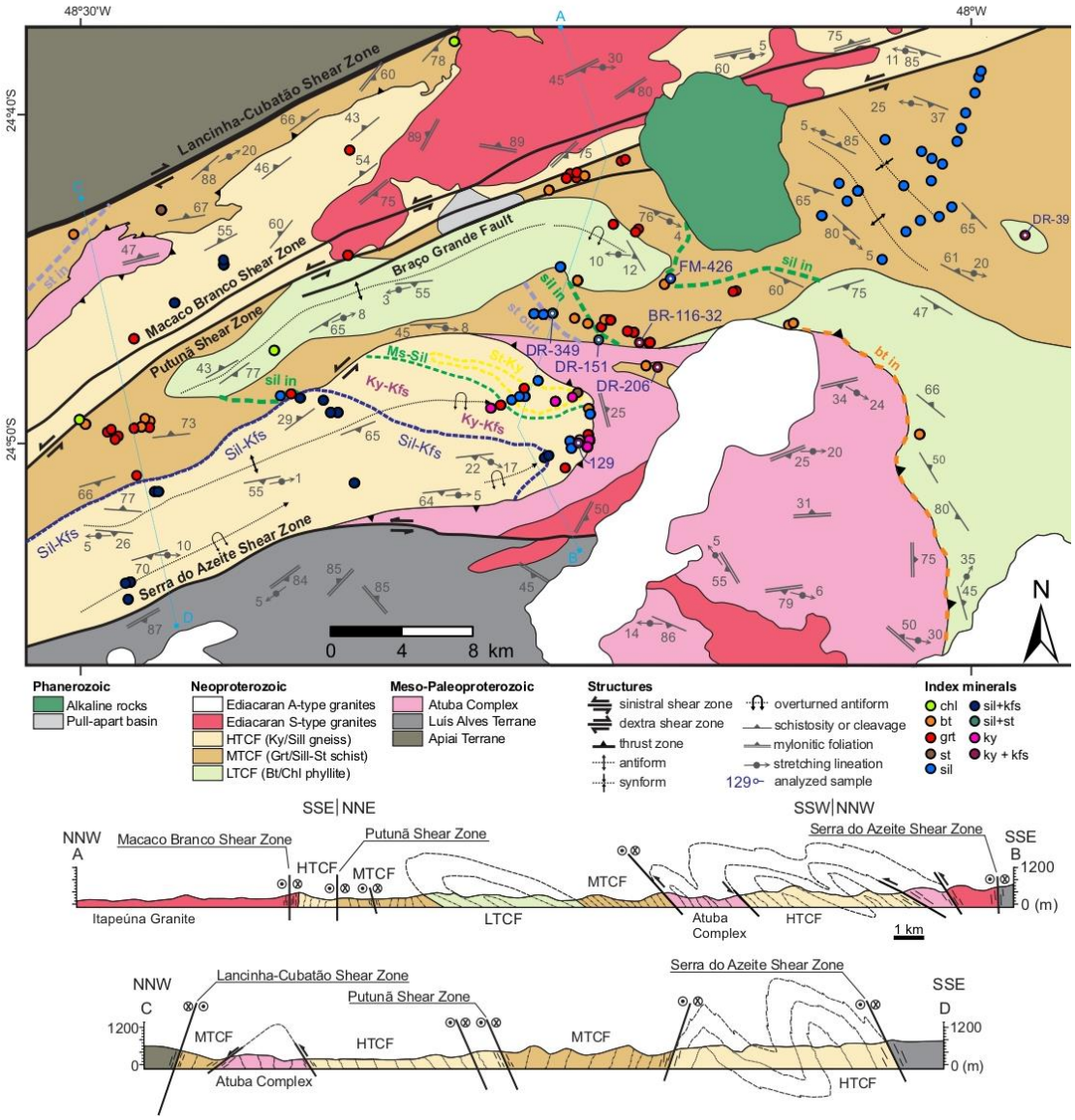

Figure 2 Geologic map and cross sections of the studied portion of the Curitiba Terrane showing sites with recognized metamorphic assemblages and isograds (modified after Faleiros et al., 2016). The map uses geographical coordinates in degrees (WGS-84 horizontal datum). Also shown are the sample localities discussed in the text. See Fig. 1b for the location of the area.

The Turvo-Cajati and Capiru Formations (Fig. 1b) are both considered shallow shelf metasedimentary units (Faleiros *et al*., 2011; Leandro, 2016). Studies with detrital zircon LA-ICP-MS U-Pb data indicate a maximum deposition age of 630-650 Ma for the TCF (Faleiros *et al*., 2016) . The TCF is divided in three sub-units, based on dominant metamorphic degree, that vary from greenschist to granulite facies, where partial melting is regionally recognized (Faleiros & Pavan, 2013; Faleiros *et al*., 2011). These metamorphic units were informally named as Low, Medium and High Turvo-Cajati Formation (LTCF, MTCF and HTCF, respectively; Faleiros *et al*., 2016) and the same denomination is adopted here. These units are organized in ENE-trending blocks bounded by sinistral transcurrent shear zones and their internal contacts are marked

by folded thrust zones (Fig. 2). Inverted metamorphic sequences occur within the blocks, with MTCF rocks overlaying LTCF rocks (A-B cross section in Fig. 2), and within units, with staurolite-kyanite-bearing rocks covered by sillimanite-bearing and kyanite-K-feldspar bearing rocks in the HTCF (Faleiros *et al*., 2011, 2016).

The LTCF is primarily composed by silver or grey phyllites with millimeter-thick sedimentary lamination alternating mica-rich and quartz-rich layers. Phyllites are interleaved with quartzite lens. The MTCF comprises medium to coarse-grained silver to dark grey schists interleaved with marble, calc-silicate rocks and quartzite. The schists are composed of muscovite, biotite, quartz, chlorite, garnet with subordinated staurolite and sillimanite.

The HTCF has a succession of mineral zones composed of: staurolite-kyanite, kyanite-K-feldspar and sillimanite-K-feldspar, all quartz and garnet-bearing. Metamorphic temperatures range within 670-810 ºC (Faleiros *et al*., 2011) with pressure around 9.5-12 kbar and sillimanite recording decompression (Faleiros *et al*., 2011). The age of the metamorphic peak in the high-temperature rocks is constrained by monazite chemical dating at 589 ± 12 Ma (Faleiros *et al*., 2011) and by LA-ICP-MS U-Pb dating of zircon at 584 ± 4 Ma (Faleiros *et al*., 2016).

Rocks from the Atuba Complex and TCF were intruded by elongated bodies of foliated, peraluminous, garnet-muscovite-biotite granites, as the Itapeúna Suite (Fig. 1b) and other stocks (Fig. 2), which have been interpreted as S-type granites recording collisional magmatism (Faleiros and Pavan, 2013). Zircon U-Pb SHRIMP data for one of these stocks gave a concordia crystallization age of 592 ± 3 Ma (Milani, 2020).

The Capiru Formation contains metadolomite, phyllite, schist and quartzite, all of them of very low to low temperature metamorphic conditions (Guimarães *et al*., 2002, Faleiros & Pavan, 2013; Faleiros, 2017; Santos *et al*., 2018). Detrital zircon U-Pb data indicate maximum depositional age of 1080 Ma (Leandro, 2016).The contact between the Capiru Formation and Turvo-Cajati Formation is tectonic and marked by a high-angle shear zone where the Capiru Formation overlies the Turvo-Cajati Formation (cross section in Fig. 1b; Faleiros, 2008).

3. Methods

3.1 Mineral chemistry

The mineral phases were analyzed with a JEOL JXA-FE-8530 Electron Probe Microanalyser (EPMA) hosted at NAP Geoanalítica, Institute of Geosciences, University of São Paulo. Operations conditions were 15 kV and 20 nA, for spot analyses and 15 kV and 150 nA for compositional maps, always with a beam size of 5 µm. The images were

treated in the program ImageJ2 (Rueden *et al*., 2017). Structural formula of each mineral phase was calculated with software AX by Tim Holland (https://www.esc.cam.ac.uk/research/research-groups/research-projects/tim-hollands-software-pages/ax).

3.2 Thermodynamic modeling

P-T pseudosections were calculated with the software Perplex (Connolly, 2005) and using database hp11ver (Holland & Powell, 2011). Solution models used for muscovite, chlorite, biotite, garnet, staurolite, cordierite, ilmenite and silicate melt are from White *et al*. (2014a), epidote from Holland and Powell (2011) and feldspar from Fuhrman & Lindsley (1988). Water is considered a pure fluid phase and in excess for melt-absent calculations. For melt-present calculations water content was chosen so that rocks were H_2O-saturated immediately below the solidus (cf. White *et al*., 2001). Fe^{3+} was estimated based on charge balance in minerals chemical formula and for the amount in the bulk rock composition it was set to reproduce the contents of observed Fe^{3+}-bearing phases (e.g., epidote, hematite) in studied samples.

Four pseudosections were modeled using the bulk rock composition from samples DR-39 (LTCF, garnet zone), DR-206 (LTCF, garnet zone), DR-151 (MTCF, sillimanite zone). The fourth pseudosection presented is an updated calculation obtained from sample 129A (HTCF) originally presented in Faleiros *et al*. (2011), with current solutions models. The composition of samples DR-206 and DR-151 were built from modal proportions and mineral chemistry obtained with the EPMA. Therefore, the modal percentage of each mineral in a thin section was multiplied by its density to obtain the weight of each phase. This number was normalized by 100%. Then, the weight of each mineral was multiplied by its chemical composition divided in oxide by oxide in molar proportion and again normalized by 100%. The molar proportion of each oxide was obtained by the sum of all molar proportion on each. The fluid was considered pure H_2O.This procedure was adopted to these samples because they had appreciable degrees of weathering and would not produce reliable bulk rock chemical composition. To obtain the bulk composition of sample DR-39 was crushed to 200 mesh, then analyzed using a XRF PANalytical equipment, model AXIOS MAX Advanced, following the routine by Mori *et al*. (1999) also in Institute of Geosciences, University of São Paulo. Composition from sample 129A is the same presented in Faleiros *et al*. (2011). The pseudosection modeling was made with the software Perple_X using the system MnNCKFMASHTO. Exception is made to sample 129A, which was modeled in NCKFMASHTO, as Mn has small effect in high metamorphic conditions such as

expected for this sample (White *et al*., 2014b).

3.3 Detrital zircon U-Pb geochronology

Five samples from TCF were selected for detrital zircon U-Pb geochronology. Mineral separation and zircon U-Pb geochronology were undertaken at the University of São Paulo. Zircon was extracted from 100-200 mesh fractions using standard isodynamic, gravimetric and magnetic techniques. The grains were hand-picked using a binocular microscope and mounted in epoxy resin. Cathodoluminescence (CL) and scanning electron microscope (SEM) images were used to identify points for U-Pb analysis, avoiding fractures, inclusions or metamict areas that may have experienced Pb loss.

The decay constants and the $^{238}U/^{235}U$ ratio of Steiger & Jager (1977) have been used to calculate ages. U-Pb analyses by LA-MC-ICP-MS were carried out on a Thermo-Finnigan Neptune MC-ICP-MS coupled with a Photon-Machines excimer ArF laser (193 nm) ablation system. The dates were treated using the software Isoplot (Ludwig, 2003). Only isotopic data with Total common Pb contents below 6% and concordance of 100 ± 10 were used for age calculations. Results are presented in combined probability density plots. The ages for zircon grains older and younger than 1300 Ma are derived from $^{207}Pb/^{206}Pb$ and $^{206}Pb/^{238}U$ ratios respectively, following correction for common Pb based on measured ^{204}Pb and the Cumming and Richards (1975) model Pb composition for the likely age of the zircon grains.

4. Petrography, mineral chemistry and mapping of metamorphic zones

Petrography was made in 22 samples from LTCF and MTCF subunits that will hereinafter be treated together (LMTCF). Summarization of the results is presented in Table 1 and the distribution of these samples is presented in Figure 2. Based on petrography and key mineral assemblages, four different metamorphic zones are defined and mapped for LMTCF metamorphic subunits. Those metamorphic zones are described in this section and represent a progressive increase in temperature conditions: biotite, garnet, staurolite and sillimanite zones. The spatial distribution of them suggests general sillimanite zone predominance in LMTCF (Fig. 2). Representative samples of the garnet zone (DR-39 and DR-206, Figs. 3 and 4) and of the sillimanite zone (DR-151, Fig. 5) were chosen to further studies and described in detail in this section. Other relevant photomicrographs are presented in Figures 6 a-d. Representative chemical analyses of each sample are presented in Tables 2 and 3.

Four zones are recognized in literature for HTCF, with the specific assemblages: muscovite-sillimanite, staurolite-kyanite, kyanite-K-feldspar and sillimanite-K-feldspar

(Faleiros *et al*., 2011, Fig. 2). Sillimanite occurs as a retrometamorphic decompression-related phase in all HTCF rocks, which present evidence of peak metamorphism within the kyanite stability field (Faleiros *et al*., 2011).

Table 1 Summarization of petrology results with described samples, lithology, main mineral assemblage and inferred metamorphic conditions, such as zone and temperature.

Sample	Lithology	Mineral Assemblage	Metamorphic Zone	Inferred T
SM-586A	Chl-Ms-Pl-Bt-Qtz schist with Ep	Chl Bt Ep	Biotite	< 450°C
DR-359	Qtz-Ms schist with Bt and Chl	Bt Chl	Biotite	< 450°C
DR-188	Pl-Bt-Chl-Qtz-Ms schist with Ep	Bt Chl Ep	Biotite	< 450°C
DR-187B	Chl-Bt-Ms-Qtz schist	Bt Chl	Biotite	< 450°C
DR-354	Ms-Bt-Qtz-Pl schist	Bt	Biotite	< 450°C
SM-590	Grt-Pl-Chl-Ms-Qtz schist	Grt Bt Chl	Garnet	550-630°C
DR-148B	Grt-Bt-Qtz-Ms schist	Grt Bt	Garnet	550-630°C
DR-150B	Ms-Qtz-Pl-Bt schist with Grt	Grt Bt	Garnet	550-630°C
SM-587	Grt-Bt-Pl-Qtz-Ms schist	Grt Bt	Garnet	550-630°C
SM-598B	Bt-Grt-Pl-Ms-Qtz schist	Grt Bt	Garnet	550-630°C
DR-206A	Grt-Pl-Bt-Qtz-Ms schist	Grt Bt	Garnet	550-630°C
DR-206B	Grt-Pl-Qtz-Bt-Ms schist with Chl	Grt Bt Chl	Garnet	550-630°C
DR-144B	Pl-Chl-Grt-Bt-Ms-Qtz schist	Grt Bt Chl	Garnet	550-630°C
DR-149	Pl-Qtz-Bt schist with Grt and Chl	Grt Bt Chl	Garnet	550-630°C
DR-396	Chl-Grt-Pl-Bt-Qtz schist with Ms	Grt Bt Chl	Garnet	550-630°C
DR-39	Grt-Ms-Pl-Chl-Bt-Qtz schist	Grt Bt Chl	Garnet	550-630°C
SM-592	Chl-Bt-St-Grt-Pl-Qtz-Ms schist	St Grt Bt	Staurolite	550-630°C
DR-151A	Pl-St-Grt-Bt-Qtz-Ms schist with Sil	Sil St Grt Bt	Sillimanite	620-690°C
DR-151	Pl-Grt-Bt-St-Qtz-Ms schist with Sil	Sil St Grt Bt	Sillimanite	620-690°C
DR-349B	Sil-Grt-St-Bt-Qtz-Ms schist	Sil St Grt Bt	Sillimanite	620-690°C
DR-351C	Grt-Pl-Sil-Bt-Qtz-Ms schist	Sil Grt Bt	Sillimanite	> 620°C
DR-353	Grt-Pl-Sil-Bt-Qtz-Ms schist	Sil Grt Bt	Sillimanite	> 620°C

Table 2: Representative microprobe analyses of garnet and plagioclase from Turvo-Cajati Formation rocks.

Mineral	Garnet				Plagioclase	
Sample	DR349B	DR151	DR-39	DR-39	DR206	DR151

	rim	core	rim	core	Rim	core			
SiO_2	36.47	36.28	36.84	36.65	36.76	36.64		60.89	67.25
TiO_2	0.06	0.12	0.05	0.04	0.16	0.20		0.01	0.00
Al_2O_3	21.09	20.97	21.53	21.33	20.98	20.92		25.08	21.47
Cr_2O_3	0.01	0.01	0.03	0.00	0.02	0.00		0.01	0.00
Fe_2O_3	1.07	0.29	0.00	0.40	0.24	0.42		0.14	0.05
FeO	31.57	25.96	38.40	37.10	21.56	21.58		0.09	0.00
MnO	2.44	7.04	0.94	1.92	14.23	14.27		0.00	0.00
MgO	1.54	0.7	2.26	2.05	1,.07	1.14		0.00	0.00
CaO	5.37	7.14	0.29	0.91	4.86	4.62		5.86	1.03
Na_2O	0.00	0.00	0.00	0.00	0.00	0.00		8.12	10.70
K_2O	0.00	0.00	0.00	0.00	0.00	0.00		0.08	0.04
Total (%)	99.61	98.51	100.34	100.40	9.87	99.79		100.27	100.54
Oxigen	12	12	12	12	12	12		8	8
Si	2,956	2,971	2,978	2,967	2,980	2,974		2,698	2,923
Ti	0.004	0.007	0.003	0.002	0.010	0.012		0.001	0.000
Al	2,015	2,025	2,052	2,036	2,005	2,002		1,310	1,100
Cr	0.001	0.001	0.002	0.000	0.001	0.000		0.001	0.000
$Fe^{3=}$	0.065	0.018	0.000	0.024	0.014	0.026		0.005	0.002
Fe^{2+}	2.14	1,778	2,596	2,512	1,462	1,465		0.003	0.000
Mn	0.168	0.488	0.064	0.132	0.977	0.981		0.000	0.000
Mg	0.186	0.086	0.272	0.247	0.129	0.138		0.000	0.000
Ca	0.466	0.627	0.025	0.079	0.422	0.402		0.278	0.048
Na	0.000	0.000	0.000	0.000	0.000	0.000		0.698	0.902
K	0.000	0.000	0.000	0.000	0.000	0.000		0.004	0.002
Total	8,000	8,000	7,992	8,000	8,000	8,000		4,996	4,978
Prp	6.28%	2.89%	9.20%	8.32%	4.31%	4.62%	Ab	0.28	0.95
Grs	15.74%	21.05%	0.85%	2.66%	13.37%	12.18%	An	0.72	0.05
Alm	72.30%	59.68%	87.79%	84.58%	48.90%	49.06%			
Sps	0.57%	16.38%	2.16%	4.44%	32.68%	32.85%			

Table 3 Representative microprobe analyses of muscovite. biotite. chlorite and staurolite from Turvo-Cajati Formation rocks.

Mineral	Muscovite			Biotite			Chlorite	Staurolite
Sample	DR39	DR206	DR151	DR39	DR206	DR151	DR39	DR151
SiO_2	45.35	47.29	46.30	34.61	36.40	34.50	28.42	27.23
TiO_2	0.29	0.28	0.52	1.39	1.44	1.80	0.08	0.63
Al_2O_3	36.23	35.35	37.61	18.57	18.90	20.56	23.26	54.51

Cr_2O_3	0.00	0.00	0.00	0.00	0.00	0.00	0.00	0.02
Fe_2O_3	0.00	0.00	0.00	2.64	0.01	0.00	0.00	0.00
FeO	1.69	1.41	1.06	19.33	18.37	23.43	23.60	14.35
MnO	0.00	0.00	0.02	0.32	0.12	0.05	0.07	0.03
MgO	0.56	1.11	0.41	9.31	9.47	7.00	11.24	0.89
CaO	0.00	0.11	0.02	0.02	0.05	0.00	1.05	0.00
Na_2O	0.56	0.25	1.45	0.06	0.09	0.12	1.21	0.01
K_2O	10.88	10.47	9.28	8.97	8.52	9.36	0.07	0.01
Total (%)	95.66	96.27	96.66	95.21	93.36	96.82	89.00	97.67
Oxigen	11	11	11	11	11	11	14	46
Si	3,021	3,108	3,018	2,658	2,789	2,631	2,905	7,583
Ti	0.015	0.014	0.025	0.080	0.083	0.103	0.006	0.131
Al	2,853	2,739	2,890	1,681	1,708	1,849	2,803	17,896
Cr	0.000	0.000	0.000	0.000	0.000	0.000	0.000	0.005
Fe^{3+}	0.000	0.000	0.000	0.153	0.001	0.000	0.000	0.000
Fe^{2+}	0.094	0.077	0.058	1,242	1,177	1,495	2,017	3,342
Mn	0.000	0.000	0.001	0.021	0.008	0.003	0.006	0.007
Mg	0.056	0.109	0.040	1,066	1,082	0.796	1,712	0.368
Ca	0.000	0.008	0.001	0.001	0.004	0.000	0.115	0.000
Na	0.073	0.032	0.183	0.008	0.013	0.018	0.241	0.003
K	0.925	0.878	0.772	0.879	0.833	0.911	0.009	0.004
Total	7,037	6,965	6,989	7,789	6,756	7,806	9,813	29,339

4.2. Biotite Zone

The biotite schist is composed of muscovite (25-30%) + quartz (25-30%) + biotite (10-15%) + plagioclase (5-10%) + ilmenite (10%) ± chlorite (10-15%) ± epidote (<3%), which form fine-grained granolepidoblastic matrix. Ilmenite is primarily fine-grained and oriented along the main S_2 continuous cleavage, although locally, it is coarse-grained and surrounded by the S_2, suggesting it grown pre-kinematic to S_2.

4.3. Garnet Zone

All samples from the garnet zone have similar mineral assemblage, with the exception of chlorite, which occurs in just some samples. The garnet-chlorite-plagioclase-biotite schist has fine to medium-grained, lepidoblastic matrix composed of muscovite (~10%), biotite (25-30%) and chlorite (~10%), all of them defining the S_2 cleavage. Bands with < 0.2 mm of thickness dominated by quartz (25-30%) and plagioclase (~20%) present interlobate granoblastic texture. Garnet (5-10%) has an average of 2 mm diameter, is anhedral and its inclusions present spiral shaped forms,

continuous with S_2 in matrix, which allow to interpret its growth as syn-S_2. Locally, some garnet crystals are elongated, well-formed and occur surrounded by the matrix foliation without external relation to it, i.e the foliation preserved inside the garnet grains is not continuous with matrix foliation. The presence of mica fish grains is evidence that non-coaxial shear acted during foliation development.

4.3.1. Sample DR-39 (LMTCF)

Sample DR-39 has main discrete crenulation cleavage S_2 defined by biotite (~20%), chlorite (~15%), muscovite (~10%) and ilmenite (~12%) in lepidoblastic domains, with quartz (~20%) and plagioclase (~15%) forming granoblastic layers. Some lepidoblastic cleavage domains are essentially composed of chlorite with minor epidote and plagioclase contents. Locally, quartz occurs as centimeter fish-shaped ribbons. Garnet porphyroblasts (~8%) are anhedral, with ilmenite inclusions oriented along an internal wavy foliation in continuity with the external foliation, denoting its syn S_2 growth (Fig. 3a).

Garnet is enriched in Fe and Mn, as reflected by Xalm ($Fe^{2+}/(Fe^{2+}$ + Mg + Ca + Mn)) and Xsps ($Mn/(Fe^{2+}$ + Mg + Ca + Mn)) values of 0.47-0.53 and 0.31-0.37, respectively. There is smooth variation between core and rim. Xalm and Xprp= $Mg/(Fe^{2+}$ + Mg + Ca + Mn) slightly increases towards rims, while Xsps and Xgrs= $Ca/(Fe^{2+}$ + Mg + Ca+ Mn) have bell-shaped profiles but with small variation 0.320-0.337 and 0.12-0.14, respectively (Fig. 3b-g).Biotite and chlorite have slightly variable X_{Mg}= (Mg/Mg+Fe) contents of 0.42-0.46 and 0.46-0.48, respectively, whereas muscovite has a more pronounced X_{Mg} variation, between 0.33 and 0.6. Plagioclase presents An $(Ca/(Ca+Na))_{35-40}$ contents.

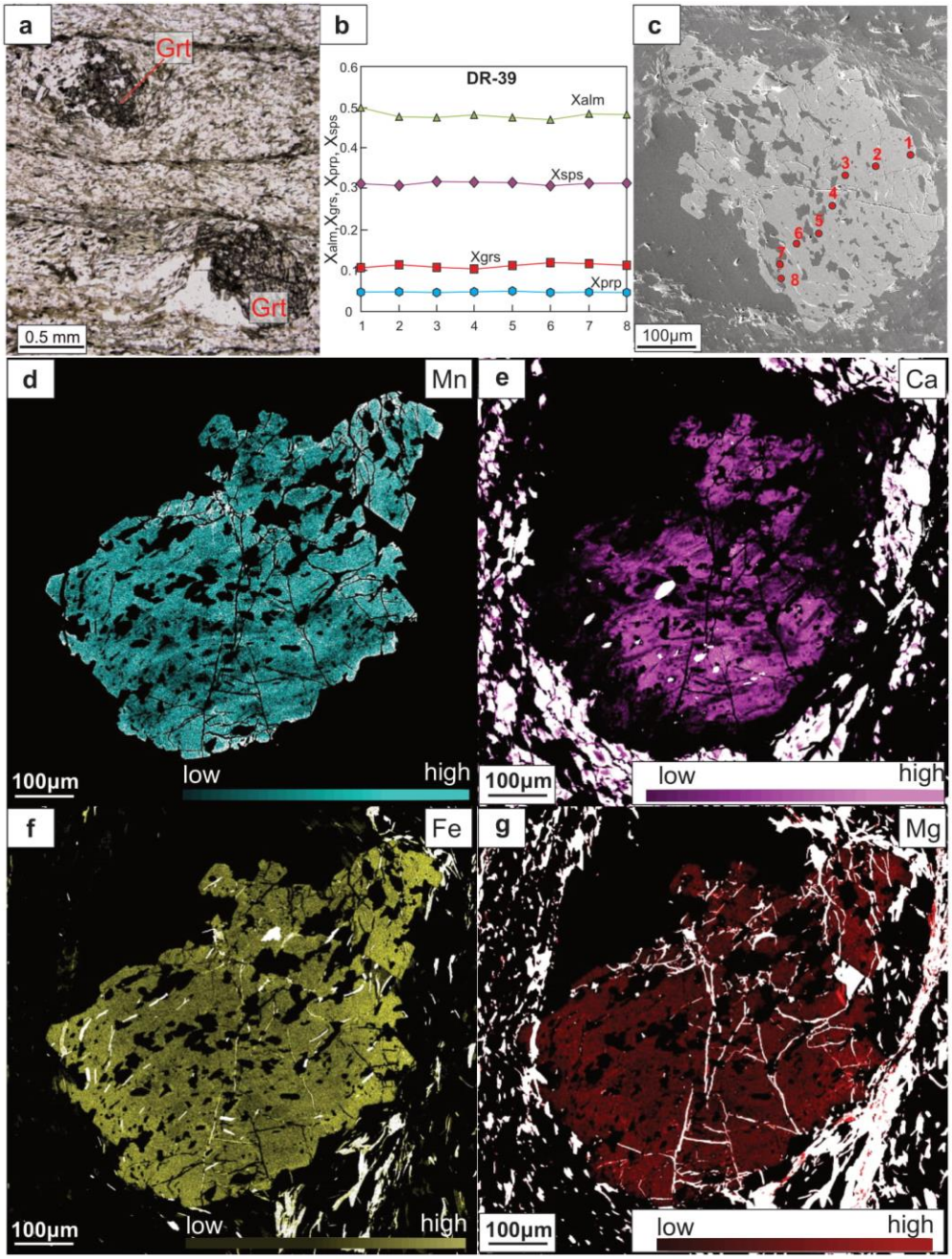

Figure 3 Detailed data from sample DR-39. (a) Optical micrographs representing garnet grains orientated along S2 cleavage. (b) Chemical garnet profiles of each garnet molecule: almandine (Xalm), spessartine (Xsps), pyrope (Xprp) and grossular (Xgrs). (c) Punctual spots where each chemical analyses where taken and approximated spot ratio. (d-g) Compositional maps in garnet grain of each element Mn (d), Ca (e), Fe (f) and Mg (g).

4.3.2. Sample DR-206 (LMTCF)

In the sample DR-206, the S_2 schistosity is primarily defined by muscovite (~30%), biotite (23%) and ilmenite (~2%), with minor chlorite (~2%) associated with biotite, which form lepidoblastic layers. These layers are interleaved with granoblastic layers composed of quartz (~20%) and plagioclase (~13%). Garnet porphyroblasts have mineral inclusions oriented in continuity with the S_2 matrix foliation, attesting its syn-S_2

growth. Some garnet porphyroblasts have deformation shadows and mineral inclusions oriented along a foliation with no continuity with the external S_2 foliation (Fig. 4b).

Chemical zonation in garnet grains is more prominent and concentric in this sample. Garnet content is Fe-rich with Xalm varying between 0.56 and 0.71, with Fe^{2+} and Mg (Xpyp varies from 0.02-0.07) increasing toward rims. Bell-shaped profiles occur with Xsps (0.06-0.20) and Xgrs (0.15-0.22) (Fig. 4a-f). The core is significant bigger than the rim and the geographic core seems to match the compositional core. Biotite has a relatively constant X_{Mg} of 0.44-0.48. Plagioclase has a small compositional variation within An_{26-28}.

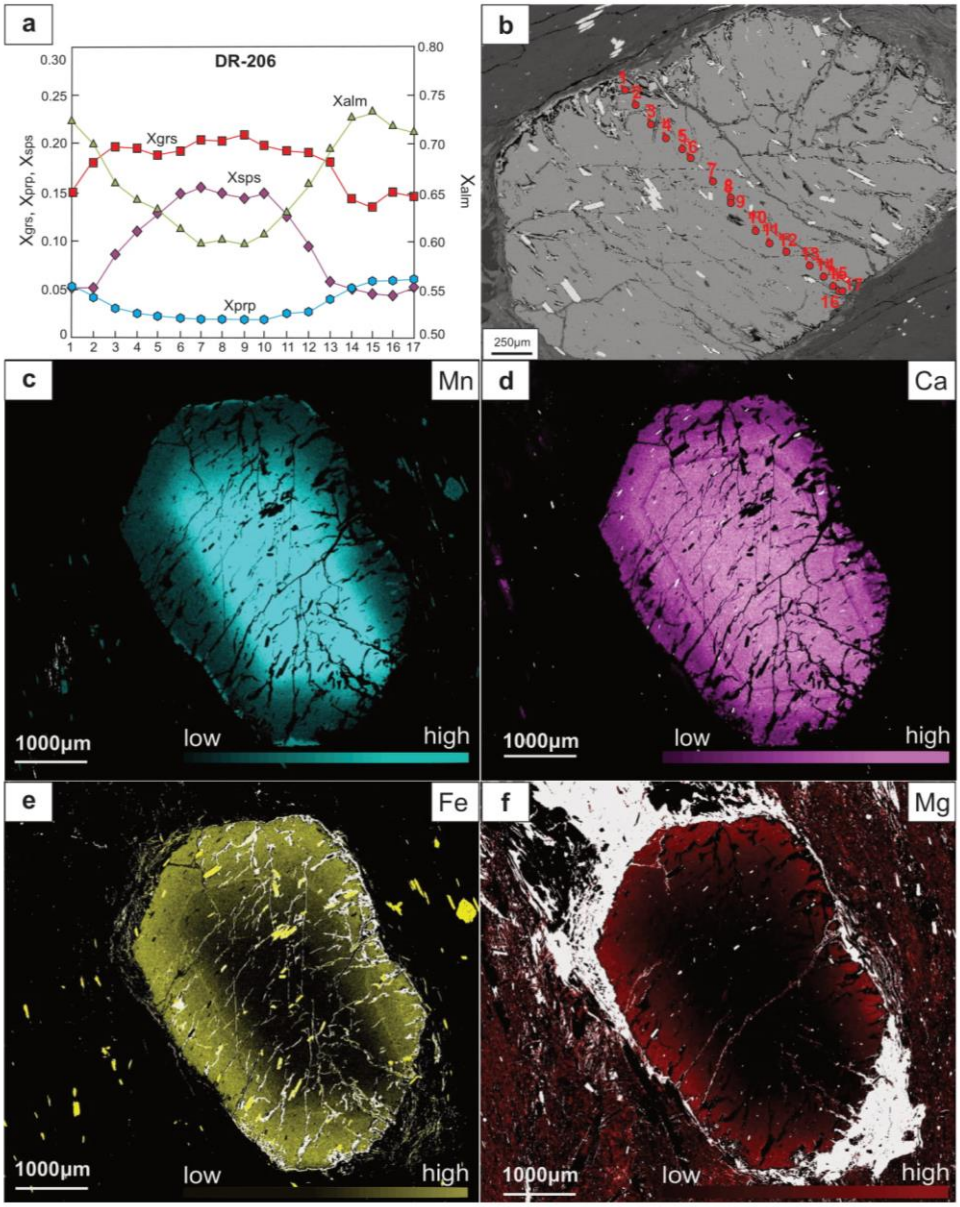

Figure 4 Detailed data from sample DR-206. (a) Chemical garnet profiles of each garnet molecule: almandine (Xalm), spessartine (Xsps), pyrope (Xprp) and grossular (Xgrs). (b) Punctual spots where each chemical analyses where taken and approximated spot ratio. (c-f) Compositional maps in garnet grain

of each element Mn (c), Ca (d), Fe (e) and Mg (f).

4.4. Staurolite Zone

Samples from the staurolite zone have a mineral assemblage composed of staurolite (<10%), biotite (10-20%), garnet (<10%), quartz (10-20%), muscovite (25-30%), with or without plagioclase (0-15%) and ilmenite (<5%). A compositional layering is defined by 0.2 to 0.5 mm thick layers, dominated by muscovite and biotite, interleaved with granoblastic quartz-plagioclase-rich ones. Garnet and staurolite porphyroblasts are 3 to 8 mm in diameter, euhedral and randomly distributed in the rock. The S_2 foliation wraps around garnet grains. Staurolite crystals occur oriented along the S_2, and present mineral inclusions oriented along an internal foliation in continuity to matrix foliation, indicating syn-S_2 growth. The S_2 foliation was later deformed in SC pairs, sometimes fracturing staurolite grains.

4.5. Sillimanite Zone

Two sillimanite-zone mineral assemblages are recognized, with or without staurolite. In staurolite-bearing ones, the assemblage is composed of sillimanite (<5%), staurolite (~7%), garnet (7-10%), biotite (~15%), muscovite (~30%), quartz (~25%), plagioclase (~5%) and ilmenite (<5%). Porphyroblasts of garnet and staurolite are 5 to 9 mm long. Sillimanite occurs in the matrix as fibrolite needle clusters, generally associated with biotite.

The S_2 schistosity is the main foliation and defined by biotite and muscovite, which is truncated by staurolite and garnet porphyroblasts (Fig. 5a). Staurolite grains have an internal foliation that may present continuity to external foliation, indicating syn-S_2 growth. Garnet porphyroblasts follow the same pattern and, occasionally, the inclusions define a spiral pattern, indicating its rotation and syn-S_2 growth. Nevertheless, some crystals might present also internal foliation without continuity with extern alone, suggesting that garnet grains have more than one generation. The prekinematic garnet porphyroblasts are more common than the synkinematic ones. Crenulations affect S_2 and form F_3 open folds with rounded hinge lines.

The second mineral assemblage is composed of sillimanite (15%), garnet (<5%), biotite (~20%), muscovite (~30%), quartz (~20%), plagioclase (~10%) and ilmenite (<%5). Muscovite-biotite-rich layers are 0.3 to 0.8 mm thick and present lepidoblastic texture. They are interleaved with granoblastic layers composed of medium-grained quartz and plagioclase. Garnet porphyroblasts are inferred as synkinematic to S_2 schistosity, as their inclusion patterns are continuous to the external foliation. Sillimanite

occurs as fibrolite and also form cluster with biotite defining the S_2 orientation. No K-feldspar is recognized in any of these two sillimanite-bearing assemblages.

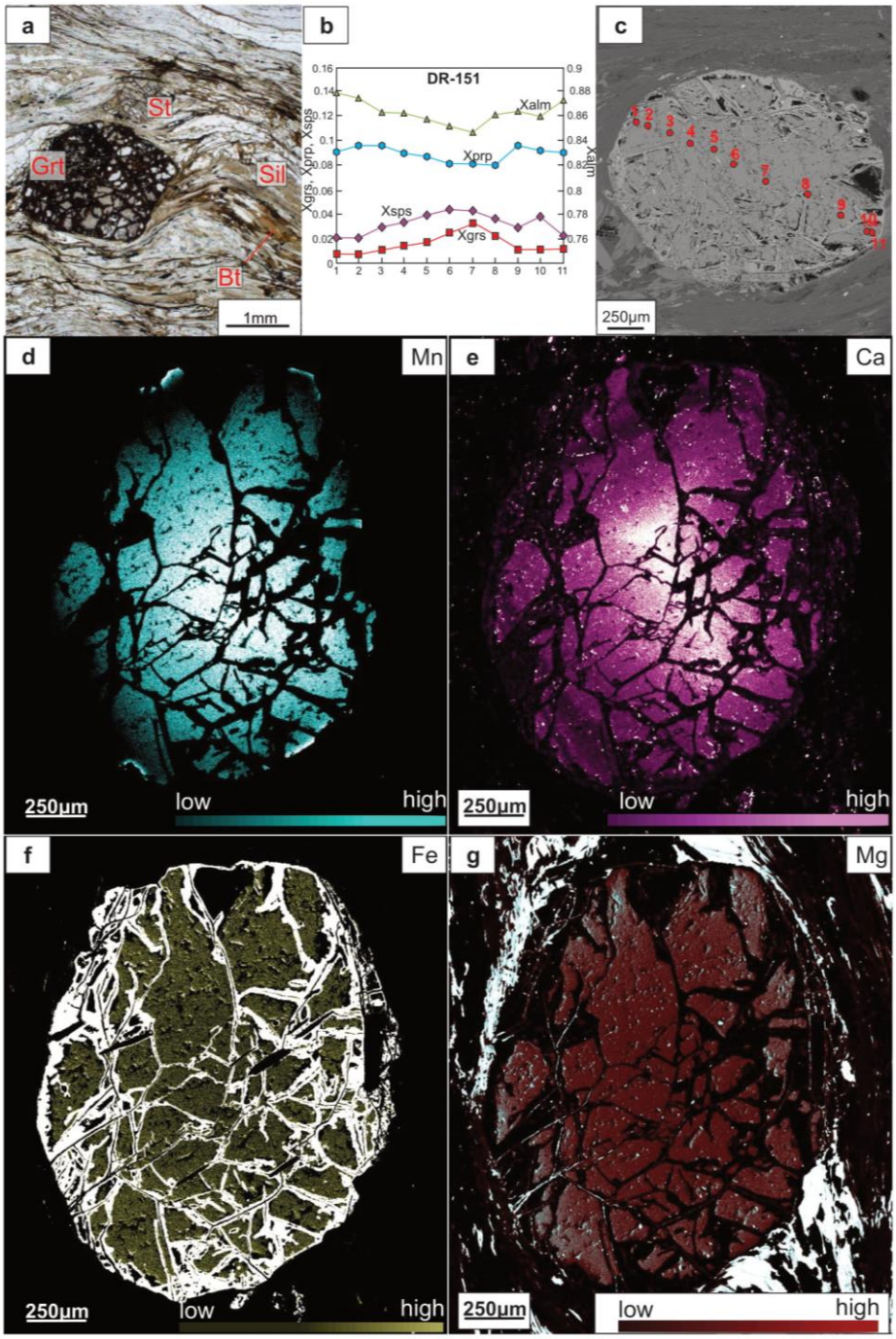

Figure 5: Detailed data from sample DR-151. (a) Optical micrographs representing garnet, sillimanite and staurolite grains in equilibrium orientated along S2 schistosity (b) Chemical garnet profiles of each garnet molecule: almandine (Xalm), spessartine (Xsps), pyrope (Xprp) and grossular (Xgrs). (c) Punctual spots where each chemical analyses where taken and approximated spot ratio. (d-g) Compositional maps in garnet grain of each element Mn (d), Ca (e), Fe (f) and Mg (g).

4.5.1 Sillimanite-Staurolite zone from LMTCF (sample DR-151)

Sample DR-151 is composed of well-developed lepidoblastic muscovite- and

biotite-rich layers interleaved with granoblastic layers rich in quartz (~20%) and plagioclase (5%). A S_2 schistosity is defined by alignment of muscovite (~40%) and biotite (~10%). It is truncated by porphyroblasts of staurolite (~13%) and garnet (~7%). Garnet grains are euhedral and 0.8 to 3 mm in size. The porphyroblasts are molded by the S_2 schistosity. Some garnet porphyroblasts have internal foliation with signs of rotation and without continuity to matrix S_2foliation, suggesting they are pre-S_2. The staurolite porphyroblasts are smaller, 0.6 to 1.5 mm long, prismatic and sub-euhedral. Some staurolite grains are considered syn-S_2, as they are aligned withS_2, whereas other grains are oblique to the S_2 foliation, suggesting they grew late in relation to its generation. Sillimanite (~3%) occurs as fibrolite orientated in S_2, generally associated with biotite (Fig.5a). Ilmenite (<2%) is scarce, mainly orientated along S_2, but may occur as inclusions in garnet and staurolite porphyroblasts.

In sample DR-151, concentric and prominent chemical variation occurs in garnet grains. Chemical core almost coincides with geographic core. Discrete variation occurs in Fe^{2+} and Mg, where their contents increase towards garnet rims (0.84-0.87 and 0.082-0.098 Xalm and X pyr, respectively) (Fig. 5b-g). On the other hand, Mn and Ca have strong variation and bell-shaped profiles increasing in core (0.022-0.045 and 0.008-0.034, Xsps and Xgrs respectively). Plagioclase is very poor in calcium, with An_{1-5}. X_{Mg} contents are slightly variable in biotite (0.33-0.35) and muscovite (0.38-0.47). In staurolite, X_{Mg} content also have small variation, with slightly bell-shaped profile with high value in core, 0.009-0.011.

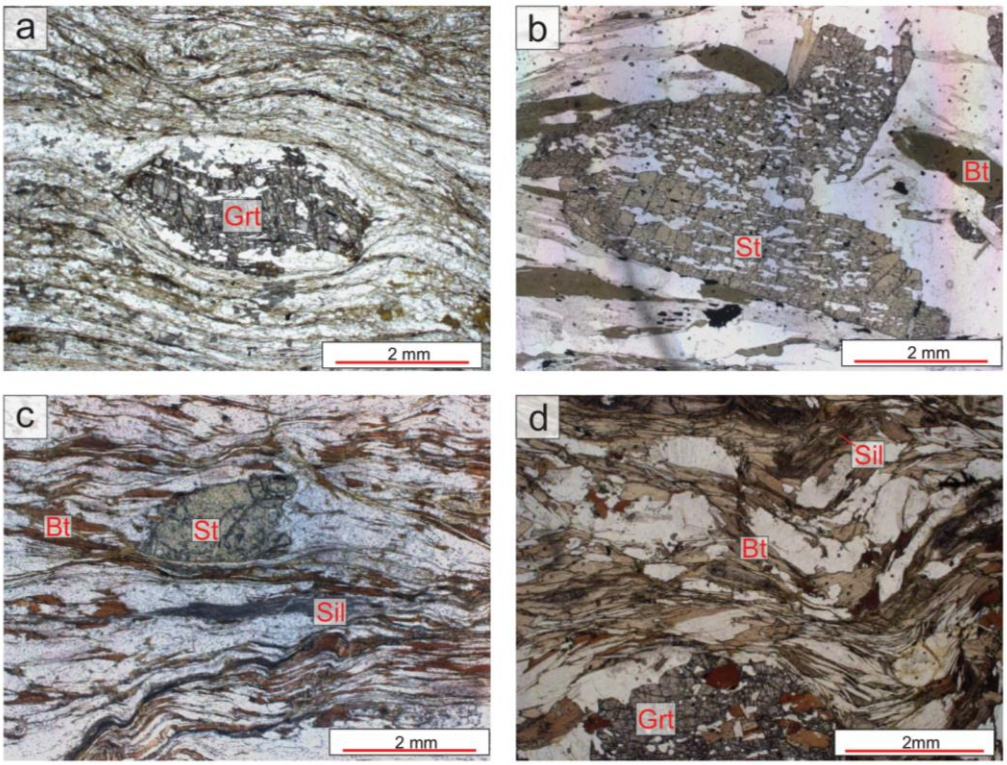

Figure 6 Optical micrographs from microstructures described in petrology section (a) garnet grain oriented along S2 schistosity in sample DR-206 (b) porphyroblast of staurolite orientated along S2 schistosity in sample DR-378. (c) sillimanite and staurolite in equilibrium orientated along S2 schistosity defined by muscovite and biotite alignment in sample DR-349 (f) sillimanite and garnet also orientated along S2 schistosity in sample DR-352 without staurolite in its mineral assemblage.

5. Pseudosection modeling

5.1 Low+Medium Turvo-Cajati Formation (LMTCF)

5.1.1 Garnet-Biotite-Chlorite zone (samples DR-39 and DR-206)

Sample DR-39 has a mineral assemblage of Grt+Bt+Chl+Pl+Ep+Qtz+Ms+Ilm. Its chemical composition is presented in Table 4. The *P-T* pseudosection modeled for this sample presents fields with chlorite and plagioclase below 550-600 °C. Biotite occurs at medium to high metamorphic conditions, above 450 °C (Fig. 7). Garnet only occurs at pressures higher than 6 kbar. The pseudosection is countered with compositional isopleths of X_{Mg} in biotite (0.45-0.47), contents of almandine (0.50-0.52) in garnet and anorthite (0.30-0.45) in plagioclase and epidote mode (2-6%mol) (Fig. 7). The measured mineral compositions within the peak assemblage field intersect at 530-560°C and 6-7 kbar (blue field and star in Fig. 7), which is inferred as the metamorphic peak conditions experienced by the rock.

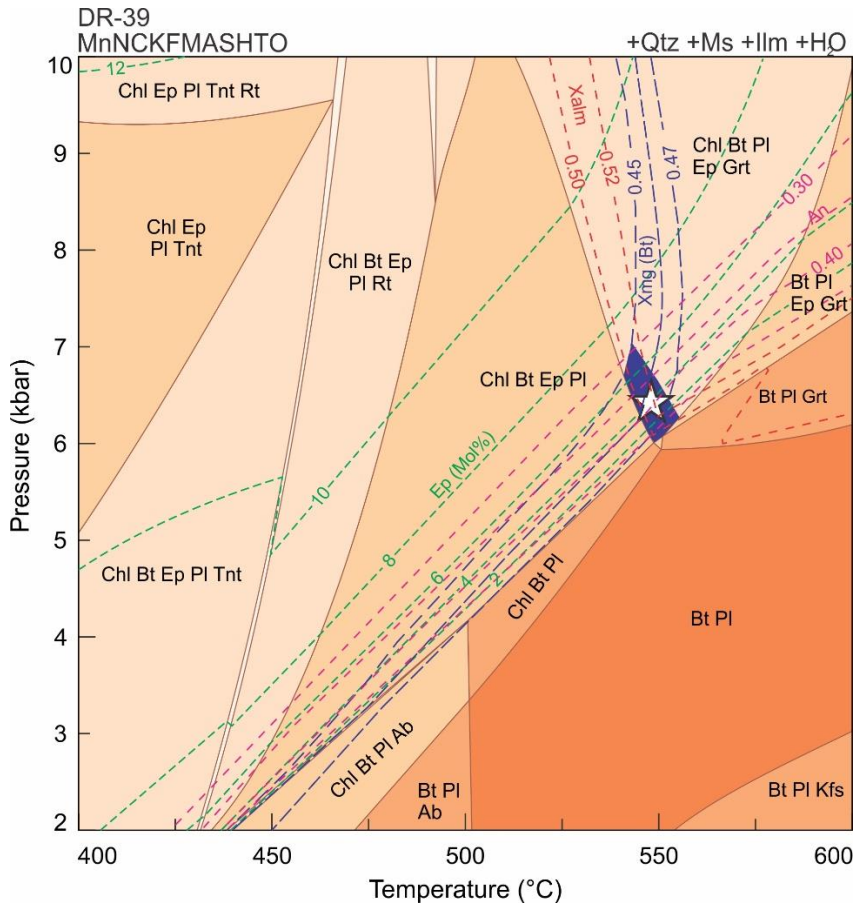

Figure 7 Pseudosection to sample DR-39 (Low-TCF) in MnNCKFMASHTO system. Isopleths of Xalm (red dashed line), XMg in biotite (blue dashed line) and epidote percentage (green dashed line) are plotted. The blue field represents the intersection where pseudosection modeling best represents the chemical and petrography of the sample. The star represents an approach of *P-T* conditions of the rock.

Table 4: Estimated bulk rock composition used in pseudosections modeling.

	DR-39	DR-206	DR-151	129A
Oxide	**mol%**			
SiO2	69.48	60.88	64.88	59.01
TiO2	0.72	0.38	0.99	0.77
Al2O3	10.60	14.87	12.13	10.80
Fe2O3	1.44	0.00	0.00	0.00
FeO	4.91	11.06	6.99	10.69
MnO	0.20	0.57	0.07	0.00
MgO	3.38	4.75	3.14	4.71
CaO	4.30	2.21	0.06	2.39
Na2O	2.24	1.72	1.29	1.3
K2O	2.01	3.51	2.35	3.14
O2	0.72	0.00	0.06	0.01
H2O	0.00	0.04	8.05	7.18
Some	100.00	100.00	100.00	100.00
A	0.36	0.21	0.33	0.08
M/F	0.41	0.43	0.31	0.31

Sample DR-206 presents Grt+Bt+Chl+Pl+Ms+Qtz+Ilm as mineral assemblage. Composition is presented in Table 4. Garnet is present in all fields in *P-T* pseudosection (Fig. 8), even in low pressure. Chlorite-Epidote association appears temperatures lower than 500 °C, and above this temperature, epidote is no longer stable. Biotite and staurolite occurs in medium-temperature fields, between 500 and 600 °C. Further, in temperatures higher than 600 °C, sillimanite/kyanite becomes stable, depending on pressure. In low pressure and high temperature (P < 5 kbar and T > 650 °C), cordierite is formed, as the rock underwent partial melting and it is associated with K-feldspar.

Isopleths of almandine in garnet (0.71-0.72), anorthite in plagioclase (0.28-0.30) and X_{Mg} in biotite (0.40-0.45) are presented in Fig. 8. Combining modeled results with mineral chemistry from this sample, the estimated *P-T* of metamorphic peak is 550-580°C and 7-7.6 kbar (pink field and black star in Fig. 8).

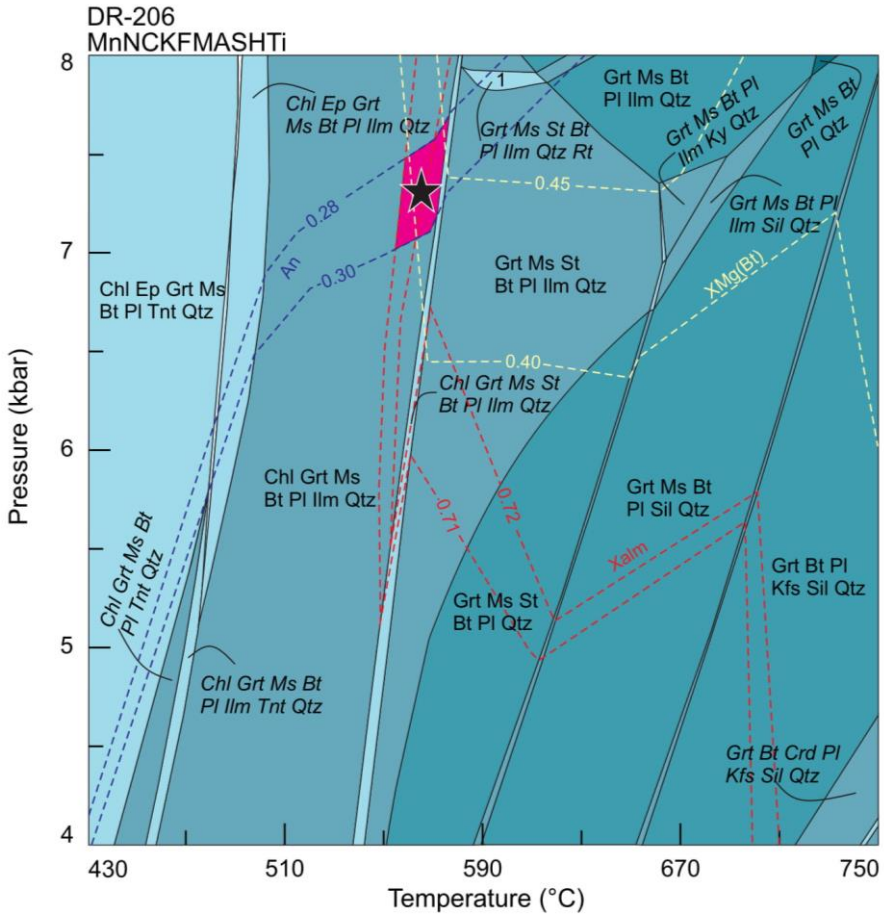

Figure 8 Pseudosection to sample DR-206 (Low-TCF) in MnNCKFMASHTO system. Isopleths of Xalm (red dashed line), XMg in biotite (white dashed line) and anorthite in plagioclase (blue dashed line) are plotted. The pink field represents the intersection where pseudosection modeling best represents the chemical and petrography of the sample. The star represents an approach of *P-T* conditions of the rock.

5.1.2. Sillimanite-staurolite zone (sample DR-151)

The sample DR-151 is from the MTCF, and its pseudosection presents very thin fields, which are equivalent to univariant reactions in KFMASH system and they are responsible for the formation of staurolite, biotite, sillimanite and the breakdown of chloritoid, chlorite and staurolite (Fig. 9). There is an additional line of plagioclase formation. At pressures higher than 6 kbar and temperature higher than 500 °C, the presence of garnet and its coexistence with staurolite and chlorite are important barometers (Fig. 9). Composition is presented in Table 4.

The peak assemblage field (Sil+St+Grt+Bt+Pl+Ms+Ilm+Qtz) was countered with isopleths of pyrope (0.05-0.10) in garnet and X_{Mg} in biotite (0.33-0.35) and staurolite (~0.05) and the measured compositions intersect at 640-670 °C and 5.9-7.0 kbar (green field and black star in Fig. 9), which is inferred as the best estimative for the peak metamorphic conditions.

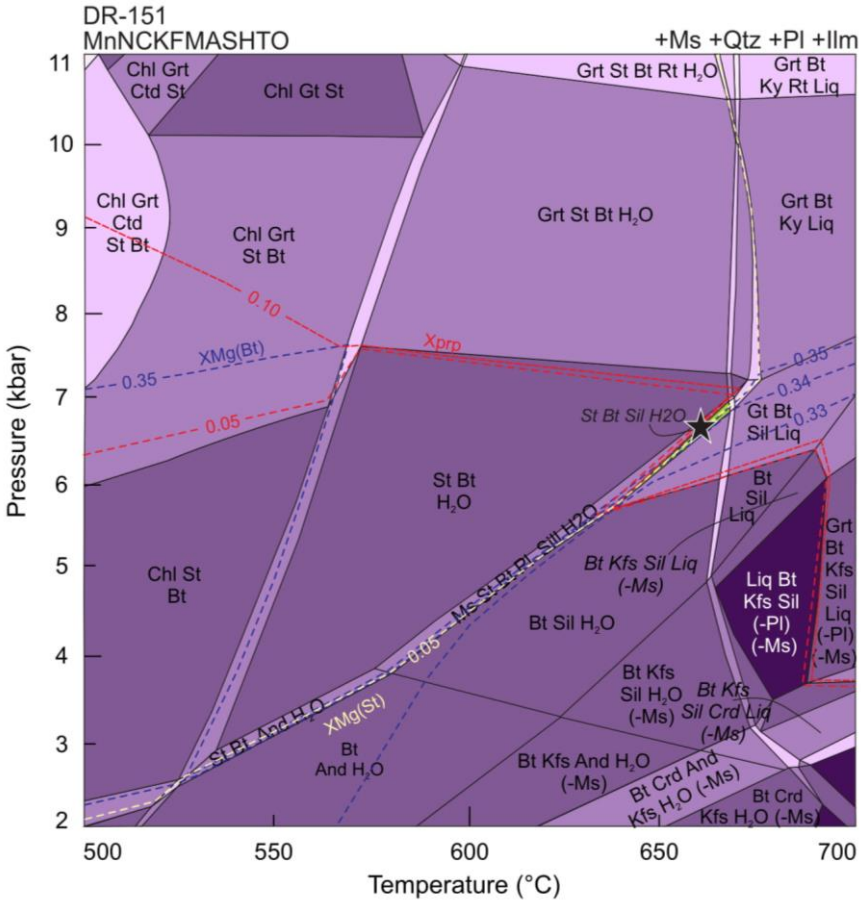

Figure 9 Pseudosection to sample DR-151 (Medium-TCF) in MnNCKFMASHTO system. Isopleths of Xprp (red dashed line), XMg in biotite (blue dashed line) and XMg in staurolite (white dashed line) are plotted. The green field represents the intersection where pseudosection modeling best represents the chemical and petrography of the sample. The star represents an approach of *P-T* conditions of the rock.

5.2 High-Turvo-Cajati Formation (HTCF)

5.2.1 Kyanite-K-feldspar-garnet (sample 129A)

This sample was originally studied by Faleiros *et al*. (2011) and its composition is presented in Table 4. As the unit is relevant to this paper, a new *P-T* pseudosection is calculated with the same activity models used here for a better comparison purpose. This rock is composed of Kfs+Ky+Grt+Rt+Qtz+granitic leucosome, taken as it underwent partial melting, and it is representative from the HTCF unit.

In the new pseudosection, smaller changes in *P-T* fields from the one calculated by Faleiros *et al*. (2011) can be observed (Fig. 10). Garnet is present in most fields, except when $T < 750$ °C and $P < 7$ kbar). Partial melting starts at 700°C by consumption of H_2O, and progress with consumption of muscovite, and biotite, respectively, with temperature increase. K-feldspar forms as a peritectic phase with partial melting. Sillimanite and kyanite have narrow occurrence, controlled by temperature.

Isopleths of grossular (0.10-0.12) and anorthite (0.35-0.40) were modeled and the measured compositions intersect at *P-T* conditions of 780-810 °C and ~11 kbar for the metamorphic peak (blue field and black star in Fig. 10). The *P-T* path presented by Faleiros *et al*. (2011) is also plotted in this new pseudosection (green ellipse in Fig. 10). These results are very similar to ones obtained in its original presentation in Faleiros *et al*., 2011 (best fit in ~800 °C and 11 kbar).

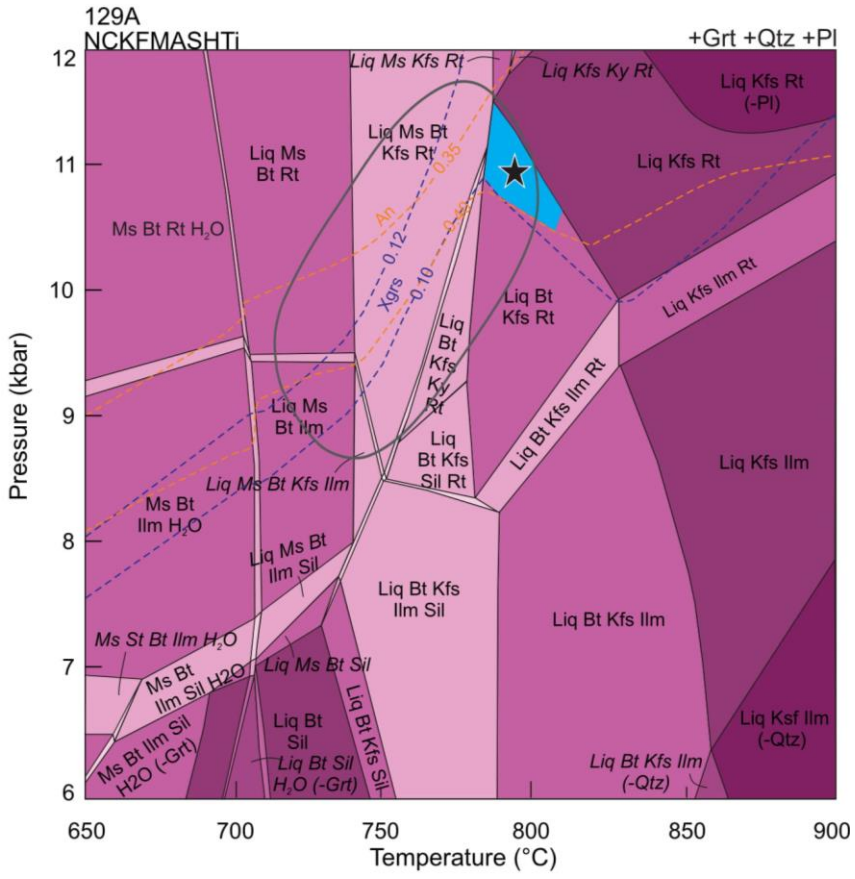

Figure 10 Pseudosection to sample 129A (High-TCF) in NCKFMASHTO system. Isopleths of Xgrs (blue

dashed line) and anorthite in plagioclase (orange dashed line) are plotted. The blue field represents the intersection where pseudosection modeling best represents the chemical and petrography of the sample. The star represents an approach of *P-T* conditions of the rock. Gray ellipse represents *P-T* path modeled by Faleiros et al. (2011) to the same sample.

6. Detrital zircon geochronology

Detrital zircon grains of four samples were analyzed by U-Pb method using LA ICP-MS, including two samples from the LTCF (FS-21, DR-39, Fig. 11a-b, Table S12-14) and two samples from the MTCF (FM-426, BR116-32, Fig 11c-d, Table S11). The results are compared with detrital zircon U-Pb data available for the HTCF in section 7 (sample 129A; Faleiros *et al*., 2016, Fig 11e). Sample locations are presented in Figures 1 and 2. Also presented is a compilation of probability density plot from all samples (Fig. 11f). The locations of representative spot analyses in cathodoluminescence images are presented in Figure 12. Finally, it is proposed a sedimentation pattern for TCF based on histogram and PDP calculate with all detrital zircon data presented here (Fig. 13).

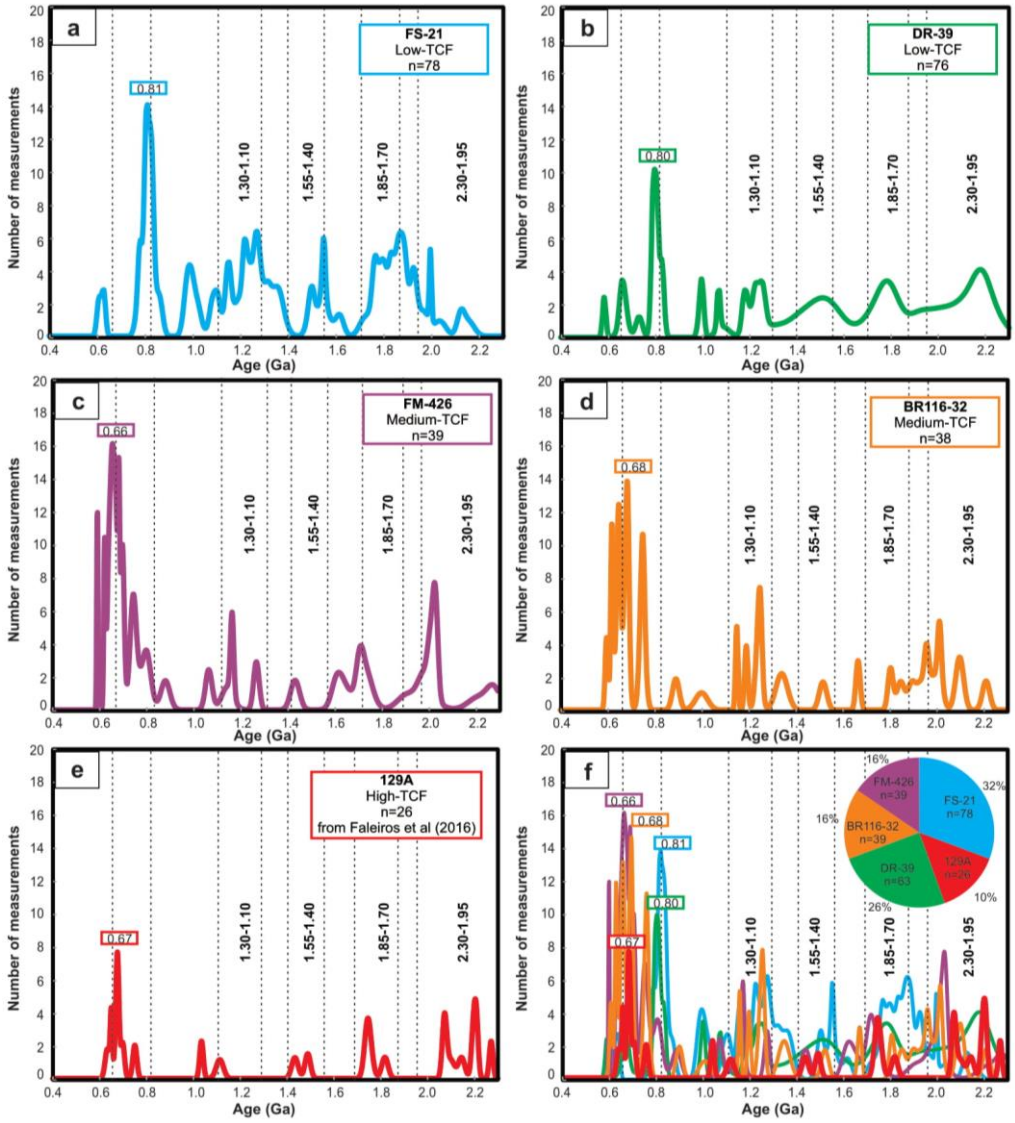

Figure 11 Probability density plot of detrital zircon from samples from TCF (a) sample FS-21 from Low-TCF, (b) sample DR-39 from Low-TCF, (c) sample FM-426 from Medium-TCF, (d) sample BR116-32 from Medium-TCF and (e) sample 129A from High-TCF (data from Faleiros et al., 2016). (f) Compilation from all samples.

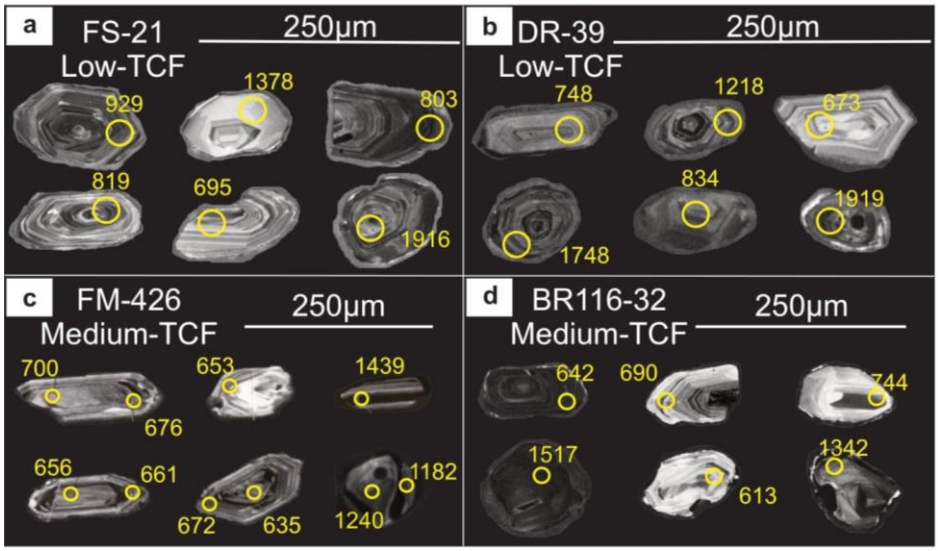

Figure 12 Cathodoluminescence images from representative detrítico zircon grains and their respective age and spot from punctual analyses (a) from sample FS-21, (b) from sample DR-39, (c) from sample FM-426 and (d) from sample BR116-32.

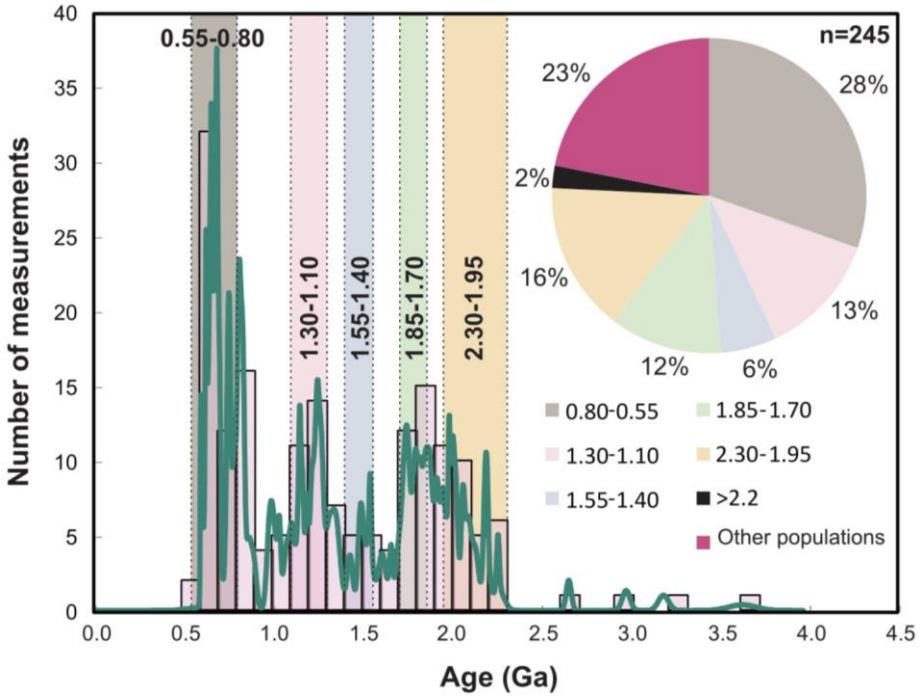

Figure 13 Probability density plot and histogram calculated for all detrital zircons data from TCF (including samples FS-21, DR-39, FM-426, BR116-32 and 129A).

6.1 Biotite Zone from LMTCF (sample FS-21)

Sample FS-21 is located in the southernmost portion of the Turvo-Cajati Formation, as defined by Silva and Algarte (1981), or in the Rio das Cobras Sequence of the Paranaguá Terrane in the perspective of some other authors (e.g., Cury, 2009; Patias *et al*., 2019, submitted). A total of 85 analyses were conducted in 85 zircon grains and 8 of them were later dismissed, because presented 10% discordant results, totalizing

78 good analyses (Fig 11a). Zircon grains are mainly rounded, occur as fragments, but some grains are prismatic crystals with preserved straight faces. All grains present internal oscillatory zoning in CL-images, even the fragmented grains (Fig. 12a). The obtained dates range from 2200 to 590 Ma, with main populations around 700-850 Ma, ~1000 Ma, 1390-1100 Ma, 1620-1500 Ma, 2100-1750 Ma. The peak around ~810 Ma is the largest and represents 17% of the obtained dates (Fig. 11a).

6.2 Garnet-Biotite-Chlorite zone from LMTCF (sample DR-39)

A total of 102 analyzes were obtained in 102 zircon grains from sample DR-39, in which 26 of them were dismissed due to 10% discordant results (Fig. 11b). Zircon grains are mainly rounded or represented by fragments with partial preservation of oscillatory zoning, which is observed under CL-imaging. Other grains are prismatic, with preserved straight faces and oscillatory zoning (Fig. 12b). The analyzed dates are in an interval of 2800-580 Ma with main age populations at 720-810 Ma, 920-1100 Ma, 1130-1300 Ma, 1400-1600 Ma, 1700-1900 Ma, 2000-2230 Ma. Very minor populations older than 2400 Ma occur, with values around ~2480 Ma and 2800 Ma (Table S11 in supplementary material). The population around ~800 Ma is the largest for the sample, representing 13% of the obtained dates (Fig. 11b).

6.3 Garnet-Biotite zone from LMTCF (sample BR-116-32)

Sample BR-116-32 is from the garnet-biotite zone of the LMTCF (Fig. 2). A total of 38 analyzes in 38 zircon grains were conducted and only 3 represent discordant results and were discarded (Fig. 11c). Euhedral prismatic grains with oscillatory zoning and also rounded zircon grains occur (Fig. 12c). The U-Pb dates spanning the interval of 2250-610 Ma (Fig. 11c). The age populations occur at 700-610 Ma, 830-790 Ma, 1350-1150 Ma and 2200-1800 Ma, with minor concentrations at 1650-1500 Ma and scarce data between 2200 Ma and 2700 Ma (Fig. 11c; Table S14 in supplementary material). The largest concentration of dates occurs at ~670 Ma, representing 34% of the dates.

6.4 Sillimanite zone from LMTCF (sample FM-426)

Sample FM-426 is from the sillimanite zone (LMTCF). A total of 41 analyzes were conduct in 41 zircon grains and 2 of them presented discordant results higher than 10% and were discarded (Fig. 11d). Zircon grains are elongated, some are euhedral and prismatic, with oscillatory zoning, especially in the rims, sometimes with inherited cores (Fig. 12d). The interval of obtained ages are 2300–580 Ma with main populations at 750-590 Ma, 1270-1130 Ma, ~1400 Ma, 1750-1590 Ma, 1950-1650 Ma and 2070-1900 Ma. The largest population occurs at ~660 Ma representing 41% of total dates (Fig. 11d).

7. Discussion

7.1. *P-T* regimes and metamorphic evolution of the LMTCF

Petrography results show distinct assemblages with metamorphism varying between greenschist facies (biotite zone) to amphibolite facies (sillimanite zone), with medium pressure regime, and no production of either kyanite or K-feldspar. Comparing with a simple petrogenetic grid in the KFMASH model system, such as the one presented by Spear & Cheney (1989), temperature ranges from 450 °C (biotite zone), to 600 °C and ~5 kbar (sillimanite-in isograd), and 650-670 °C and 6-7 kbar (staurolite-out isograd), within the sillimanite stability field. The presence of sillimanite, instead of kyanite or andalusite, points to pressures between 5 and 8 kbar in LMTCF. This pressure peak is distinct for HTCF estimations presented in Faleiros *et al*. (2011) and also presented here for sample 129A (9-12 kbar).

Pseudosection modeling results are in agreement with the inferences from petrography and petrogenetic grids, with calculated temperatures varying from 580 to 670 °C and pressures between 6 and 7.5 kbar (Table 5). These results define a metamorphic field gradient within the lowest pressure boundary of Barrovian-type metamorphism (Fig. 14a). Comparing with the results from the HTCF (Fig. 14b), which includes rocks with garnet, kyanite, K-feldspar and bearing granitic leucosome, the *P-T* conditions are much higher, with temperature higher than 750 °C and pressure up to 12 kbar (Faleiros *et al*., 2011, Table 5). This defines a steep metamorphic field gradient, similar to the ones observed in subduction-to-collision settings (Fig. 14a,b).

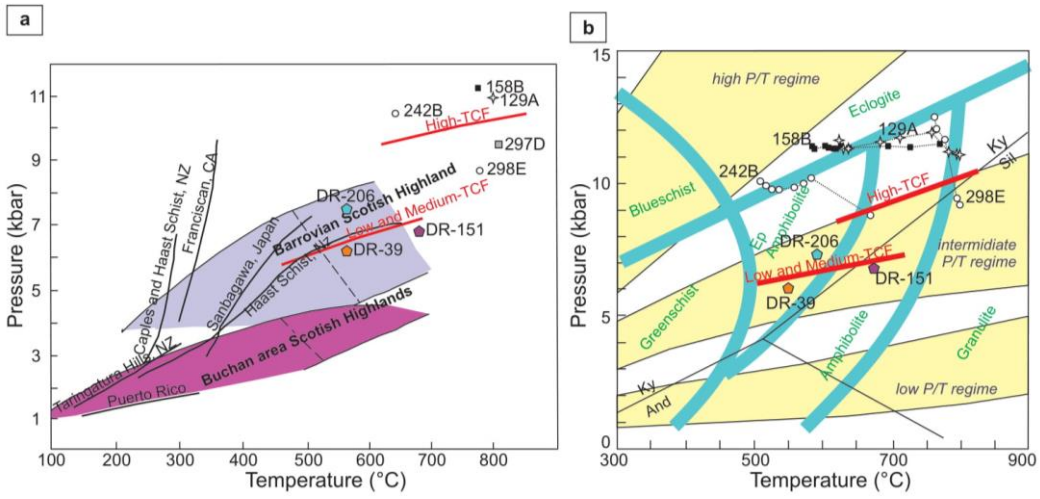

Figure 14 (a) *P-T* diagram showing metamorphic field gradients from several metamorphic belts (adapted from Winter, 2010) with data from TCF samples. The pentagons represent the samples from the LMTCF studied in this paper and others symbols are HTCF data from Faleiros et al. (2011). (b) *P-T* diagram showing geothermobarometric data and estimated metamorphic field gradients for HTCF, LMTCF (modified after Faleiros et al., 2011).The isograd map comprising the LMTCF units displays four metamorphic zones: biotite, garnet, staurolite-sillimanite and sillimanite, where the latter is the dominant zone (Fig. 2).

Table 5 Summarization of pseudosection modeling results, mineral assemblage of each sample and results extracted from Faleiros et al. (2011).

Sample	Study	Metamorphic zone	Mineral assemblage	Temperature interval (°C)	Pressure interval (kbar)
DR39	this article	Grt	Grt-Bt-Chl-Qtz-Pl-Ms	530-560	6.0-7.0
DR206	this article	Grt	Grt-Bt-Chl-Qtz-Pl-Ms	550-580	7.0-7.6
DR151	this article	Sil	Sil-St-Grt-Bt-Pl-Qtz-Ms	640-670	5.9-7.0
129A	this article	Ky - Kfs	Bt-Pl-Qtz-ksp-Grt	780-810	10.5-11.5
129A	Faleiros *et al*., 2011	Ky - Kfs	Bt-Pl-Qtz-ksp-Grt	800	11
158B	Faleiros *et al*., 2011	Ky - Kfs	Bt-Pl-Qtz-ksp-Grt-Ms	770	11.5
242B	Faleiros *et al*., 2011	St - Ky	Qtz-Ms-Bt-Ky-Grt-Pl-St	615-660	8.5-10.5
297D	Faleiros *et al*., 2011	Sil – Kfs	Qtz-Bt-Sil-Kfs-Grt-Pl	760-820	8.0-10.3
298E	Faleiros *et al*., 2011	Sil - Kfs	Qtz-Bt-Sil-Kfs-Grt	790-820	8.0-10.0

The garnet composition has mainly Fe^{2+}, Mg and Ca with very minor amounts of Mn and Fe^{3+}. Elemental maps indicate that Fe^{2+} and Mg increases from core to rims, which are richer in Ca and Mn (Fig 3, 4 and 5). This indicates that garnet growth occurred concomitantly with consumption of plagioclase and ilmenite. Ilmenite is a phase that concentrates Mn and could be a source of this element to garnet nucleation (Woodsworth, 1977). Ca could come from plagioclase, and locally epidote, consumption and breakdown, also during the garnet nucleation stage. Later, the continuation of garnet growth involved staurolite consumption to produce Fe enrichment at rims. The final enrichment of Mn might be related to retrometamorphism and partial resorption via net-transfer reaction, which has the effect to raise the amount of Mn at garnet rims, while Mg and Fe are unaffected (Kohn & Spear, 2000).

7.2. Regional metamorphic signatures and its tectonic implications

The TCF metamorphic zones are sectioned in south and north compartments by the Putunã Shear Zone, a major sinistral transcurrent structure (Fig. 2). The contact between the metamorphic zones of the HTCF and LMTCF is not continuous in terms of

metamorphic grade. The discontinuity is more evident in western portion where migmatites from the melt-bearing sillimanite-K-feldspar zone are in contact with garnet zone rocks (Fig. 2).

When the LMTCF and HTCF metamorphic field gradients are compared (Fig. 14), it is evident that both metamorphic units probably underwent metamorphism under different tectonic settings, with the first requiring a higher input of heat for a lower pressure regime.

Kyanite-bearing pelitic migmatites from the HTCF present metamorphic paths characterized by near isobaric heating at relatively high-pressure conditions, starting at low-temperature eclogite facies conditions, *ca*. 500-600 °C and 10-12 kbar (Fig. 14a,b; Faleiros *et al*., 2011). Although there are no records of the burial stage, the HTCF metamorphic paths suggest a subduction-related stage followed by an episode of thermal relaxation without immediate association of erosion and/or tectonic exhumation.

Rocks from LMTCF including sillimanite-bearing pelites present metamorphic zonation from greenschist to high-amphibolite facies conditions, *ca*. 580-680 ºC and 6.2-7.5 kbar. Tectonically, this may represent an arc-related stage with temperature-influx in low-to-medium pressure. This heat flow could come from intense magmatism as described in Colombian Andes (Rios *et al*., 2003), but this is not the case for the LMTCF proximities where granitic intrusions are scarce (Figs. 1b, 2). An arc-related granitic unit (Piên-Mandirituba Suite) is present at the southwestern most portion of the Curitiba Terrane, but it is not in direct contact with TCF rocks (Fig. 1b). Another possibility is that these rocks suffered metamorphism in a back-arc setting (e.g., Brown, 2014). As no regional magmatic arc rocks are described near or intruding the TCF, the back-arc-related hypothesis is more likely. Brown (2014) defends that high dT/dP gradients may occur in arc-back-arc systems, which explain medium pressure regime with heat-influx associated with extensional-mechanism. This extensional component would bring asthenospheric mantle closer to the thinned crust and increase the temperature during the metamorphism in LMTCF. This magmatic arc would be equivalent to the Piên-Mandirituba Suite (Fig. 1b).

The juxtaposition of the LMTCF and HTCF can be inferred as a pair of high-*T*/low-*P* with high-*T*/high-*P* rocks similar to the paired metamorphic belts described along the metamorphic history on Earth (Brown, 2006; Brown & Johnson, 2018). In this case, LMTCF and HTCF are part of same subduction-to-collision orogeny, probably developed in an active margin of a Japan-like microcontinent, where the metamorphism affecting the LMTCF (high dT/dP) occurred in the back-arc setting and HTCF (low dT/dP) was

located in the subducting plate (Fig. 15). Nevertheless, post-collisional terrane dispersion of Ribeira Belt units along the anastomosing crustal-scale transcurrent shear zone system (Fig. 1) was intense (Faleiros *et al*., 2011), and most original contact relationships between the units were lost. On the other rand, the scenario suggests that the Curitiba Terrane presents two major Ediacaran suture zone in the Ribeira Belt (Fig. 1b), which is corroborated by: (1) the very discrepant ages of supracrustal units from the Apiaí Terrane, dominated by Calymmian sedimentation and volcanism (Campanha *et al*., 2015) and the Curitiba Terrane, which is dominated by Ediacaran sedimentation, as the Turvo-Cajati Formation (Faleiros *et al*., 2016; this work); (2) the existence of Ediacaran ophiolite remnants of the Piên Mafic-Ultramafic Suite (Fig. 1b; Harara, 2001; Passarelli *et al*., 2018). In this scenario the Atuba Complex would represent the basement of the microcontinent, which was subsequently involved in the regional deformation and metamorphism related with the final collision of the Paranapanema, São Francisco and Congo cratonic masses.

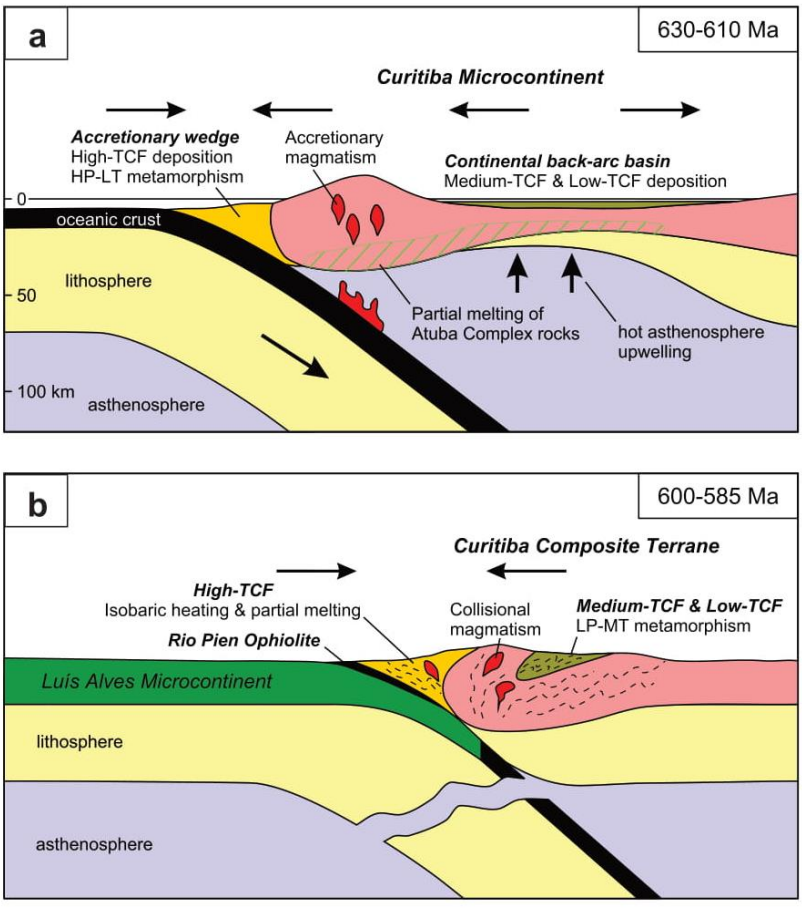

Figure 15: Proposed model from Curitiba Terrain evolution, based on TCF detailed study presented in this paper. (a) 630-610 Ma initial stages of subduction in the Curitiba Microcontinent, arc-development in Atuba Complex with partial melting, deposition in Low and Medium-TCF and deposition followed by metamorphism type high-P and low-T in High-TCF. Asthenospheric mantle upwelling in back-arc. (b) 600-585 Ma: Collision of Curitiba Microcontinent and Luis Alves Microcontinent. metamorphism type low-P medium-T in Low and Medium-TCF and isobaric heating and partial melting in High-TCF.

7.3 Detrital zircon U-Pb data and their tectonic setting implications

Analyzing probability density plots from detrital zircon from all three subunits from the TCF, a common pattern raises. All three subunits have age population peaks of 1300-1100 Ma, 1550-1400 Ma, 1850-1700 Ma and 2300-1950 Ma (Fig. 11a-f, 13). Also, in all three subunits, these age populations are less representative than a younger age peak, at 700-610 Ma. It is also notable that these younger zircon grains have their igneous euhedral habit preserved, with elongated and straight faces, prismatic habit and oscillatory zoning pattern. The lack of evidence that these grains suffered long-term transport indicates depositional sites proximal to the sources. Additionally, those late-Neoproterozoic ages are primarily related to voluminous arc-related granitic magmatism in the Piên-Mandirituba magmatic arc (620-595 Ma, Harara, 2001). Additional evidence for this interpretation is the detrital zircon age signature for the Campo Alegre Basin (Fig. 1b), which is very similar to the TCF samples, and was undoubtedly developed proximal to the Piên-Mandirituba arc that was its main source of detrital zircon grains (Quiroz-Valle *et al*., 2019). This suggests that all Turvo-Cajati Formation subunits have late-Neoproterozoic magmatic arcs as important detrital source rocks. Considering that metamorphic peak in the Turvo-Cajati Formation occurred between 590 and 585 Ma (Faleiros *et al*., 2011, 2016), its deposition probably occurred coeval or slightly later than the late-Neoproterozoic arc magmatism. In a Phanerozoic global perspective, similar age signature pattern occurs in sedimentary basins from accretionary wedge and back-arc basin settings (Cawood *et al*., 2012).

Older age populations present in all TCF samples, such as 1300-1100 Ma, 1550-1400 Ma, 1850-1700 Ma and 2300-1950 Ma, indicate that older source areas are similar for all metamorphic subunits, indicating that they represent at least neighboring basins. Strong age peak at 2300-1950 Ma is compatible with the main age population of Atuba Complex rocks, which is composed of migmatitic orthogneiss with Archaean protoliths and extensive partial melting stages at around 2200–2100 Ma and 630-590 Ma (Sato *et al*., 2003, 2009). This suggests that the Atuba Complex could have been a basement and/or a detrital source for the Turvo-Cajati Formation subunits basins. This scenario is compatible with the Atuba Complex being a Japan-like microcontinent with a late-Cryogenian-to-Ediacaran magmatic arc developed in one of its margins. Thus, both the Atuba Complex and the Piên-Mandirituba Arc would be the source rocks for detrital grains deposited in the Turvo-Cajati Formation basins.

According to Cawood *et al.* (2012) back-arc basin settings have higher amounts of older detrital zircon from adjoining craton, while trench/forearc basins have less

influence of older zircon grains than the arc-related ones. Another distinction between those basin settings is that deposition in back-arc lasts a little longer than in accretionary wedge and forearc settings, probably related to the proximity that accretionary wedge basins have to subduction (Cawood *et al*., 2012). Detrital zircon U-Pb age signatures suggest that the LMTCF have larger duration of deposition than HTCF, based on comparison with phanerozoic settings (Cawood *et al*., 2012). This could indicate that the LMTCF are located in the back-arc setting, while the HTCF is on the accretionary wedge, the latter already suggested due to its metamorphic signatures (Faleiros *et al*., 2011). Considering the northwestward subduction polarity, as already inferred in previous works (e.g., Basei *et al*., 2000, 2008; Passarelli *et al*., 2018; Quiroz-Valle *et al*., 2019), the accretionary wedge (HTCF) should be located along the suture zone between the Curitiba and Luís Alves Terranes, and the back-arc basin (LMTCF) to the NW. These relationships are partially preserved in blocks limited by transcurrent shear zones, where the HTCF rocks are always located in the southeastern side (Figs. 1b, 2). But significant displacement along the regional shear zones obscured the original relationships between the tectonic units.

The age difference of about 200Ma, between the detrital zircon age peak of HTCF and MTCF (630-650Ma) and samples FS-21 and DR-039 of the LTCF (~800 Ma), may be explained by different distances from the sources of zircon grains. This could indicate that the magmatic arc developed in a margin of the proto-Curitiba Terrane Microplate may have initiated around 800 Ma. . These older ages indicate that the LTCF probably was closer to the arc in its earlier stages. This zircon age population is also present in MTCF and HTCF rocks, although with less prominence. The 630-650 Ma zircon population also appears in the LTCF samples (Fig. 11a-b), but as a less remarkable signature, which indicates that the Piên-Mandirituba Arc was also a source for the LTCF basin although more distant to this source.

Considering the metamorphic patterns coupled with detrital zircon signatures, the HTCF is compatible with an accretionary wedge position related to the proto-Curitiba Terrane microplate, while the LMTCF are compatible to deposition and further metamorphism in a back-arc basin setting developed over the Atuba Complex paleocontinent.

The Atuba Complex would be the basement where TCF was deposited, LMTCF in the back-arc and HTCF in accretionary wedge. The Atuba Complex was also zircon source area to older age populations. Later, this proto-Curitiba Terrane microplate (Atuba Complex + TCF) collided with the Luis Alves Microcontinent (Fig 15) and developed the

Piên-Mandirituba Arc on the proto-Curitiba Terrane microplate. This model corroborates with earlier proposed model (Basei *et al*., 2008). In this model, Atuba Complex appears as basement to Capiru Formation deposition, but we propose that LMTCF was also deposited above Atuba Complex basement. The magmatic arc proposed here is equivalent to the previously proposed Piên-Mandirituba Arc (Harara, 1996, 2001; Basei *et al*., 2008; Passarelli *et al*., 2018; Quiroz-Valle *et al*., 2019).

Also, comparing sample FS-21 and DR-39, their detrital zircon pattern is very similar. Thus, it is inferred that the original definition by Silva & Algarte (1981) is more likely. Thus, sample FS-21 is located in TCF unit (Fig. 1b), instead of the Rio das Cobras Sequence, in Paranaguá Terrane, as proposed by Cury (2009).

7.4 A tectonic model evolution

The new data coupled with compiled information presented on this paper allow proposing an evolution model for the Turvo-Cajati Formation and the whole Curitiba Terrane (Fig. 15), with the following sequence of events:

630-610 Ma: Subduction of oceanic crust and sediments on the accretionary wedge on the active margin of the Curitiba Microcontinent, composed of the Atuba Complex basement and beginning of high-pressure metamorphism of the proto-HTCF (Fig. 15a). Deposition of the proto-LMTCF in a back-arc basin developed over the Curitiba Microcontinent (Fig. 15a). Asthenospheric mantle upwelling produced a high geothermal gradient in the back-arc setting, producing extensive partial melting of the Atuba Complex rocks at the base of the continental crust (Fig. 15a). Both sedimentary units in back-arc and accretionary wedge settings receive sediments and detrital zircon from the Piên-Mandirituba Arc and Atuba Complex basement sources.

600-585 Ma: Collision of the Curitiba Microcontinent with the Luis Alves Microcontinent (Fig. 15b). This collision causes isobaric heating and partial melting in the HTCF and the obduction of the Piên Mafic-Ultramafic Suite. The collision of two microcontinents also generates deformation and magmatism that caused low-to-medium pressure metamorphism in the back-arc basin (LMTCF). Continued deformation produced stacking of nappes and juxtaposition of rocks of contrasting metamorphic signatures.

8. Conclusions

Previous studies in rocks with high metamorphic degree from the Turvo-Cajati Formation, Curitiba Terrane, pointed to peak pressure up to 10-12 kbar, culminating with the formation of kyanite-bearing migmatites. This study in same unit, but made in low

and medium grade metamorphic rocks points to metamorphic evolution until the sillimanite zone under maximum pressures of 6.5-7.5 kbar. This scenario indicates that the Turvo-Cajati Formation assembles more than one group of metamorphic rocks, with distinct metamorphic field gradients, reflecting very different tectonic settings. The metamorphic record associated with available petrological and geochronological data suggests that the Turvo-Cajati Formation comprises a paired low-*P* and high-*P* belt associated with a major Ediacaran suture zone in the southern Ribeira Belt. It is inferred that the high metamorphic gradient recorded in the LMTCF was related with asthenospheric upwelling in the back-arc region, which also produced extensive partial melting in the Atuba Complex basement. Detrital zircon ages indicate that all the Turvo-Cajati Formation metamorphic units received detrital grains from a ca. 650-630 Ma (late-Cryogenian to Ediacaran) magmatic arc compatible with the Piên-Mandirituba Arc and from a ca. 2000-2200 Ma (Rhyacian) basement, the latter compatible with the Atuba Complex, the major unit forming the Curitiba Terrane. Detrital zircon U-Pb age signatures coupled with metamorphic records suggest that the Turvo-Cajati Formation is made up of juxtaposition of an accretionary wedge, HTCF, and a back-arc basin, LMTCF, related to a microplate that includes a Rhyacian basement microcontinent (Atuba Complex).

Acknowledgments

Financial support was provided by grants 2018/10012-0, 2018/01572-1, 2016/12986-6 and 2015/04487-7 from São Paulo Research Foundation (FAPESP). FMF thanks the research productivity scholarship grant 307732/2019-3, National Counsel of Technological and Scientific Development (CNPq). BSR also thanks Coordination of Superior Level Staff Improvement (CAPES) for financial support by scholarship grant. An earlier version of this paper was reviewed by Kathryn Cutts and an anonymous reviewer.

References

Barrow, G. 1912. On the geology of Lower Dee-side and the southern Highland Border. *Proceedings of the Geologists' Association*, *23*(5), 274-IN1.

Basei, M.A.S., Siga Júnior, O., Machiavelli, A., Mancini, F. 1992. Evolução tectônica dos terrenos entre os cinturões Ribeira e Dom Feliciano (PR-SC). *Revista Brasileira de Geociências*, 22(2): p. 216-221.

Basei, M., Siga, O., Masquelin, H., Harara, O., Reis, N., & Preciozzi, F. 2000. The Dom Feliciano belt (Brazil-Uruguay) and its fore land (Rio de la Plata Craton):

framework, tectonic evolution and correlations with similar terranes of southwestern Africa.

Basei, M. A. S., Frimmel, H. E., Nutman, A. P., & Preciozzi, F. 2008. West Gondwana amalgamation based on detrital zircon ages from Neoproterozoic Ribeira and Dom Feliciano belts of South America and comparison with coeval sequences from SW Africa. *Geological Society, London*, Special Publications, 294(1), 239-256.

Basei, M. A., Nutman, A., Júnior, O. S., Passarelli, C. R., & Drukas, C. O. 2009. .2 The Evolution and Tectonic Setting of the Luis Alves Microplate of Southeastern Brazil: An Exotic Terrane during the Assembly of Western Gondwana. Developments in Precambrian Geology, 16, 273-291.

Brito Neves, B.B., Campos Neto, M.C.,Fuck, R.A. 1999. From Rodinia to Western Gondwana: an approach to the Brasiliano-Pan African Cycle and orogenic collage. *Episodes*, 22, 155-166.

Brown, E. H., & Walker, N. W. 1993. A magma-loading model for Barrovian metamorphism in the southeast Coast Plutonic Complex, British Columbia and Washington. *Geological Society of America Bulletin*, 105(4), 479-500.

Brown, M. 2006. Duality of thermal regimes is the distinctive characteristic of plate tectonics since the Neoarchean. *Geology*, *34*(11), 961-964.

Brown, M. 2014. The contribution of metamorphic petrology to understanding lithosphere evolution and geodynamics. *Geoscience Frontiers*, *5*(4), 553-569.

Brown, M., Johnson, T. 2018. Secular change in metamorphism and the onset of global plate tectonics. *American Mineralogist*, *103*(2), 181-196.

Burg, J. P., & Gerya, T. V. 2005. The role of viscous heating in Barrovian metamorphism of collisional orogens: thermomechanical models and application to the Lepontine Dome in the Central Alps. *Journal of Metamorphic Geology*, *23*(2), 75-95.

Campanha, G. A. C., Faleiros, F. M., Basei, M. A. S., Tassinari, C. C. G., Nutman, A. P., & Vasconcelos, P. M. 2015. Geochemistry and age of mafic rocks from the Votuverava Group, southern Ribeira Belt, Brazil: Evidence for 1490 Ma oceanic back-arc magmatism. *Precambrian Research*, *266*, 530-550.

de Capitani, C., Brown, T. H. 1987. The computation of chemical equilibrium in complex systems containing non-ideal solutions. *Geochimica et Cosmochimica Acta*, *51*(10), 2639-2652.

de Capitani, C. 1994. Gleichgewichts-Phasendiagramme: theorie und Software. *Beihefte zum Jahrestagung der Deutschen Mineralogischen Gesellschaft. European Journal of Mineralogy, 72, 6-48.*

Catalán, J. R. M., Arenas, R., & Balda, M. A. D. 2003. Large extensional structures developed during emplacement of a crystalline thrust sheet: the Mondoñedo nappe (NW Spain). *Journal of Structural Geology*, 25(11), 1815-1839.

Cawood, P. A., Hawkesworth, C. J., & Dhuime, B. 2012. Detrital zircon record and tectonic setting. *Geology, 40(10), 875-878.*

Connolly, J. A. 2005. Computation of phase equilibria by linear programming: a tool for geodynamic modeling and its application to subduction zone decarbonation. *Earth and Planetary Science Letters*, *236*(1-2), 524-541.

Cumming, G.L., Richards, J.R., 1975. Ore lead isotope ratios in a continuously changing Earth. Earth and Planetary Science Letters 28, 155-171.

Cury, L. F. 2009. *Geologia do Terreno Paranaguá* .Doctor of Science Thesis, University of São Paulo.

Elhlou, S., Belousova, E., Griffin, W. L., Pearson, N. J., & O'Reilly, S. Y. 2006. Trace element and isotopic composition of GJ-red zircon standard by laser ablation. *Geochimica et Cosmochimica Acta Supplement*, *70*, A158-A158.

England, P. C., Thompson, A. B. *1984.* Pressure—temperature—time paths of regional metamorphism I. Heat transfer during the evolution of regions of thickened continental crust. *Journal of Petrology, 25(4), 894-928.*

Faleiros, F. M. 2008. *Evolução de terrenos tectono-metamórficos da serrania do ribeira e planalto alto turvo (SP, PR)*. Tese de Doutorado, Instituto de Geociências, University of São Paulo, 304 p.https://doi.org/10.11606/T.44.2008.tde-02092008-113513.

Faleiros, F. M., Campanha, G.A.C., Martins, L., Vlach, S.R.F., Vasconcelos, P.M., 2011. Ediacaran high-pressure collision metamorphism and tectonics of the southern Ribeira Belt (SE Brazil): evidence for terrane accretion and dispersion during Gondwana assembly. *Precambrian Research,*189, 263–291.

Faleiros, F. M., Pavan, M. 2013. Geologia e Recursos Minerais da Folha Eldorado Paulista-SG-22-XB-XI, Estado de São Paulo (geological mapping in scale: 1: 100.000). *CPRM – Geological Survey of Brazil*. São Paulo.

Faleiros, F.M., Campanha, G.A.C., Pavan, M., Almeida, V.V., Rodrigues, S.W.O., Araújo, B.P., 2016. Short-lived polyphase deformation during crustal thickening and exhumation of a collisional orogen (Ribeira Belt, Brazil). *Journal of Structural Geology* 93, 106-130.

Fuhrman,M, L., Lindsley, D. H. 1988. Ternary-Feldspar Modeling and Thermometry. *American Mineralogist* 73:201-15.

García, C. A., Ríos, C. A., & Castellanos, O. M. 2005. Medium-pressure metamorphism

in the central Santander massif, eastern Cordillera, Colombian Andes. *Boletín de Geología*, 27(2), 43-68.

Guimarães, S. B., dos Reis Neto, J. M., & Siqueira, R. B. 2002. Caracterização dos estromatólitos da Formação Capiru (Proterozóico) nas regiões de Morro Azul e Morro Grande: leste do Paraná. *Boletim Paranaense de Geociências*, *51, 77-88*.

Harara, O. M. 1996. Structural, petrological and geochronological analysis of the lithotypes from the Piên region (Parana State, Brazil) and adjacences. Analise estrutural, petrologica e geocronologica dos litotipos da Regiao de Piên (PR) e adjacencias. Master Thesis, University of São Paulo.

Harara, O. M. M. 2001. *Mapeamento e Investigação Petrológica e Geocronológica dos Litotipos da Região do Alto Rio Negro (PR-SC): um exemplo de sucessivas e distintas atividades magmáticas durante o Neoproterozóico III*. Doctor of Science Thesis, University of São Paulo.

Hartmann, L. A., Santos, J. O. S., McNaughton, N. J., Vasconcellos, M. A. Z., & Silva, L. C. 2000. SHRIMP dates recurrent granulite facies metamorphism in the Santa Catarina granulites, southern Brazil. Anais Academia Brasileira de Ciências, 72, 559-572.

Holland, T. J. B., Powell, R. 2011. An improved and extended internally consistent thermodynamic dataset for phases of petrological interest, involving a new equation of state for solids. *Journal of Metamorphic Geology*, 29 (3), 333-383.

Kohn, M. J. & Spear, F. 2000. Retrograde net transfer reaction insurance for pressure-temperature estimates, *Geology*, 28: 1127-1130.

Leandro, R. 2016. *Caracterização tectonoestratigráfica da sequência terrígena da formação Capiru na Região de Morro Grande, Colombo-PR.* Masters Thesis, Federal University of Paraná.

Ludwig, K.R., 2003. Isoplot 3.00: A Geochronological Toolkit for Microsoft Excel. Berkeley, California, Berkeley Chronology Center Special Publication No. 4.

Machiavelli, A., Basei, M. A. S., & Siga Jr, O. 1993. Suíte Granítica Rio Piên: um arco magmático do Proterozóico Superior na Microplaca Curitiba. *Geochimica Brasiliensis*, *7*(2), 113-129.

Mori, P.E.; Reeves, S.; Correia, C. T.; Haukka, M. 1999. Development of a fused glass disc xrf facility and comparison with the pressed powder pellet technique at Instituto de Geociencias, São Paulo University. Revista Brasileira de Geociências, 29(3): 441-446.

Passarelli, C. R., Basei, M. A. S., Wemmer, K., Siga, O., & Oyhantçabal, P. 2011. Major shear zones of southern Brazil and Uruguay: escape tectonics in the eastern

border of Rio de La plata and Paranapanema cratons during the Western Gondwana amalgamation. International Journal of Earth Sciences, 100(2-3), 391-414.

Passarelli, C. R., Basei, M. A. S., Siga, O., Harara, O. M. M. 2018. The Luis Alves and Curitiba Terranes: Continental Fragments in the Adamastor Ocean. In *Geology of Southwest Gondwana* (pp. 189-215). Springer, Cham.

Philpotts, A.R., Ague, J. 2009. Principles of Igneous and Metamorphic Petrology. 2nd Edition. Cambridge University Press, 684p.

Powell, R., Holland, T. J. B. 1988. An internally consistent dataset with uncertainties and correlations: 3. Applications to geobarometry, worked examples and a computer program. *Journal of metamorphic Geology*, *6*(2), 173-204.

Quiroz-Valle, F.R., Basei, M.A.S., Lino, L.M., 2019. Petrography and detrital zircon U-Pb geochronology of sedimentary rocks of the Campo Alegre Basin, Southern Brazil: implications for Gondwana assembly. Brazilian Journal of Geology 49, e20180080, https://doi.org/10.1590/2317-4889201920180080.

Rıos, C., Garcıa, C., &Takasu, A. 2003. Tectono-metamorphic evolution of the Silgará Formation metamorphic rocks in the southwestern Santander Massif, Colombian Andes. *Journal of South American Earth Sciences*, *16*(2), 133-154.

Rueden, C. T., Schindelin, J., Hiner, M. C., DeZonia, B. E., Walter, A. E., Arena, E. T., Eliceiri, K. W. 2017. ImageJ2: ImageJ for the next generation of scientific image data. *BMC bioinformatics*, *18*(1), 529.

Sadowski, G. R. 1991. A megafalha de Cubatão no sudeste brasileiro. Boletim IG-USP. Série Científica, 22, 15-28.

Sato, K., Siga Jr, O., Nutman, A. P., Basei, M. A., McReath, I., Kaulfuss, G. 2003. The Atuba Complex, southern South American Platform: Archean components and Paleoproterozoic to Neoproterozoic tectonothermal events. *Gondwana Research*, *6*(2), 251-263.

Sato, K., SigaJúnir, O., Silva, J. D., McReath, I., Liu, D., Iizuka, T., Rino, S., Hirata, T., Sproesser, W., Basei, M. A. S. 2009. In situ isotopic analyses of U and Pb in zircon by remotely operated SHRIMP II, and Hf by LA-ICP-MS: an example of dating and genetic evolution of zircon by 176Hf/177Hf from the ItaQuarry in the Atuba Complex, SE Brazil. *Geologia USP, Série Cientifica São Paulo*, *9*, 61-69.

Siga Júnior, O. de Barros Gomes, C., Sato, K., Passarelli, C. R. 2007. O maciço alcalino de Tunas, PR: novos dados geocronológicos. *Geologia USP. Série Científica*, *7*(2), 71-80.

Silva, A. T. S., & Algarte, J. P. 1981. Contribuição à geologia da seqüência Turvo-Cajati

entre o Rio Pardo e Pariquera-Açu, Estado de São Paulo I: litologia e petrografia. *Atas III Simpósio Regional de Geologia, Curitiba, PR, Brasil*, 109-120.

Siqueira, R., Hollanda, M. H. B. M. D., Basei, M. A. S. 2014. A novel approach to (LA-ICP-MS acquired) U-Th-Pb data processing. *9th SSAGI: Program and Abstracts*.

Spear, F. S., Pyle, J. M., Storm, L. C. 2001. Short course: Thermodynamic modeling of mineral reactions: An introduction to Program Gibbs. *Northeast Section, Geological Society of America, Burlington, Vermont*.

Stacey, J. T., & Kramers, 1. 1975. Approximation of terrestrial lead isotope evolution by a two-stage model. *Earth and planetary science letters*, *26*(2), 207-221.

Steiger, R., & Jäger, E. 1977. Subcommission on geochronology: convention on the use of decay constants in geo-and cosmochronology. *Earth and planetary science letters*, *36*(3), 359-362.

Tilley, C. E. 1925. A preliminary survey of metamorphic zones in the southern Highlands of Scotland. *Quarterly Journal of the Geological Society*, *81*(1-4), 100-112.

Turner, F.J. 1981. Metamorphic Petrology - mineralogical, field and tectonic aspects, 2nd ed. McGraw-Hill, Nova York.

White, R. W., Powell, R., &Holland, T. J. B. 2001. Calculation of partial melting equilibria in the system Na2O–CaO–K2O–FeO–MgO–Al2O3–SiO2–H2O (NCKFMASH). *Journal of metamorphic Geology*, *19*(2), 139-153.

White, R. W., Powell, R., Holland, T. J. B., Johnson, T. E., & Green, E. C. R. 2014a. New mineral activity–composition relations for thermodynamic calculations in metapelitic systems. *Journal of Metamorphic Geology*, *32*(3), 261-286.

White, R. W., Powell, R., & Johnson, T. E. 2014b. The effect of Mn on mineral stability in metapelites revisited: New a–x relations for manganese-bearing minerals. *Journal of Metamorphic Geology*, *32*(8), 809-828.

Winter, J. D. 2010. *An introduction to igneous and metamorphic petrology*. New York: Prentice Hall.

Woodsworth, G. J. 1977. Homogenization of zoned garnets from pelitic schists. *The Canadian Mineralogist*, *15*(2), 230-242.

CHAPTER 3 – RESULTS – ARTICLE TO BE SUBMITTED

Challenges in untangling the tectonometamorphic evolution of ancient accretionary orogens: a case of petrochronology study in the Ribeira Belt, SE, Brazil

B.S. Ricardo[1]*, Renato Moraes[1], Catherine M. Mottram[2], Frederico M. Faleiros[1*], Sílvio Roberto Farias Vlach [1]

[1] Instituto de Geociências, Universidade de São Paulo, Rua do Lago, 562, CEP 05508-080, São Paulo, SP, Brazil

[2] School of the Environment, Geography and Geosciences, University of Portsmouth, Burnaby Building, Burnaby Rd, PO1 3QL, Portsmouth, Hampshire, United Kingdom

*Corresponding author at: IGc-USP (Instituto de Geociências, Universidade de São Paulo), Rua do Lago, 562, CEP 05508-080, São Paulo, São Paulo, Brazil. Tel.: +55 11 3091-3958

E-mail addresses: bruna.ricardo@usp.br (Bruna. S. Ricardo), rmoraes@usp.br (Renato Moraes), catherine.mottram@port.ac.uk (Catherine M. Mottram), ffalei@usp.br (Frederico M. Faleiros), srfvlach@usp.br (Sílvio R. F. Vlach)

Keywords: accretionary orogen; metamorphic evolution; monazite dating; petrochronology; Ribeira Belt

Abstract

Ancient accretionary orogens occur all over the globe and their reconstruction present challenges once a great part of information is missing, due to erosion and fault displacement. The Ribeira Belt, SE Brazil, is an example of an accretionary orogen formed during the amalgamation of Gondwana in the Neoproterozoic. The understanding of its tectonometamorphic history is limited, especially, in its southernmost part, therefore this study uses high precision in-situ geochronology coupled with systematic thermodynamic modelling to provide new constraints for the *P-T*-t paths that some metasedimentary rocks have experienced. Schists and paragneiss in distinct metamorphic conditions crop out and they are all assumed to be part of the same unit, the Turvo-Cajati Formation (TCF). Preliminary studies in the sedimentation and metamorphic settings indicate that part of the TCF formed in the accretionary wedge (High-TCF) and part in the back-arc basin (Medium-TCF) of an ancient microcontinent. We detail the metamorphic studies by implementing petrography, pseudosection modelling in the MnNCKFMASHTO chemical system with Perple_X software and metamorphic isotopic and chemical monazite dating. *P-T* pseudosections are modelled

considering different stages of garnet growth and their respective *P-T* conditions. *P-T*-t paths indicate complex distribution, even within rocks from the same metamorphic zone. Monazite ages indicate an overlap on the metamorphism of High-TCF and Medium-TCF yielding growth between 620-580 Ma, but two sample record older ages (~640 Ma). This period between 640-600 Ma anticipates our understanding of the timing of metamorphic events. The younger cores record metamorphic events coeval to deposition. By comparing the *P-T*-t paths in High-TCF and Medium-TCF, we can better understand the relation of the metamorphic events on both units and their current tectonic disposition. Bimodal thermobaric ratios are observed by interpreting a large set of samples. Therefore, a Japan-like microcontinent previous proposed still is a good hypothesis but its evolution is more complex than previous proposed. More than one monazite population occurs but within the uncertainties associated to isotopic dating, the temporal relation between them could not be established. Nevertheless, without petrochronological constrains, monazite ages could be miss-interpretate. Monazite chemical ages corroborate with the time spam of metamorphic events.

1. Introduction

Accretionary Orogens are formed over millions of years of geodynamics and tectonic in process more complicated than one Wilson's cycle (Cawood et al., 2009). A consequence of this is a complex evolution that may include accreted continental fragments from different tectonic settings (i.e. pieces of the downgoing plate, the back-arc basin, island arcs, the upper plate, among others) juxtaposed together (Cawood et al., 2009). Therefore, reconstructing the evolution of this ancient accretionary orogens may be tricky once lots of information may be missed. When the ocean closes, a final collisional phase is established and it may lead to significant structural modification (Cawood et al., 2009). The instauration of strike-slip shear zones may obliviate original structural relations during the final collisional stages. This can occur either by juxtaposing tectonic units that originally were separated either geographically and/or temporally. The opposite may also happen, a strike-slip shear zone may separate rocks that had a correlated origin (Cawood et al., 2009). Considering all that, the current distribution of units may have been severely affected, and caution is recommended when interpreting the evolution of those units.

In the Brazilian cost, one accretionary orogen, the Mantiqueira Province, crop out (Almeida, 1977 and Almeida et al., 1981, Figure 16a). This Province was assembled in the formation of West Gondwana, during the amalgamation of the São Francisco-Congo, Paranapanema, Luís Alves and Rio de la Plata Plates, on the closure of the Adamastor

Ocean (e.g., Brito Neves et al., 1999, Basei et al., 2009, Trouw et al., 2013). This collision resulted in NE-trending fold belts such as the Araçuaí, the Dom Feliciano and the Ribeira Belts sectioned by strike-slip shear zones (Almeida, 1977 and 1981, Figure 16a), and the last one is studied here.

As a result of millions of years of subduction, thrusting and crustal-shortening, the Ribeira Belt is dominated by terranes with distinct origins separated by strike-slip shear zones (Heilbron et al., 2004, Campanha and Faleiros, 2005, Faleiros et al., 2011). One example is the contact between the Mesoproterozoic (Apiaí Terrane) and Neoproterozoic (Curitiba Terrane) metasedimentary units (Faleiros et al., 2011, Figure 16b). Currently they are juxtaposed and separated by the Lancinha-Cubatão Shear Zone, even though, they have sedimentation setting ages separated by hundreds of My (Figure 16b).

Nevertheless, strike-slip faults can also affect units within the same Terrane; changing the distribution of rocks interpreted to share the same tectonic origin. A metasedimentary unit in the Ribeira Belt was picked to detail studies to evaluate its evolution, the Turvo-Cajati Formation (TCF). Ricardo et al. (2020) presented a not commonly used approach by combining metamorphic studies and detrital zircon to address both the sedimentation and metamorphic settings to this unit. This resulted in some temporal constraints and an evolution model to the TCF. Nevertheless, with advances in petrochronology, detailed *P*-*T*-t paths studies can be used to improve the understanding of the metamorphic evolution of rocks and units. Therefore, we re-evaluate our studies to the TCF by presenting here detailed petrochronological information about the TCF. This approach presents new insights in our understanding of the area and address some questions of the validity of using just a small set of samples to evaluate the evolution of tectonic complex areas.

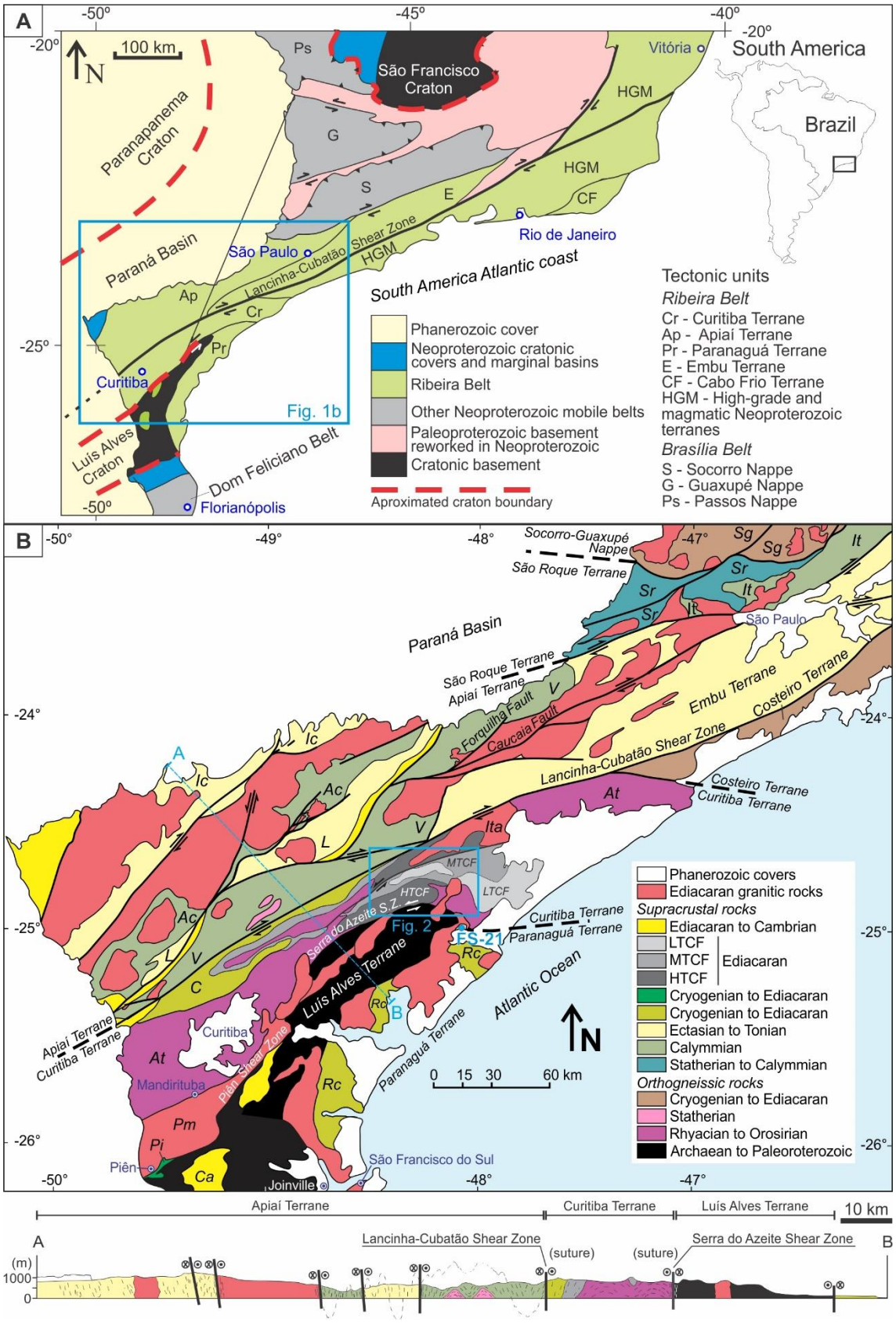

Figure 16 Regional geological context of south and southeastern Brazil (adapted from Faleiros et al., 2016, extracted from Ricardo et al., 2020). (b) Southern and Central Ribeira Belt simplified geotectonic map with the location of the studied area (modified from Malta et al., 2020, extracted from Ricardo et al., 2020). Geological units: Itaiacoca Group (Ic), Água Clara Formation (Ac), Lajeado Group (L), Votuverava Group (V), São Roque Group (Sr), Serra do Itaberaba Group (It), Socorro-Guaxupé Nappe

(Sg), Capiru Formation (C), Low, Medium and High Turvo-Cajati Formation (LTCF, MTCF, HTCF), Piên-Mandirituba Suite (Pm), Piên Mafic-Ultramafic Suite (Pi), Rio das Cobras Formation (Rc), Atuba Complex (At) and Campo Alegre Basin (Ca). The maps use geographical coordinates in degrees (WGS-84 datum).

2. Geological Setting

The Ribeira Belt is composed of several tectonic domains delimited by both thrust and transpressive shear zones (Heilbron et al., 2004, Faleiros et al., 2011, Passareli et al., 2018, Figure 16b). The southernmost part of the Ribeira Belt is divided into four tectonic domains: Apiaí, Curitiba, Embu and Costeiro/Paranaguá Terranes (Basei et al., 1992; Faleiros et al., 2011; Passarelli et al., 2018). Those domains are composed of geological units such as Archean-Paleoproteozoic crystalline basement, Paleo- to Neoproterozoic metasedimentary sequences and voluminous Neoproterozoic granitic batholiths (e.g., Heilbron et al., 2000, 2017, Meira et al., 2019). It is interpreted as an accretionary orogen (i.e. Heilbron et al., 2000, Trouw et al., 2000, Campanha et al., 2015), but some recent studies have been questioning this origin; the authors interpret the whole belt as an intracontinental orogen (Meira et al., 2015, 2019).

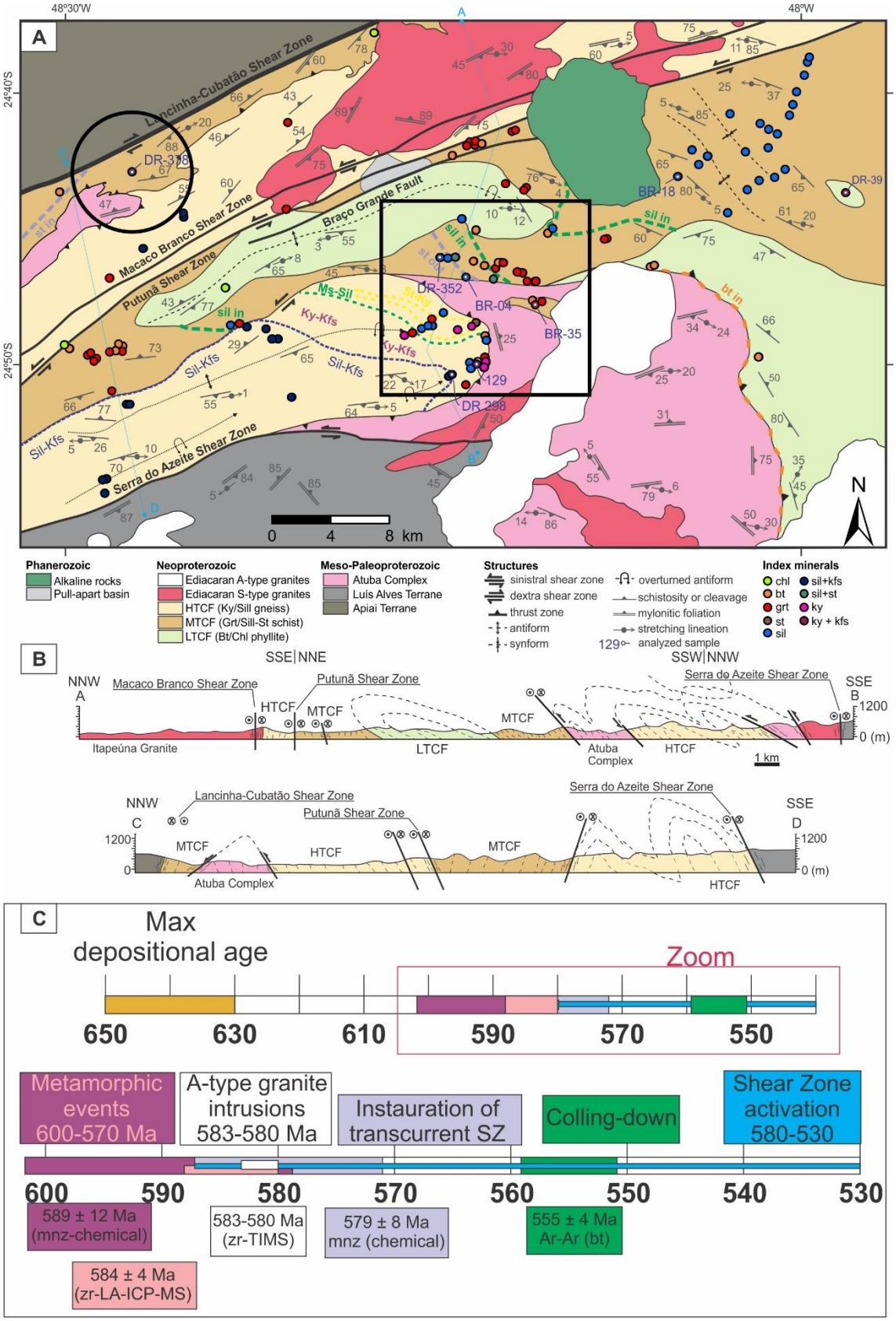

Figure 17(a) Updated geologic map of the studied portion of the Curitiba Terrane showing sites with recognized metamorphic assemblages and isograds (modified after Faleiros et al., 2016 and Ricardo et al., 2020). The map uses geographical coordinates in degrees (WGS-84 horizontal datum). The location of samples is also plotted. See Fig. 1b for the location of the area. (b) Cross sections in the studied area extracted from Ricardo et al., 2020. (c) Timeline of known ages in the area. Maximum depositional age

extracted from Faleiros et al., 2016 and Ricardo et al., 2020. Metamorphic events are presented in Faleiros et al., 2011 (monazite) and 2016 (zircon). A-type granite inclusions from Vlach et al., 2011. Transcurrent shear-zones and Ar-Ar ages are extracted from Faleiros et al., 2011.

The Curitiba Terrane is located between two opposite NE-trending strike-slip shear zones: in the north, the dextral Lancinha-Cubatão Shear zone and in the south, the sinistral Serra do Azeite/Piên Shear Zone (Figure 16b). The Lancinha-Cubatão Shear Zone represents an important boundary between different geochronological domains: (i) on the north, the Apiaí Terrane composed of Mesoproterozoic metasedimentary units and (ii) on the south, the Curitiba Terrane, with Neoproterozoic metasedimentary units (Figure 16b). It is interpreted as a reworked Ediacaran suture zone (e.g., Basei et al., 2008, Faleiros et al., 2011, 2016, Passarelli et al., 2011). The Serra do Azeite/Piên Shear Zone represents the tectonic boundary between the Curitiba Terrane and the Luis Alves Terrane, this last is a small Archean-Paleoproterozoic cratonic remanent (Basei et al., 2009, Faleiros et al., 2011, Passarelli et al., 2018).

The Curitiba Terrane is composed of three units with distinct tectonic origins (Figure 17a). The Atuba Complex (AC) is a fragment of an Archean TTG-type crust reworked on the three events: on the Rhyacian (ca. 2200-2100 Ma), Staterian (~1700 Ma) and the latest on the Ediacaran (630-590 Ma) (Sato et al., 2003, 2009). The Turvo-Cajati (TCF) and the Capiru Formations complement the units on the Curitiba Terrane. They are both metasedimentary units with distinct sedimentary and metamorphic signatures. The Capiru Formation contains metasedimentary rocks metamorphosed on greenschist facies at most (Guimarães et al., 2002, Faleiros, 2017, Santos et al., 2018). Detrital zircon on the Capiru Formation indicates maximum depositional age of 1080 Ma (Leandro, 2016).

The Turvo-Cajati Formation, otherwise, is composed of metasedimentary rocks from lower greenschist to granulite facies, with evidence of partial melting (Faleiros et al., 2011, Ricardo et al., 2020, Figure 17a). The unit is divided in three subunits based on their metamorphic conditions as follow: (i) phyllites and schists bellow garnet zone occur on the Low-TCF (LTCF), (ii) schists on the staurolite and sillimanite zones are named Medium-TCF (MTCF) and (iii) paragneiss and migmatites from granulite facies occur in the High-TCF (HTCF). Provenance studies based on detrital zircon indicates maximum depositional age on ca. 650-630 Ma (Faleiros et al., 2016, Ricardo et al., 2020). Ricardo et al. (2020) also argues different depositional settings for the subunits. According to the authors, LTCF and MTCF have depositional signatures compatible with back-arc basin and HTCF with accretionary wedge setting (Faleiros et al., 2016, Ricardo et al., 2020). Structurally, they occurred in an inversed zoning setting, where younger

rocks overlie older ones and low metamorphic rocks are thrusted over high metamorphic ones (Faleiros et al., 2011, aboveFigure 17b).

Previous metamorphic studies also indicate different tectono-metamorphic settings where these sub-units would metamorphized. *P-T* metamorphic peak conditions on LTCF and MTCF indicates 530-690 °C within pressure regime at 8 kbar at most, as staurolite breaks straight to sillimanite (Ricardo et al., 2020). Nevertheless, the HTCF has passed through higher metamorphic conditions, with partial melting in granulite facies, 670-810 °C and 9.5-12 kbar (Faleiros et al., 2011, Ricardo et al., 2020). HTCF is composed by migmatites with signs of two distinct metamorphic paths: (i) the kyanite-bearing migmatites that have a *P-T* trajectory interpreted as a near isobaric heating and (ii) sillimanite-bearing migmatites with *P-T* path interpreted as a near isothermal decompression (Faleiros et al., 2011).

This scenario would comprise a paired low-*P* and high-*P* metamorphic belt for all TCF (Ricardo et al., 2020). The LTCF+MTCF deposited and was later metamorphized under barrovian-type baric regime on the back-arc setting and the HTCF on the accretionary wedge. This context also includes an active margin of a Japan-like microcontinent, the proto-Curitiba Terrane, comprising the Atuba Complex, as basement and sediment-source for all TCF basins (Ricardo et al., 2020). A-type granites intruded the area at c.a. 580 Ma (580 ± 2 Ma, 583 ± 3 Ma, zircon – ID-TIMS, Vlach et al., 2011).

Even though the TCF and its tectonic relation with the AC is now better understood, the unit was never dated under the light of modern petrochronological approach. The only metamorphic ages on literature so far are (Figure 17c):

(i) 589 ± 12 Ma from chemical monazite dating on sillimanite-bearing HTCF migmatite, interpreted as the metamorphic peak (Faleiros et al., 2011);
(ii) 584 ± 4 Ma LA-ICP-MS U-Pb zircon age from kyanite-bearing rocks from HTCF, also interpreted as metamorphic peak (Faleiros et al., 2016);
(iii) 579 ± 8 Ma also from monazite chemical dating, interpreted as greenschist facies metamorphic overprint (Faleiros et al., 2011);
(iv) 555 ± 4 Ma from ^{40}Ar-^{39}Ar biotite data indicates that HTCF cooled below 250-300 °C (Faleiros et al., 2011).

Petrochronology is broadly used in recent orogens such as the Himalayas (i.e. Mottram et al., 2014, 2015). Nevertheless, it can be challenging in older terranes duo to the method uncertainties but can produce very interesting and coherent results (Rocha et al., 2017; Motta et al., 2021). A more detailed petrochronological study on the *P-T*-t

paths were never conducted on these rocks of the Ribeira Belt. Therefore, applying petrochronology on different samples from the TCF could open a new perspective to better understand its tectonic evolution, its relation between the unit with the Southern Ribeira Belt and attest the validity of applying such method in older terranes.

3. Methods

3.1 Sample Selection

To compare *P-T*-t paths from different rocks, the sample selection was made following two criteria: (1) rocks from different metamorphic conditions and (2) from different structural domains separated by strike-slip faults. Therefore, samples from staurolite zone (DR378), sillimanite zone (DR352, BR04, BR18, BR07), sillimanite-K-feldspar (DR298) and kyanite-K-feldspar (129) zones were picked. In most of them, metamorphic data and U-Pb monazite dating were performed with different techniques following the characteristics of each sample. For instance, samples with bigger monazite grains were picked for LA-ICP-MS technique and only chemical dating was performed in samples with smaller monazites. Details on the methods are presented below.

3.2 Mineral Chemistry

Mineral major phases were analyzed with a JEOL JXA-FE-8530 Electron Probe Microanalyser (EPMA) hosted at NAP Geoanalítica, Institute of Geosciences, University of São Paulo. Operations conditions were 15 kV and 20 nA for spot analyses and 15 kV and 150 nA for compositional maps. Beam size was 5 µm in all analyses. Compositional maps were treated in the software ImageJ2 (Rueden *et al*., 2017). Structural formula of each mineral phase was calculated with software AX by Tim Holland (https://www.esc.cam.ac.uk/research/research-groups/research-projects/tim-hollands-software-pages/ax).

Monazite data was collected in the same equipment under operation conditions of 15 kV and 300 nA for spot analyses and 15 kV and 200 nA for compositional maps. Beam size was 4 µm in most analysis, but some were conducted with 3 µm. Compositional maps were treated in the software ImageJ2 (Rueden *et al*., 2017). Monazite structural formula and U-Th-Pb ages were calculated following Vlach (2010).

3.3 Thermodynamic modeling

P-T pseudosections were calculated with the software Perple_X (Connolly, 2005) using the database hp11ver (Holland & Powell, 2011) in MnNCKFMASHTO and NCKFMASHTO chemical systems. Solution models used for muscovite, chlorite, biotite, garnet, staurolite, cordierite, ilmenite and silicate melt are from White *et al*. (2014a), epidote from Holland and Powell (2011) and feldspar from Fuhrman and Lindsley (1988).

Water is considered a pure fluid phase and in excess for melt-absent calculations. Fe^{3+} was estimated based on charge balance in minerals chemical formula and for the amount in the bulk rock composition it was set to reproduce the contents of observed Fe^{3+}-bearing phases (e.g., epidote, hematite) in studied samples.

Pseudosections were modeled to samples BR-04, BR-18, BR-35, DR-352 and DR-378 using estimated bulk rock composition. The estimative was chosen instead of obtained by XRF, because they have appreciable degrees of weathering and would not produce reliable bulk rock chemical composition. Compositions were built from modal proportions and mineral chemistry obtained with the EPMA. Therefore, the modal percentage of each mineral in a thin section was multiplied by its density to obtain the weight of each phase. This number was normalized by 100%. Then, the weight of each mineral was multiplied by its chemical composition divided in oxide by oxide in molar proportion and again normalized by 100%. The molar proportion of each oxide was obtained by the sum of all molar proportion on each.

Three samples (BR-04, DR-352 and DR-378) were picked to obtain *P-T* paths following the methodology proposed by Cutts *et al*. (2009, 2010). Garnet on those samples show distinct domains of growth in compositional maps. Therefore, the percentual representing these different garnet growth stages were removed from the bulk composition and new pseudosections were modeled for each stage. This produces, at least, two pseudosections to each sample and two *P-T* conditions of each garnet growth stage. An estimative of a *P-T* path is proposed based on that.

3.4 LA-ICP-MS monazite/garnet punctual analysis

Monazite were located using the same EPMA equipment and BSE images were also collected. In-situ monazite U-Th-Pb analyses were performed in twelve sessions at the University of Portsmouth using a Jena PlasmaQuant Elite ICP-MS coupled to an ASI RESOlution 193 nm ArF excimer Laser system. Trace element analyses in monazite were performed separately in five sessions and an extra session was performed to obtain trace element content in garnet. Monazite Stern (512 ± 0.7 Ma; Palin et al., 2013) was used as the primary reference material and 44069 (~424.9 Ma; Aleinikoff et al., 2006), Bananeira (507.7 ± 1.3 Ma; Gonçalves et al., 2016), Itambé (506.4 ± 0.7 Ma; Gonçalves et al., 2016), Trebilcock (272 ± 4 Ma, Tomascak et al., 1996) and Vermillion (2653.7 ± 6.8, University of Portsmouth internal reference material) were used as secondary reference materials to monitor reproducibility throughout the analytical period. Two of each reference materials were ablated between every 8 unknowns. For trace element analysis, NIST610 glass was used as the primary reference material. BHVO-2G (Jochum

et al., 2007), BCR-2G and Trebilcock (Tomascak et al., 1996) were used as secondary reference material. Laser condition and reproducibility were different for each type of analysis and the conditions are detailed in the supplementary material.

Monazite data were processed, corrected for down-hole fractionation and instrumental drift using the Iolite 3.4 software (Paton et al., 2011). Data is presented using IsoplotR (Vermeesch, 2018) and Isoplot v.4.15 (Ludwig, 2008). Uncertainties include instrumental drift and were increased in quadrature to include 2.0% reproducibility of the secondary reference material.

3.5 LA-ICP-MS monazite/garnet chemical mapping

Two monazite grains a little larger than 150 µm were picked from sample DR298 to more detailed studies on the trace element distribution and its possible association with different U-Th-Pb ages. Two approaches were adopted: (1) punctual trace element and U-Th-Pb analysis to later data integration on QGIS software (https://www.qgis.org/) and (2) detailed compositional maps made with equal-length lines ablated and data treatment on CellSpace Monaco function from Iolite v 3.4 (Paul et al., 2012, Paton et al., 2011).

LA-ICP-MS maps were also made for garnet grains. The methodology for both monazite and garnet were similar. Equal-length lines were made on each grain to cover all the grains surface. Those analysis were interleaved with lines on reference material. NIST610 was used as primary reference material to monazite and NIST612 to garnet. The second reference material was BHVO in both cases. 80% of overlapping was made on the cleaning of each line. Length, spot size, repetition rate, laser energy and speed were different in each map. The conditions for each of them can be found on the supplementary material. Data reduction was also made with plug-in CellSpace Monaco from Iolite v 3.4 software (Paul et al., 2012, Paton et al., 2011). This function integrates the MS-data and generates compositional images.

4. Sample Characterization

The sample selection was made so most metamorphic zones would be represented by their best rock samples. Therefore, three samples from MTCF and two from HTCF were picked. From MTCF, one sample represents the staurolite zone (DR-378) and two samples represent the sillimanite zone (BR-04 and DR-352). From HTCF two samples were selected representing the sillimanite-K-feldspar zone (DR-298) and kyanite-K-feldspar zone (129A). Both samples were previously studied by Faleiros et al. (2011). The authors provide a description of the samples and metamorphic conditions estimates based on both thermodynamic modelling and conventional thermobarometry.

They did not obtain any geochronological information for sample DR-298. Therefore, it is presented here a brief description of the sample, new phase equilibria modelling and geochronological data for it. Sample 129A is also studied by Ricardo et al. (2020), therefore a brief description and geochronological/trace element data are presented here for this sample. Representative EPMA analysis from each sample are presented in Tables 1 and 2 in the end of the text. Samples BR-07, BR-18 and BR-35 were also studied, and they are described in the supplementary material.

Table 1 Representative microprobe analyses of garnet and plagioclase from TCF. Selected points are the ones used to constrain isopleths in the pseudosection modeling.

Mineral	Garnet									Plagioclase	
Sample	BR04			DR352			DR378			BR04	DR352
	Z1	Z2	Z3	Z1	Z2	Z3	Z1	Z2	Z3		
	grt1.9	grt1.11	grt1.14	grt1.13	grt1.7	grt1.4	grt2.5	grt2.9	grt2.3	pl4.3	pl3
SiO2	36.70	36.60	36.69	36.33	36.61	36.18	36.55	36.83	36.90	63.19	64.99
TiO2	0.15	0.11	0.02	0.01	0.02	0.05	0.01	0.00	0.00	0.00	0.00
Al2O3	20.70	20.71	21.01	20.78	20.81	20.81	21.02	21.02	21.31	24.51	22.97
Cr2O3	0.04	0.04	0.04	0.02	0.03	0.05	0.02	0.00	0.00	0.00	0.00
Fe2O3	1.38	1.38	1.38	2.17	2.17	2.17	0.55	0.55	0.55	0.18	0.04
FeO	29.84	29.25	34.00	32.75	36.03	38.00	31.73	31.13	31.27	0.15	0.01
MnO	6.10	5.27	3.09	3.68	1.80	0.53	4.69	4.49	4.88	0.00	0.02
MgO	1.53	1.29	2.28	1.14	1.64	2.15	3.58	4.07	3.83	0.00	0.00
CaO	4.31	5.57	3.28	4.52	3.36	1.97	2.11	1.97	1.94	4.89	1.37
Na2O	0.04	0.02	0.01	0.03	0.02	0.00	0.01	0.02	0.01	8.69	9.70
K2O	0.00	0.00	0.00	0.00	0.00	0.00	0.00	0.00	0.00	0.05	1.06
Total (%)	100.79	100.23	101.79	101.44	102.49	101.92	100.27	100.09	100.69	101.66	100.16
Oxigen	12.000	12.000	12.000	12.000	12.000	12.000	12.000	12.000	12.000	8.000	8.000
Si	2.958	2.959	2.933	2.926	2.924	2.908	2.943	2.956	2.948	2.751	2.853
Ti	0.009	0.007	0.001	0.001	0.001	0.003	0.001	0.000	0.000	0.000	0.000
Al	1.967	1.974	1.980	1.973	1.959	1.972	1.995	1.989	2.007	1.258	1.189
Cr	0.002	0.003	0.002	0.001	0.002	0.003	0.001	0.000	0.000	0.000	0.000
Fe3	0.083	0.084	0.083	0.132	0.131	0.131	0.033	0.033	0.033	0.006	0.001
Fe2	2.011	1.978	2.273	2.206	2.406	2.554	2.137	2.090	2.090	0.006	0.000
Mn	0.416	0.361	0.209	0.251	0.122	0.036	0.320	0.305	0.330	0.000	0.001
Mg	0.184	0.155	0.272	0.137	0.195	0.258	0.430	0.487	0.456	0.000	0.000
Ca	0.372	0.483	0.281	0.390	0.288	0.170	0.182	0.169	0.166	0.228	0.065
Na	0.006	0.003	0.002	0.005	0.003	0.001	0.001	0.004	0.001	0.734	0.826
K	0.000	0.000	0.000	0.000	0.000	0.000	0.000	0.000	0.000	0.003	0.059
Total	8.010	8.005	8.035	8.022	8.030	8.036	8.042	8.034	8.032	4.985	4.994
Alm	0.67	0.66	0.75	0.74	0.80	0.85	0.70	0.69	0.69	0.76	0.93
Prp	0.06	0.05	0.09	0.05	0.06	0.09	0.14	0.16	0.15	0.24	0.07

Grs	0.12	0.16	0.09	0.13	0.10	0.06	0.06	0.06	0.05
Sps	0.14	0.12	0.07	0.08	0.04	0.01	0.10	0.10	0.11

Table 2 Representative microprobe analyses of muscovite, biotite and staurolite from TCF.

Mineral	Muscovite			Biotite			Staurolite
Sample	BR04	DR352	DR378	BR04	DR352	DR378	DR378
	ms6	ms2	ms1	bt1	bt4	bt3	st1.4
SiO2	45.430	46.87	44.91	35.26	33.99	35.99	27.84
TiO2	0.840	0.55	0.48	1.84	3.00	1.56	0.63
Al2O3	36.820	38.74	35.27	20.11	19.52	19.59	54.50
Cr2O3	0.000	0.00	0.00	0.00	0.00	0.00	0.04
Fe2O3	0.470	1.06	1.51	0.00	0.36	0.61	0.00
FeO	1.590	1.23	1.33	20.71	24.55	17.82	13.05
MnO	0.010	0.00	0.00	0.14	0.13	0.13	0.47
MgO	0.660	0.60	0.66	8.91	6.16	11.22	1.73
CaO	0.030	0.00	0.01	0.10	0.02	0.03	0.01
Na2O	0.990	0.50	1.40	0.05	0.14	0.39	0.00
K2O	9.330	6.49	8.94	8.97	8.95	8.97	0.02
Total (%)	96.170	96.03	94.50	96.09	96.82	96.30	98.28
Oxigen	11.000	11.000	11.000	11.000	11.000	11.000	46.000
Si	2.992	3.018	3.016	2.667	2.613	2.684	7.670
Ti	0.042	0.026	0.024	0.105	0.173	0.088	0.130
Al	2.859	2.941	2.793	1.793	1.769	1.722	17.702
Cr	0.000	0.000	0.000	0.000	0.000	0.000	0.009
Fe3	0.023	0.051	0.076	0.000	0.021	0.034	0.000
Fe2	0.088	0.066	0.075	1.310	1.578	1.111	3.007
Mn	0.000	0.000	0.000	0.009	0.009	0.008	0.109
Mg	0.065	0.058	0.066	1.004	0.706	1.247	0.710
Ca	0.002	0.000	0.001	0.008	0.001	0.002	0.003
Na	0.127	0.062	0.182	0.007	0.021	0.056	0.001
K	0.784	0.533	0.766	0.865	0.878	0.853	0.006
Total	6.981	6.757	7.000	7.768	7.769	7.806	29.347
XMg	0.42	0.47	0.47	0.43	0.31	0.53	0.19
Al/Si	0.96	0.97	0.93	0.67	0.68	0.64	

4.1 Staurolite Zone from MTCF (sample DR-378)

Sample DR-378 is composed of quartz (~40%)-rich granoblastic layers interleaved with less expressive biotite (~20%) and muscovite (~15%) -rich lepidoblastic

layers and both define a schistosity. Biotite may occur either euhedral and oriented along the schistosity or anhedral. Staurolite (~15%) porphyroblasts can be 1cm-long and occur sub-euhedral full of matrix minerals inclusions, such as quartz, muscovite, ilmenite, and apatite may occur following the main external schistosity. Garnet (~3%, Figure 18a) porphyroblasts are also sub-euhedral but slightly smaller than staurolite ones (~1mm). They are also full of inclusions of matrix minerals such as quartz, muscovite, ilmenite, apatite, but chlorite and allanite also occur following the matrix schistosity. Accessory phases are ilmenite (~3%), apatite, tourmaline, and sulfide. They occur as inclusions and associate with lepidoblastic layers following the main schistosity. Allanite also occurs as metamict and isotropic grains along the matrix. Plagioclase is rare (<2%) but occurs associated with quartz. Chlorite also occurs locally as anhedral grains associated with also anhedral biotite.

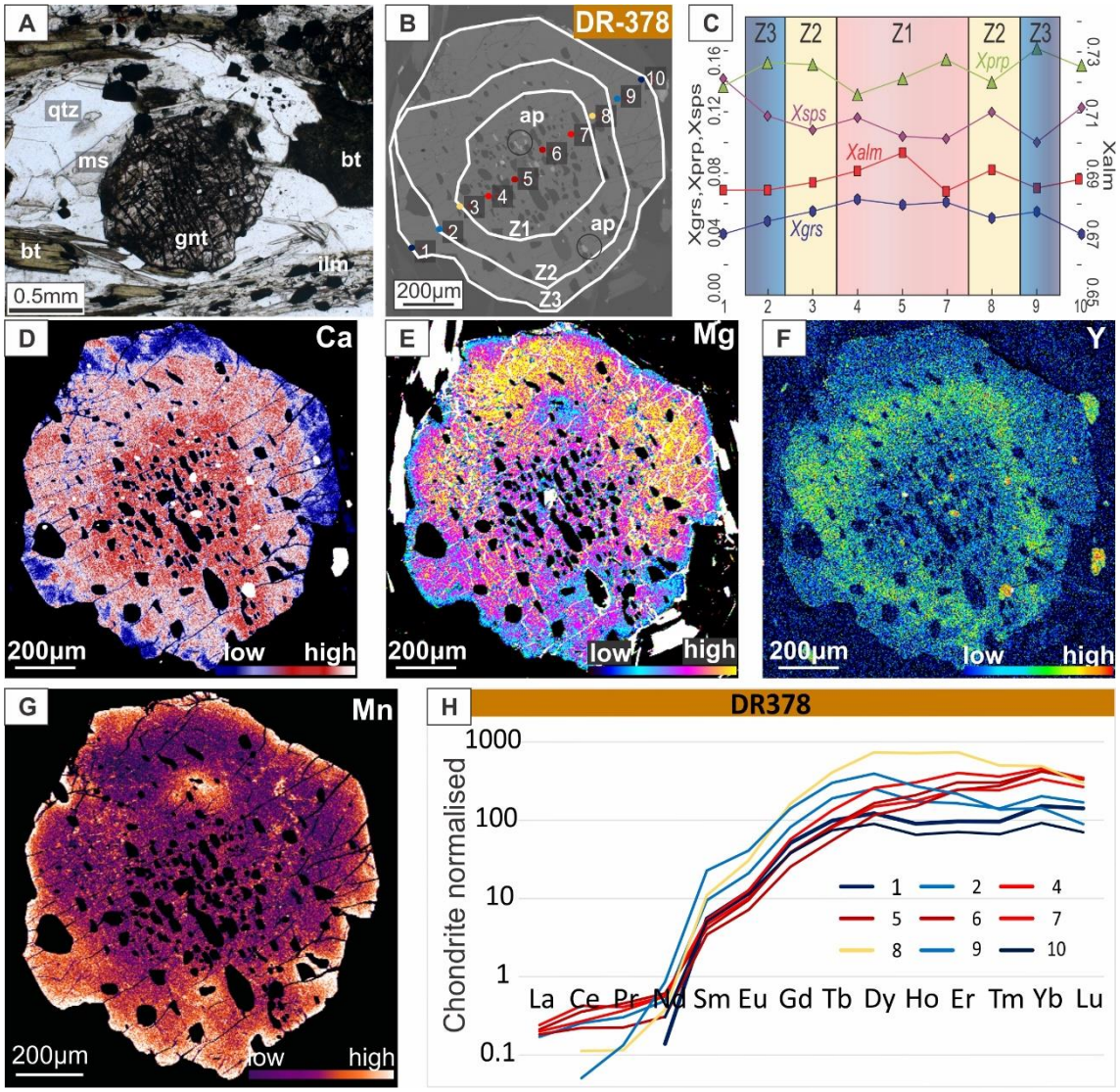

Figure 18 Characterization of garnet from sample DR378 from the staurolite zone. (a) optical microphotograph; (b) back-scattered image from garnet grain, spot analysis location and inferred growth zones described in the text; (c) chemical profiles of major elements in garnet based on EPMA

spot analysis and inferred growth zones; (d-g) compositional maps obtained with EPMA, Ca, Mg, Y and Mn, respectively; (h) chemical profiles of trace element **in garnet.**

Garnet geographical and chemical core match (Figure 18b-c) and they indicate a concentric growth with Ca (0.04-0.06) and Fe (0.68-0.70)-rich core, Mg (0.13-0.16) and Mn (0.10-0.14). EPMA compositional maps (Figure 18d-g) and chemical profiles show distinct behavior for *X*alm ($Fe^{2+}/(Fe^{2+}+Ca+Mg+Mn)$) and *X*sps ($Mn/(Fe^{2+}+Ca+Mg+Mn)$) when compared to other samples. Y compositional map (Figure 18f) shows a high-Y ring around a poor-Y core. X_{Mg} ($Mg/(Mg+Fe^{2+})$) varies from 0.47-0.53 in biotite and 0.29-0.47 in muscovite. X_{Mg} in staurolite varies from 0.13-0.24 with higher values located near core in chemical profiles. The Al/Si ratio in muscovite is between 0.90-0.93. This sample does contain plagioclase, but it is very scarce and could not be measured in the analyzed thin section, in which it was not identified.

Trace element in this sample were analyzed close to the same spot that the EPMA analysis (Figure 18h). Garnet can be divided in 3 zones following the trace element distribution: Z1 is the core, Z2 is an outer ring and Z3 is the rim. Z1 has intermediate values of HREE (points 4-7). Z2 has the highest HREE and is represented by point 8, and Z3 has the lowest HREE values (points 1, 2, 9 and 10). Z1 contains apatite inclusion while Z2 and Z3 do not.

Trace element maps were made in a different garnet grain to compare possible distinct behavior and are presented in supplementary material. Major elements are more diffuse than the trace element distribution, which is more concise. Nevertheless, major and trace element seem to have similar distribution. Core is impoverished in almost all trace element analyzed; exception is made to Yb. Y is slightly higher in the core, followed by a continuous impoverished in this element. The rim has higher amounts of all trace element, including Y, but as seen in EPMA compositional Y map, this may be just an outer ring (Z2), not the rim (Z3), which would be impoverished in trace element.

4.2 Sillimanite Zone from MTCF (sample DR-352)

Sample DR-352 is composed of a well-developed S2 schistosity interleaved with millimeter-thick muscovite (~27%), biotite (~34%)-sillimanite (~7%) -rich lepidoblastic layers and quartz (~20%)-rich granoblastic layers. Plagioclase is scarce (<5%) and occur associated with quartz. Biotite occurs either euhedral oriented along the schistosity and anhedral not-necessarily in alignment. Garnet porphyroblasts are euhedral (~4mm, Figure 19a) and occur aligned to S2 foliation with deformation-shadow. They also have corroded rims. Ilmenite is scarce (<3%) and occurs as inclusions in garnet without alignment with external foliation or included in the matrix minerals. Apatite and tourmaline occur as accessory phases on the matrix. Allanite also occurs as metamict and isotropic

grains included in garnet and along the matrix. The S2 schistosity is folded in a D3 crenulation.

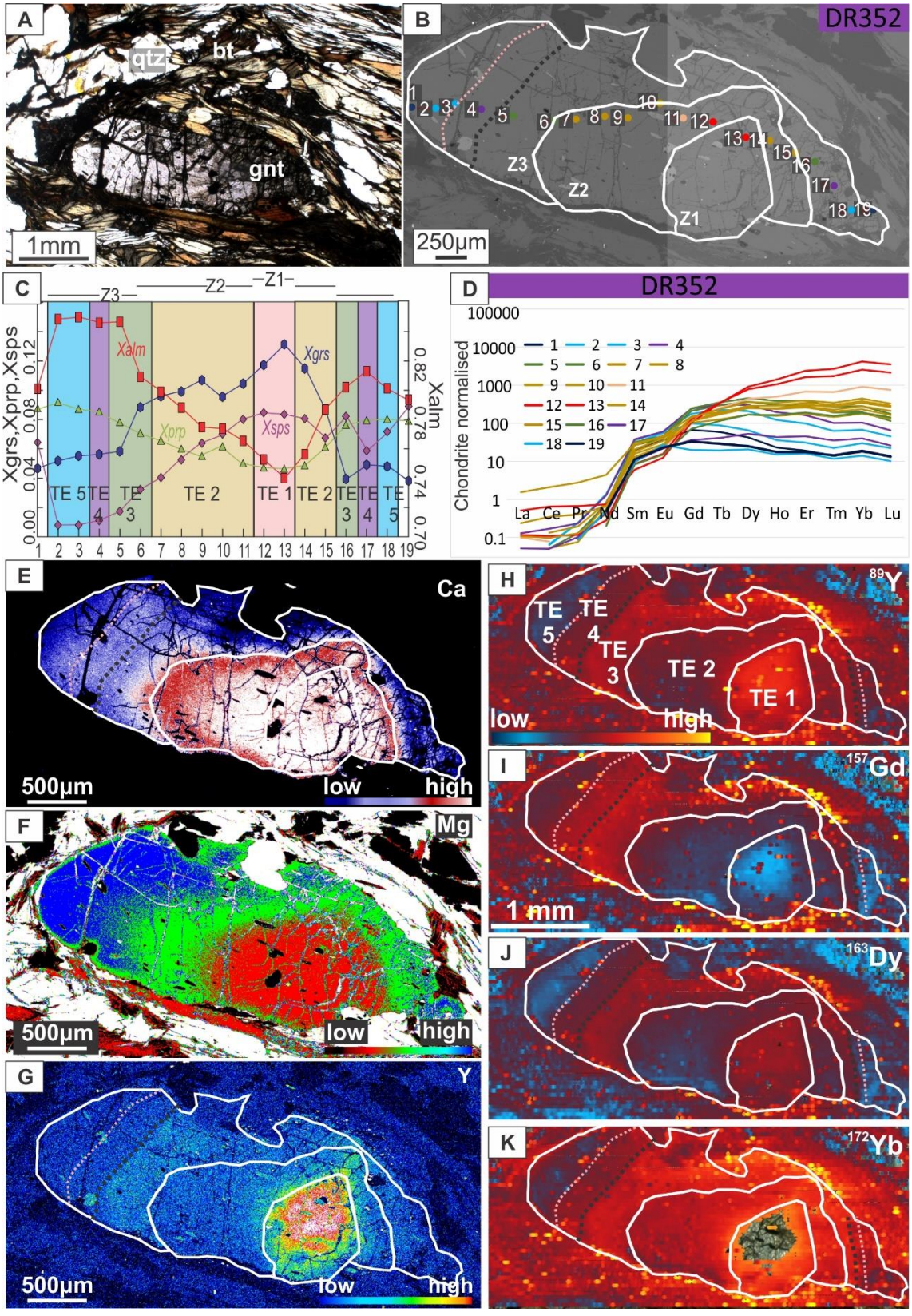

Figure 19 Characterization of garnet from sample DR352 from the sillimanite zone. (a) optical microphotograph; (b) back-scattered image from garnet grain, spot analysis location and inferred

growth zones described in the text; (c) chemical profiles of major elements in garnet based on EPMA spot analysis. Inferred growth zones named Z1-Z3 are chosen based on major elements and TE1-TE5 are made based on trace element**; (d) chemical profiles of** trace element **in garnet (e-g) compositional maps obtained with EPMA, Ca, Mg, Y, respectively; (h-k) compositional maps obtained with LA-ICP-MS, Y, Gd, Dy and Yb, respectively.**

Garnet EPMA compositional maps and chemical profile show diffusion chemical zoning and the geographic core does not match the chemical one (Figure 19b-g). *X*alm and *X*prp (Mg/(Fe^{2+}+Ca+Mg+Mn)) increase towards the rim with 0.74-0.85 and 0.05-0.09 values, respectively. In other hand, *X*grs (Ca/(Fe^{2+}+Ca+Mg+Mn)) and *X*sps have decrease towards the rim profiles with 0.04-0.13 and 0.01-0.08 values, respectively. Y compositional map also shows a high-Y concentric core, Fe and Mn maps show a Mn-rich and Fe-poor external rim. X_{Mg} in biotite is constant (0.28-0.31) and muscovite has a wider range (0.35-0.70). The Al/Si ratio in muscovite is between 0.96-1.00. Anorthite content varies from 0.01 to 0.12.

Trace element in this sample were analyzed close to the same spot that the EPMA analysis (Figure 19d). Trace element maps were also made in LA-ICP-MS in the same garnet (Figure 19h-k). Their distribution marks same zoning pattern than major elements. Nevertheless, the behavior of major and trace element differs. Y and HREE record at least five zones while only three-four zones can be observed in major elements. Following the trace element distribution, five zones can be distinguished (TE1-5). TE1 occurs within the garnet chemical core (points 12-13). This zone represents the highest content in HREE/Y. TE2 is slightly depleted in HREE and Y, when compared to TE1 (points 7-11 and 14-15). TE3 represents a high-Y/HREE ring very evident in the maps (points 5-6, 16). TE4 occurs within a Y/HREE-depleted ring (points 4,17). TE5 represents the most depleted zone and the garnet rim (points 1-3,18-19).

On the other hand, major elements maps indicate 3-4 zones (Z1-3). Z1 matches TE1 and is the garnet chemical-core (points 12-13), enriched in Ca and Mn and depleted in Fe and Mg. Z2 is the garnet mantle (points 6-11, 14-15) where Ca and Mn are decreasing, and Fe and Mg increase. Z3 represents the garnet rim (points 2-5, 16-18) and the lowest values of Ca and Mn and highest of Fe and Mg. Finally, the outermost thin rim presents a sharp increase in Mn and decrease in Fe, Ca, and Mg (points 1 and 19).

4.3 Sillimanite Zone from MTCF (sample BR-04)

Sample BR-04 is composed of well-developed millimeter-thick muscovite (~30%) and biotite (~20%)-rich lepidoblastic layers interleaved with granoblastic layers composed of quartz (~20%) and plagioclase (~20%). S_2 schistosity is defined by

alignment of muscovite, biotite and sillimanite (~6%), and folded in an open D_3 crenulation. Garnet porphyroblasts are sub-anhedral (~2mm, ~5%, Figure 20a) and inclusion-rich, forming a spiral pattern that indicates rotation and it is continuous with external S_2 schistosity. Deformation-shadows occur around garnet are filled with quartz and are disposed parallel to S_2 schistosity. Ilmenite is scarce (~2%) and occurs in alignment with lepidoblastic layers and as inclusion in garnet, shaping the schistosity rotation inside the porphyroblasts. Apatite and tourmaline occur as accessory phases.

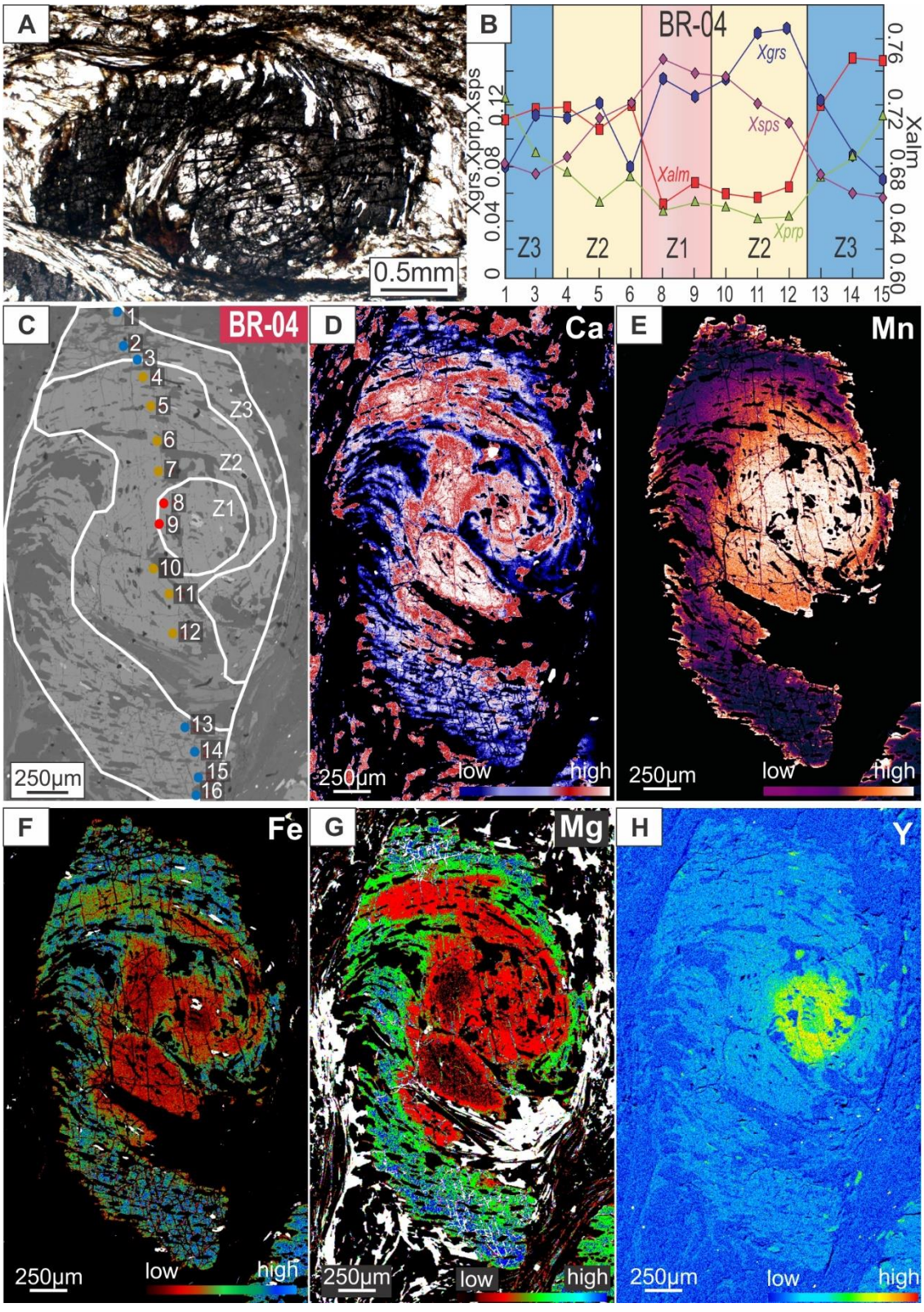

Figure 20 Characterization of garnet from sample BR04 from the sillimanite zone. (a) optical microphotograph; (b) chemical profiles of major elements in garnet based on EPMA spot analysis and inferred growth zones; (c) back-scattered image from garnet grain, spot analysis location and inferred growth zones described in the text; (d-h) compositional maps obtained with EPMA, Ca, Mn, Fe, Mg, respectively.

Both garnet compositional maps and chemical profiles show prominent chemical variation following the snowball-like rotation (Figure 20b-h). Geographic core almost matches chemical core. Y compositional map indicates a concentric Y-rich core. Mn (0.06-0.15) and Ca (0.07-0.16) compositional maps show bell-shaped profile in these elements while Fe (0.66-0.75) and Mg (0.05-0.12) have increase towards rim. X_{Mg} in biotite and muscovite varies from 0.43-0.47 and 0.42-0.62, respectively. The Al/Si in muscovite is between 0.94-0.97. Anorthite content varies from 0.20-0.24.

Due to the alteration caused by weathering in this sample, trace element maps were not produced on LA-ICP-MS. Based on EPMA compositional maps, 3 zones can be distinguished on this garnet. Z1 is the core, best delimited on Y-map, Z2 is the middle and Z3 is the rim (Figure 20a-c).

4.4 Sillimanite-K-feldspar Zone from HTCF (Sample DR298)

This sample is a migmatitic paragneiss composed of a leucosome of granoblastic layer enriched in quartz, K-feldspar and subordinate plagioclase. Muscovite only occurs as inclusions in other phases. Sillimanite also occurs aligned in the main foliation along with biotite. Kyanite occurs locally included in K-feldspar. Garnet occurs as porphyroblasts with inclusions of quartz, K-feldspar, and, locally, kyanite (Figure 21a-b). It has corroded rims and is surrounded by biotite, sillimanite, quartz and K-feldspar. Ilmenite is scarce (<2%) and occurs included in matrix minerals. Biotite may also occur as anhedral crystals and disperse along the foliation, interpreted as a retrograde phase.

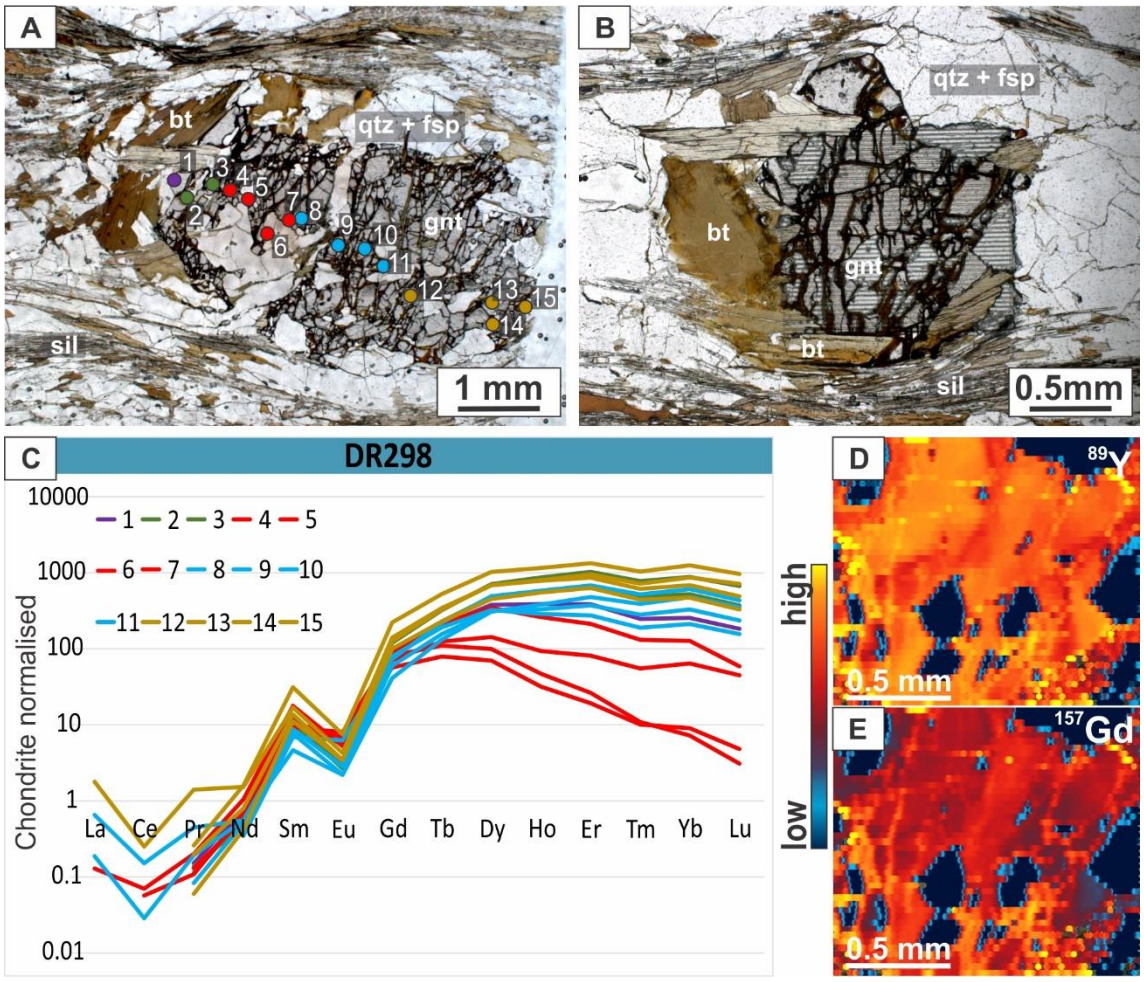

Figure 21 Characterization of garnet from sample DR298 from the K-feldspar- sillimanite zone. (a) optical microphotograph with the location of spot analysis of LA-ICP-MS analysis; (b) optical microphotograph of mapped garnet and LA-ICP-MS map lines; (c) chemical profiles of trace element **in garnet (d-e) compositional maps obtained with LA-ICP-MS, Y and Gd, respectively.**

Mineral chemistry from this sample is extracted from Faleiros et al. (2011), which describe garnet with flat chemical profiles generated by diffusion, with discrete increase in both *X*sps and *X*alm towards garnet rim. A slow decrease in *X*prp is also observed in their profile (Fig. 9f from Faleiros et al., 2011). Chemical composition of K-feldspar and biotite was obtained for comparison (Table 3 from Faleiros et al., 2011), which indicates An (Ca/(Ca+Na+K)) 0.50%, Ab (Na/(Ca+Na+K)) 10.62% and Or (K/(Ca+Na+K)) 88.88%. X_{Mg} in biotite is 0.372.

Two garnet grains were analyzed in this sample, in the biggest one spot analysis were made and compositional maps were obtained in a smaller. Compositional diagrams show some zoning with lower HREE values represented by points 4-7 and higher HREE on points 1-3 and 8-15 (Figure 21c). LA-ICP-MS compositional trace element maps from

this sample did not produce good results either by the lack of range in the elements content or because the garnet contains several large inclusions (Figure 21d-e).

4.5 Kyanite-K-feldspar Zone from HTCF (Sample 129)

This sample was studied in previous works by Faleiros et al. (2011) and Ricardo et al. (2020). Therefore, only a brief description is presented here with new trace element information added. This sample has a schistosity defined by the alignment of leucosome layers enriched in quartz (~25%), K-felspar (~8), plagioclase (~20%) interleaved with mesocratic neosome layers with Qtz+Kfs+Pl+thin-Bt (~30%). Muscovite (~3%) may occur as coarse-grained lens. Garnet occurs as corroded porphyroblasts (~13%, Figure 22a), with reaction coronas of Bt+Pl+Kfs±Qtz±Ms. Kyanite occurs locally as a residual phase included in plagioclase. Ilmenite is rarely observed.

EPMA compositional maps show decrease towards the rim of Mn and Ca profiles and increase towards the rim of Fe and Mg in the profiles (Figure 22b-c). This matches the profiles presented by Faleiros et al. (2011), that indicate to *X*sps and *X*grs bell-shaped profiles, opposing *X*alm and *X*prp profiles.

Trace element spot analyses and compositional maps Figure 22were made on the highlighted portion of Figure 22 (white rectangle at Figure 22a; Figure 22d-g). Points near the garnet core (6 and 7) show the highest values of HREE with a decrease in HREE content in the points in blue (1-5 and 15) and even lower in the red points (9-12). The lowest HREE values occur in point 14. Points with orange X did not produce good analysis. This chemical zoning is not clear on LA-ICP-MS trace element maps. They show more uniform distribution on all trace element. Y-EPMA compositional map also shows this homogeneous distribution (Supplementary material).

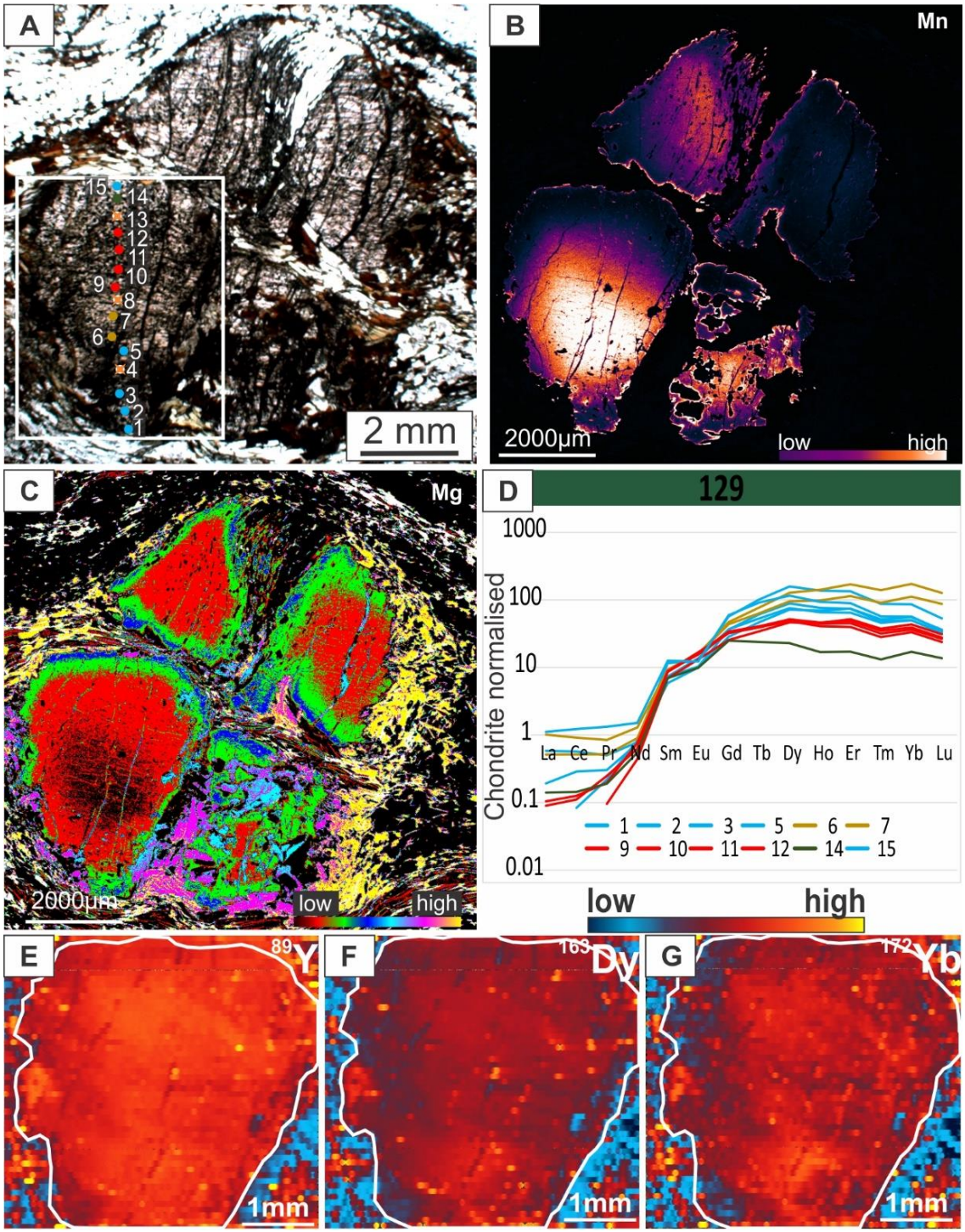

Figure 22 Characterization of garnet from sample 129 from the K-feldspar-kyanite zone. (a) optical microphotograph with the location of spot analysis of LA-ICP-MS analysis; (b-c) compositional maps obtained with EPMA, Mn and Mg, respectively; (d) chemical profiles of trace element **in garnet; (e-g) compositional maps obtained with LA-ICP-MS, Y, Dy and Yb, respectively.**

5. Thermodynamic Modeling

Pseudosections were modeled to constrain the metamorphic history, including the *P-T* paths and peak conditions. As described in petrography and mineral chemistry, garnet grains present more than one stage of growth. The pseudosection calculation considered that the equilibrium composition changes dynamically once elements get 'trapped' inside

garnet grains and stops being reactive in the rest of the rock. Therefore, the pseudosection calculation was made step-by-step adapting the equilibrium composition to the garnet growth zone/stage. This produced two-three pseudosections for each sample. For each pseudosection, the respective volume of each garnet zone was considered, calculated, and removed from the equilibrium composition for the next stage. A new pseudosection was calculated from this new reactive composition to constrain another garnet growth stage. Isopleths were used to constrain each one of those stages following the garnet composition obtained on the EPMA to one representative spot analysis for each zone. Pseudosections are presented to samples DR-378, DR-352 and BR-04 in this section. Samples BR-18 and BR-35 are presented in Supplementary Material. The composition used in each one of the pseudosections are presented in Table 3 below.

Table 3 Estimated bulk rock composition for each sample/zone used in pseudosection modeling.

	DR378			DR352			BR04		BR 18	BR35	
	Z11	Z2	Z3	Z1	Z2	Z3	Z1	Z2+Z3		Z1	Z2
Oxide						mol%					
SiO2	64.78	65.05	65.34	58.49	58.64	58.99	62.30	62.39	63.68	56.49	55.58
TiO2	2.93	2.96	3.00	3.04	3.07	3.14	1.85	1.86	2.51	1.99	2.07
Al2O3	13.84	13.84	13.83	16.50	16.52	16.57	16.63	16.65	14.63	15.54	15.95
Fe2O3	0.00	0.00	0.00	0.00	0.00	0.00	0.00	0.00	0.00	0.00	0.00
FeO	9.98	9.74	9.49	13.23	13.03	12.51	8.18	8.07	9.62	11.86	11.95
MnO	0.32	0.28	0.22	0.17	0.12	0.09	0.35	0.32	0.51	0.43	0.37
MgO	4.99	4.97	4.95	4.00	4.05	4.14	3.80	3.82	4.34	7.61	7.87
CaO	0.26	0.24	0.21	0.43	0.38	0.29	1.45	1.43	0.63	0.85	0.78
Na2O	0.44	0.44	0.45	0.67	0.68	0.70	1.94	1.94	0.98	0.89	0.93
K2O	2.29	2.32	2.35	3.38	3.41	3.49	3.37	3.39	3.02	4.29	4.45
O2	0.17	0.17	0.17	0.09	0.09	0.09	0.13	0.13	0.09	0.04	0.04
H2O	saturated	saturated	saturated	saturated	saturated	saturated	saturated	saturated	saturated	saturated	saturated
Some	100.00	100.00	100.00	100.00	100.00	100.00	100.00	100.00	100.00	100.00	100.00
A	0.32	0.32	0.32	0.27	0.27	0.27	0.35	0.35	0.29	0.12	0.12
M/F	0.33	0.34	0.34	0.23	0.24	0.25	0.32	0.32	0.31	0.39	0.40

5.1 Staurolite Zone from MTCF (sample DR-378)

Three garnet growth stages were defined with compositional maps named Z1, Z2 and Z3 (Figure 18b). Z1 represents the Y-poor core, Z2 the Y-rich ring and Z3 represents the most external garnet rim. Three pseudosections were modeled to reproduce the *P-T* conditions in which garnet grew in each of these stages. Pseudosections from Z1 and Z3 are presented here (Figure 23a-b, respectively), and Z2 is represented by pink-star

and presented in Supplementary Material. Small differences occur between the three pseudosections, stands out the garnet stability field decrease in Z3 in comparison to Z1 (Figure 23a-b). Chlorite, chloritoid and epidote are present in low-*T* conditions. Chloritoid is replaced by staurolite with temperature increase before the biotite appearance. Chlorite is replaced by biotite and finally kyanite/sillimanite occurs around 650 °C, depending on pressure. Ilmenite occurrence is constricted to medium-*T*/*P* conditions and is replaced by rutile in other fields.

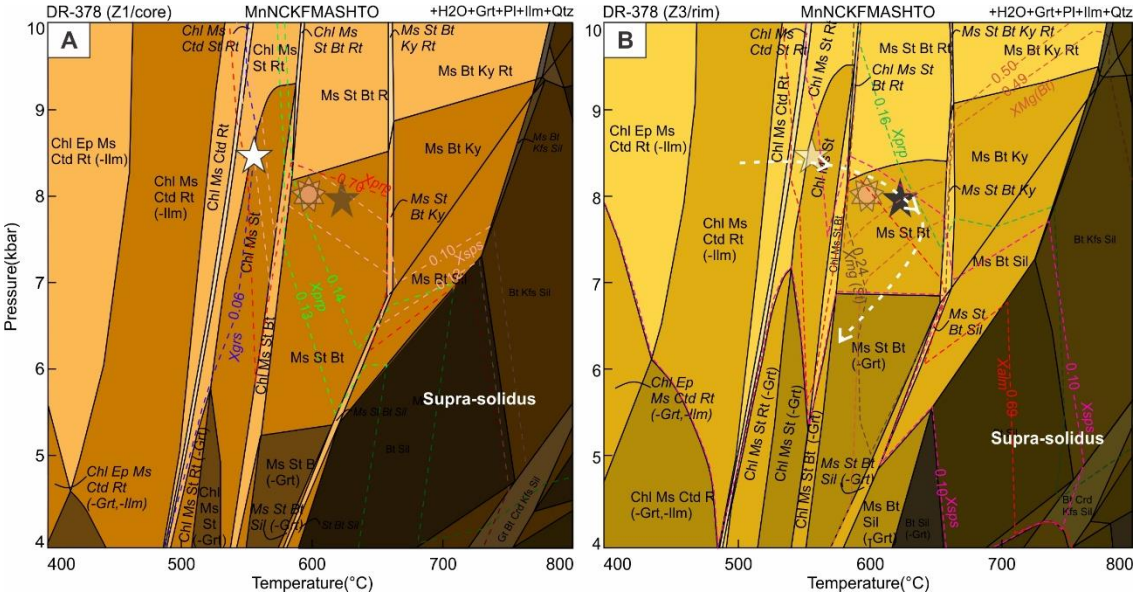

Figure 23 Figure 8: Pseudosections modeled to sample DR378 adapting the equilibrium composition as described in 3.2 Methods – Thermodynamic Modelling section. (a) Pseudosection representing the garnet core (Z1) growth, the *P-T* estimative is represented by white star; (b) Pseudosection representing garnet rim (Z3) growth, the *P-T* estimative is represented by black star. The inferred *P-T* path is represented in white dashed line. Z2 is represented by the pink star in (a) and (b) and is presented in Supplementary Material.

Isopleths of almandine (0.68-0.70), pyrope (0.13-0.16) and spessartine (0.10-0.12) are used to constrain Z1 and Z2 *P-T* conditions. Grossular is also modeled but as plagioclase analyses were not made, it is less likely to reproduce the best fit to *P-T* conditions. Another problem with the Ca content is that apatite was not considered, and the mineral occurs in the rock. In Z3 pseudosection, X_{Mg} in staurolite (~0.24) and biotite (0.48-0.49) were also modeled to constrain *P-T* conditions. The variation of *P-T* conditions is small which could indicate a diffuse growth in garnet. *P-T* conditions vary from 550-580 °C, ~8 kbar; ~610 °C, ~7.5 kbar and 610-650 °C, 6.8-7.2 kbar (Z1, Z2, Z3 respectively). Z1 occurs within the Grt + Chl + St + Ms + Qtz + Ilm + Pl ± Rt which indicates that garnet and staurolite start to grow associated. Z2 and Z3 occurs after the chlorite being replaced by biotite, within the Grt + Bt + St + Ms + Qtz + Pl + Ilm stability field.

5.2 Sillimanite Zone from MTCF (sample DR-352)

Three garnet growth stages were defined with compositional maps named Z1, Z2 and Z3 (Z1-garnet core and Z3 most external garnet rim, Figure 19b). Three pseudosections were modeled to reproduce the *P-T* growth conditions of each of these stages. Pseudosections from Z1 and Z3 are presented here (Figure 24a-b, respectively) and Z2 is presented in Supplementary Material, but its *P-T* conditions are represented by the pink-star. Small differences occur between both pseudosections, the biggest of them is the garnet stability field that increases in the Z1 composition (Figure 24a). Overall, the pseudosections present reactions of formation and consumption of chloritoid and chlorite, staurolite, biotite, sillimanite/kyanite with temperature increase. Ilmenite occurs in most modeled fields and is only replaced by rutile in low temperature conditions. Garnet field behaves as a barometer.

Isopleths of *X*alm (~0.74, 0.80), *X*grs (~0.13, 0.10), *X*prp (~0.05, 0.06) and *X*sps (~0.08, 0.04) were used to counter the Z1 and Z2 growths and they indicate *P-T* conditions of 520 °C, 8.4 kbar and 540 °C, 7.5 kbar, respectively. Isopleths of *X*alm (~0.80), *X*prp (0.06-0.09), *X*sps (0.01-0.04) and X_{Mg} in biotite (0.29-0.31) were used to constrain the *P-T* conditions of Z3 (Figure 24b). The peak assemblage of Sil + Grt + Bt + Ms + Pl + Qtz + Ilm is constrained at 650-720 °C and 5.8-7.5 kbar that is also the mineral assemblage observed in petrography.

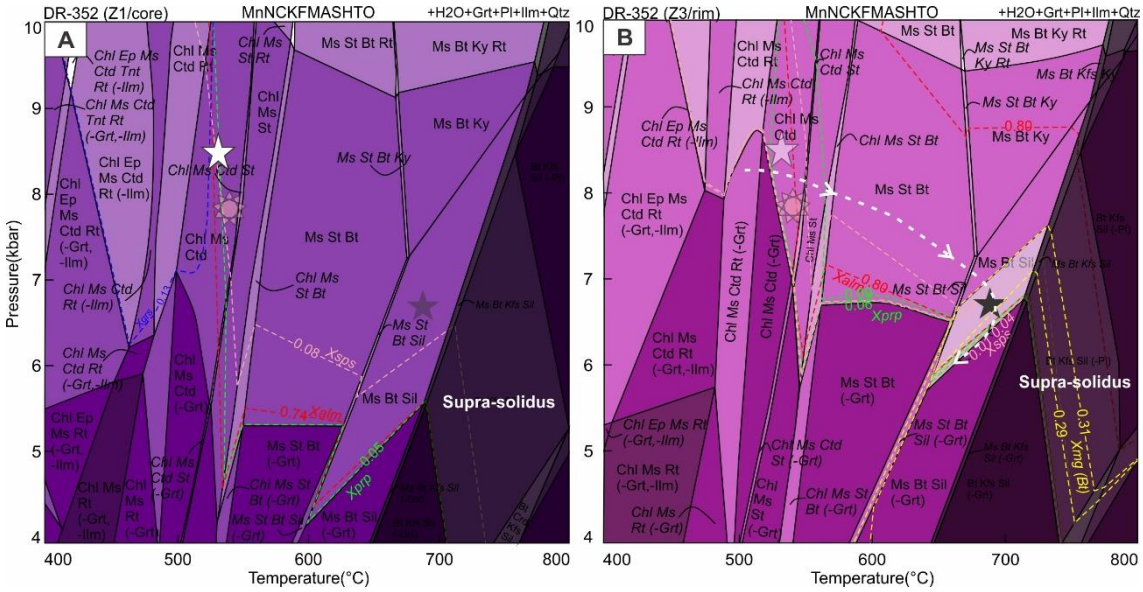

Figure 24 Pseudosections modeled to sample DR352 adapting the equilibrium composition as described in 3.2 Methods – Thermodynamic Modelling section. (a) Pseudosection representing the garnet core (Z1) growth, the *P-T* estimative is represented by white star; (b) Pseudosection representing garnet rim (Z3) growth, the *P-T* estimative is represented by the white rectangle and the black star. The inferred *P-T* path is represented in white dashed line. Z2 is represented by the pink star in (a) and (b) and is presented in Supplementary Material.

Z1 and Z2 occur within the same stability field of Chl + Ctd + Grt + Ms + Qtz + Pl + Ilm before the appearance of staurolite. With increase in temperature, chloritoid is consumed to produce staurolite before biotite formation. Chlorite them is consumed to biotite formation. Finally, staurolite is substituted within sillimanite stability field, where Z3 occurs, where Grt + Sil + Bt + Ms + Qtz + Pl + Ilm is stable.

5.3 Sillimanite Zone from MTCF (sample BR-04)

Three zones were delimited in compositional maps (Z1, Z2, Z3) of garnet growth and two pseudosections were modeled to obtain the *P-T* conditions of growth of core (Z1, Figure 25a) and rim (Z2 + Z3, Figure 25b). Small changes occur in comparison between pseudosections from core and rim. Reactions of formation and consumption of chloritoid, chlorite, staurolite, biotite and sillimanite/kyanite occur with temperature increase. Garnet is present in almost all fields.

Isopleths of *X*alm (0.66-0.68), *X*prp (~0.06), *X*grs (~0.12) and *X*sps (~0.14) were used to counter *P-T* conditions of garnet core growth and they point to ~550 °C and ~6.9 kbar. The peak assemblage field Sil + Grt + Bt + Ms + Pl + Qtz + Ilm is constrained by isopleths of *X*alm (0.71-0.72), *X*sps (0.08-0.10) and X_{Mg} in biotite (0.42-0.44). Isopleths indicate *P-T* conditions of 650-750 °C and 6.5-8.2 kbar. Anorthite isopleth (~0.22) behaves as a barometer and counters the pressure condition around 7.2 kbar.

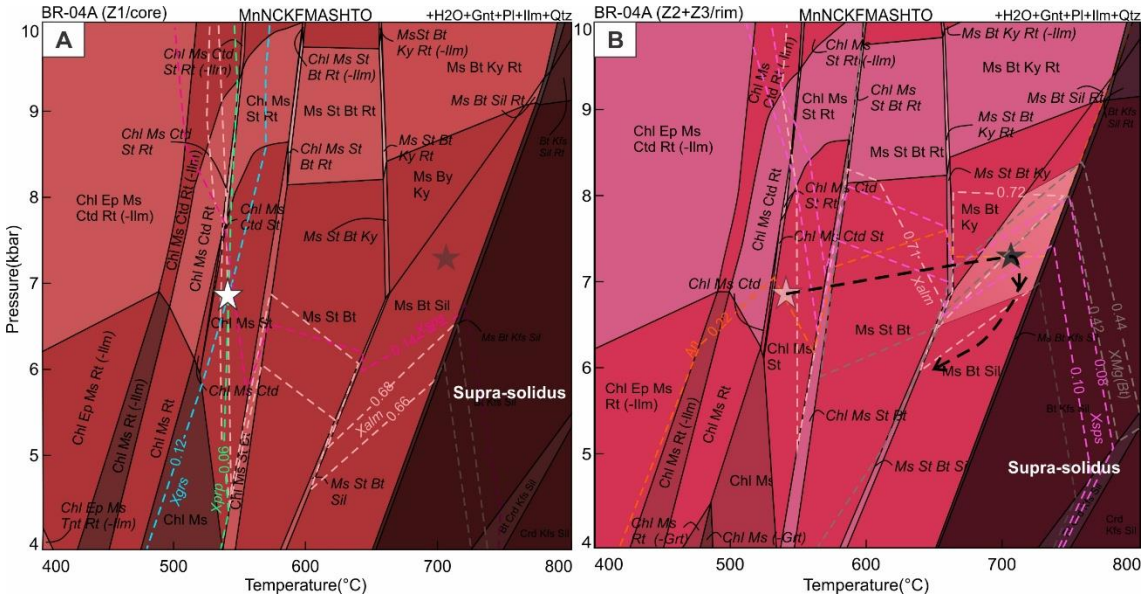

Figure 25 Pseudosections modeled to sample BR04 adapting the equilibrium composition as described in 3.2 Methods – Thermodynamic Modelling section. (a) Pseudosection representing the garnet core (Z1) growth, the *P-T* estimative is represented by white star; (b) Pseudosection representing garnet rim (Z2+Z3) growth, the *P-T* estimative is represented by the white rectangle and the black star. The inferred *P-T* path is represented in black dashed line.

6. Monazite U-Pb Geochronology and Trace Element characterization

All compositional diagrams presented in this session represent values of analysis normalized by chondrite values from McDonough & Sun (1995). Whenever Th-Pb age is indicated in this session, it is related to the $^{208}Pb/^{232}Th$ age calculated by Isoplot software. This ratio is preferred instead ^{206}Pb-^{207}Pb, ^{206}Pb-^{238}U or ^{207}Pb-^{235}U because the data presents more concordant plots than the ages that do not consider Th. Representative compositional maps are presented and all of them can be found on the supplementary material.

6.1 DR378 - Staurolite Zone from MTCF (sample DR-378)

6.1.1 Monazite characterization

Monazite grains on this sample are mainly rounded, but elongated ones also occur, which are anhedral, 10-40 µm long and disposed mainly included on matrix minerals as muscovite, biotite, quartz or orientated along the matrix. Rarely, they are included in garnet or staurolite. Trace elements distribution indicates a substantial continuous range on HREE and smaller ranges on MREE and LREE (Figure 26a). The Eu anomaly is present but is not intensely pronounced. Distinct populations occur within trace element distribution, i.e. based on the inclination of HREE/Y content and on the location of the grain. They also differ on the amount of Y (ppm) and slightly in the Eu/Eu* ratio (Figure 26a, b). Five populations can be distinguished:

- Purple: oldest grains (>640 Ma), no clear pattern on trace element;
- Light blue: constant Eu anomaly (Eu/Eu* ~ 0.7), variable and highest Y values, regular and highest HREE;
- Red: similar pattern to light-blue but they occur included in garnet grains;
- Yellow: variable Eu/Eu*, constant and smaller Y content, variable and lowest HREE;
- Green: similar pattern to yellow, but grains occur included in staurolite.

Compositional maps were made on EPMA for some monazite grains, and they present complex distribution of both Th and Y (Figure 26c-e and supplementary material) that not necessarily match with each other. On the other hand, U distribution is almost uniform along the grains.

6.1.1 Isotopic LA-ICP-MS dating

On the LA-ICP-MS, 63 analysis were conducted on monazite grains, from which forty-five produced both good trace element and U-Pb results. Considering the trace element distribution, especially Y and HREE, some populations can be distinguished (Figure 26a-b). Populations P2 and P3 seem to have similar composition, while P4 and P5 also show a chemical correlation. P1 represents the older grains, and they vary on trace element.

LA-ICP-MS dating of these rocks produced range of dates between 640–570 Ma (Figure 26f). Nevertheless, even though different populations seem to occur, they overlap within the uncertainties associated with the method. The Y distribution is also complex and indicate that the monazite growth could have occurred with different pulses with distinct Y-availability.

6.1.2 Chemical EPMA dating

On monazite grains, twenty-three analysis were conducted on this sample and nineteen produced good results. Up to five different points were collected in each grain. There is an intense variation on the Th content on monazite grains from this sample. Nevertheless, the dates in all of them overlap within their uncertainties (Figure 26g). Two younger dates also occur (<550 Ma) in the same monazite rim. Weighted mean including all analyzes yields an average of 591 ± 8 Ma (n=19) and the average without 2 younger grains yields 594 ± 8 Ma (n=17).

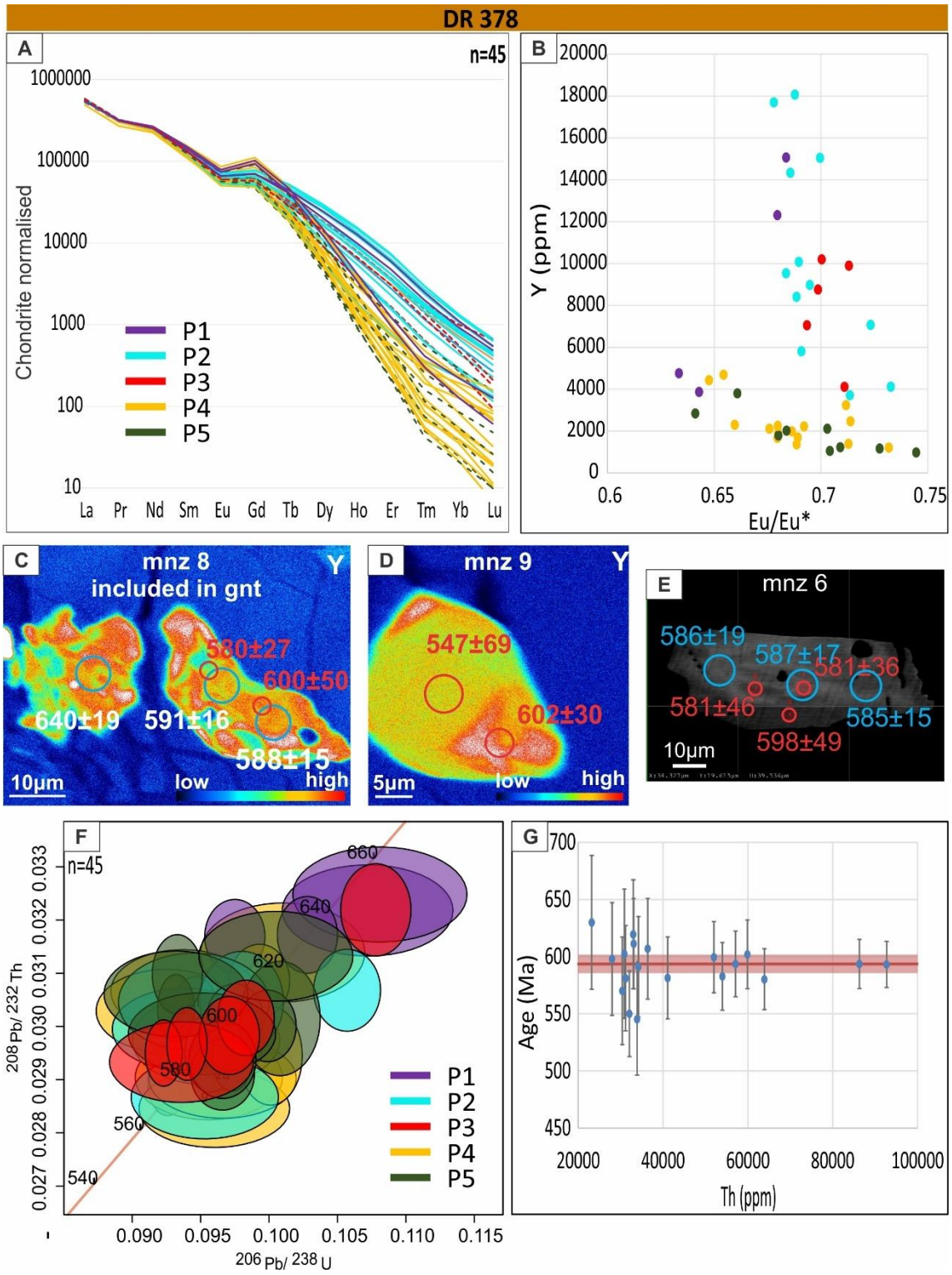

Figure 26 Monazite data obtained from sample DR378. (a) chemical profiles obtained with LA-ICP-MS for REE in monazite grains color-coded by populations described in the text; (b) Y (ppm) x Eu/Eu* plot color-coded by populations described in the text; (c-e) representative monazite grains with maps obtained with EPMA and BS-images. Red circles indicate chemical ages and blue/white circles indicate isotopic ages. (f) 208Pb/232Th x 206Pb/238U plot calculated with IsoplotR also color-coded by populations described in text; (g) chemical ages x Th (ppm) obtained with EPMA. Red line represents the weighted mean and its uncertainty.

6.2 Sillimanite Zone from MTCF (sample DR-352)

6.2.1 Monazite Characterization

Monazite grains on sample DR352 are anhedral, mostly are elongated, but round also occur, 10-30 µm long and occur mainly associated with the matrix either included in muscovite, biotite, quartz or on the contact between them. Trace element distribution indicates smaller range in all REE when compared to other samples (Figure 27a, b). Weak correlations can be made between the REE distribution and either Th/U ratio or Th-Pb age (Figure 27a, b). The oldest monazite grains seem to have slightly higher HREE values.

Compositional maps were made on EPMA for some monazite grains. They present almost uniform Th distribution but complex Y patterns, at least three zones can be identified in some maps (Figure 27c-e). These zones are very thin (< 10 µm) and could not be reached with the spatial resolution of the LA-ICP-MS technique. However, some of them could be dated with the EPMA spatial resolution but even with it, some zones are too thin to be analyzed with due confidence.

6.2.2 Isotopic LA-ICP-MS dating

On monazite grains, forty-five analysis were conducted from which twenty-seven produced both good trace element and U-Pb results. Considering the trace element distribution, it is hard to divide the monazite grains in different populations (Figure 27a-b). Even though it is clear from the chemical maps that they have some Th and Y variations (Figure 27c-e), it would be unwise to divide them based only on the trace element distribution. A range of dates between 610-580 Ma can be observed on the U-Th-Pb plots (Figure 27f). Some exceptions are made to slightly older and discordant dates 620-610 Ma (mnz1 and 43) and a younger one ~570-560 Ma (mnz 29).

6.2.3 Chemical EPMA dating

On monazite grains, nineteen analysis were conducted from which fourteen produced good results, in most grains more than one point was analyzed. Even though Y-zoning is evident in compositional maps, the intensity is lower in other elements, such as Th or U, and they not always match the pattern of each other (Figure 27c-e). Some Th difference is seen on spot analysis, but the dates in different zones overlap within the errors associated to each analysis (Figure 27g). Dates range between 620-570 Ma and 4 points may indicate a younger population around 550-540 Ma (Figure 27g). Nevertheless, these younger points also overlap withing uncertainties with the main population. Weighted mean dates counting all fourteen points yields dates of 586 ± 13 Ma and 595 ± 14 Ma considering only older points (n=10).

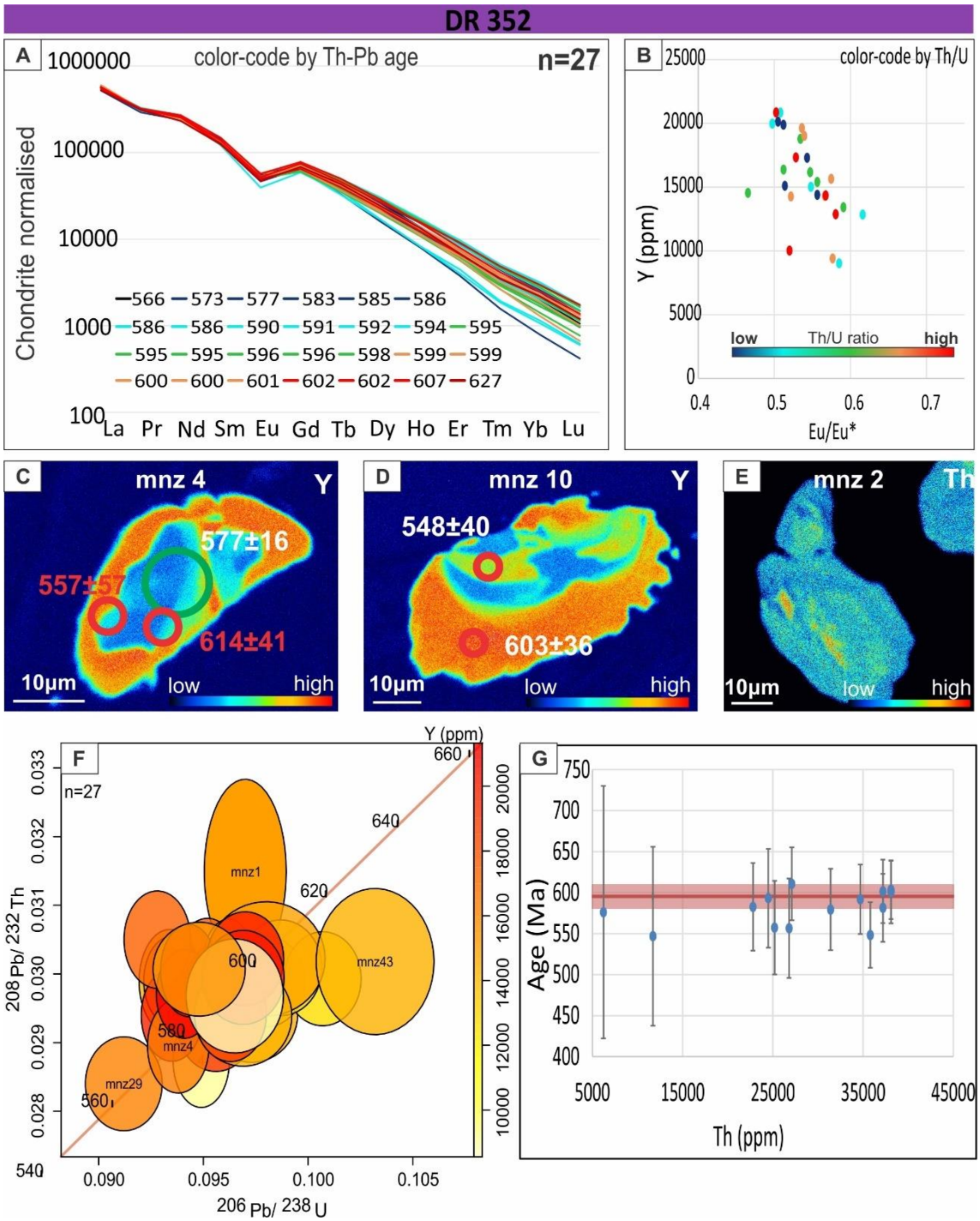

Figure 27 Monazite data obtained from sample DR352. (a) chemical profiles obtained with LA-ICP-MS for REE in monazite grains color-coded by the Th-Pb age calculated in Isoplot; (b) Y (ppm) x Eu/Eu* plot color-coded by the Th/U ratio; (c-e) representative monazite grains with Y and Th maps obtained with EPMA. Red circles indicate chemical ages and green circles indicate isotopic ages. (f) 208Pb/232Th x 206Pb/238U plot calculated with IsoplotR color-coded by Y content in ppm; (g) chemical ages x Th (ppm) obtained with EPMA. Red line represents the weighted mean and its uncertainty.

6.3 Sillimanite Zone from MTCF (sample BR-04)

Monazite grains in sample BR04 are very small (<20µm) and occur in different shapes, rounded, elongated, euhedral and anhedral. This sample is intensely affected

by weathering and this affected the data collection on the LA-ICP-MS. It is presented here only information collected on the EPMA.

6.3.1 Chemical EPMA dating

On monazite grains, twelve points were successfully dated on this sample from fourteen conducted analysis. One or two points were conducted per grain. Th and Y zoning is observed in compositional maps, Th variation is also observed in spot analysis. Nevertheless, dates distribution is consistent along these differences and yield a range between 610-580 Ma (Figures in supplementary material), exception is made to one older date, 627 ± 37 Ma (point 13). Weighted mean yields an age of 600 ± 12 Ma (n=12).

6.4 Sillimanite-K-feldspar-Garnet Zone from HTCF (sample DR-298)

Monazite grains on sample DR298 are larger than in other samples. Most of them are at least 100 µm, but they can occur as large as 400 µm (Figure 28d-e). Smaller ones also occur, mainly included in other minerals. They are anhedral and mainly elongated. They occur related to matrix minerals, but not necessarily included on them.

Trace element distribution indicates a big continuous range on HREE and MREE and smaller ranges on LREE (Figure 28a). The Eu anomaly is very pronounced in most analysis. Y (ppm) x Eu/Eu* plots show a trend with continuous decrease in Y (ppm) content around almost fixed Eu/Eu* value of ~0.1 (Figure 28a-b). Some exceptions are made on 5 points with Eu/Eu* > 0.3. Five populations were defined based on the trace element distribution and their geographic disposition:

- Purple: oldest ages, Eu/Eu* constant ~0.1, variable Y and HREE (P1);
- Yellow: constant Eu/Eu* (~0.1), low Y and HREE (P2)
- Green: constant Eu/Eu* (~0.1), high Y and HREE (P3)
- Black: higher Eu/Eu* (~0.45), high HREE and Y, located on cores (P4);
- Light blue: variable Eu/Eu*, similar and high Y and HREE, located on rims (P5);

6.4.1 Isotopic LA-ICP-MS dating

Isotopic data was collected in three different sections: the first on general grains all over the thin section, where ninety analysis were conducted and forty-four of them produced both trace elements and U-Th-Pb results; the second and third sections were conducted on coarse monazite grains, named ‘mnz 5 and 6’. From those grains, another twenty-eight and sixty-two points were conducted in ‘mnz 5 and 6’, respectively. They produced twenty-five and fifty-seven good results. This data is used to present maps

based on spot analysis (Section 7) and they are compiled with other analysis in other grains in the compositional plots presented here (Figure 28a-c). Those grains were also picked to obtain detail compositional trace element maps which will be presented in **section 7 – LA-ICP-MS mapping of monazite grains.** Compiling all isotopic and chemical information, a total of one hundred and twenty-six good analysis were obtained (Figure 28a-b).

Two large groups of ages distinguish in sample DR298 (Figure 28c). The first one includes older monazites (purple P1, 760 – 650 Ma), those points occur in the cores of mnz 5 and 6. The second group includes all other different populations (P2-P5), they occur between a range from 640 to 570 Ma. Different populations overlap within their respective uncertainties. Nevertheless, the light blue one seems to be younger them the rest, while black ones are slightly older. Green and yellow populations overlap, but the yellow seems to be slightly older (Figure 28c).

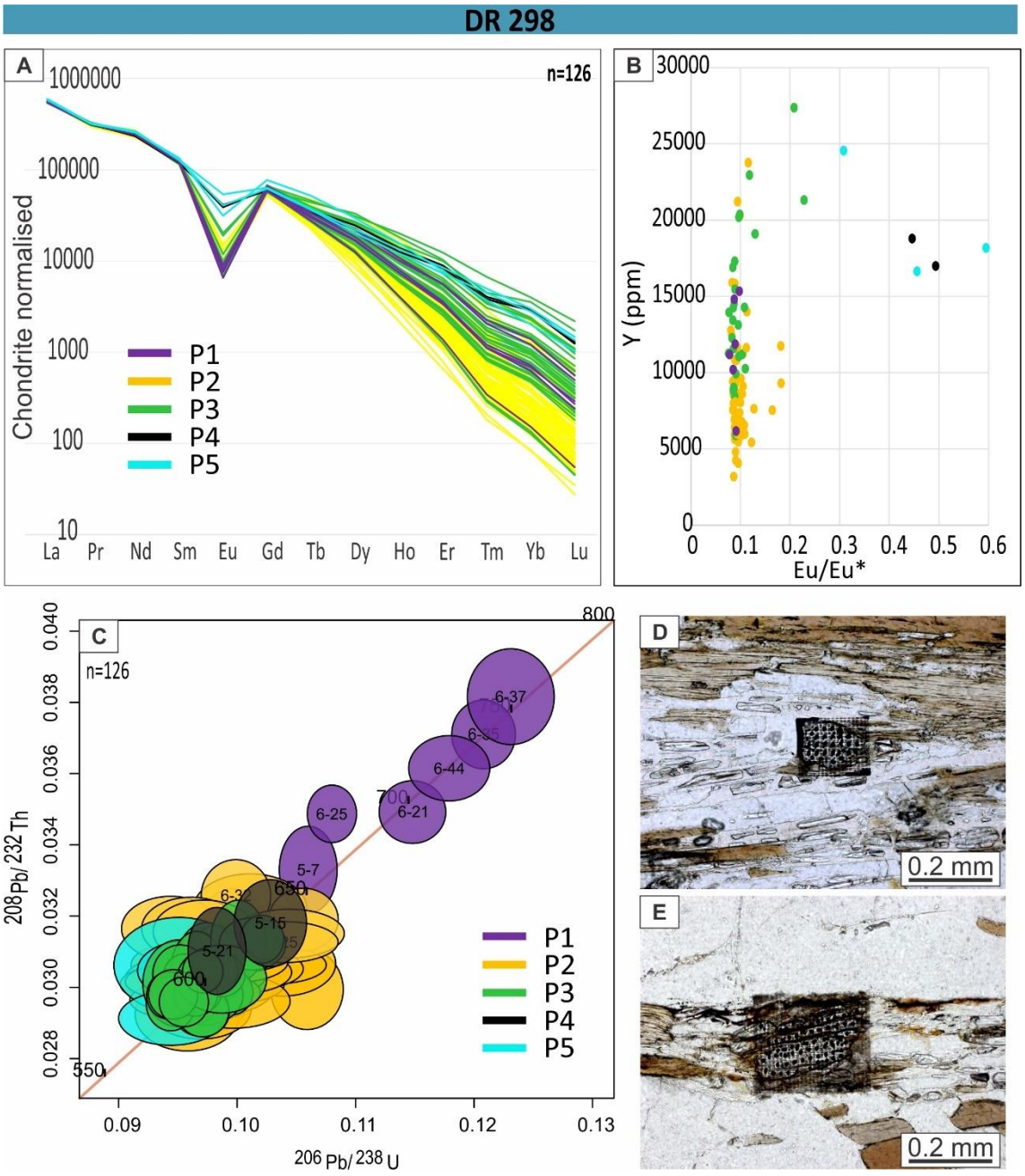

Figure 28 Monazite data obtained from sample DR298. (a) chemical profiles obtained with LA-ICP-MS for REE in monazite grains color-coded by populations described in the text; (b) Y (ppm) x Eu/Eu* plot color-coded by populations described in the text; (c) 208Pb/232Th x 206Pb/238U plot calculated with IsoplotR also color-coded by populations described in text; (d-e) monazite grains analyzed and mapped; (d) is the grain 'mnz5' and (e) is the grain 'mnz6'.

6.5 Kyanite-K-feldspar Zone from HTCF (Sample 129)

Monazite grains on sample 129 are anhedral and small; they rarely are bigger than 20 µm, they can occur as elongated or rounded grains. They are related to matrix minerals but not necessarily included in them. Trace element distribution indicates a continuous range on HREE and smaller ranges on LREE. Three distinct populations can be distinguished based on the Eu anomaly and the HREE/Y distribution (Figure 29a-b).

- Light blue: less pronounced Eu* anomaly and low HREE/Y values (P1);
- Yellow: strong Eu anomaly (<0.2) and higher HREE/Y values (P2);
- Red: one monazite grain, youngest, highest Eu/Eu* and lowest HREE/Y values (P3).

EPMA compositional maps were made for some monazite grains but, they did not produce good LA-ICP-MS analysis. They present a complex Y distribution pattern in opposition to homogenous Th and U dispersion (Figure 29c-e).

6.5.1 Isotopic LA-ICP-MS dating

On monazite grains of this sample, sixty analysis were conducted, from which only eighteen produced both good trace element and U-Pb results, due to the grains size. Two groups of dates occur, one on a range between 610 – 570 Ma and a younger one around 560 – 540 Ma (Figure 29f). The last one occurs only in the rim of one longer monazite grain. Dates of light blue and yellow population overlap within their uncertainties (Figure 29f).

6.5.2 Chemical EPMS dating

A number of fourteen points were analyzed and all of them presented good results, one or two points were made per grain. Even though there is a complex Y distribution on the maps and some Th variation also occur in spot analysis, all ages yield a similar range between 620 – 580 Ma (Figure 29g). One exception is made to one older grain (652 ± 31 Ma) located in a small monazite core. Weighted mean considering all points yields an age of 606 ± 10 Ma (n=14).

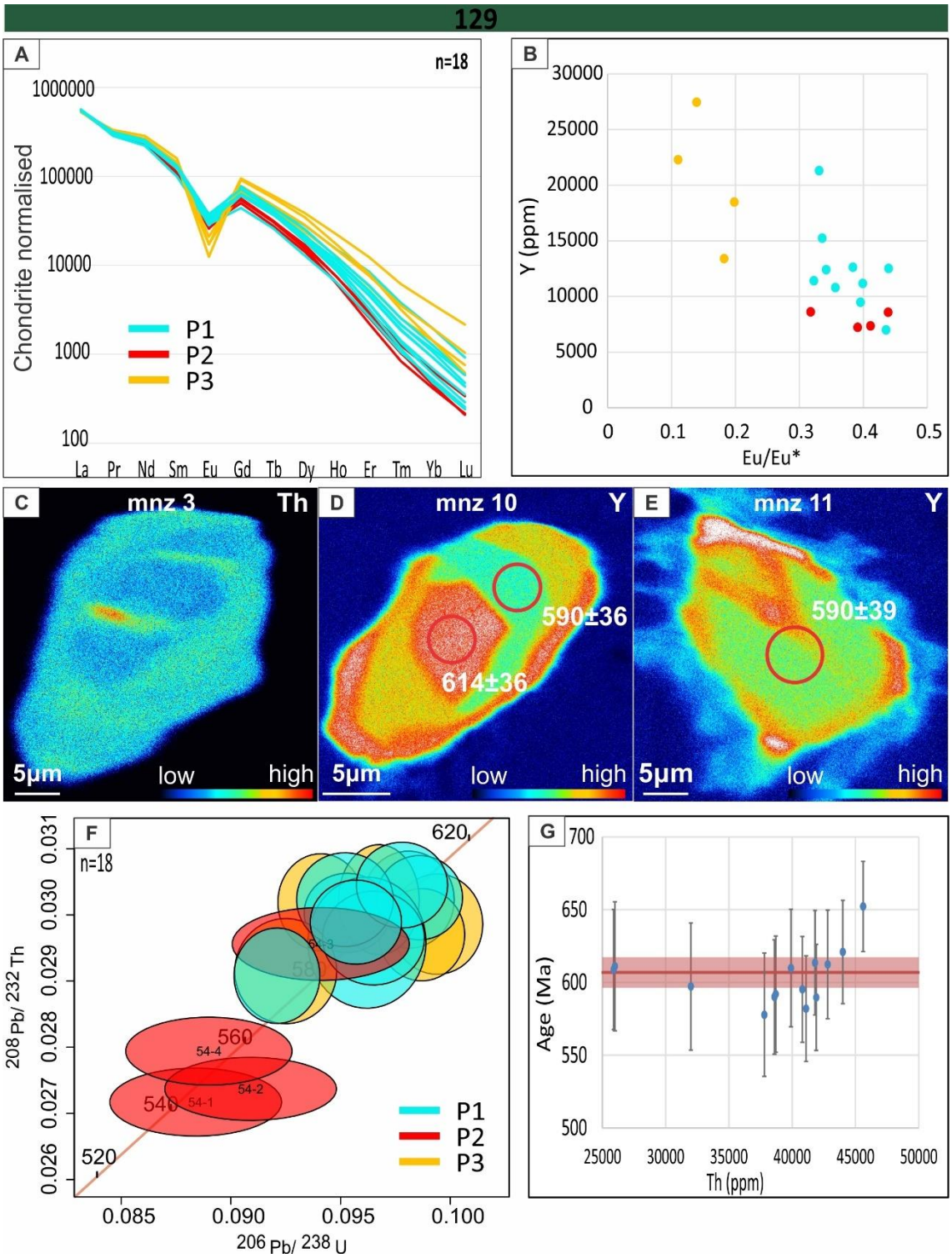

Figure 29 Monazite data obtained from sample 129. (a) chemical profiles obtained with LA-ICP-MS for REE in monazite grains color-coded by populations described in the text; (b) Y (ppm) x Eu/Eu* plot color-coded by populations described in the text; (c-e) representative monazite grains with Y and Th maps obtained with EPMA. Red circles indicate chemical ages. (f) 208Pb/232Th x 206Pb/238U plot calculated with IsoplotR also color-coded by populations described in text; (g) chemical ages x Th (ppm) obtained with EPMA. Red line represents the weighted mean and its uncertainty.

6.6 Chemical EPMA dating of other samples

Three other samples from the MTCF were also picked for chemical dating to constrain geographically the metamorphic evolution. As monazite grains on those samples are too small (<15 μm), samples were not dated with the LA-ICP-MS. A brief description of each sample is presented in the supplementary material and only their ages are presented here.

Sample BR 18 is a schist in the sillimanite zone. Only six monazite grains produced good results from ten analysis. They present similar range of Th (ppm) and the dates are within the range of 620 – 580 Ma. One exception is made to a younger anhedral grain (543 ± 38 Ma), slightly richer in Th.

Sample BR 07 is a phyllite composed of fine-grained muscovite, biotite, sillimanite, quartz and plagioclase. Very thin (< 10 μm) monazite grains occur dispersed along the matrix, and are mainly rounded. In these, fifteen analysis were conducted and only five of them produced good results. They occur within a small range of Th content and yield a date range between 630 – 560 Ma.

7. LA-ICP-MS Mapping of monazite grains (DR298)

As described on methods session, two monazite grains larger than 150 μm were picked from sample DR298 (mnz 298-5 and mnz 298-6) to detail the trace element distribution and its possible association with different U-Pb dates (Figure 30 and Figure 31). Maps based on spot analysis are compared to CellSpace images. From the spot analysis, compositional trace element diagrams and Y x (Eu/Eu*) plots are also presented.

Monazite grain 298-5 is anhedral, round, ~150 μm long and occurs along the matrix, near a biotite-sillimanite-rich layer. On this grain, twenty-eight points were analyzed, from which twenty-five produced good trace element and U-Pb analysis. Compositional plots indicate that points with highest Th/U ratio have lowest HREE content. It also indicates that the oldest points (>615 Ma) have higher HREE values. The oldest point (5-7, 662 Ma) has similar trace element profile than other points (Figure 30a).Y x (Eu/Eu*) plot indicates majorly similar values of Eu/Eu* (~0.15) and a trend to lower-Y content related to higher values of Th/U ratio (Figure 30b). Only two analysis present Eu/Eu*>0.4, points 5-15 and 5-21.

Both spot-analysis maps and CellSpace images present similar results on the distribution of Eu and Y (Figure 30c-p). Eu distribution differs from other trace element, while Eu is concentric, other trace element present complex distribution (Figure 30c-p). High values of HREE are concentrated near the monazite core, followed by a decrease on HREE near the mantle. The monazite thin rim presents an increase in most trace

element. Exceptions are made for Eu. These nuances are not clear in the punctual-Y map and are only observed in CellSpace images. The Th-Pb age map (Figure 30f) indicates that oldest dates are located near the low-Eu zone, but the ages distribution is also complex. This map was made based on the Th-Pb ages calculated by Isoplot, therefore, the distribution is probably not very precise once all dates have associated uncertainties not considered on heat maps.

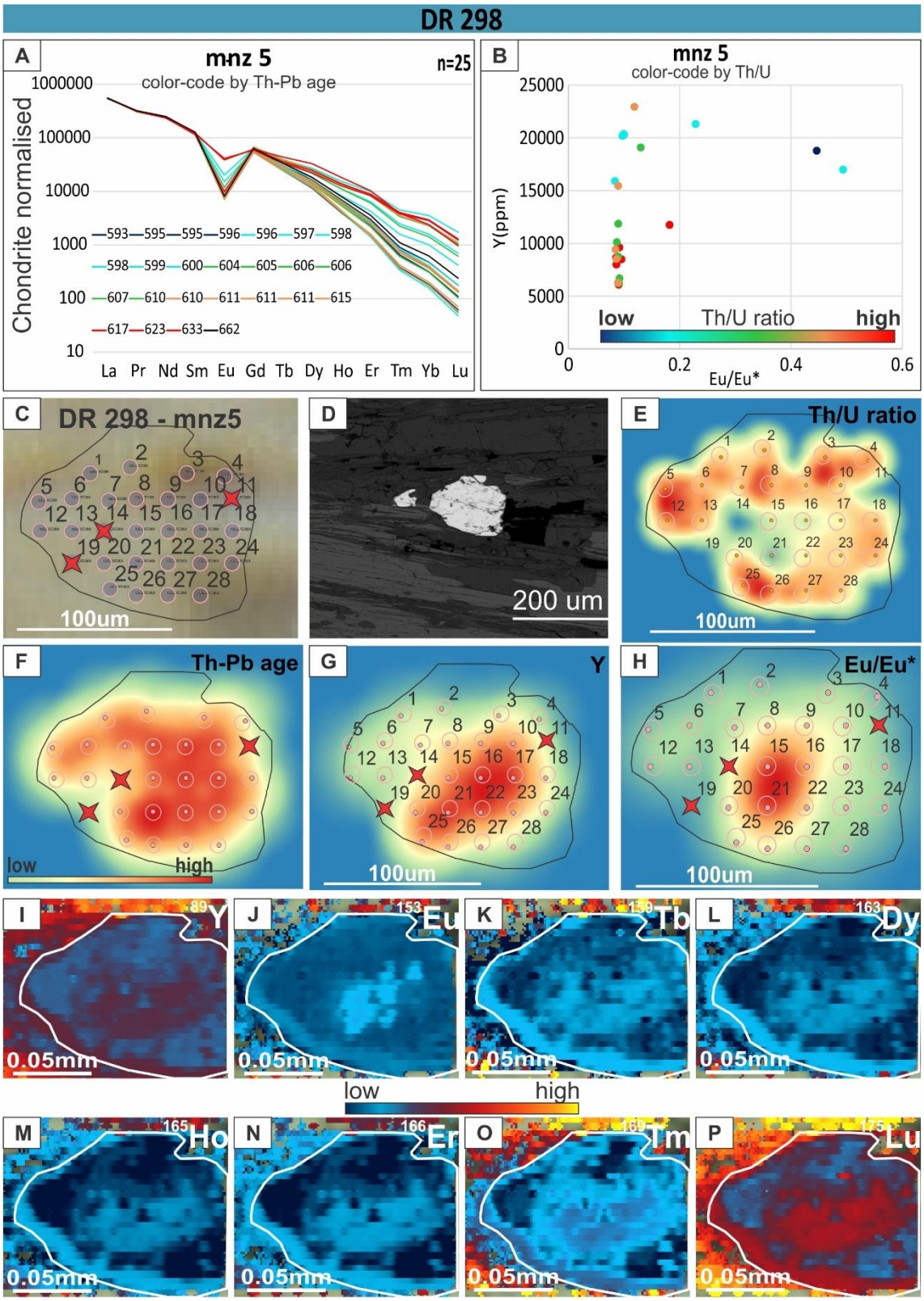

Figure 30 Monazite data obtained from one grain 'mnz5' from sample DR298. (a) chemical profiles obtained with LA-ICP-MS for REE in monazite grains color-coded by the Th-Pb age calculated with Isoplot; (b) Y (ppm) x Eu/Eu* plot color-coded by the Th/U ratio; (c) spot location within the grain. Red X represent discarded analysis; (d) BS-image of the monazite grain; (e-h) heat chemical maps calculated with interpolation of spot analysis for the Th/U ratio, Th-Pb age from Isoplot, Y (ppm) and Eu/Eu*, respectively; (i-p) compositional maps obtained with LA-ICP-MS, Y, Eu, Tb, Dy, Ho, Er, Tm and Lu, respectively.

Monazite 298-6 is also anhedral, elongated, ~300x200 µm and occur along the matrix, near a sillimanite-rich layer interleaved with leucosome composed of quartz and K-feldspar. Among chosen grains, sixty-two points were analyzed, from which fifty seven produced good trace element and U-Pb analysis. These monazite grains have a consistent Eu negative anomaly in all analysis and a larger dispersion on HREE (Figure 31a). Compositional and Y x (Eu/Eu*) plots indicate similar values of Eu/Eu* (~0.08) and trend to low-Y/HREE content with higher values of Th/U ratio (Figure 31b). Alternatively, lower Th/U ratio analysis present higher Y/HREE content (Figure 31a-b).

Spot analysis map indicates that oldest areas also have higher Y content and Eu/Eu* ratio (Figure 31c-h). Again, the Th-Pb map is made based on the Isoplot Th-Pb age and does not consider the errors bars present in each analysis on the heat map, what may affect the ages distribution. CellSpace images match the punctual analysis maps, but with very complex distribution on trace element (Figure 31i-p). The distribution is not concentric with clusters scattered on the grain. They also indicate higher values of Y and HREE near the monazite core, followed by a depletion on these elements on the monazite mantle. A thin Y/HREE-rich rim also occurs like in monazite 298-5.

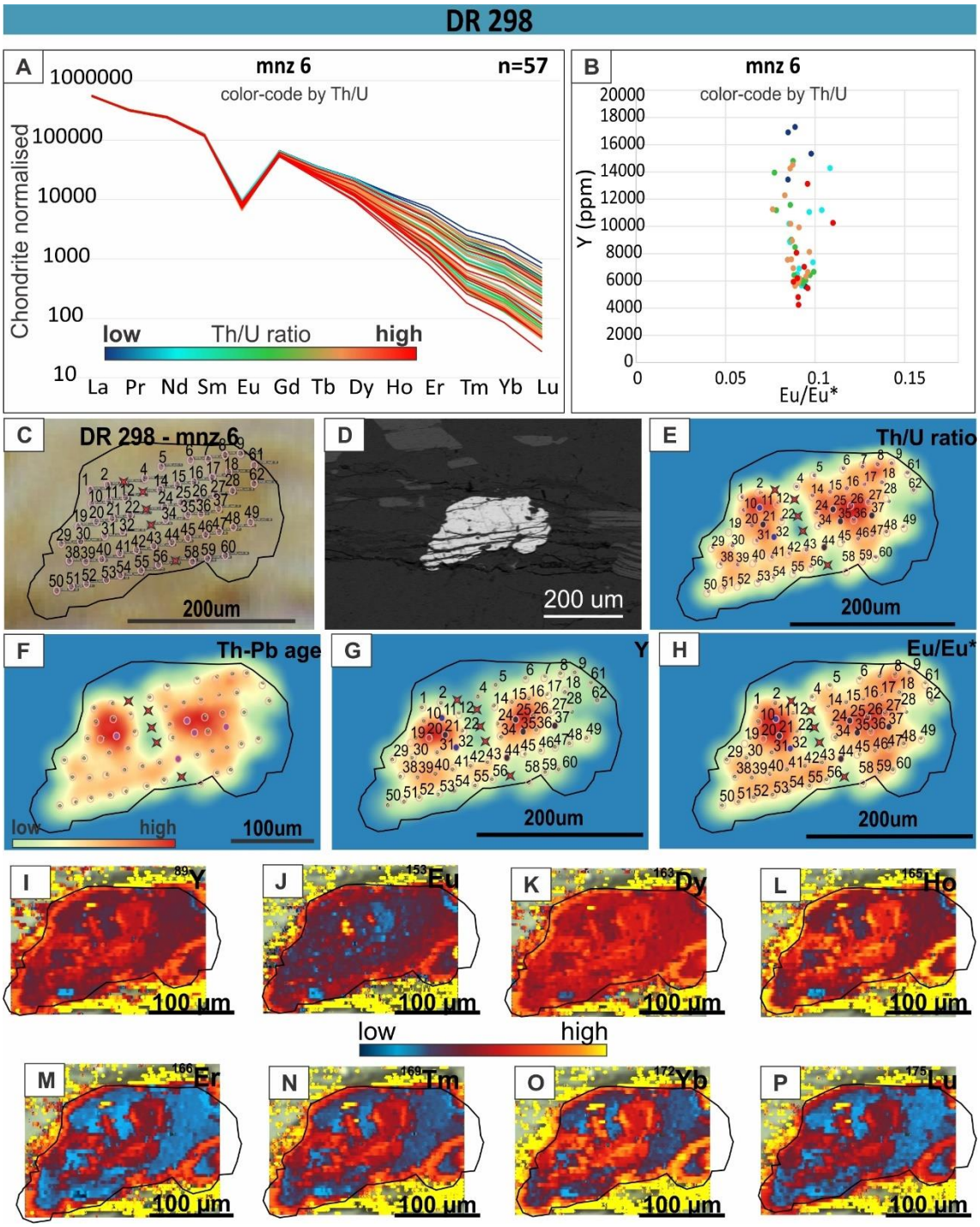

Figure 31 Monazite data obtained from one grain 'mnz6' from sample DR298. (a) chemical profiles obtained with LA-ICP-MS for REE in monazite grains color-coded by the Th/U ratio; (b) Y (ppm) x Eu/Eu* plot color-coded by the Th/U ratio; (c) spot location within the grain. Red X represent discarded analysis; (d) BS-image of the monazite grain; (e-h) heat chemical maps calculated with interpolation of spot analysis for the Th/U ratio, Th-Pb age from Isoplot, Y (ppm) and Eu/Eu*, respectively; (i-p) compositional maps obtained with LA-ICP-MS, Y, Eu, Dy, Ho, Er, Tm, Yb and Lu, respectively.

8. Discussion

8.1 Metamorphic history and P-T-t paths

Correlations in this section are made following classic interpretation in the literature that compare the trace element distribution in monazite and correlate with major

phases. They include correlating monazite growth with garnet and feldspar, for instance, based on their HREE and Eu anomaly content, respectively (p.e. Hermann and Rubatto, 2003, Rubatto et al., 2006, 2013, Dumond et al., 2015). Nevertheless, some recent studies have questioned and evaluate some of the problems with those assumptions (Catlos, 2013, Weller et al., 2020), especially on monazites that present complex trace element chemistry. They found small correlation between domains assumed to be formed during the same reaction, their HREE distribution and the dates obtained in them. Therefore, caution is recommended while interpreting this information.

P-T-t paths are presented to samples BR-04, DR378 and DR352 based on the metamorphic studies presented here. *P-T* conditions to samples BR18 and BR35 presented in Supplementary Material are also plotted. *P-T*-t paths of samples DR298 and 129 are extracted from Faleiros et al. (2011). *P-T* conditions to samples DR151, DR206 and DR39 extracted from Ricardo et al. (2020) are presented for the purpose of comparison. A summary of the calculated *P-T* conditions is presented in Table 4 below. Figures compiling minerals relations for samples DR378 and DR352 are presented in the supplementary material.

Table 4Summarization of pseudosection modeling results and the respective mineral assemblage of each sample. Samples DR298 and 129 are extracted from Faleiros et al. (2011) and Ricardo et al. (2020). Samples DR39, DR151 and DR206 are extracted from Ricardo et al. (2020).

Sample		Metamorphic Zone	Mineral Assembladge	Temperature (°C)	Pressure (kbar)
DR378	Z1	Staurolite	St + Grt + Bt + Ms + Qtz + Ap + Pl	~530	~8.2
	Z2			~580	~8
	Z3			550-620	7.5-8.0
DR352	Z1	Sillimanite	Sil + Grt + Bt + Ms + Qtz + Ap + Pl	~520	~8.2
	Z2			~520	~7.8
	Z3			650-700	6.0-7.0
BR04	Z1	Sillimanite	Sil + Grt + Bt + Ms + Qtz + Ap + Pl	~520	~6.8
	Z2+Z3			650-720	6.5-7.5
BR18	peak	Sillimanite	Sil + Grt + Bt + Ms + Qtz + Ap + Pl	650-710	6.0-7.0
BR35	Z1	Garnet	Grt + Bt + Chl + Ms + Qtz + Ap + Pl	550	~8
	Z2			560	~8
DR298	peak	Sillimanite - K-feldspar	Ky + Kfs + Grt + Bt + Qtz + Pl	820	10
	retrograde		Sil + Kfs + Grt + Bt + Qtz + Pl	790	8
129	peak	Kyanite - K-feldspar	Ky + Kfs + Grt + Bt + Qtz + Pl±Ms	800	11
DR39	peak	Garnet	Grt + Bt + Chl + Ep + Ms + Qtz + Pl	530-560	6.0-7.0

DR151	peak	Sillimanite	Sil + St + Grt + Bt + Ms + Qtz + Pl	640-670	5.9-7.0
DR206	peak	Garnet	Grt + Bt + Ms + Qtz + Pl	550-580	7.0-7.6

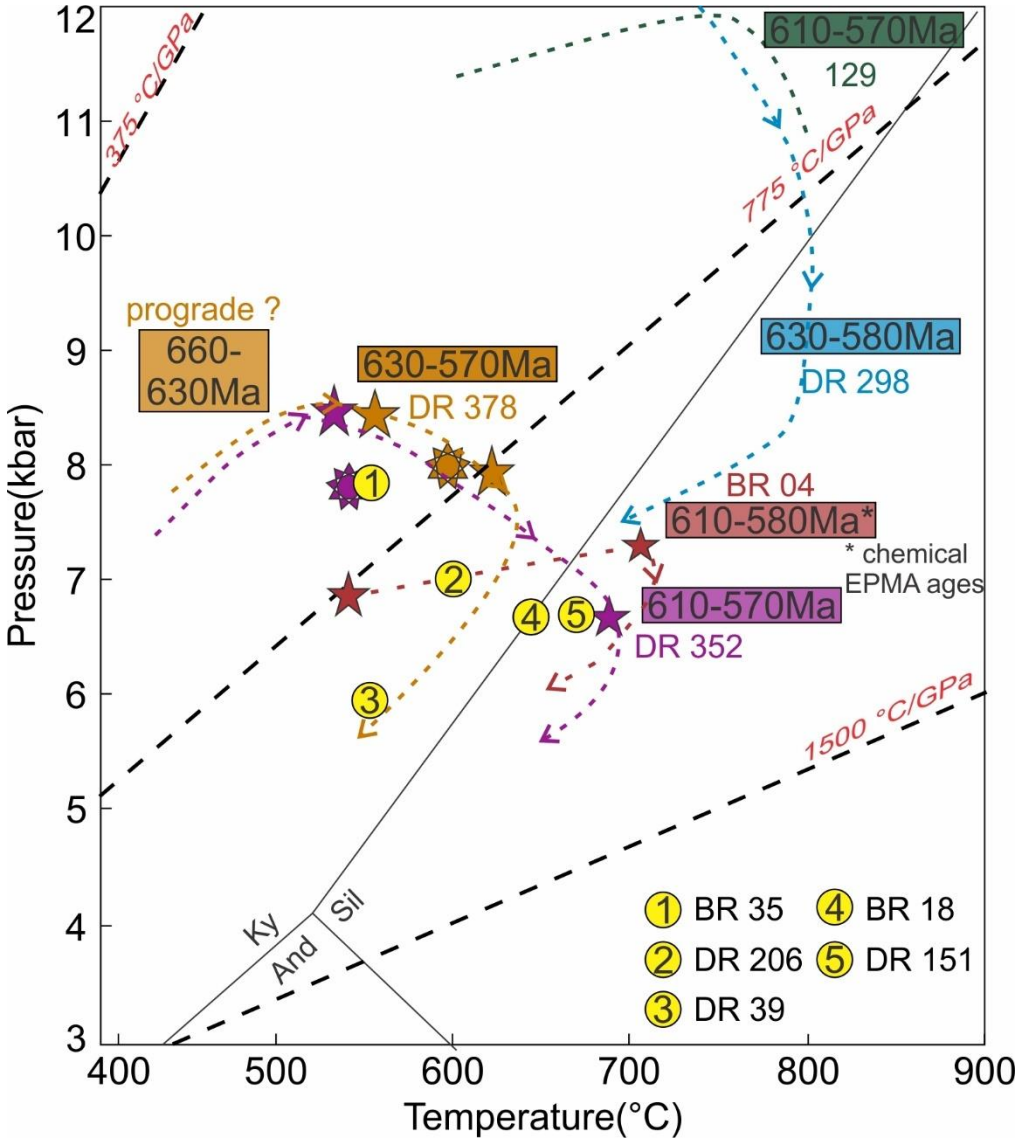

Figure 32 Metamorphic conditions to samples from the TCF. Inferred *P-T*-t paths are presented to samples studied here, DR378, DR352 and BR04. *P-T* paths to samples DR298 and 129 are extracted from Faleiros et al. (2011). Peak *P-T* conditions to samples BR18 and BR35 are presented in the Supplementary Material. Peak *P-T* conditions to samples DR39, DR206 and DR151 are extracted from Ricardo et al. (2020). The thermobaric ratios plotted are extracted from Brown and Johnson, 2019).

8.1.1 Staurolite Zone from MTCF (sample DR-378)

The trace element maps to this sample indicates three zones of garnet growth (Figure 18). The major elements show different distribution when compared with trace element and among them. The Ca, Mn, Mg and Fe maps not always overlap. Fe has a small variation while Ca shows the strongest zoning. Combining major elements distribution with the pseudosections a couple of patterns appear (Figure 18, Figure 23). The Ca distribution could be related to apatite consumption. Apatite occurs as inclusions

in the garnet core but is absent in the garnet mantle and rim. This could indicate that this mineral is being consumed and Ca is being incorporated into its composition. This is also corroborated by the Y map. The distribution of Ca and Y is similar with a Ca-Y-enriched ring (Z2 in Figure 18). The rim is enriched in Mg which could be related to the chlorite consumption. Chlorite occurs included in the core but is absent in other parts of the garnet. The chlorite break-down reaction is present in the pseudosection between Z1 and Z2, which matches the Mg distribution within the grain (Figure 23). Finally, the Mn distribution records a specific part of the *P-T* trajectory of the rock. It is Mn-depleted on the core and gets enriched in the rim (Figure 18g). This can be interpreted as a relation with the proportion of ilmenite in the sample. Isopleths of ilmenite's volume can be compared with the spessartine in garnet (Figures in supplementary material). They indicate a turning point between Z1 and Z2 where ilmenite turns from growing to being consumed. On the other hand, spessartine on the same point behaves in opposition, i.e., it goes from lower values to higher ones within the field. This indicates that the garnet core grew while ilmenite was also being produced, therefore incorporating part of the Mn. On the transition between Z2-Z3, ilmenite started being consumed, Mn was released to the system and incorporated in garnet, which gets enriched on this element on its rim (Figure 18g).

Evidence of the retrograde path also occur. Firstly, a thin Mn-rich rim occurs within the garnet grain that also shows some signs of consumption. This could indicate that garnet was consumed on the retrograde path and this caused the later Mn enrichment, following Kohn and Spear (2000). Staurolite also presents an inclusion-free rim depleted in Mg when compared to the core (more photomicrographs can be found in the supplementary material). Some staurolite grains also show some signs of being consumed, as irregular contours. This could indicate with a later growth of staurolite, followed by some consumption of this mineral. Finally, both biotite and chlorite occur within the matrix anhedral and could be retrograde phases.

The trace element distribution between different mineral seems to be more complex once different trace element reservoirs phases occur (garnet, monazite, apatite, and allanite). Apatite occurs within the garnet cores and along the matrix. Monazite, on the other hand, occur either within the rims of garnet and staurolite or in the matrix. Allanite occurs along the matrix. Wing et al. (2003) describe some reactions to allanite and monazite formation that could explain the distribution observed in this sample. The reaction Mnz + Chl + Pl + Cal + Qtz = Aln + Ap could have formed included-in-garnet allanite and apatite. On the other hand, the reaction Aln + Ap + Ms + St + Qtz = Mnz + Bt + Pl possibly formed monazite near the biotite-in reaction. Allanite on the matrix could

have formed both on the prograde or retrograde path with monazite consumption, without temporal information from this mineral is hard to attest.

The *P-T*-t path of this sample records a long period of monazite growth in isobaric setting with small temperature increase (~550-650 °C, Figure 32) all in the staurolite zone. Monazite grains record ages between 630-570 Ma and some older cores present even older stages 660-630 Ma (Figure 26), that could be from the prograde path. After that the decompression records garnet consumption and possibly allanite and apatite later formation.

8.1.2 Sillimanite Zone from MTCF (sample DR-352)

Garnet presents an intense zoning in both trace and major elements distribution, where a couple of different stages of growth can be observed (Figure 19). The trace element has an irregular distribution, garnet core (TE1) is enriched in HREE, followed by a heterogenous mantle, where TE2 is impoverished in HREE and TE3 has higher contents again. Finally, the garnet rim, TE4 and TE5, have the lowest HREE content (Figure 19). Pseudosections were modeled to reproduce the *P-T* conditions of different stages of garnet growth following the major elements distribution once they affect the bulk/local composition (Figure 24). Therefore *P-T* pseudosections are modeled to zones Z1, Z2 and Z3. They indicate that Z1 and Z2 grew in similar conditions before the staurolite-in reaction within the stability field of Grt + Chl + Ctd + Ms + Qtz + Pl + Ilm at ~550 °C and ~8 kbar. On the other hand, Z3 zone grew in higher temperature and lower pressure conditions at 650 – 700 °C and 6.5 – 7 kbar within the stability field of Sil + Grt + Bt + Ms + Pl + Qtz + Ilm (Figure 24).

Signs of the retrograde path can be observed in the consumption of garnet. This is indicated both by corroded rims and the Mn-enrichment (Kohn and Spear, 2000). Some biotite grains occur anhedral on the matrix that could indicate later growth on the retrograde path. Nevertheless, staurolite was not identified, indicating that the retrograde path did not cross the staurolite stability field.

The trace element distribution in garnet may record relation with the monazite formation on the staurolite-biotite zone. Following the reaction Aln + Ap + Ms +St + Qtz = Mnz + Bt + Pl (Wing et al., 2003), monazite is produced by the consumption of two trace element reservoirs, possibly allanite and apatite. This could be the cause of the enrichment of Y/HREE on TE3/contact to Z3 (Figure 19). Monazite grew within garnet production field, which could explain its low-Y core. On the retrograde path, with garnet consumption, some monazite may also have grown, causing monazite rims to enrich in Y.

Monazite grains show Y zoning with at least three different zones (Figure 27). Even using chemical and isotopic approaches on dating monazite grains, the difference between those zones is not precisely defined. Nevertheless, the dates yield a range spam of 40-50 Ma (620 – 570 Ma) for monazite growth.

This population may be represented by some spot EPMA analysis on monazite grains indicates a younger age around 546 ± 40 Ma on monazite rims (Figure 27). Nevertheless, it was not possible to date all zones systematically. Therefore, caution must be used to avoid overinterpretation of the data. On garnet Z3 there is an increase on trace element, that could indicate that other trace element-bearing phases were consumed prior/during this stage.

The *P-T*-t path of sample DR352 present an increase in temperature (from 500 to 700 °C in the sillimanite zone, Figure 32) with small decompression (from 8 to ~6.8 kbar) during a period of ca. 40 Ma (610-570 Ma). The retrograde path also registers garnet consumption and some biotite production.

8.1.3 Sillimanite Zone from MTCF (sample BR-04)

Garnet grains in this sample presents three zones based on Y and major elements (Figure 20). The Y distribution is simple with a high-Y core (Z1) followed by both poor-Y mantle (Z2) and poor-Y rim (Z3). Pseudosection modeling also produced better results when combining Z2 + Z3 and removing Z1 from bulk composition. The *P-T* conditions modeled to represent Z1 growth are ~550 °C and ~7 kbar on the stability field of Grt + Chl + Ms + St + Pl + Qtz + Ilm. The pseudosection modeled to garnet growth of Z2 + Z3 yields *P-T* conditions of ~700 °C and 7 kbar within the sillimanite stability field (Figure 25).

Monazite compositional maps show some Y and Th zoning, nevertheless it is not clear that these zones have different ages (Figures in the supplementary material). Chemical EPMA dating yield a range between 610 – 580 Ma. Due to the size of monazite grains, LA-ICP-MS collection was not made. Therefore, there is a lack of chemical information about trace element distribution of this sample, especially the HREE, so it is unwise to make correlations with garnet growth.

The *P-T*-t path of this sample indicates an isobaric heating from 550 to 720°C at approximately 7 kbar (Figure 32). The duration of this event recorded in monazite grains is ~30 Ma (610-580 Ma). The retrograde path indicates some garnet consumption once garnet grains present high-Mn rim and some corroded rims. Nevertheless, staurolite is absent, therefore the retrograde path did not cross the staurolite stability field.

8.1.4 Sillimanite-K-feldspar-Garnet Zone from HTCF (sample DR-298)

Garnet grains in this sample do not present intense chemical zoning, but they have signs of consumption, such as corroded rims (Figure 21). Previous metamorphic studies to this sample indicates that the sample passed through partial melting due to both muscovite and biotite break-down reactions. Those reactions caused growth of garnet and K-feldspar during melting (Faleiros et al., 2011). Kyanite inclusions in K-feldspar indicates that some melting occurred within the kyanite stability field at 750 – 810 °C and pressure at 12.5 kbar. Nevertheless, sillimanite is broadly observed in the matrix, which indicates that part of the melting occurred within the sillimanite stability field at 790 – 820 °C and 8 – 10 kbar (Faleiros et al., 2011). According to the authors, the substitution of kyanite to sillimanite during high-*T* conditions can be interpreted as a near isothermal decompression.

Monazite grains show complex chemical zoning of trace element distribution (Figure 30, Figure 31). The detailed LA-ICP-MS maps indicates that the chemical core does not match geographic core and the distribution is also not uniform. At least three zones can be observed based on the HREE distribution, the high-Y/HREE core, followed by a depleted-Y/HREE mantle and a thin high-Y/HREE rim (Figure 30, Figure 31). Eu distribution does not match other trace element ones. Spot analysis in different grains also indicates that Eu/Eu* distribution is more uniform than other HREE, i.e., all Eu/Eu* ratios occur between 0.08 – 0.12 (Figure 28).

Based on compositional plots, five populations are defined (Figure 28). All points from population P1 (purple) are locate in ‘mnz 6’ core. This population presents the oldest dates (750 – 650 Ma) and the trace element within the group is variable, exception is made to the Eu/Eu* that is regular in all points. Those dates are interpreted as detrital monazite grains that were encompassed during later monazite growth. It is likely that they all grew during/later melt crystallization considering that all of them has low values of Eu/Eu*, possibly related to an igneous source.

Populations P2 (yellow) and P3 (green) have similar Eu/Eu* content (~0.1), but they vary significantly in HREE and Y content; P2 (yellow) is depleted in Y/HREE (<10000 ppm) and green is enriched in Y/HREE (>10000 ppm). The fact that they both have low-Eu values indicate that they grew during melt crystallization. The HREE/Y content could be related to the garnet stability while monazite was growing. P2 (yellow) possibly grew while peritetic garnet was also forming and consuming all the HREE and Y available. P3 (green) on the other hand could have formed while garnet was either not growing or being consumed.

Due to the method uncertainties, these both populations, P2 and P3, overlap when plotted in a U-Th-Pb plot (Figure 28), so it is hard to confirm that P2 is older than P3. Nevertheless, the monazite maps may indicate that a large population with high-Y/HREE content grew (cores) grew before low-Y/HREE content (mantle). This could be interpreted as P2 being slightly older than P3. Another relation that can be made with garnet is the high-Y/HREE thin rim observed on the monazite maps. This domain was not dated due to spatial resolution. This later enrichment could be related to garnet consumption. Garnet grains present petrographic signs of consumption (Figure 21) as corroded rims that could release some trace element to a later monazite growth that occurred within monazite rims.

Finally, two populations that appeared in just some analysis, P4 (black) and P5 (light blue) present variable Eu/Eu* and high-HREE/Y content (Figure 28). They can be either preserved from the prograde path or they can be retrograde, after melting crystallized. P4 occurs in some monazite cores, which could indicate that it is a group of inherited older cores, possibly from the prograde path, with different compositions, which were trapped. On the other hand, P5 occurs in monazite rims. Those grains also present some of the youngest dates, but, again, they overlap with P2 and P3, within uncertainties. All this could indicate that they are slightly younger, and these are the ages that mark moments of the retrogression (Figure 28).

8.1.5 Kyanite-K-feldspar Zone from HTCF (Sample 129)

Garnet grains in this sample shows preserved zoning on major elements but trace element seem to have almost flat profiles (Figure 22). Garnet also shows signs of instability and consumption, such as corroded rims replaced by Kfs + Qtz + Bt. Previous *P-T* paths studies of this sample indicates that the sample passed through a near isobaric heating at high pressure from 620 °C to 760 °C at 11.6 - 11.9 kbar (Faleiros et al., 2011, Ricardo et al., 2020). This is followed by quick exhumation stage that preserved zoning profiles on garnet and some microstructures indicating the presence of melt, such as ‘melt pockets’ near garnet. The studies also indicates that the melting occurred mainly due to H_2O reactions and the sample would slightly cross the muscovite break-down reaction within the kyanite stability field (Faleiros et al., 2011, Ricardo et al., 2020). The sample contains some muscovite and does not present a well-developed leucosome segregation.

Monazite grains in this sample are small (<40 µm), mainly rounded and just eighteen analysis produced good results on the LA-ICP-MS (Figure 29). Based on their chemical composition, three populations were defined. P1 (light blue) presents less

pronounced Eu anomaly (Eu/Eu* > 0.3) and low HREE/ Y content. This could indicate that this population grew on the prograde path before partial melting and while garnet was also growing.

P2 (yellow) present well pronounced Eu anomaly and higher HREE/Y content. This indicates that the population grew during/after melt crystallization and garnet consumption. Again, within the uncertainties of the method, it is not possible to interpret age correlations. Petrographically, monazites from both P1 and P2 occur in matrix minerals, making it harder to address specific conditions in which they grew. P1 and P2 occur within a range between 610-580 Ma and they overlap within uncertainties (Figure 29).

Finally, P3 (red) occurs only in the rim of one dated monazite grain, and it presents the youngest dates (540-560 Ma). It has similar composition to P1, low Eu* and HREE/Y content (Figure 29). A possibility is that this domain could be formed during recrystallization of a previous P1 grain. Another hypothesis is that this domain formed without garnet consumption and after melt crystallization.

Monazite preservation conditions corroborate with the original interpretation of a peak conditions of partial melting within the kyanite field slightly after the muscovite break-down reaction. Those peak conditions would be followed by quick exhumation, preserving prograde features such as major elements zoning in garnet. The age range of prograde path and partial melting occurred between 610–580 Ma observed in both LA-ICP-MS and EPMA dating techniques. One older age appears in EPMA (652 ± 51 Ma, Figure 29), but as no other chemical information was obtained for this sample, it is hard to interpret the data. Younger dates (550–540 Ma) are also present in monazites from other samples. This could indicate a later common event/conditions shared by them all, but it is unclear if it is another tectonic event or just cooling.

8.1.6 Dating of other samples and summary of metamorphic ages

The metamorphic ages registered in monazite grains indicate that all samples passed through metamorphic events between 620 and 580 Ma (Figure 33). Older populations are recorded in two samples (DR378 and DR298) and indicates that metamorphic events in these samples could be as old as 640 Ma. Even older ages (750-650 Ma) only occur in one monazite core (mnz6 – DR298) and it is interpreted as detrital grains preserved on the monazite cores. Nevertheless, as all those detrital grains have well defined Eu anomaly, it is inferred that they formed while feldspar was also being produced, possibly from an igneous source.

Chemical dating of other samples may indicate some patterns that LA-ICP-MS did not cover. It indicates two populations, an older one with an average of 604 ± 17 Ma and a younger with an average of 543 ± 43. This younger population (560 – 540 Ma) only appears in one sample (129) on LA-ICP-MS occurs in at least five other samples on EPMA. This could indicate that all of them share the same event that formed monazite. It can be either a regional event or a late hydrothermal reactivation of the system. As such young ages have never been reported on the area, we interpret as a hydrothermal event, but more studies are recommended to understand those ages.

Finally, some correlations were made considering monazite and garnet as the main trace element reservoirs which are the classic relations presented in literature. Some other phases enriched in HREE were considered in some samples such as allanite and apatite. Nevertheless, it is important to mention that Weller et al. (2020) contest the validity of this classic correlation between garnet-monazite as main HREE phases.

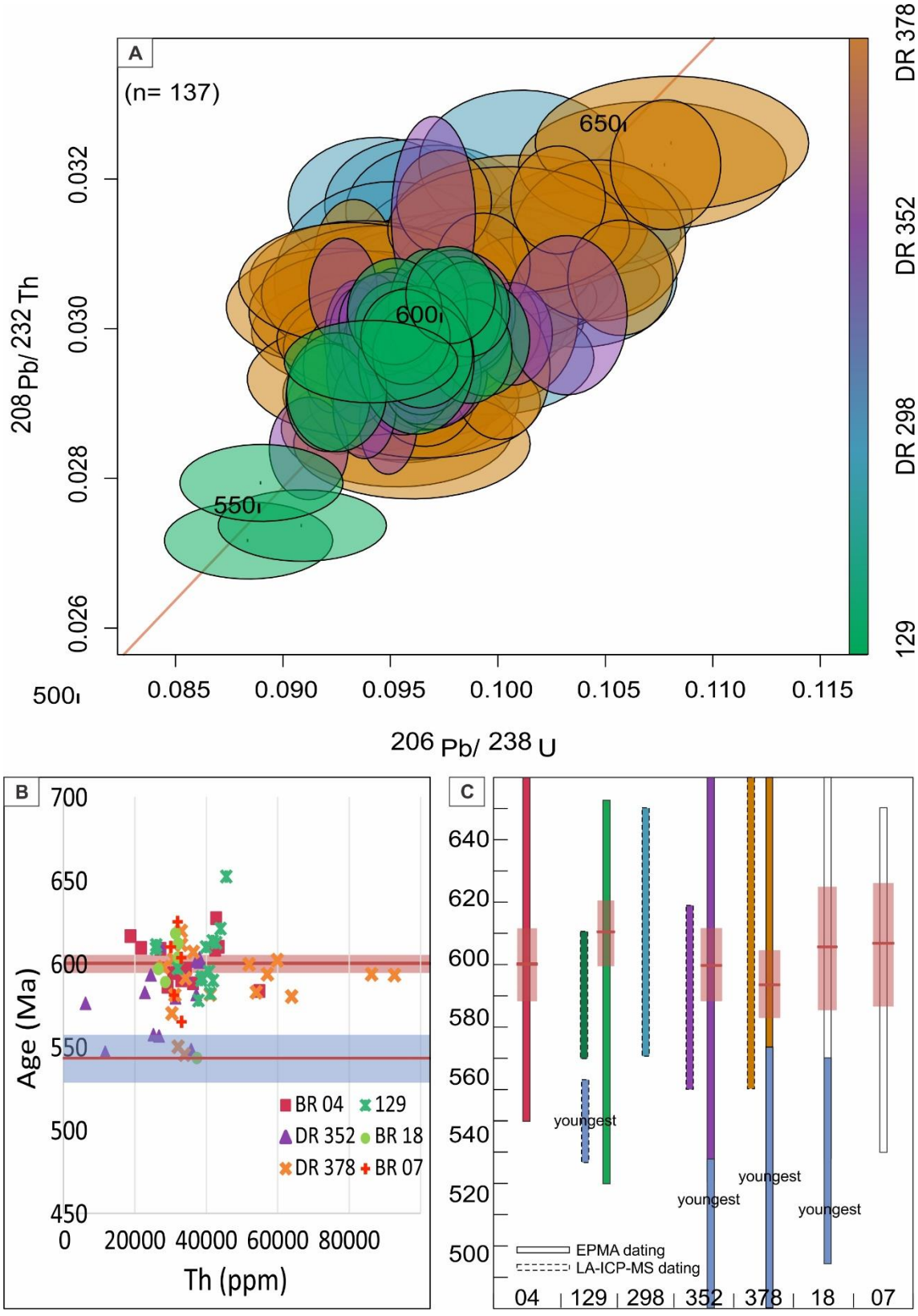

Figure 33 Compilation of monazite data obtained in the study. (a) 208Pb/232Th x 206Pb/238U plot calculated with IsoplotR to all studied samples. Only inferred detrital ages from sample DR298 are omitted (>700 Ma). (b) Chemical ages of all analyzed grains x Th content in ppm. Red and blue bars represent weighted mean and their respective uncertainties associated; the red based on oldest monazite grains (≥560 Ma) and the blue on youngest grains (<560 Ma); (c) summary of the age range obtained with both LA-ICP-MS and EPMA techniques. To chemical ages, the weighted mean is plotted

in red rectangles with respective uncertainty to each sample.

8.2 Tectonic implications and methodology

It can be noticed that samples in the TCF present bimodal thermobaric ratios (following definition by Brown and Johnson, 2019, Figure 32). Some samples record °C/GPa ratios in the 1500 °C/GPa field (DR352, BR04, DR151, DR206, BR18, DR39), while others present 775 °C/GPa ratios (DR378, BR35, 129). The authors suggest that different thermobaric ratios could be related to distinct tectonic settings (Brown and Johnson, 2019). Ricardo et al. (2020) proposes that the TCF sedimented and metamorphosed in a microcontinent tectonic setting where part of those rocks would be in the accretionary wedge (HTCF, lowT-highP, 775°C/GPa) and the other in the back-arc setting (LTCF and MTCF, highT-lowP, 1500°C/GPa). The temperature increase in the back-arc would come from an asthenospheric upwelling duo to extensional regime as proposed originally by Hindman et al. (2005). They would later be amalgamated with the continuous collisions including with the Luis Alves Plate (Ricardo et al., 2020).

Detailed metamorphic studies presented here still indicates this dual setting (Figure 32). Nevertheless, comparing the *P*-*T*-t trajectories this distribution of those rocks seems even more complex. Some samples seem to record longer periods of stable temperature (sample DR378) while others have quicker periods of high-*T* followed by quick decompression preserving prograde signatures (sample 129). They record distinct thermobaric ratios, *P*-*T*-t paths and even metamorphic ages – monazite ages between 640-620 Ma are present in just two samples (DR378, DR298). Nevertheless, all of them share part of the same metamorphic events (620-570 Ma). Monazite seems to have stopped being produced at the same time in all samples (~580-570 Ma). Those dates match the instauration of the A-type granites from the Graciosa Province (580-583 Ma, Vlach et al., 2011, U-Pb in zircon ID-TIMS). Faleiros et al. (2011) also obtained metamorphic ages at ~579 ± 8 Ma (monazite chemical dating) that is interpreted as a greenschist overprint related to the strike slip shear zones. Ricardo et al. (2020) also presents maximum depositional age for the TCF between 650-630 Ma.

Therefore, combining the available ages in literature with new U-Th-Pb in monazites ages presented here we evaluate the tectonic evolution for the TCF as follows:

- 650-630 Ma – Maximum depositional age of TCF sediments marked on detrital zircon (Ricardo et al., 2020);

- 640-620 Ma – Beginning of metamorphic events with monazite production recorded in two samples from the TCF (DR378, DR298), possibly associated to samples in the accretionary wedge;
- 620-570 Ma – Metamorphic events recorded broadly in the TCF, i.e. all samples;
- 580-570 Ma – Cease of metamorphism in the TCF. All samples stop recording monazite production;
- 580 Ma - Intrusion of A-type granites dated on zircon grains by TIMS (Vlach et al., 2011);
- 580 – 530 Ma – Shear zones activation (Faleiros et al., 2011);
- ~540 Ma – Younger monazite grains recorded in some samples. More studies are recommended to address the origin of this process.

Monazite grains were being produced for at least 50 Ma (between 620-570 Ma). We did not observe any chemical/isotopic evidence in monazite grains that the metamorphic events were either continuous or occurred within different pulses. In some samples, they record different chemical signatures that could be related to different reactions forming monazite. Nevertheless, ages overlap within their uncertainties in different populations, making it impossible to wisely distinguish pulses of monazite formation related to different reactions. Faleiros et al. (2016) and Ricardo et al. (2020) proposed a division of the TCF rocks based on their metamorphic grade, i.e. low (LTCF), medium (MTCF) and high (HTCF). The authors also proposed that rocks from LTCF+MTCF would have passed through sedimentation and metamorphic events on the back-arc basin. The HTCF, on the other hand, would have deposited and metamorphosed in the accretionary wedge. Under the light of more detailed metamorphic studies, it seems that this division may be an oversimplification. For instance, samples DR206 and BR35 present thermobaric ratios closer to high-*P*-low-*T* (Figure 32), even though they occur in the garnet zone. This high-*P*-low-*T* ratio could indicate their presence also on the accretionary wedge. Therefore, they should be revaluated as HTCF, not MTCF as presented in Ricardo et al. (2020).

On the MTCF, two samples in the sillimanite zone, close to each other, BR04 and DR352 also present different *P*-*T*-t paths. BR04 presents a near isobaric heating path and DR352 presents an increase in temperature associated to a small decompression. This indicates that even samples in the same sillimanite metamorphic zone, and currently located close to each other may record slightly distinct *P*-*T* histories. Therefore, the isograd map presented by Ricardo et al. (2020; Figure 17) may also be a simplification of the real distribution of metamorphic zones.

Samples from the HTCF already present different paths. The sample 129 records a near isobaric heating, while DR298 indicates a near isothermal decompression (Faleiros et al., 2011, Figure 32). This difference is also preserved in the metamorphic ages recorded in monazite. While sample 129 records metamorphism between 610 - 570 Ma, DR298 records a much older story, from 640 – 570 Ma. Monazite grains are also much bigger in sample DR298 than in sample 129. They could be interpreted as rocks that started to be subducted in different moments, DR298 at least 30 Ma before 129.

Finally, sample DR378 present an even more distinct trajectory. The *P-T*-t path of this sample records at least 60 Ma of metamorphic events forming monazite without great changes in the *P-T* conditions within the staurolite zone stability field. This sample is separated from the others by two shear zones and studies were never conducted with rocks located in this area. Therefore, more studies are recommended once they could even belong to another geological unit.

More studies are also recommended to address the origin of younger ages (~540 Ma) recorded in some samples. They appeared mainly on the chemical dating and only three spot isotopic analysis records them. Their origin could be hydrothermal or from the regional metamorphism, but as those ages were never reported before, we recommend more studies to attest their origin.

9. Conclusion

Interpreting tectonic settings of ancient accretionary orogens may be more challenge than it seems. Millions of years of lateral displacement caused by strike slip shear zones may have major impacts on their current distribution (Cawood et al., 2009). In the Curitiba Terrane, in the Ribeira Belt, one single Neoproterozoic metasedimentary unit (TCF) records complex evolution with samples with distinct sedimentation and metamorphic settings.

Detailed petrochronological studies proved able to constrain *P-T*-t paths to some samples in different metamorphic grades. Nevertheless, combining all *P-T*-(t) information available for metamorphic rocks on the TCF, it seems naïve to assume one simple tectonic explanation to all samples. Samples present one coeval story between 620-570 Ma, but older ages are recorded in just some samples (640-620 Ma). All this could indicate that even though they share part of their tectonic history, this evolution is more complex than the originally proposed by Ricardo et al. (2020).

The metamorphism on the area was previously dated at 600-580 Ma (Faleiros et al., 2011, 2016). Our new metamorphic data anticipates these events in at least 20 Ma

(620 Ma) and even 40 Ma to some samples. Considering that detrital zircon records maximum depositional ages at 650-630 Ma (Ricardo et al., 2020), we interpret that the deposition and the metamorphism were concomitant at least in some samples (DR378, DR298). Our new data indicates that monazite was being produced with K-feldspar crystallization at ~640 Ma. Therefore, we interpret that while sedimentation was still occurring, part of the unit (part of the High-TCF) was already being submitted to high-*T*-high-*P* conditions with partial melting. This also corroborates to the setting proposed by Ricardo et al. (2020) of the development of a magmatic arc concomitant to the deposition and metamorphism in its neighbor basins. Trace element information from monazite and garnet indicates that multiple reactions may have caused the formation of those minerals. Nevertheless, within the uncertainties of both chemical and isotopic methods, it is impossible to infer the timing of those reactions.

Petrochronology applied with systematic thermodynamic modelling was crucial into evaluating the different *P-T*-t paths that samples record. The isotopic information in monazite grains was critical to estimate some reactions that caused monazite formation related to partial melting. By studying samples from different metamorphic conditions and structural positions, it was possible to recognize the complexity of the studied area. Nevertheless, more detailed study still indicates that rocks within the TCF have two different baric regimes, as originally proposed by Ricardo et al. (2020). Therefore, our data corroborates with the first model proposed for the area by Ricardo et al. (2020) and add important temporal constraints in the metamorphism involved. These features would probably be missed with a common metamorphic approach obtaining just the peak conditions of a small set of samples and classical geochronology instead of petrochronology.

Acknowledgements

Financial support was provided by grants 2018/10012-0, 2018/01572-1 and 2019/19651-8 from São Paulo Research Foundation (FAPESP). BSR also thanks Coordination of Superior Level Staff Improvement (CAPES) for financial support by scholarship grant. FMF, RM and SRFV are CNPq fellow researchers.

References

Aleinikoff, J. N., Schenck, W. S., Plank, M. O., Srogi, L., Fanning, C. M., Kamo, S. L., & Bosbyshell, H. 2006. Deciphering igneous and metamorphic events in high-

grade rocks of the Wilmington Complex, Delaware: Morphology, cathodoluminescence and backscattered electron zoning, and SHRIMP U-Pb geochronology of zircon and monazite. Geological Society of America Bulletin, 118(1-2), 39-64.

Almeida, F.F.M. 1977. O Cráton do São Francisco. Revista Brasileira de Geociências, 7: 349-364.

De Almeida, F. F. M., Hasui, Y., de Brito Neves, B. B., & Fuck, R. A. 1981. Brazilian structural provinces: an introduction. Earth-Science Reviews, 17(1-2), 1-29.

Basei, M.A.S., Siga Júnior, O., Machiavelli, A., Mancini, F. 1992. Evolução tectônica dos terrenos entre os cinturões Ribeira e Dom Feliciano (PR-SC). Revista Brasileira de Geociências, 22(2): p. 216-221.

Basei, M. A. S., Frimmel, H. E., Nutman, A. P., & Preciozzi, F. 2008. West Gondwana amalgamation based on detrital zircon ages from Neoproterozoic Ribeira and Dom Feliciano belts of South America and comparison with coeval sequences from SW Africa. Geological Society, London, Special Publications, 294(1), 239-256.

Basei, M. A., Nutman, A., Júnior, O. S., Passarelli, C. R., & Drukas, C. O. 2009. The evolution and tectonic setting of the Luis Alves Microplate of Southeastern Brazil: an exotic terrane during the assembly of Western Gondwana. Developments in Precambrian Geology, 16, 273-291.

Brito Neves, B.B., Campos Neto, M.C.,Fuck, R.A. 1999. From Rodinia to Western Gondwana: an approach to the Brasiliano-Pan African Cycle and orogenic collage. Episodes, 22, 155-166.

Brown, M., & Johnson, T. 2019. Time's arrow, time's cycle: Granulite metamorphism and geodynamics. Mineralogical Magazine, 83(3), 323-338.

Campanha, G. D. C., & Faleiros, F. M. 2005. Neoproterozoic terrane collage in the southern and central Ribeira Belt, Brazil. In Gondwana 12 Conference: Geological and Biological Heritage of Gondwana (Vol. 1, p. 81). National Academy of Sciences Argentina, Mendoza.

Campanha, G. A. C., Faleiros, F. M., Basei, M. A. S., Tassinari, C. C. G., Nutman, A. P., & Vasconcelos, P. M. 2015. Geochemistry and age of mafic rocks from the Votuverava Group, southern Ribeira Belt, Brazil: Evidence for 1490 Ma oceanic back-arc magmatism. Precambrian Research, 266, 530-550.

Catlos, E. J. 2013. Generalizations about monazite: Implications for geochronologic studies. American Mineralogist, 98(5-6), 819-832.

Cawood, P. A., Kröner, A., Collins, W. J., Kusky, T. M., Mooney, W. D., & Windley, B. F. 2009. Accretionary orogens through Earth history. Geological Society, London, Special Publications, 318(1), 1-36.

Connolly, J. A. 2005. Computation of phase equilibria by linear programming: a tool for geodynamic modeling and its application to subduction zone decarbonation. Earth and Planetary Science Letters, 236(1-2), 524-541.

Cutts, K. A., Hand, M., Kelsey, D. E., Wade, B., Strachan, R. A., Clark, C., & Netting, A. 2009. Evidence for 930 Ma metamorphism in the Shetland Islands, Scottish Caledonides: implications for Neoproterozoic tectonics in the Laurentia–Baltica sector of Rodinia. Journal of the Geological Society, 166(6), 1033-1047.

Cutts, K. A., Kinny, P. D., Strachan, R. A., Hand, M., Kelsey, D. E., Emery, M., ... & Leslie, A. G. 2010. Three metamorphic events recorded in a single garnet: Integrated phase modelling, in situ LA-ICPMS and SIMS geochronology from the Moine Supergroup, NW Scotland. Journal of Metamorphic Geology, 28(3), 249-267.

Dumond, G., Goncalves, P., Williams, M. L., & Jercinovic, M. J. 2015. Monazite as a monitor of melting, garnet growth and feldspar recrystallization in continental lower crust. Journal of Metamorphic Geology, 33(7), 735-762.

Faleiros, F. M., Campanha, G.A.C., Martins, L., Vlach, S.R.F., Vasconcelos, P.M., 2011. Ediacaran high-pressure collision metamorphism and tectonics of the southern Ribeira Belt (SE Brazil): evidence for terrane accretion and dispersion during Gondwana assembly. *Precambrian Research,*189, 263–291.

Faleiros, F. M., Moraes, R., Pavan, M., Campanha, G. A. C. 2016. A new empirical calibration of the quartz c-axis fabric opening-angle deformation thermometer. Tectonophysics, 671, 173-182.

Faleiros, F.M., 2017. Metamorfismo e termobarometria de pelitos da Formação Capiru: Implicações tectônicas para a Faixa Ribeira Meridional. X International Symposium on Tectonics, Salvador, Short Papers 109–111.

Fuhrman, M, L., Lindsley, D. H. 1988. Ternary-Feldspar Modeling and Thermometry. American Mineralogist 73:201-15.

Gonçalves, G. O., Lana, C., Scholz, R., Buick, I. S., Gerdes, A., Kamo, S. L., ... & Nalini Jr, H. A. 2016. An assessment of monazite from the Itambé pegmatite district for use as U–Pb isotope reference material for microanalysis and implications for the origin of the “Moacyr” monazite. Chemical Geology, 424, 30-50.

Guimarães, S. B., dos Reis Neto, J. M., & Siqueira, R. B. 2002. Caracterização dos estromatólitos da Formação Capiru (Proterozóico) nas regiões de Morro Azul e Morro Grande: leste do Paraná. Boletim Paranaense de Geociências, 51, 77-88.

Heilbron, M., Mohriak, W. U., Valeriano, C. M., Milani, E. J., Almeida, J., & Tupinambá, M. 2000. From collision to extension: the roots of the southeastern continental margin of Brazil. Geophysical Monograph-American Geophysical Union, 115, 1-32.

Heilbron, M., Pedrosa-Soares, A. C., Campos Neto, M. D. C., Silva, L. D., Trouw, R. A.

J., & Janasi, V. D. A. 2004. Província mantiqueira. Mantesso-Neto, V.; Bartorelli, A.; Carneiro, CDR, 203-234.

Heilbron, M., Cordani, U. G., & Alkmim, F. F. 2017. The São Francisco craton and its margins. In São Francisco Craton, Eastern Brazil (pp. 3-13). Springer, Cham.

Holland, T. J. B., Powell, R. 2011. An improved and extended internally consistent thermodynamic dataset for phases of petrological interest, involving a new equation of state for solids. Journal of Metamorphic Geology, 29 (3), 333-383.

Hyndman, R. D., Currie, C. A., & Mazzotti, S. P. 2005. Subduction zone backarcs, mobile belts, and orogenic heat. GSA Today, 15(2), 4-10.

Jochum, K. P., Nohl, U., Herwig, K., Lammel, E., Stoll, B., & Hofmann, A. W. 2007. GeoReM: A new geochemical database for reference materials and isotopic standards. Geostandards and Geoanalytical Research, 29, 333–338.

Kohn, M. J., & Spear, F. 2000. Retrograde net transfer reaction insurance for pressure-temperature estimates. Geology, 28(12), 1127-1130.

Leandro, R. 2016. Caracterização tectonoestratigráfica da sequência terrígena da formação Capiru na Região de Morro Grande, Colombo-PR.Masters Thesis, Federal University of Paraná.

Ludwig, K. 2008. Isoplot version 4.15: a geochronological toolkit for microsoft Excel. Berkeley Geochronology Center, Special Publication, (4).McDonough, W. F., & Sun, S. S. 1995. The composition of the Earth. Chemical geology, 120(3-4), 223-253.

Malta, I. S., Faleiros, F. M., Monteiro, L. V., Andrade, M. B., Coldebella, B., & Esteves, M. C. 2020. PT-fluid-deformation regime of the Ediacaran Serra do Cavalo Magro orogenic gold deposit, Ribeira Belt, Brazil. Ore Geology Reviews, 120, 103384.

McDonough, W. F., & Sun, S. S. 1995. The composition of the Earth. Chemical geology, 120(3-4), 223-253.

Meira, V. T., García-Casco, A., Juliani, C., Almeida, R. P., & Schorscher, J. H. D. 2015. The role of intracontinental deformation in supercontinent assembly: insights from the Ribeira Belt, Southeastern Brazil (Neoproterozoic West Gondwana). Terra Nova, 27(3), 206-217.

Meira, V. T., Garcia-Casco, A., Hyppolito, T., Juliani, C., & Schorscher, J. H. D. 2019. Tectono-metamorphic evolution of the Central Ribeira Belt, Brazil: A case of late Neoproterozoic intracontinental orogeny and flow of partially molten deep crust during the assembly of West Gondwana. Tectonics, 38(8), 3182-3209.

Motta, R. G., Fitzsimons, I. C., Moraes, R., Johnson, T. E., Schuindt, S., & Benetti, B. Y. 2021. Recovering P–T–t paths from ultra-high temperature (UHT) felsic

orthogneiss: An example from the Southern Brasília Orogen, Brazil. Precambrian Research, 359, 106222.

Palin, R. M., Searle, M. P., Waters, D. J., Parrish, R. R., Roberts, N. M. W., Horstwood, M. S. A., ... & Anh, T. T. 2013. A geochronological and petrological study of anatectic paragneiss and associated granite dykes from the Day Nui Con Voi metamorphic core complex, North Vietnam: constraints on the timing of metamorphism within the Red River shear zone. Journal of Metamorphic Geology, 31(4), 359-387.

Paul, B., Paton, C., Norris, A., Woodhead, J., Hellstrom, J., Hergt, J., & Greig, A. 2012. CellSpace: a module for creating spatially registered laser ablation images within the Iolite freeware environment. Journal of Analytical Atomic Spectrometry, 27(4), 700-706.

Passarelli, C. R., Basei, M. A. S., Wemmer, K., Siga, O., & Oyhantçabal, P. 2011. Major shear zones of southern Brazil and Uruguay: escape tectonics in the eastern border of Rio de La plata and Paranapanema cratons during the Western Gondwana amalgamation. International Journal of Earth Sciences, 100(2), 391-414.

Passarelli, C. R., Basei, M. A. S., Siga, O., Harara, O. M. M. 2018. The Luis Alves and Curitiba Terranes: Continental Fragments in the Adamastor Ocean. In *Geology of Southwest Gondwana* (pp. 189-215). Springer, Cham.

Paton, C., Hellstrom, J., Paul, B., Woodhead, J., & Hergt, J. 2011. Iolite: Freeware for the visualisation and processing of mass spectrometric data. Journal of Analytical Atomic Spectrometry, 26(12), 2508-2518.

Ricardo, B. S., Faleiros, F. M., de Moraes, R., Júnior, O. S., & Campanha, G. A. 2020. Tectonic implications of juxtaposed high-and low-pressure metamorphic field gradient rocks in the Turvo-Cajati Formation, Curitiba Terrane, Ribeira Belt, Brazil. Precambrian Research, 345, 105766.

Rocha, B. C., Moraes, R., Möller, A., Cioffi, C. R., & Jercinovic, M. J. 2017. Timing of anatexis and melt crystallization in the Socorro–Guaxupé Nappe, SE Brazil: Insights from trace element composition of zircon, monazite and garnet coupled to UPb geochronology. Lithos, 277, 337-355.

Rubatto, D., & Hermann, J. 2003. Zircon formation during fluid circulation in eclogites (Monviso, Western Alps): implications for Zr and Hf budget in subduction zones. Geochimica et Cosmochimica acta, 67(12), 2173-2187.

Rubatto, D., Hermann, J., & Buick, I. S. 2006. Temperature and bulk composition

control on the growth of monazite and zircon during low-pressure anatexis (Mount Stafford, central Australia). Journal of Petrology, 47(10), 1973-1996.

Rubatto, D., Chakraborty, S., & Dasgupta, S. 2013. Timescales of crustal melting in the Higher Himalayan Crystallines (Sikkim, Eastern Himalaya) inferred from trace element-constrained monazite and zircon chronology. Contributions to Mineralogy and Petrology, 165(2), 349-372.

Rueden, C. T., Schindelin, J., Hiner, M. C., DeZonia, B. E., Walter, A. E., Arena, E. T., Eliceiri, K. W. 2017. ImageJ2: ImageJ for the next generation of scientific image data. *BMC bioinformatics*, *18*(1), 529.

Santos, L. D. R., Leandro, R., Bahniuk, A., & Cury, L. F. 2018. Low-temperature metamorphism in the Capiru Formation, Morro Grande Synform, Southern Ribeira Belt. Brazilian Journal of Geology, 48(1), 95-113.

Sato, K., Siga Jr, O., Nutman, A. P., Basei, M. A., McReath, I., Kaulfuss, G. 2003. The Atuba Complex, southern South American Platform: Archean components and paleoproterozoic to neoproterozoic tectonothermal events. Gondwana Research, 6(2), 251-263.

Sato, K., Siga Júnir, O., Silva, J. D., McReath, I., Liu, D., Iizuka, T., Rino, S., Hirata, T., Sproesser, W., Basei, M. A. S. 2009. In situ isotopic analyses of U and Pb in zircon by remotely operated SHRIMP II, and Hf by LA-ICP-MS: an example of dating and genetic evolution of zircon by 176Hf/177Hf from the ItaQuarry in the Atuba Complex, SE Brazil. Geologia USP, Série Cientifica São Paulo, 9, 61-69.

Trouw, R. A. J., Heilbron, M., Ribeiro, A., Paciullo, F., Valeriano, C. M., Almeida, J. C. H., ... & Andreis, R. R. 2000. The central segment of the Ribeira Belt. Tectonic Evolution of South America, 31, 287-310.

Trouw, R. A., Peternel, R., Ribeiro, A., Heilbron, M., Vinagre, R., Duffles, P., ... & Kussama, H. H. 2013. A new interpretation for the interference zone between the southern Brasília belt and the central Ribeira belt, SE Brazil. Journal of South American Earth Sciences, 48, 43-57. Tilley, C. E. 1925. A preliminary survey of metamorphic zones in the southern Highlands of Scotland. Quarterly Journal of the Geological Society, 81(1-4), 100-112.

Tomascak, P. B., Krogstad, E. J., & Walker, R. J. 1996. U-Pb monazite geochronology of granitic rocks from Maine: implications for late Paleozoic tectonics in the Northern Appalachians. The Journal of Geology, 104(2), 185-195.

Vermeesch, P. 2018. IsoplotR: A free and open toolbox for geochronology. Geoscience Frontiers, 9(5), 1479-1493.

Vlach, S. R. F. 2010. Th-U-PbT dating by electron probe microanalysis, part I. Monazite:

analytical procedures and data treatment. Geologia USP: Série Científica, 10(1), 61-85.

Vlach, S. R., Siga Jr, O., Harara, O. M., Gualda, G. A., Basei, M. A., & Vilalva, F. C. 2011. Crystallization ages of the A-type magmatism of the Graciosa Province (Southern Brazil): Constraints from zircon U-Pb (ID-TIMS) dating of coeval K-rich gabbro-dioritic rocks. Journal of South American Earth Sciences, 32(4), 407-415.

Weller, O. M., Jackson, S., Miller, W. G., St-Onge, M. R., & Rayner, N. 2020. Quantitative elemental mapping of granulite-facies monazite: Textural insights and implications for petrochronology. Journal of Metamorphic Geology, 38(8), 853-880.

White, R. W., Powell, R., Holland, T. J. B., Johnson, T. E., & Green, E. C. R. 2014. New mineral activity–composition relations for thermodynamic calculations in metapelitic systems. *Journal of Metamorphic Geology*, *32*(3), 261-286.

Wing, B. A., Ferry, J. M., & Harrison, T. M. 2003. Prograde destruction and formation of monazite and allanite during contact and regional metamorphism of pelites: petrology and geochronology. Contributions to Mineralogy and petrology, 145(2), 228-250.

CHAPTER 4 - DISCUSSIONS

Detailed metamorphic studies were previously conducted in the TCF (Faleiros et al., 2011, 2016). Nevertheless, the authors focused the investigation on the high-grade rocks with evidence of partial melting. Faleiros et al. (2011) present the most important contribution to the area detailing the metamorphic conditions to rocks from two different metamorphic zones in the TCF: the Kyanite-K-feldspar Zone and the Sillimanite-K-feldspar Zone. The authors used conventional geothermobarometry compiled with thermodynamic modelling to obtain the *P-T* peak conditions and the Gibbs method to constrain *P-T* paths. They obtained *P-T* conditions between 670-810 °C and 9.5-12 kbar as the metamorphic peaks to the rocks from the High-TCF. As for the trajectories they obtained, they interpret that the rocks from the Kyanite-K-feldspar zone as a near isobaric heating and the rocks from the Sillimanite-K-feldspar zone as a near isothermal decompression. They also obtained U-Pb chemical dating of monazite to constrain the metamorphic events in the area. They obtained 589 ± 12 Ma as the metamorphic peak followed by a greenschist facies overprint at 579 ± 8 Ma that they interpret to be related to the instauration of regional shear zones (Faleiros et al., 2011). Faleiros et al. (2016) also studied the High-TCF but from a different front. The authors present the first detrital zircon results to the area to one sample from the Kyanite-K-felspar Zone. They indicate that the maximum depositional age for the unit is between 650-630 Ma.

In this MSc dissertation, we investigated samples on the TCF that were not studied before. Metapelites from the garnet, staurolite and sillimanite zones crop out in the area and they were not investigated before. The MSc aimed to evaluate the tectonic evolution of those rocks and compare them to previous studies in the High-TCF. Some contributions to both the methodology and the tectonic understanding of the area will be addressed below.

To have a better understanding on the evolution of the unit, two fronts were approached. The first to collect data about the sedimentation conditions of the previous basin that originated the current TCF. Therefore, in Ricardo et al. (2020) (**section 2.0** in this manuscript) new and greater detrital zircon analysis are compiled and compared. Data from four new samples are presented and compared to the sample presented by Faleiros et al. (2016). Probability density plots are presented for samples from the Low-TCF (FS-21, DR-39), Medium-TCF (FM-426 and BR116-32) and sample 129A from the High-TCF from Faleiros et al. (2016). They indicate a shared source of detrital zircon with common peaks at 2300-1950 Ma, 1850-1700 Ma, 1550-1400 Ma and 1300-1100 Ma. Nevertheless, the youngest and highest peak is dislocated when samples from the Medium/High-TCF are compared to the Low-TCF. High/Medium-TCF have a higher peak at ~680-660 Ma and samples from the Low-TCF at ~800 Ma. Nevertheless, they also record younger ages with less prominence. The interpretation to this difference is the distance to the source. Low-TCF is interpret as more distal to the source than Medium/High-TCF.

The other shared age peaks indicate that the sub-units share source areas, therefore they are at least, neighbor basins. The older peak at 2300-1950 Ma is compatible with the main age population of the Atuba Complex (2200-2100 Ma, Sato et al., 2003, 2009). Therefore, the Atuba Complex is a potential detrital source to TCF, and possibly the basement to the TCF basin. Interpreting the probability density plots (pdp) and comparing to the tectonic setting proposed by Cawood et al. (2012), the pdp obtained to the Low and Medium-TCF present curves similar to back-arc basin setting, i.e. higher amount of older detrital zircons from the adjoining craton and greater younger peak. On the other hand, the High-TCF present a pdp plot similar to an accretionary wedge setting proposed by Cawood et al. (2012), i.e. faster deposition on the peak reflected by smaller number of analysis and lower contribution of older detrital zircon/basement.

To evaluate the metamorphism that affected those rocks, the initial approach was to have a general constrain on the *P-T* peak conditions that affected the rocks in the

area. By compiling field work, data from previous studies and petrography, it was possible to evaluate the isograd distribution of the sub-units. It becomes clear that the sillimanite zone is the main zone in the Medium-TCF. This already indicates that rocks from this sub-unit passed through metamorphism below 6 kbar in the sillimanite stability field. Thermodynamic modelling was then implemented to constrain the *P-T* peak for some samples. Two samples were selected from the garnet zone in the Low-TCF (DR39 and DR206) and one sample from the sillimanite-staurolite zone (DR151). Pseudosection modelling indicates that metamorphic peak to these samples were reached at 530-560 °C, 6.0-7.0 kbar (DR39), 550-580 °C, 7.0-7.6 kbar (DR206) and 640-670 °C, 5.9-7.0 kbar (DR151).

This pressure regime (6.0-7.5 kbar) contrasts with the pressure conditions obtained to the High-TCF (~10-12 kbar). They also indicate different metamorphic field gradients when comparing the Low/Medium-TCF *P-T* peak conditions and the High-TCF. Faleiros et al. (2011) studying the High-TCF obtained these 10-12 kbar pressures and trajectories of quick exhumation associated with isothermal decompression. They already interpret that this could be a subduction-related metamorphic setting, probably in the accretionary wedge. The pressure regime (6.0-7.5 kbar) on the Low/Medium-TCF, on the other hand indicates a low-*P* regime that could be related to the metamorphism on the back-arc setting with an increase in temperature caused by an asthenospheric upwelling due to extension. This metamorphic contrast between a high-*P* (High-TCF) and low-*P* (Low/Medium-TCF) metamorphic setting associated is interpret as a paired metamorphic belt in a Japan-like microcontinent (Brown, 2006, Brown &. Johnson, 2018).

Based on the sedimentation setting and the metamorphic *P-T* peaks obtained for all TCF sub-units, a modeled is proposed for the evolution of the area and is presented in Ricardo et al. (2020) and in the session 3 of this dissertation. In this model, we interpret that rocks from the TCF developed in related but different settings. Both the sedimentation and the metamorphic data indicate that the Low and Medium-TCF would be in the back-arc setting. On the other hand, the High-TCF sedimentation and metamorphic setting indicate that the unit would be in the accretionary wedge. Those basins are correlated with a shared micro-continent that would be both the basement and detrital source to both basins. Based on the detrital zircon record, we interpret that the Atuba Complex could be this basement, forming this Japan-like microcontinent, the proto-Curitiba Terrane Microplate. The subduction of part of the Adamastor Ocean would cause the development of a magmatic arc, the Piên Magmatic Arc. This arc is the main source for those younger detrital grains in both TCF basins in the back-arc and the

accretionary wedge. The development of this magmatic arc is long-lived and between 630-610 Ma, it would reach its final stages before the final collision with the Luis Alves Microcontinent. This collision at 600-585 Ma would have caused the main metamorphism in the back-arc (Low/Medium-TCF), also in the accretionary wedge (High-TCF) and exhumation of this sub-unit.

Nevertheless, the evaluation of the metamorphic conditions was made without considering the fractionation that occurs within garnet grains that affects the reactive bulk composition (Cutts et al., 2009, 2010). Therefore, more detail and systematic thermodynamic modelling was made to obtain the *P-T*-t paths that the rocks passed by and the possible implications on the tectonic evolution model. Metamorphic temporal data was also collected with petrochronology of monazite with both isotopic and chemical dating, with LA-ICP-MS and EPMA techniques, respectively. The results of this approach are discussed in the section 4 of this dissertation.

Phase diagrams were modeled in the MnNCKFMASHTO chemical system considering the evolution of the effective bulk composition to three samples from the Medium-TCF (BR04, DR352 and DR378). A *P-T* path is also proposed to each sample based on the *P-T* conditions constrained with isopleths of mineral compositions. Sample DR378 is in the staurolite zone, the *P-T* conditions calculated to the growth of garnet core is 520-530 °C and ~8.2 kbar and for the garnet rim 550-620 °C and 7.5-8.0 kbar. The trajectory indicates small increase in temperature within the same pressure conditions. Sample DR352 has mineral assemblage in the sillimanite zone, the *P-T* conditions obtained to the garnet growth are ~520 °C and ~8.2 kbar to the core and 650-700 °C and 6.0-7.0 kbar to the rim. Sample BR04 is a sample from the sillimanite zone, the *P-T* conditions obtained to the growth of the garnet core and rim are ~520 °C and ~6.8 kbar and 660-720 °C and 6.5-8.0 kbar and the *P-T* trajectory is interpreted as a near isobaric heating.

Monazite U-Th-Pb dating is also presented to understand the temporal scale of those events. Both techniques of isotopic and chemical dating were used duo to the characteristics of each sample. The isotopic dating was made with the LA-ICP-MS equipment combing the U-Th-Pb isotopic ages with trace element chemistry. Some correlations can be made between monazite growth and other minerals such as garnet, allanite, apatite and K-feldspar following their chemistry. Four samples were analyzed, DR352 and DR378 from Medium-TCF and DR298 and 129 from the High-TCF. Different populations were evaluated in each one of the samples but due to the conditions of the method, they overlap within uncertainties. The metamorphic ages range varies from 620-

580 Ma in the samples DR352 and 129 and from 640-580 Ma in samples DR378 and DR298. Chemical dating was made in samples DR378, DR352, BR04, BR07 and BR18 from the Medium-TCF and 129 from the High-TCF. Chemical ages record a high value of uncertainties in each analyzes, therefore the range is bigger. Two populations were identified based on their age, an older which gives an average of 600 ± 5 Ma and the younger 543 ± 14 Ma. Nevertheless, no chemical control was used in these calculations, the grains record some Y and Th zoning that was not considered due to the small set of analysis from each domain. The average, therefore, considers all the collected data, not possible different domains.

Finally, collecting all the metamorphic data, *P-T*-t paths are proposed, and they indicate different evolution for each sample. With more detailed studies on the metamorphism, it becomes clear that the area presents high complexity. For instance, two samples studied here and located close to each other (BR4 and DR352) present similar mineralogy, on the sillimanite zone and similar temporal interval. Nevertheless, the pressure regime registered in both samples varies from near isobaric heating in sample BR04 and heating associated with decompression in sample DR352. Sample DR378 records metamorphism with monazite production for 60 Ma (630-570 Ma).

Samples from the High-TCF also records differences in both their *P-T* paths as already proposed by Faleiros et al. (2011) but in the timescale of this metamorphism. Sample DR298 from the Sillimanite-K-feldspar zones also records a long-lived (50 Ma, from 630-580 Ma) process of monazite growth related to partial melting. On the other hand, sample 129 from the Kyanite-K-feldspar zone records a shorter history (610-570 Ma).

Nevertheless, when comparing the *P-T* peak conditions to all samples presented here, a bimodal tectonic setting still seems to be the best option to explain this origin. Some samples record thermobaric ratios (definition from Brown and Johnson, 2019) and in the intermediate-*P* (775 °C/Ga) and others in the low-P (1500°C/Ga). Therefore, the model proposed by Ricardo et al. (2020) and in the session 3 of this dissertation still seems to be valid. The evolution is probably more complex than the model, with rocks within the same tectonic setting, i.e. the back-arc or the accretionary wedge, recording slightly different *P-T*-t paths. But Low/Medium-TCF and High-TCF still records distinct pressure regimes that could be explained by paired metamorphic belts. This petrochronological approach revealed that some samples with low-grade association (i.e. garnet or staurolite zone) may record high *T/P* ratios. Therefore, the distribution of the sub-units based only on the mineral assemblage is an oversimplification. The Low-

TCF could not be dated duo to the absence of monazite grains, we suggest that the unit should be dated in the future with a different technique.

CHAPTER 5 - CONCLUSIONS

Understanding the tectonic evolution of a metasedimentary unit in an accretionary wedge setting can be challenging. Millions of years of tectonic events such as collisions, subduction and lateral displacement may rearrange the original geographic distribution (Cawood et al., 2012). Nevertheless, implementing the investigation of both the sedimentation and the metamorphic setting can be good approach to decipher not only the setting but the tectonic evolution. Systematic thermodynamic modelling coupled with petrochronology in older rocks is a crucial tool to evaluate the evolution of metamorphic trajectories, not only the *P-T* peak of some samples.

As for the evolution of the Turvo-Cajati Formation, it is proposed that the unit can be divided in three different sub-units: the Low, Medium and High-TCF. Low/Medium-TCF have a depositional setting in a back-arc setting and High-TCF in the accretionary wedge. The maximum depositional age obtained in this study is between 650-630 Ma. The metamorphism history is more complex, different samples share part of their histories but more in a complementary way. What is clear is that samples record a bimodal pressure regime with Low/Medium-TCF rocks with metamorphism between 6.0-7.0 kbar and High-TCF with pressure regime between 10.0-12.0 kbar. Metamorphic ages also indicate different time-scale processes. All studied samples record metamorphic ages from 620-580 Ma. This anticipates our understanding of the metamorphic events in at least 20 Ma from previous studies. Nevertheless, two samples record an even older metamorphic history, from 640-580 Ma. This period of metamorphism overlaps the sedimentation ages. We interpret this as a corroboration of the proposed tectonic setting of a subduction-to-collision orogeny in a Japan-like microcontinent. A good approach to have a more robust control on the history of the sample would be to apply all those techniques in the same samples. With this, the temporal and tectonic controls would be higher, therefore, lessening over and possible misinterpretation.

We propose the evolution of the TCF along with other units in the Curitiba Terrane as the following:

- 650-630 Ma – Maximum depositional age of TCF sediments marked on detrital zircon (Ricardo et al., 2020);
- 640-620 Ma – First records of metamorphic events associated to subduction of an oceanic crust on the active margin of the Curitiba Microcontinent. This subduction formed a magmatic arc in this microcontinent, the Piên Arc. This

metamorphism produced monazite recorded in two samples from the TCF (DR378, DR298) possibly located in the accretionary wedge;

- 620-570 Ma – Metamorphic events recorded broadly in the TCF, i.e. all samples; somewhere in between this period, the collision with the Luis Alves Microcontinent would occur. Possibly around ~600 Ma where most monazites are recorded. The collision caused metamorphism in the back-arc and accretionary wedge basin and the exhumation of part of the High-TCF rocks;
- 580-570 Ma – Cease of metamorphism in the TCF. All samples stop recording monazite production related to the instauration of the transcurrent shear zones;
- 580 Ma - Intrusion of A-type granites dated on zircon grains by TIMS (Vlach et al., 2011);
- 580 – 530 Ma – Shear zones activation (Faleiros et al., 2011).
- ~540 Ma – Younger monazite grains recorded in some samples. More studies are recommended to address the origin of this process.

DISSERTATION'S REFERENCES

Brito Neves, B.B., Campos Neto, M.C., Fuck, R.A. 1999. From Rodinia to Western Gondwana: an approach to the Brasiliano-Pan African Cycle and orogenic collage. Episodes, 22, 155-166.

Brown, M. 2006. Duality of thermal regimes is the distinctive characteristic of plate tectonics since the Neoarchean. Geology, 34(11), 961-964.

Brown, M., Johnson, T. 2018. Secular change in metamorphism and the onset of global plate tectonics. American Mineralogist, 103(2), 181-196.

Campanha, G. D. C., & Sadowski, G. R. 1999. Tectonics of the southern portion of the Ribeira Belt (Apiaı Domain). Precambrian Research, 98(1-2), 31-51.

Campanha, G. A. C., Faleiros, F. M., Basei, M. A. S., Tassinari, C. C. G., Nutman, A. P., & Vasconcelos, P. M. 2015. Geochemistry and age of mafic rocks from the Votuverava Group, southern Ribeira Belt, Brazil: Evidence for 1490 Ma oceanic back-arc magmatism. Precambrian Research, 266, 530-550.

Cavalcante, C., Lagoeiro, L., Fossen, H., Egydio-Silva, M., Morales, L. F., Ferreira, F., & Conte, T. 2018. Temperature constraints on microfabric patterns in quartzofeldsphatic mylonites, Ribeira belt (SE Brazil). Journal of Structural Geology, 115, 243-262.

Cawood, P. A., Hawkesworth, C. J., & Dhuime, B. 2012. Detrital zircon record and tectonic setting. Geology, 40(10), 875-878.

Cordani, U. G., Delhal, J., & Ledent, D. 1973. Orogenéses superposées dans le

Précambrien du Brésil sud-oriental (États de Rio de Janeiro et de Minas Gerais). Revista Brasileira de Geociências, 3(1), 1-22.

Cutts, K. A., Hand, M., Kelsey, D. E., Wade, B., Strachan, R. A., Clark, C., & Netting, A. 2009. Evidence for 930 Ma metamorphism in the Shetland Islands, Scottish Caledonides: implications for Neoproterozoic tectonics in the Laurentia–Baltica sector of Rodinia. Journal of the Geological Society, 166(6), 1033-1047.

Cutts, K. A., Kinny, P. D., Strachan, R. A., Hand, M., Kelsey, D. E., Emery, M., ... & Leslie, A. G. 2010. Three metamorphic events recorded in a single garnet: Integrated phase modelling, in situ LA-ICPMS and SIMS geochronology from the Moine Supergroup, NW Scotland. Journal of Metamorphic Geology, 28(3), 249-267.

Faleiros, F. M., Campanha, G.A.C., Martins, L., Vlach, S.R.F., Vasconcelos, P.M., 2011. Ediacaran high-pressure collision metamorphism and tectonics of the southern Ribeira Belt (SE Brazil): evidence for terrane accretion and dispersion during Gondwana assembly. Precambrian Research,189, 263–291.

Faleiros, F. M., Pavan, M. 2013. Geologia e Recursos Minerais da Folha Eldorado Paulista-SG-22-XB-XI, Estado de São Paulo (geological mapping in scale: 1: 100.000). CPRM – Geological Survey of Brazil. São Paulo.

Faleiros, F. M., Moraes, R., Pavan, M., Campanha, G. A. C. 2016. A new empirical calibration of the quartz c-axis fabric opening-angle deformation thermometer. Tectonophysics, 671, 173-182.

Guimarães, S. B., dos Reis Neto, J. M., & Siqueira, R. B. 2002. Caracterização dos estromatólitos da Formação Capiru (Proterozóico) nas regiões de Morro Azul e Morro Grande: leste do Paraná. Boletim Paranaense de Geociências, 51, 77-88.

Heilbron, M., Mohriak, W. U., Valeriano, C. M., Milani, E. J., Almeida, J., & Tupinambá, M. 2000. From collision to extension: the roots of the southeastern continental margin of Brazil. Geophysical Monograph-American Geophysical Union, 115, 1-32.

Heilbron, M., Cordani, U. G., & Alkmim, F. F. 2017. The São Francisco craton and its margins. In São Francisco Craton, Eastern Brazil (pp. 3-13). Springer, Cham.

Malta, I. S., Faleiros, F. M., Monteiro, L. V., Andrade, M. B., Coldebella, B., & Esteves, M. C. 2020. PT-fluid-deformation regime of the Ediacaran Serra do Cavalo Magro orogenic gold deposit, Ribeira Belt, Brazil. Ore Geology Reviews, 120, 103384.

Meira, V. T., García-Casco, A., Juliani, C., Almeida, R. P., & Schorscher, J. H. D. 2015. The role of intracontinental deformation in supercontinent assembly: insights from the Ribeira Belt, Southeastern Brazil (Neoproterozoic West Gondwana). Terra Nova, 27(3), 206-217.

Meira, V. T., Garcia-Casco, A., Hyppolito, T., Juliani, C., & Schorscher, J. H. D. 2019. Tectono-metamorphic evolution of the Central Ribeira Belt, Brazil: A case of late Neoproterozoic intracontinental orogeny and flow of partially molten deep crust during the assembly of West Gondwana. Tectonics, 38(8), 3182-3209.

Passarelli, C. R., Basei, M. A. S., Siga, O., Harara, O. M. M. 2018. The Luis Alves and Curitiba Terranes: Continental Fragments in the Adamastor Ocean. In *Geology of Southwest Gondwana* (pp. 189-215). Springer, Cham.

Passarelli, C. R., Verma, S. K., McReath, I., Basei, M. A., & Siga Jr, O. 2019. Tracing the history from Rodinia break-up to the Gondwana amalgamation in the Embu Terrane, southern Ribeira Belt, Brazil. Lithos, 342, 1-17.

Ribeiro, B. V., Faleiros, F. M., Campanha, G. A. C., Lagoeiro, L., Weinberg, R. F., & Hunter, N. J. R. 2019. Kinematics, nature of deformation and tectonic setting of the Taxaquara Shear Zone, a major transpressional zone of the Ribeira Belt (SE Brazil). Tectonophysics, 751, 83-108.

Sato, K., Siga Jr, O., Nutman, A. P., Basei, M. A., McReath, I., Kaulfuss, G. 2003. The Atuba Complex, southern South American Platform: Archean components and paleoproterozoic to neoproterozoic tectonothermal events. Gondwana Research, 6(2), 251-263.

Sato, K., Siga Júnior, O., Silva, J. D., McReath, I., Liu, D., Iizuka, T., Rino, S., Hirata, T., Sproesser, W., Basei, M. A. S. 2009. In situ isotopic analyses of U and Pb in zircon by remotely operated SHRIMP II, and Hf by LA-ICP-MS: an example of dating and genetic evolution of zircon by 176Hf/177Hf from the ItaQuarry in the Atuba Complex, SE Brazil. Geologia USP, Série Cientifica São Paulo, 9, 61-69.

Santos, L. D. R., Leandro, R., Bahniuk, A., & Cury, L. F. 2018. Low-temperature metamorphism in the Capiru Formation, Morro Grande Synform, Southern Ribeira Belt. Brazilian Journal of Geology, 48(1), 95-113.

ANNEX 1 – Extra information

Other samples description

BR07 – Sillimanite Zone from MTCF

Sample BR-07 is composed of a discreate schistosity defined by the orientation of thin-size sub-euhedral muscovite (~10%), chlorite (~10%) and biotite (~20%) grains. Sillimanite (~15%) occurs as clusters mainly aligned to the main schistosity but folded also occurs. Granoblastic grains of quartz (~30%) and plagioclase (~10%) also occur. There is no clear separation of layers with different minerals. Ilmenite (<5%) occurs

distributed along the matrix. Quartz-rich ribbons occur folded. The sample has evidence of shear zones such as SC pairs.

XMg and Al/Si in biotite are regular and varies from 0.44-0.47 and 0.61-0.64, respectively. Chlorite is also regular, the XMg is ~0.53 and the Al/Si is ~0.95. On the other hand, muscovite shows greater ranges in both ratios. The XMg varies from 0.26-0.49 and the Al/Si from 0.84-0.91. The anorthite content varies from 0.20-0.31.

BR18 Sillimanite Zone from MTCF

Sample BR-18 is composed of S2 schistosity poor-developed with mixed layers of lepidoblastic biotite (~25%), muscovite (~20%) and sillimanite (~9%)-rich and quartz (~30%) and plagioclase (~8%) granoblastic layers. Ilmenite (~3%) occurs aligned with S2 schistosity and as inclusions in garnet. Garnet porphyroblasts (~5%) are euhedral and occur 0.6 – 0.8 mm long truncating the S2 schistosity with deformation-shadow. Ilmenite-inclusions in garnet show a trace of a previous S1 schistosity without apparent relation with the external S2 schistosity, indicating that the garnet could have rotated after the S1 development. Staurolite (<2%) is scarce and occur anhedral with corroded rims indicating that it is consumed and not stable.

Compositional maps and chemical profiles show small variation in elements (i.e. not so clear chemical zoning). Nevertheless, it is still possible to see small increase of Xalm (0.68-0.70) and Xprp (0.09-0.10) to rims and Xgrs (0.05-0.06) and Xsps (0.14-0.15) to cores. Chemical core is not evident in this sample. X_{Mg} in biotite varies from 0.36-0.43 and in muscovite from 0.42-0.47. Anorthite content varies in a small range of 0.20-0.23. X_{Mg} in staurolite is constant along the staurolite grains (0.15-0.17).

BR35 Garnet Zone from HTCF

Sample BR-35 is composed of a well-developed S2 schistosity with lepidoblastic layers of biotite (~15%), muscovite (~40%) and chlorite (~12%)-rich and granoblastic layers enriched in quartz (~12%), plagioclase (~8%) and apatite (~5%) granoblastic layers. Ilmenite (~3%) occurs aligned with S2 schistosity and as inclusions in garnet. Garnet porphyroblasts (~5%) are euhedral and occur 1.5 – 2.0 mm long truncating the S2 schistosity with signs of rotation such as deformation-shadow. Ilmenite-inclusions in garnet show a trace of a previous S1 schistosity with no alignment with S2 schistosity, also indicating rotation signs after the S1 development. Biotite grains also have evidence of non-coaxial shear-related deformation such as fish-shape.

Compositional maps show that the geographic and chemical cores do not match, possibly the garnet is cut in its half as half of chemical profile is preserved. They also

show grow-to-rim profiles of Fe and Mg and grow-to-core profiles of Ca and Mn. Y compositional map does not show any zoning to this element. Chemical profiles show Xalm (0.63-0.71) and Xgrs (0.12-0.18)-enrichment with bigger-size garn*et al*so showing high Xsps values (0.09-0.16). Xprp varies between 0.04-0.08. X_{Mg} in biotite (0.43-0.47), muscovite (0.54-0.61) and chlorite (0.45-0.50) show small variance. Anorthite content is between 0.19-0.26.

Detailed Methodology

Laser Ablation Inductively Coupled Mass Spectrometry (LA-ICP-MS)

U-Pb methods

Monazite were located and mapped in BSE using a JEOL JXA-FE-8530 Electron Probe Microanalyser (EPMA) hosted at NAP Geoanalítica, Institute of Geosciences, University of São Paulo, Brazil. In-situ monazite U-Pb analyses were performed in twelve sessions at the University of Portsmouth using a Jena PlasmaQuant Elite ICP-MS coupled to an ASI RESOlution 193 nm ArF excimer Laser system. Trace element analyses in monazite were performed separately in five sessions and an extra session was performed to garnet. Monazite Stern (512 ± 0.7 Ma; Palin et al., 2013), was used as the primary reference material and 44069 (~424.9 Ma; Aleinikoff et al., 2006), Bananeira (507.7 ± 1.3 Ma; Gonçalves et al., 2016), Itambé (506.4 ± 0.7 Ma; Gonçalves et al., 2016), Trebilcock (272 ± 4 Ma, Tomascak et al., 1996) and Vermillion (2653.7 ± 6.8, University of Portsmouth internal reference material) monazite were used as secondary reference materials to monitor reproducibility throughout the analytical period. Two of each reference materials were ablated between every 8 unknowns. Secondary reference material yielded a weighted average of 424.79 ± 1.19 Ma, MSWD=1.06 (44069), 512.85 ± 1.18 Ma, MSWD=1.87 (Bananeira), 513.17 ± 1.36 Ma, MSWD=1.94 (Itambé), 279.02 ± 0.58 Ma, MSWD=1.89 (Trebilcock) and 2673.80 ± 3.11 Ma, MSWD=1.97 (Vermillion), within 2.5% of the reported ages. Laser conditions were 9 µm spot size, laser fluency was ~2.7 J.cm^2 and its repetition rate was 2 Hz. There was a 20 seconds of background measurement, followed by 30 seconds of ablation and 15 seconds of washout for each analysis. Three pulses of pre-ablation using 11 µm spot size were used to clean the area before each analysis. He carrier gas flow was set between 0.300-0.320 L/min and plasma generation was set at 1300 W with 10 L/min of Ar plasma flow, auxiliary gas flow of 1.65 L/min and nebulizer flow between 0.90-0.96 L/min. The following masses were measured and had integration time of 10 ms ^{89}Y, ^{90}Zr, ^{202}Hg, ^{232}Th, ^{235}U, ^{238}U, 20 ms

^{204}Hg, ^{204}Pb, ^{206}Pb, ^{208}Pb and 30 ms ^{207}Pb. Masses 89, 90 and 232 were attenuated in auto mode (meaning every time signal exceeds 10^6 cps attenuation is activated).

Monazite data were processed, corrected for down-hole fractionation and instrumental drift using the Iolite 3.4 software (Paton et al., 2011). Data was presented using IsoplotR (Vermeesch, 2018). Uncertainties include instrumental drift and were increased in quadrature to include 2.0% reproducibility of the secondary reference material. A table compiling the reproducibility of each sample can be found in the main LA-ICP-MS data spreadsheet also in the supplementary material.

Stern (primary)

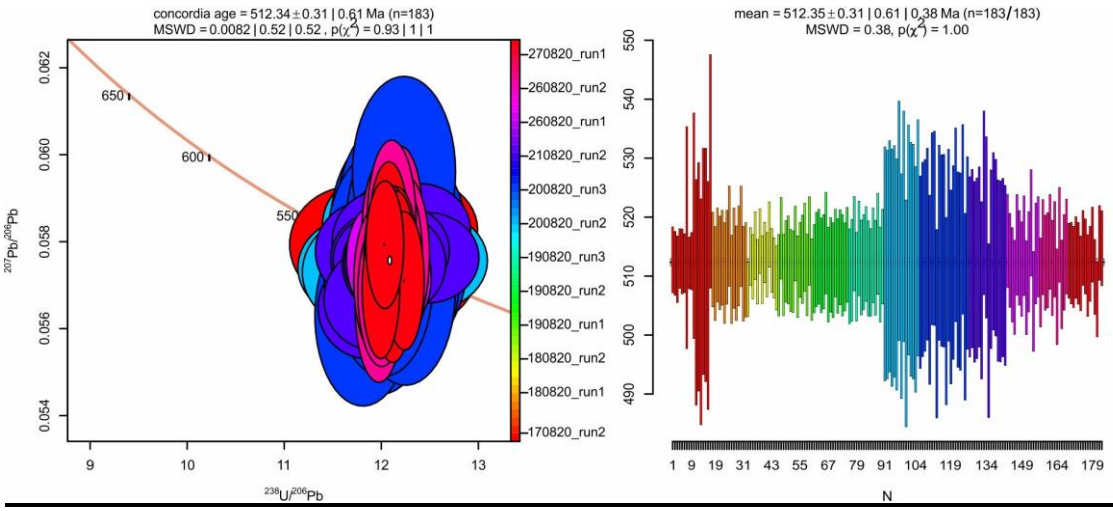

Trebilcock reproducibility

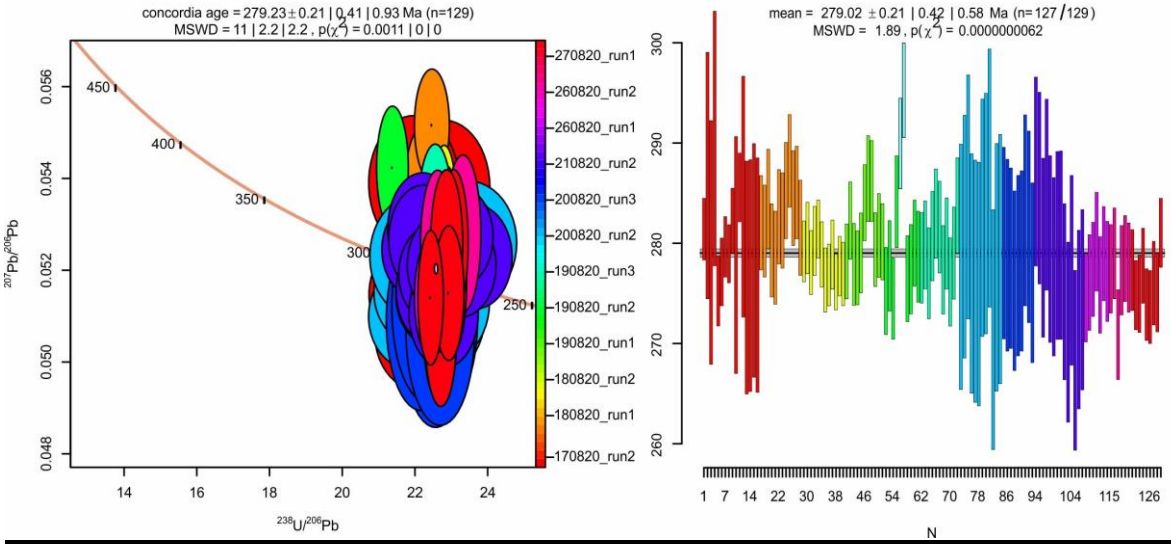

Bananeira reproducibility

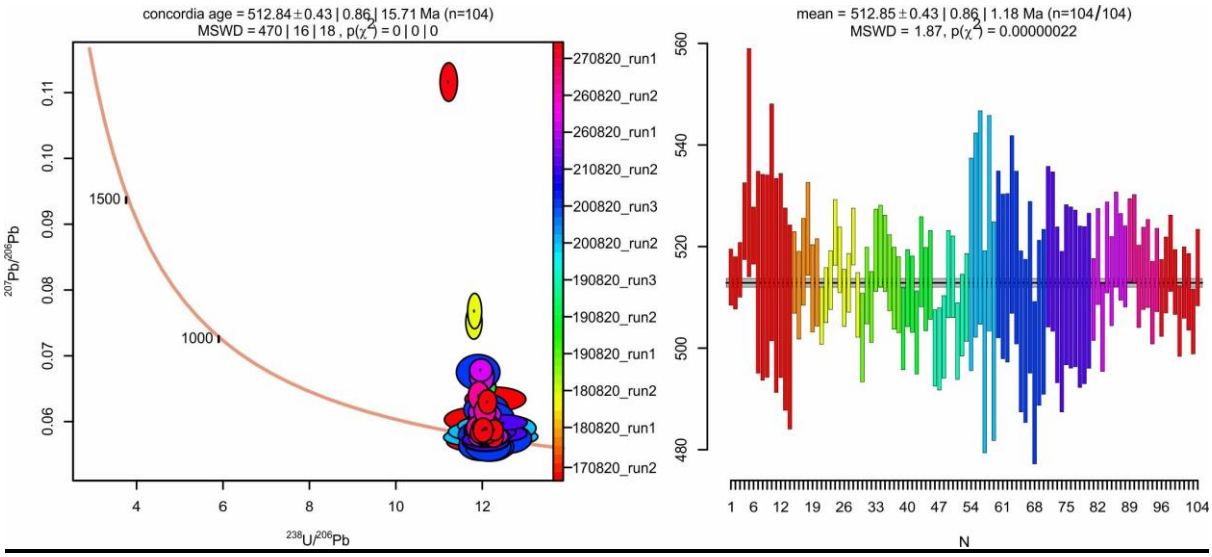

44069 reproducibility

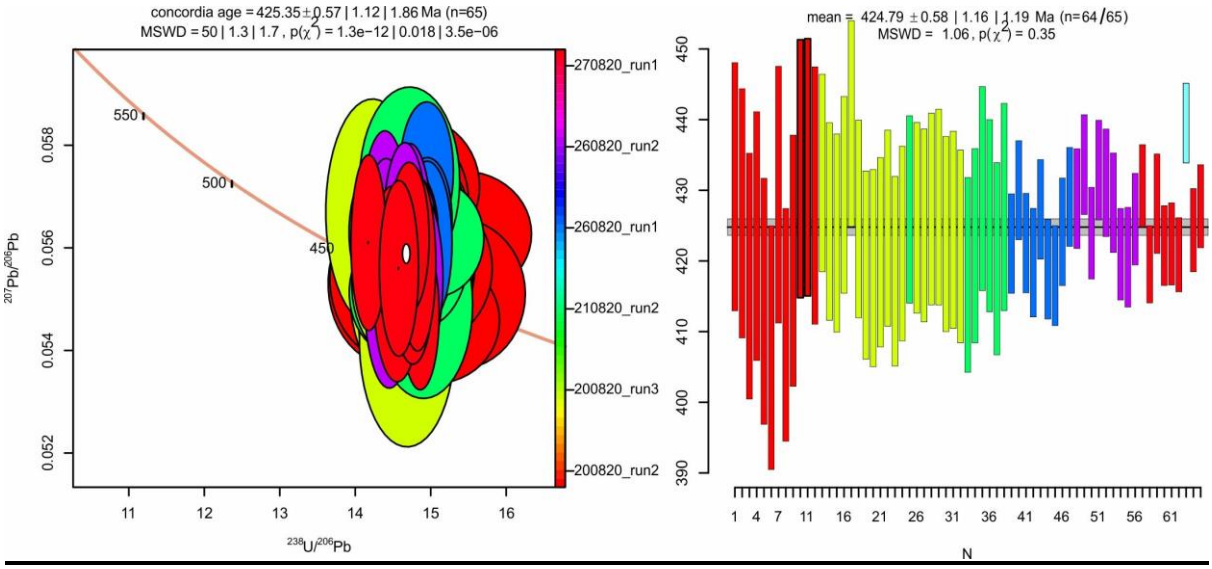

Vermillion reproducibility

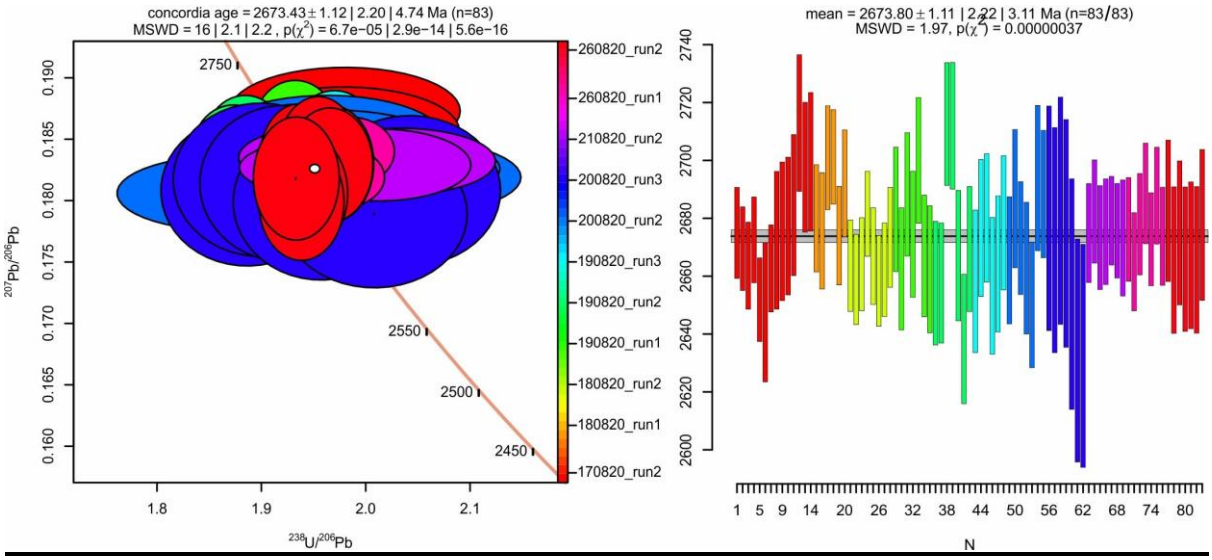

Itambe reproducibility

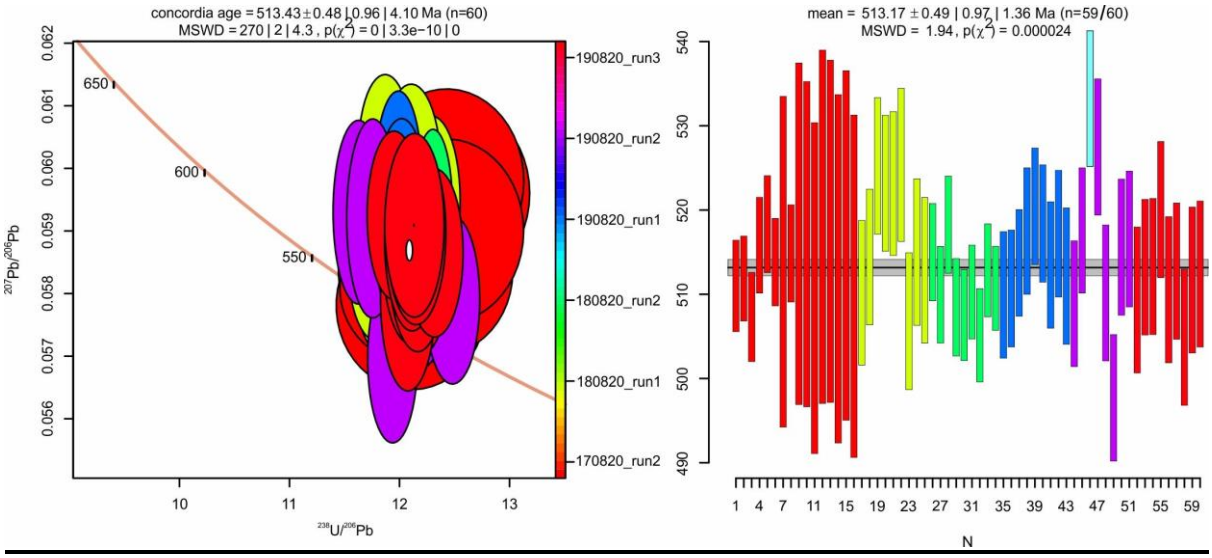

Trace element methods - monazite

In-situ monazite trace element analyses were performed in six sessions (five in monazite and one in garnet) at the University of Portsmouth, UK using a Jena PlasmaQuant Elite ICP-MS coupled to an ASI RESOlution 193 nm ArF excimer Laser system. NIST610 glass was used as the primary reference material. BHVO-2G, BCR and Trebilcock monazite were used as secondary reference material. BHVO-2G gave an average reproducibility of 9.56%, Trebilcock an average reproducibility of 3.08% and BCR an average reproducibility of 3.47%. Laser conditions for monazite were 11 µm spot size, laser fluency was ~3 J.cm^2 and its repetition rate was 3 Hz. 20 seconds of background measurement was followed by 30 seconds of ablation and 15 seconds of washout for each analysis. Three pulses of pre-ablation using 13 µm spot size were used

to clean the area before each analysis. He carrier gas flow was set between 0.30-0.32 L/min and plasma generation was set at 1300 W with 10 L/min of Ar plasma flow, auxiliary gas flow of 1.65 L/min and nebulizer flow between 0.90 - 0.97 L/min. The following masses were measured and had integration time of 10 ms: ^{43}Ca, ^{88}Sr, ^{89}Y, ^{90}Zr, ^{93}Nb ^{139}La, ^{140}Ce, ^{141}Pr, ^{146}Nd, ^{147}Sm, ^{153}Eu, ^{157}Gd, ^{159}Tb, ^{163}Dy, ^{165}Ho, ^{166}Er, ^{169}Tm, ^{172}Yb, ^{175}Lu, ^{178}Hf, ^{208}Pb, ^{232}Th, ^{238}U. All masses were attenuated in auto mode. Monazite data were processed, corrected for down-hole fractionation and instrumental drift using the Iolite 3.4 software (Paton et al., 2011). 25.5 wt% Ce was used as an internal standard for unknowns. Data was presented using Isoplot 4.1 (Ludwig, 2003). Individual REE are normalised to chondrite values of McDonough and Sun, 1995. Uncertainties include instrumental drift.

BHVO reproducibility in monazite

	La	Pr	Nd	Sm	Eu	Gd	Tb	Dy	Ho	Er	Tm	Yb	Lu
Average (ppm)	16.32	5.09	24.74	6.11	2.20	3.69	0.87	5.19	0.98	2.31	0.31	1.86	0.27
Reference value (ppm)	15.20	5.35	24.50	6.10	2.07	6.16	0.92	5.28	0.98	2.56	0.34	2.01	0.28
Reproducibility (%)	6.83	5.03	0.95	0.13	5.92	66.81	5.79	1.66	0.33	10.79	9.10	7.92	3.02

Average reproducibility= **9.56%**

Ref value: GeoReM

Trebilcock reproducibility

	La	Pr	Nd	Sm	Eu	Gd	Tb	Dy	Ho	Er	Tm	Yb	Lu
Average (ppm)	71387	24174	101667	3626	190	23662	2814	9280	851	1163	101	415	33
Reference value (ppm)	70050	24450	96300	35400	-	23500	3350	8500	-	1150	-	-	-
Reproducibility (%)	2	1	5	2	-	1	19	8	-	1	-	-	-

Average reproducibility= **3.08%**

Ref value: Pyle et al., 2002

BCR reproducibility

	La	Pr	Nd	Sm	Eu	Gd	Tb	Dy	Ho	Er	Tm	Yb	Lu

Average (ppm)	26.74	6.57	29.31	6.66	2.09	6.05	1.02	6.32	1.29	3.52	0.49	3.34	0.50
Reference value (ppm)	64.7	6.7	1.02	6.59	1.97	6.71	1.02	6.44	1.27	3.7	0.51	3.39	0.50
Reproducibility (%)	7.62	2.00	1.41	1.08	5.84	10.97	0.31	1.96	1.55	5.10	4.39	1.59	1.23
Average reproducibility= **3.47%**													
Ref value: GeoReMh													

Trace element methods - garnet

NIST612 glass was used as the primary reference material. BHVO-2G and NIST614 glass were used as secondary reference material. BHVO-2G gave an average reproducibility of 7.84%, and NIST614 an average reproducibility of 2.25%. Laser conditions for garnet were 50 µm spot size, laser fluency was ~4.7 J.cm^2 and its repetition rate was 6 Hz. 20 seconds of background measurement was followed by 30 seconds of ablation and 15 seconds of washout for each analysis. Three pulses of pre-ablation using 13 µm spot size were used to clean the area before each analysis. He carrier gas flow was set at 0.31 L/min and plasma generation was set at 1300 W with 10 L/min of Ar plasma flow, auxiliary gas flow of 1.65 L/min and nebulizer flow at 0.94 L/min. The following masses were measured and had integration time of 10 ms: ^{49}Ti, ^{43}Ca, ^{52}Ca, ^{88}Sr, ^{89}Y, ^{90}Zr, ^{93}Nb ^{139}La, ^{140}Ce, ^{141}Pr, ^{146}Nd,^{147}Pm, ^{147}Sm, ^{153}Eu, ^{157}Gd, ^{159}Tb, ^{163}Dy, ^{165}Ho, ^{166}Er, ^{169}Tm, ^{172}Yb, ^{175}Lu, ^{178}Hf, ^{208}Pb, ^{232}Th, ^{238}U. All masses were attenuated in auto mode. Garnet data were processed, corrected for down-hole fractionation and instrumental drift using the Iolite 3.4 software (Paton et al., 2011). Individual REE are normalised to chondrite values of McDonough and Sun, 1995. Uncertainties include instrumental drift.

BHVO reproducibility in garnet

	Sr	Y	Zr	Nb	La	Ce	Pr	Nd	Sm	Eu	Gd	Tb	Dy	Ho	Er	Tm	Yb	Lu	Hf	pb	Th	U
Average (ppm)	375.21	22.48	151.76	17.53	14.53	37.28	4.99	23.56	5.82	1.94	5.58	0.82	4.93	0.91	2.33	0.31	1.87	0.26	3.91	1.84	1.15	0.43
Reference value (ppm)	396	26	170	18.30	15.20	37.60	5.35	24.50	6.10	2.07	6.16	0.92	5.28	0.98	2.56	0.34	2.01	0.28	4.32	1.70	1.22	0.40
Reproducibility (%)	5.54	15.67	12.02	4.37	4.58	0.87	7.27	4.00	4.85	6.85	10.36	12.69	7.19	8.23	9.78	9.83	7.71	8.88	10.50	7.66	6.54	7.04

Average reproducibility= **7.84%**

Ref value: GeoReM

NIST614 reproducibility

	Sr	Y	Zr	Nb	La	Ce	Pr	Nd	Sm	Eu	Gd	Tb	Dy	Ho	Er	Tm	Yb	Lu	Hf	pb	Th	U
Average (ppm)	46.04	0.78	0.88	0.84	0.71	0.79	0.75	0.75	0.78	0.75	0.74	0.72	0.76	0.75	0.75	0.75	0.77	0.73	0.69	2.63	0.76	0.84
Reference value (ppm)	45.80	0.79	0.85	0.82	0.72	0.81	0.77	0.75	0.75	0.77	0.76	0.74	0.75	0.75	0.74	0.73	0.78	0.73	0.71	2.32	0.75	0.82
Reproducibility (%)	0.53	0.78	3.25	1.54	1.81	3.47	2.37	0.03	3.08	2.30	2.84	2.15	1.60	0.54	1.81	2.48	0.77	0.17	2.77	11.70	1.41	2.19

Average reproducibility= **2.25%**

Ref value: GeoReM

Laser map conditions

Trace element maps were collected in four sessions (two in monazite and two in garnet) at the University of Portsmouth, UK using a Jena PlasmaQuant Elite ICP-MS coupled to an ASI RESOlution 193 nm ArF excimer Laser system. NIST610 glass was used as the primary reference material. BHVO-2G was used as secondary reference material. Laser conditions for monazite were 5 μm spot size, laser fluency was ~3 J.cm^2 and its repetition rate was 20 Hz, sample translation speed was 2.5 μm/s. 20 seconds of background measurement was followed by ablation of each line with different lengths

per sample and 15 seconds of washout for each analysis. One pulse of pre-ablation using 7 µm spot size was used to clean the area before each analysis with 80% overlapping. Laser conditions for garnet were 30, 30, 40, 50 µm spot size for samples DR378, DR298, DR352 and 129, respectively. Laser fluency was ~4.5 J.cm^2, its repetition rate was 10 Hz (DR378, DR298) and 20 Hz (DR352, 129) and the sample translation speed was 5 µm/s (DR378, DR298) and 20 µm/s (DR352, 129). 20 seconds of background measurement was followed by ablation of each line with different lengths per sample and 15 seconds of washout for each analysis. One pulse of pre-ablation using 35, 35, 45, 90 µm spot size was used to clean the area before each analysis with 80% overlapping. Only on run 2808_run1 of mapping sessions the 4th delay was 5 seconds, on others it was 20 seconds. He carrier gas flow was set as 0.32 L/min and plasma generation was set at 1300 W with 10 L/min of Ar plasma flow, auxiliary gas flow of 1.65 L/min and nebulizer flow 0.97 L/min. The following masses were measured and had integration time of 10 ms: ^{26}Mg, ^{43}Ca, ^{49}Ti, ^{52}Cr, ^{55}Mn, ^{57}Fe, ^{88}Sr, ^{89}Y, ^{90}Zr, ^{93}Nb ^{139}La, ^{140}Ce, ^{141}Pr, ^{146}Nd, ^{147}Sm, ^{149}Sm, ^{153}Eu, ^{157}Gd, ^{159}Tb, ^{163}Dy, ^{165}Ho, ^{166}Er, ^{169}Tm, ^{172}Yb, ^{175}Lu, ^{178}Hf, ^{208}Pb, ^{232}Th, ^{238}U. ^{26}Mg, ^{43}Ca, ^{49}Ti, ^{52}Cr, ^{55}Mn, ^{57}Fe and ^{232}Th masses were attenuated in auto mode. Monazite and garnet data were processed, corrected for down-hole fractionation and instrumental drift using the Iolite 3.4 software (Paton et al., 2011). Maps were produced using the CellSpace Monacle plugin for Iolite. Uncertainties include instrumental drift.

Table 1: Monazite Petrochronology and Garnet Trace Elements details

Laboratory & Sample Preparation	
Laboratory name	University of Portsmouth (LA-ICP-MS)
Sample type/mineral	Metasediments/Monazite and garnet
Sample preparation	In thin section

Imaging	EPMA compositional maps and BSE maps and some images (University of São Paulo) BSE images (University of Portsmouth)
Laser ablation system	
Make, Model & type	ASI RESOlution 193 nm ArF excimer Laser system
Ablation cell & volume	Large format, dual volume cell
Laser wavelength (nm)	193
Pulse width (ns)	5-8 ns
Fluence ($J.cm^{-2}$)	**U-Pb** 2.7 $J.cm^{-2}$/ **TE - mnz** 3 $J.cm^{-2}$/ **TE - gnt** 4.5 $J.cm^{-2}$
Repetition rate (Hz)	**U-Pb** 2 Hz/ **TE - mnz** 3 Hz/ **TE - gnt** 6 Hz
Spot size (um)	**U-Pb** 9 µm/ **TE - mnz** 11 µm/ **TE - gnt** 50 µm
Sampling depth	**8** µm
Sampling mode / pattern	Spot, with pre-ablation cleaning spot 15 µm U-Pb/ 20 µm TE - mnz/ 90 µm TE - gnt
Carrier gas	100% He (0.30-0.32 l $min^{-1)}$, Ar make-up gas (0.92 l min^{-1}) combined 50% along sample line in mixing bulb.

Ablation duration (secs)	30 secs, 15 s washout, 20 s background between pulses
Cell carrier gas flow (l/min)	0.30-0.32 l/min
ICP-MS Instrument	
Make, Model & type	Jena PlasmaQuant Elite ICP-MS
Carrier gas flow rate	0.30-0.32 l min^{-1} He and 0.92 l min^{-1} Ar
Auxilary gas flow rate	1.65 l min^{-1} Ar
RF power (W)	1300 W
Detection system	3 MHz quadrupole
Masses measured	**U-Pb:** ^{89}Y, ^{90}Zr, ^{202}Hg, ^{232}Th, ^{235}U, ^{238}U, ^{204}Hg, ^{204}Pb, ^{206}Pb, ^{208}Pb, ^{207}Pb **Trace elements - mnz:** ^{43}Ca, ^{88}Sr, ^{89}Y, ^{90}Zr, ^{93}Nb ^{139}La, ^{140}Ce, ^{141}Pr, ^{146}Nd, ^{147}Sm, ^{153}Eu, ^{157}Gd, ^{159}Tb, ^{163}Dy, ^{165}Ho, ^{166}Er, ^{169}Tm, ^{172}Yb, ^{175}Lu, ^{178}Hf, ^{208}Pb, ^{232}Th, ^{238}U **Trace elements - gnt:** ^{49}Ti, ^{43}Ca, ^{52}Ca, ^{88}Sr, ^{89}Y, ^{90}Zr, ^{93}Nb ^{139}La, ^{140}Ce, ^{141}Pr, ^{146}Nd,^{147}Pm, ^{147}Sm, ^{153}Eu, ^{157}Gd, ^{159}Tb, ^{163}Dy, ^{165}Ho, ^{166}Er, ^{169}Tm, ^{172}Yb, ^{175}Lu, ^{178}Hf, ^{208}Pb, ^{232}Th, ^{238}U
Integration time per peak (ms)	10-30 ms
Data Processing	

Gas blank	20 second on-peak zero subtracted
Reference Material info	**U-Pb:** Monazite Stern (512 ± 0.7 Ma; *Palin et al., 2013*), was used as the primary reference material and 44069 (~424.9 Ma; Aleinikoff et al., 2006), Bananeira (507.7±1.3 Ma; Gonçalves et al., 2016), Itambé (506.4±0.7 Ma; Gonçalves et al., 2016), Trebilcock (272 ± 4 Ma, Tomascak et al., 1996), and Vermillion (2653.7 ± 6.8, *University of Portsmouth internal RM*), were used as secondary reference materials. **Trace elements - mnz:** NIST 610 Glass was used as the primary reference material for trace elements (Ce). BHVO-2G, BCR and Trebilcock (Pyle et al., 2002) were used as secondary reference materials. **Trace elements - gnt:** NIST 612 Glass was used as the primary reference material for trace elements (Ce). BHVO-2G and NIST 614 were used as secondary reference materials.
Data processing package used / Correction for LIEF	Iolite version 3.4 (Paton et al., 2011) was used to correct measured isotopic ratios for baselines, time-dependent laser-induced inter-element fractionation, plasma induced fractionation and instrument drift.
Common-Pb correction, composition and uncertainty	U-Th-Pb ages are reported.No common Pb correction was applied
Uncertainty level & propagation	Propagated uncertainties quoted at 2σ absolute were added in quadrature to all final ages to account for the reproducibility of the secondary RM for each analytical period
Elements Mapping	
Spot size	**Mnz** - 5 µm; **Gnt 129** - 80 µm **DR298** - 30 µm; **DR352** - 40 µm **DR378** - 30 µm

Sample transition speed	**Mnz** - 2.5 µm/s; **Gnt 129** - 20 µm/s **DR298** - 5 µm/s; **DR352** - 20 µm/s **DR378** - 5 µm/s
Pre-ablation cleaning	**1 pulse, 80% overlapping** **Mnz** - 7 µm; **Gnt 129** - 90 µm **DR298** - 35 µm; **DR352** - 45 µm **DR378** - 35 µm
Laser repetition rate	**Mnz** - 20 Hz; **Gnt 129** - 20 Hz **DR298** - 10 Hz; **DR352** - 20 Hz **DR378** - 10 Hz
Fluency	**Mnz** - 3 J/cm^2; **Gnt** 4.5 J/cm^2

ANNEX 2 - Supplementary Material from CHAPTER 3.

Supplementary Material

Sample BR07

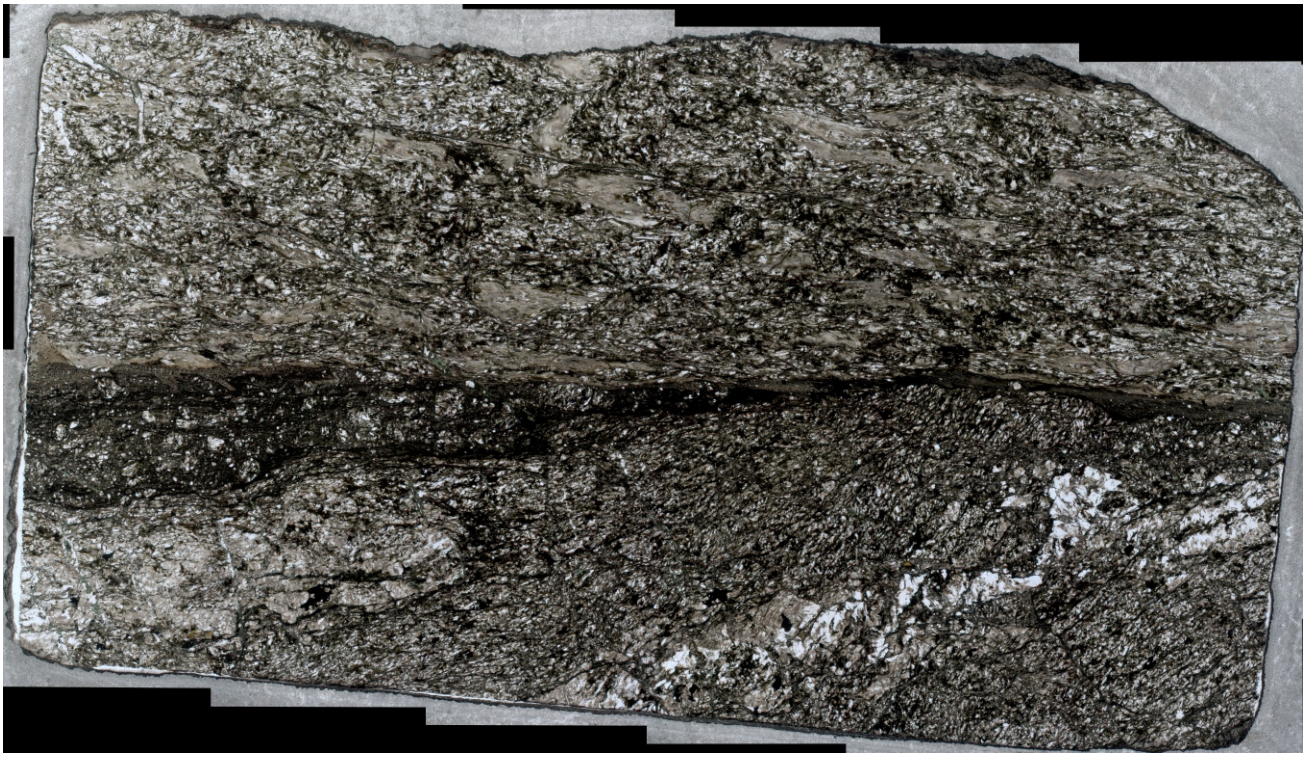

Supplementary Material

Sample BR18

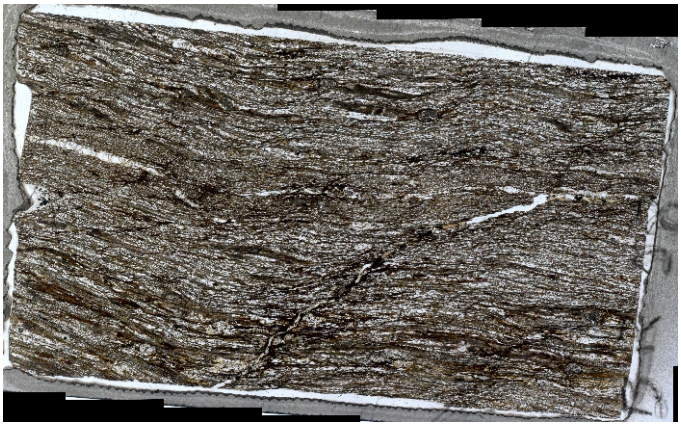

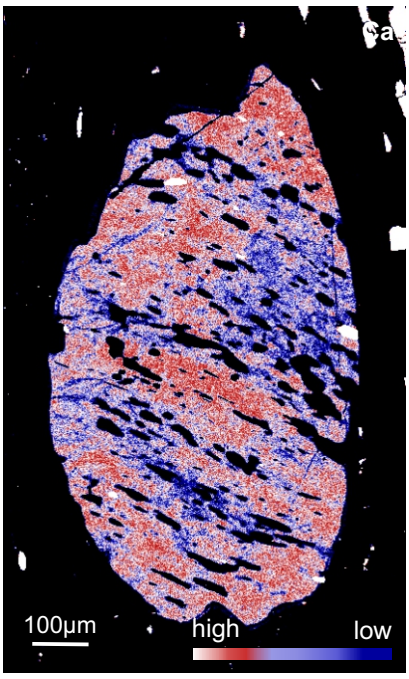

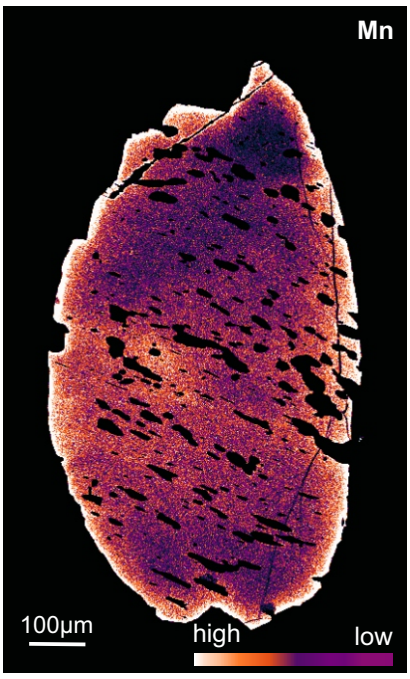

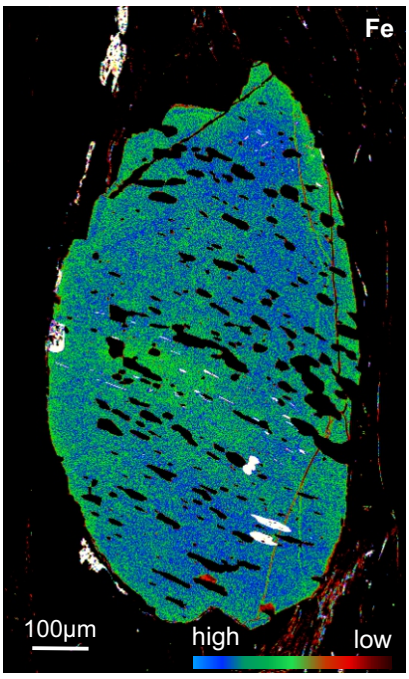

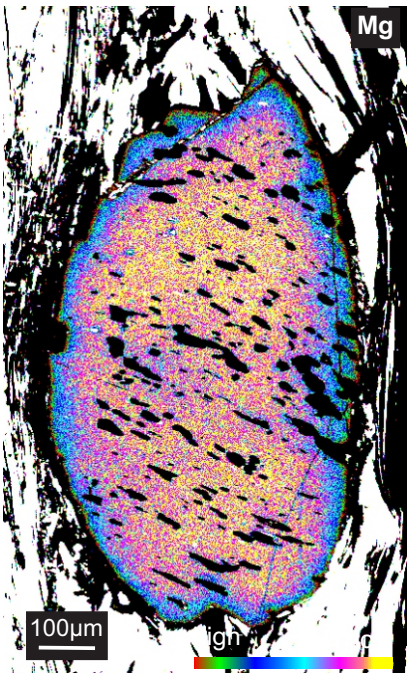

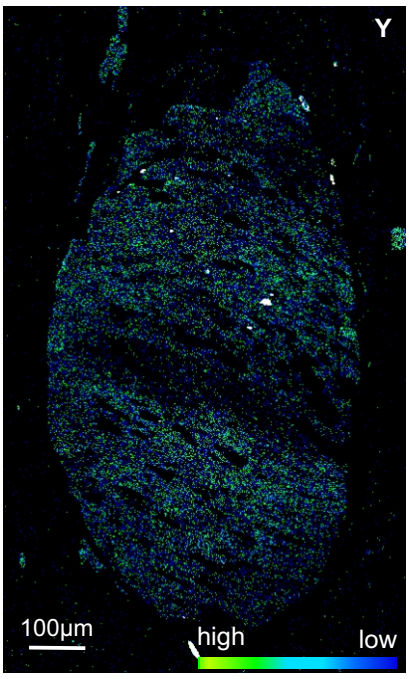

Ricardo et al.(2021)

Supplementary Material

Sample BR18

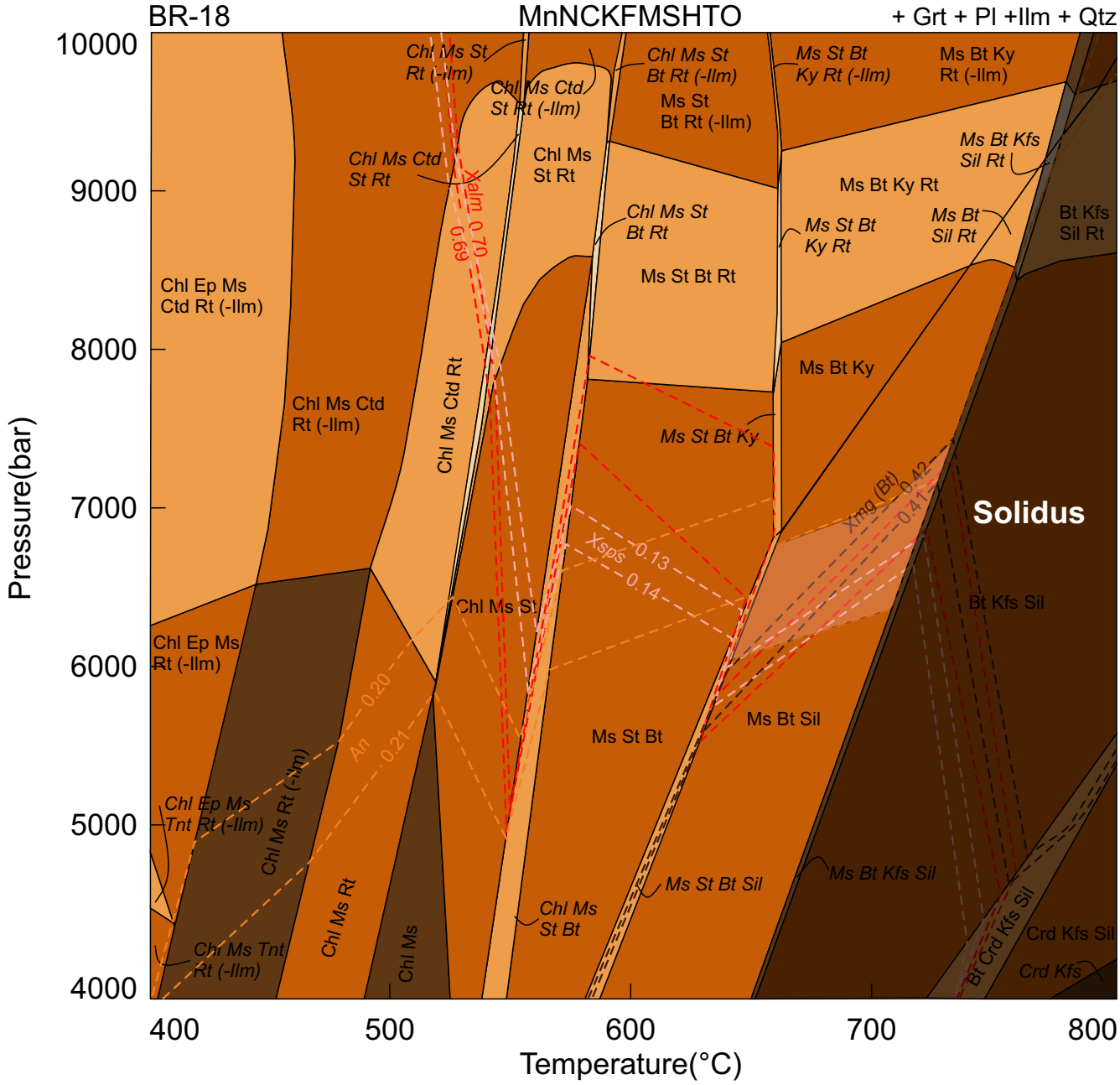

Ricardo et al.(2021)

Supplementary Material

Sample BR35

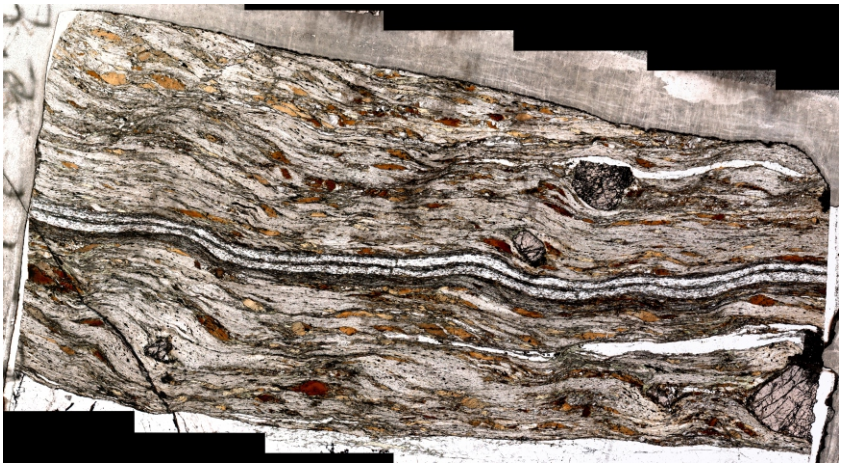

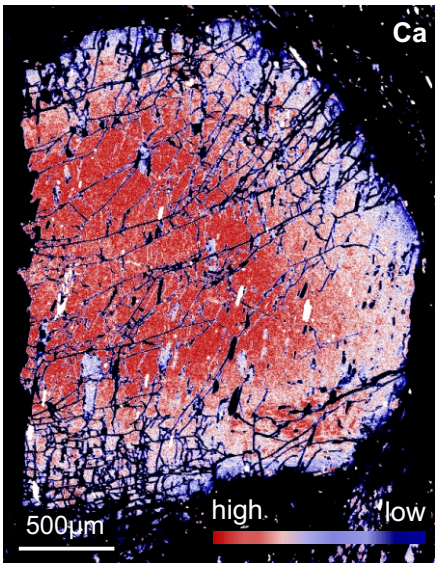

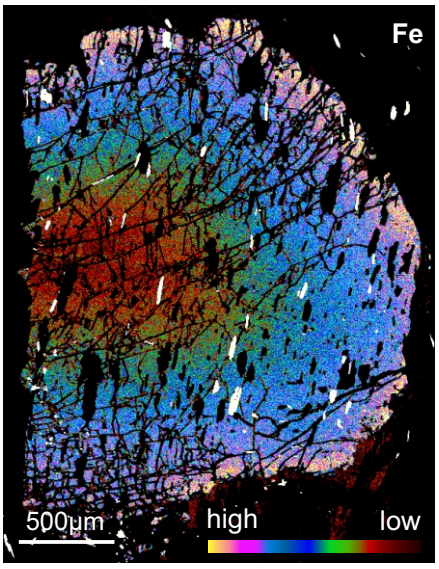

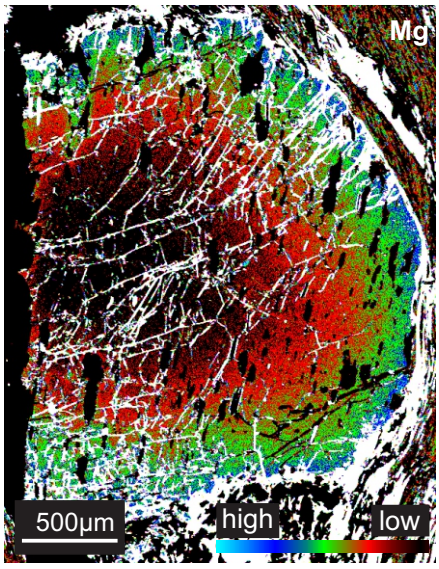

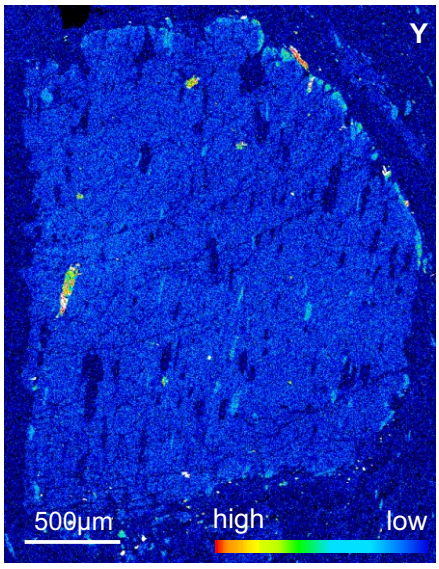

Ricardo et al.(2021)

Supplementary Material

Sample BR35

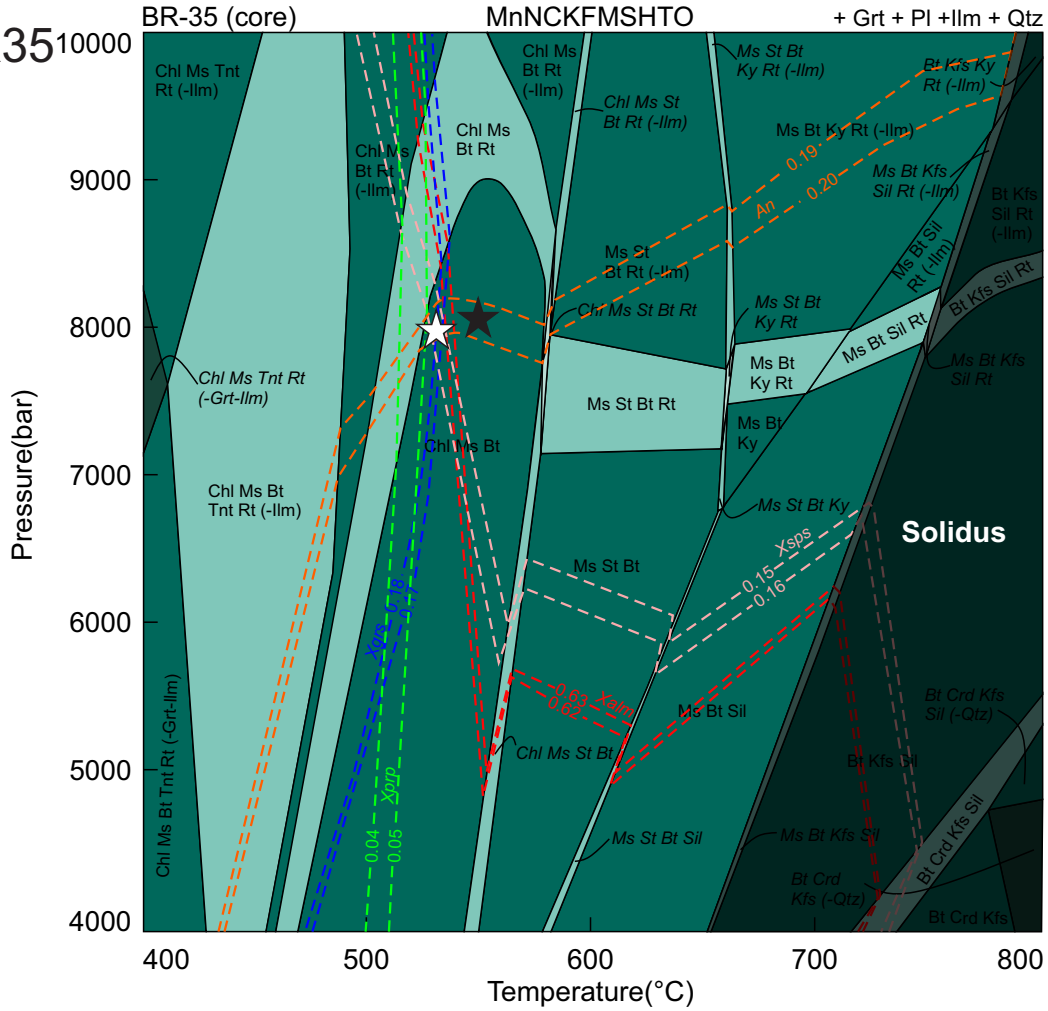

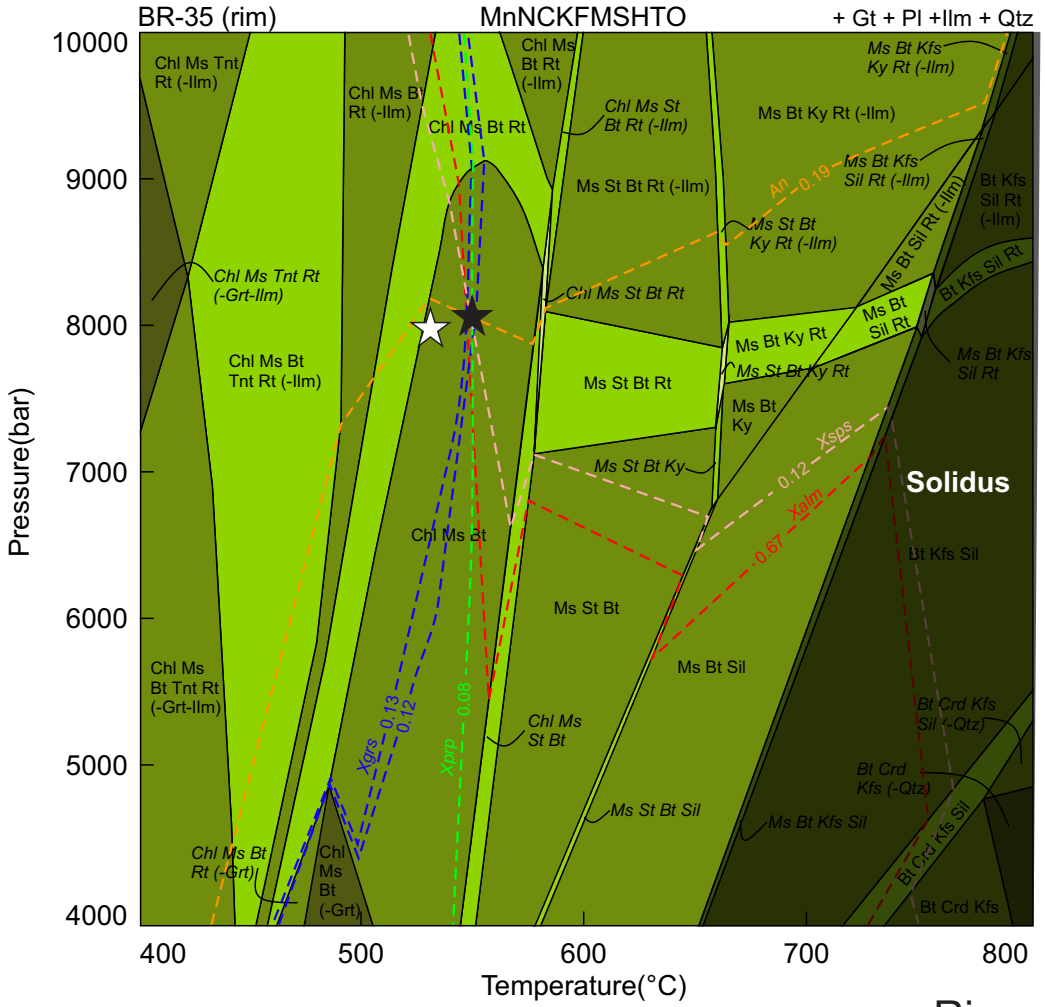

Ricardo et al.(2021)

Supplementary Material

Sample DR378

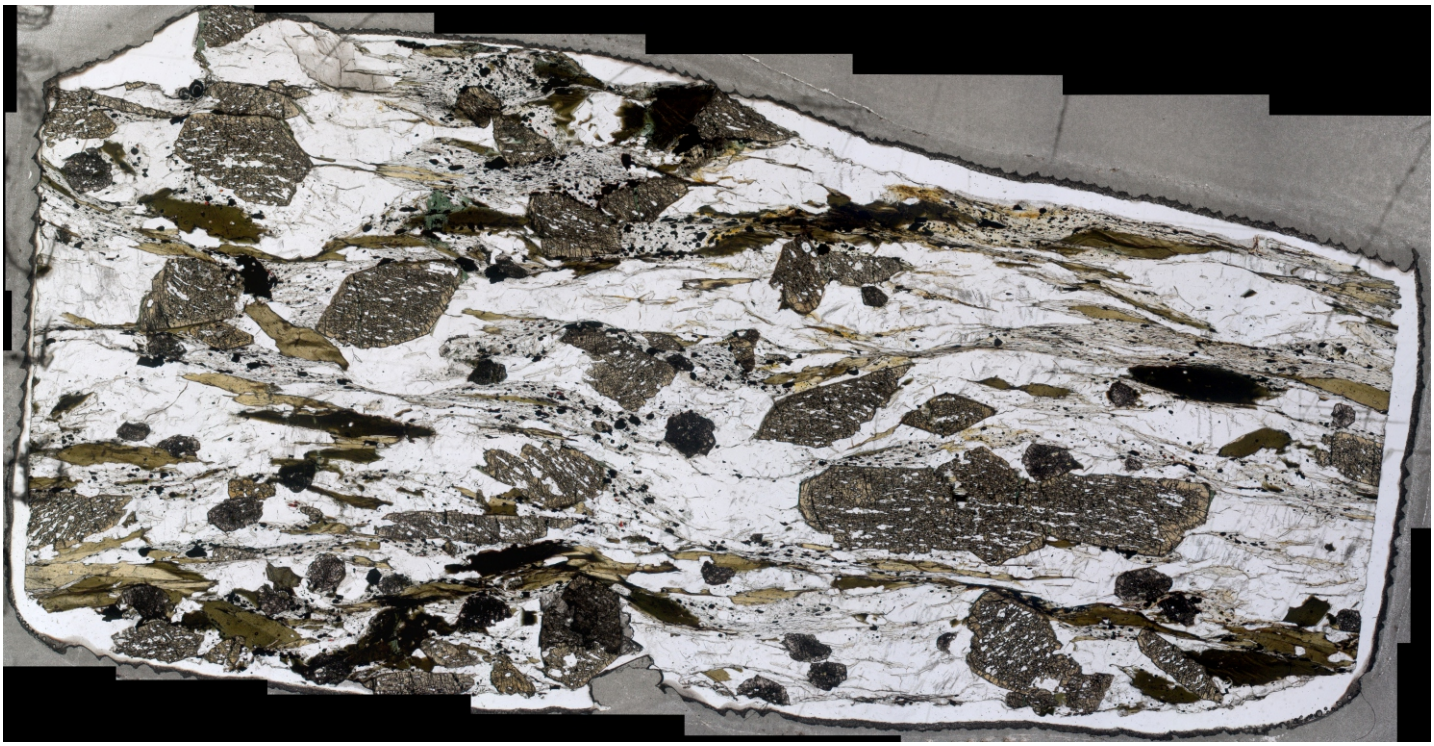

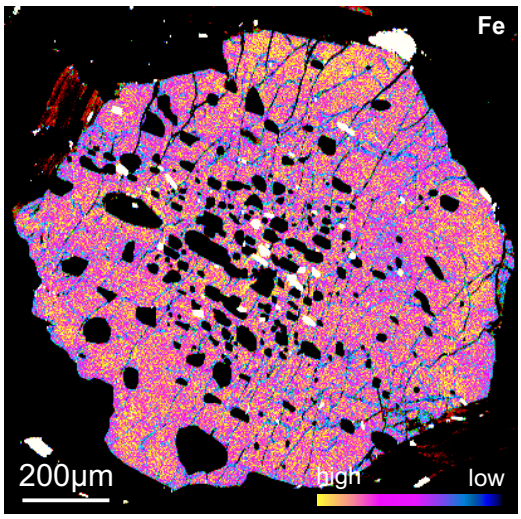

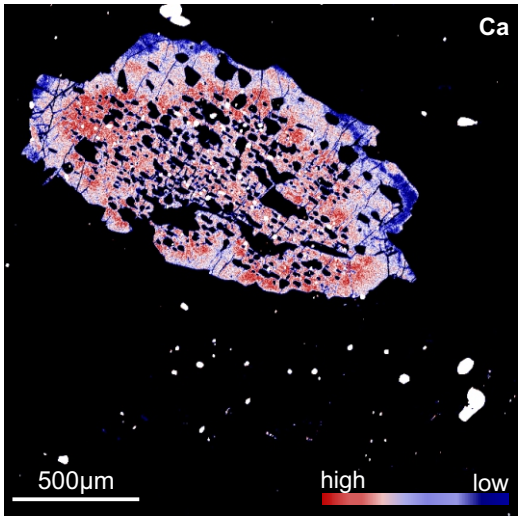

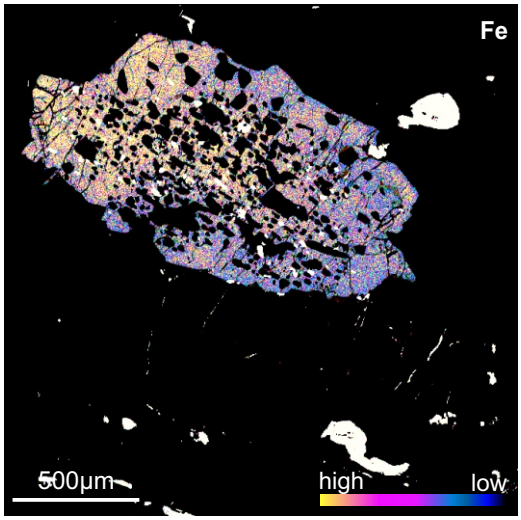

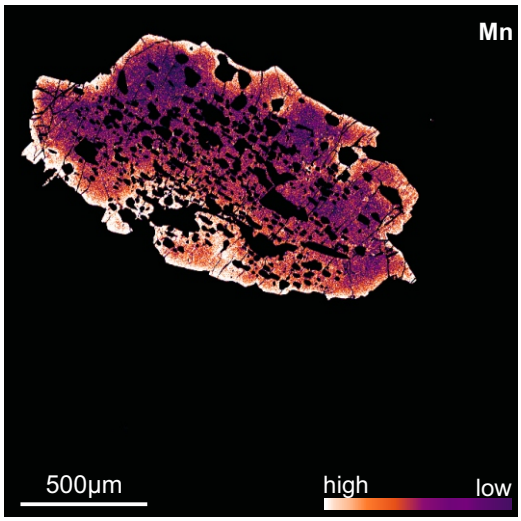

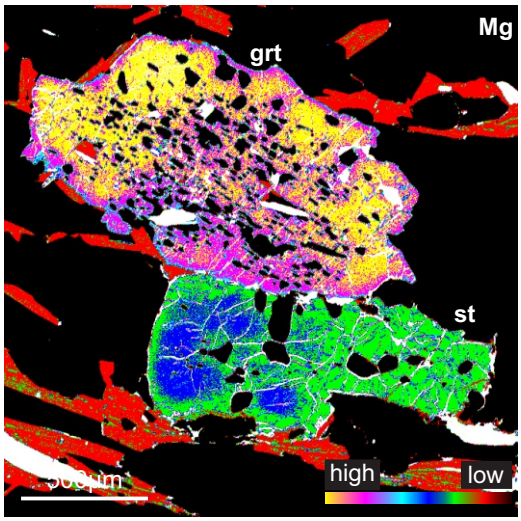

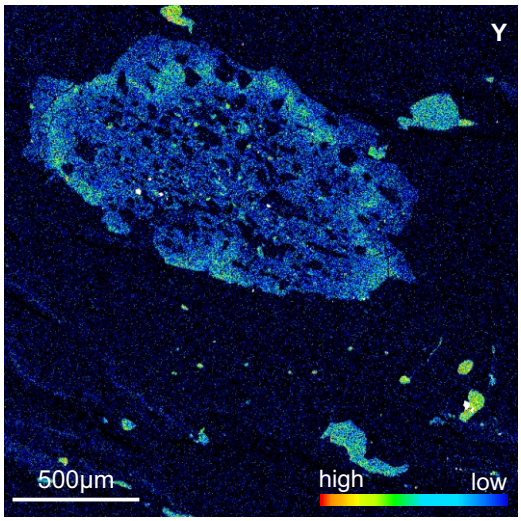

Ricardo et al.(2021)

Supplementary Material

Sample DR378

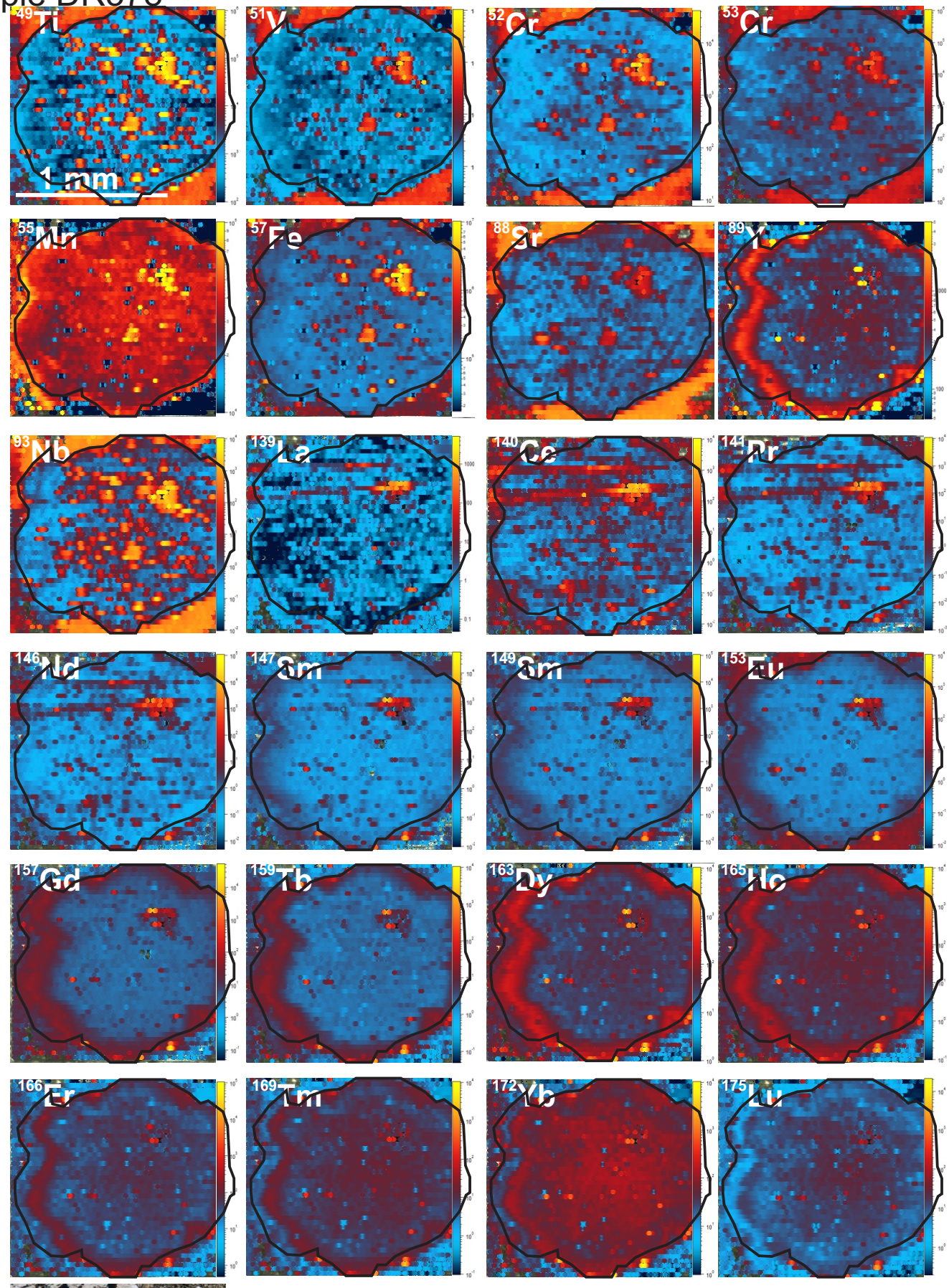

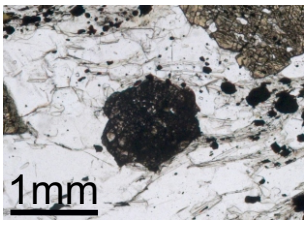

Ricardo et al.(2021)

Supplementary Material

Sample DR352

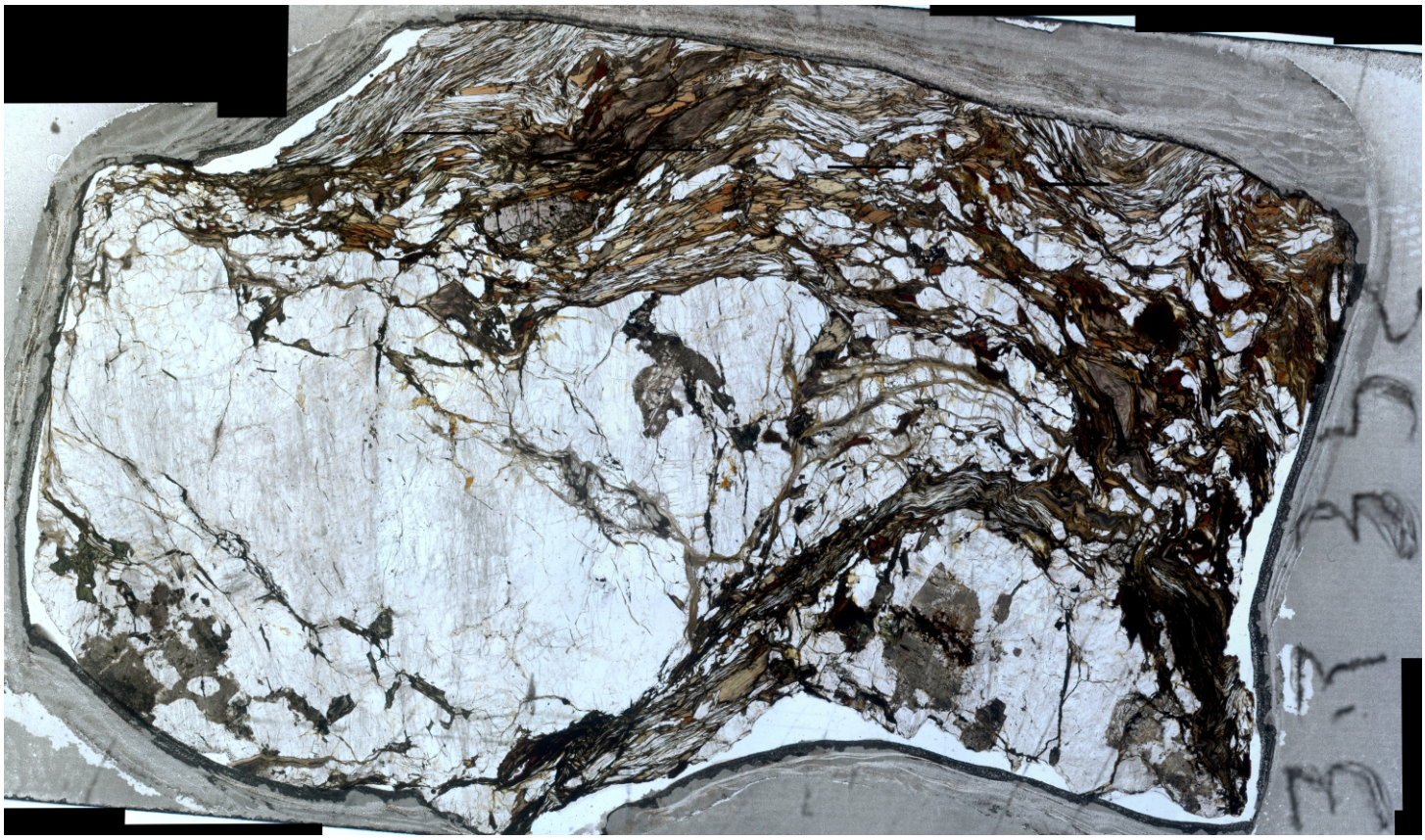

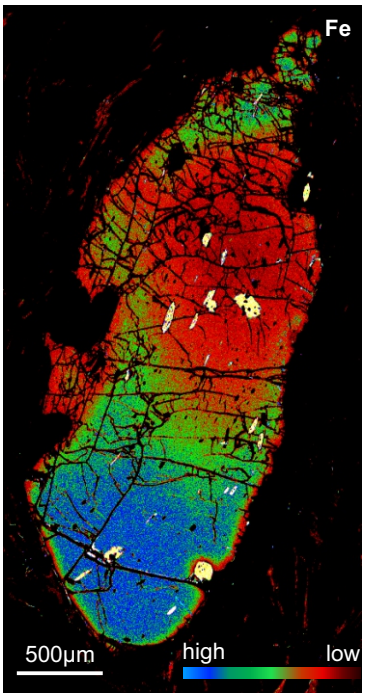

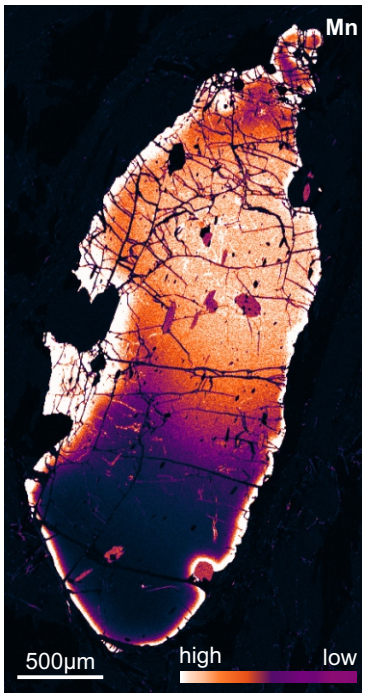

Ricardo et al.(2021)

Supplementary Material

Sample DR352

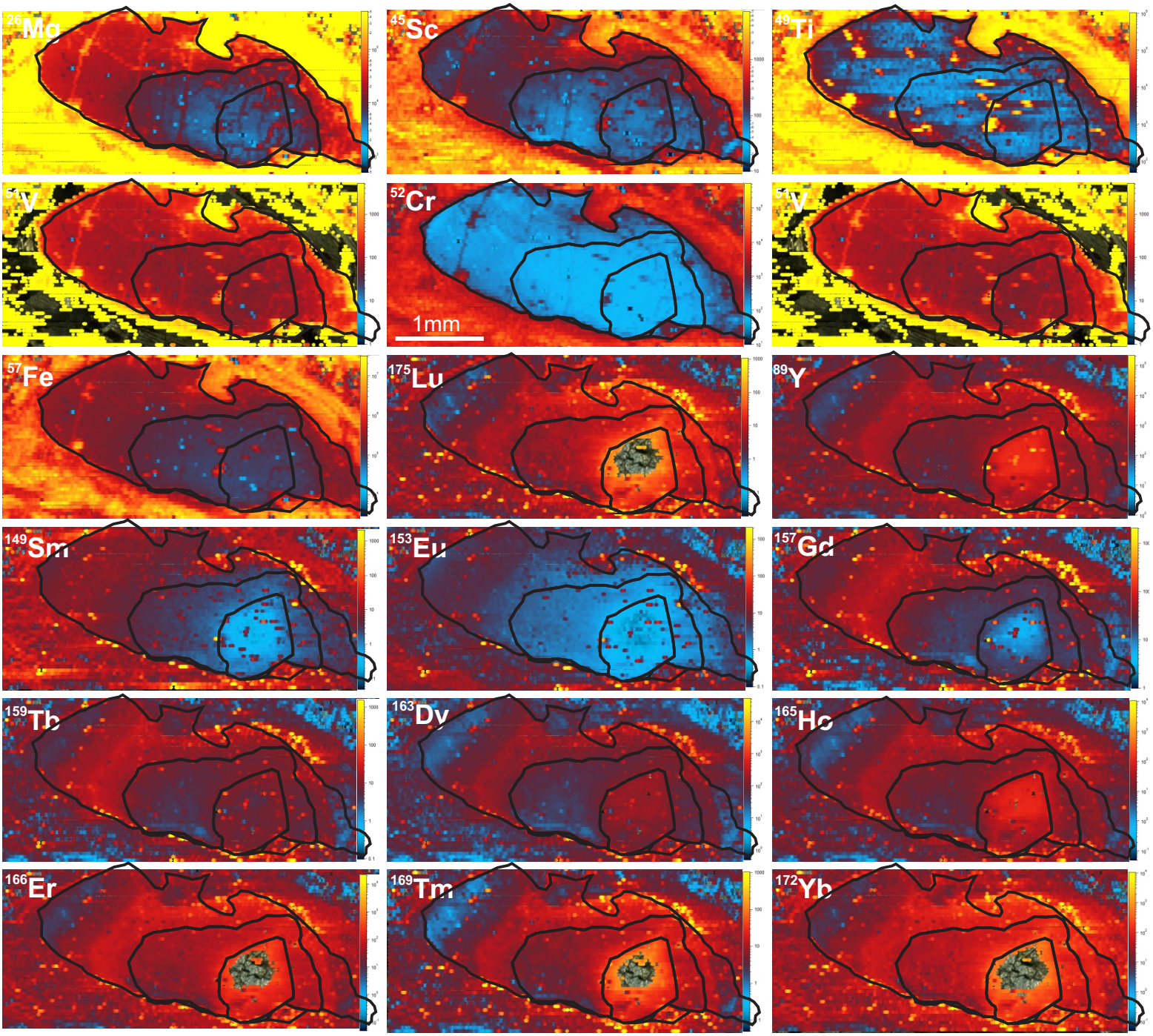

Ricardo et al.(2021)

Supplementary Material

Sample DR298

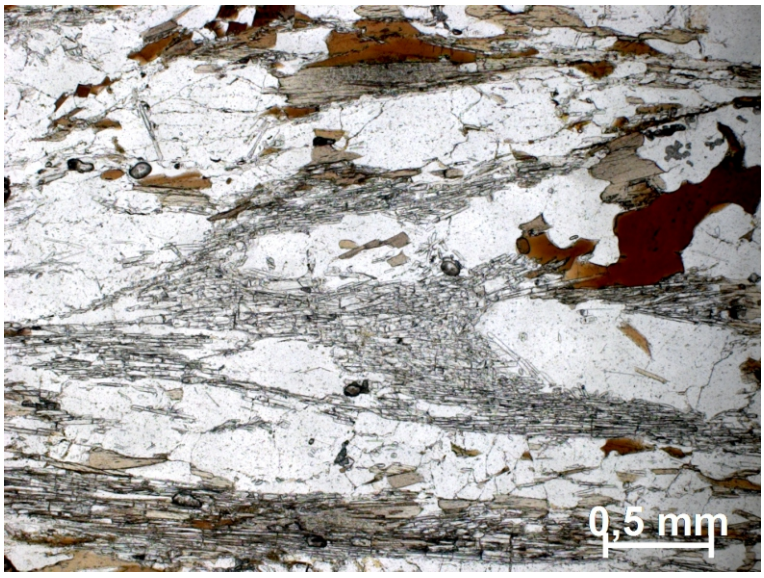

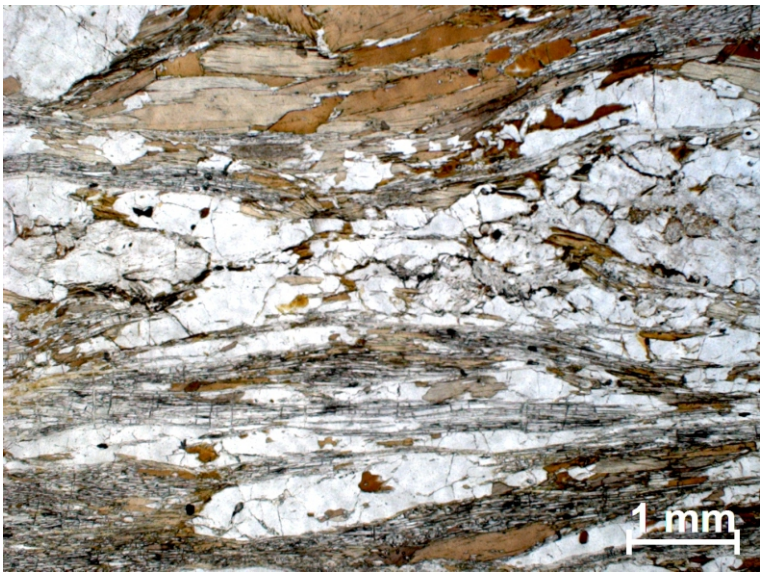

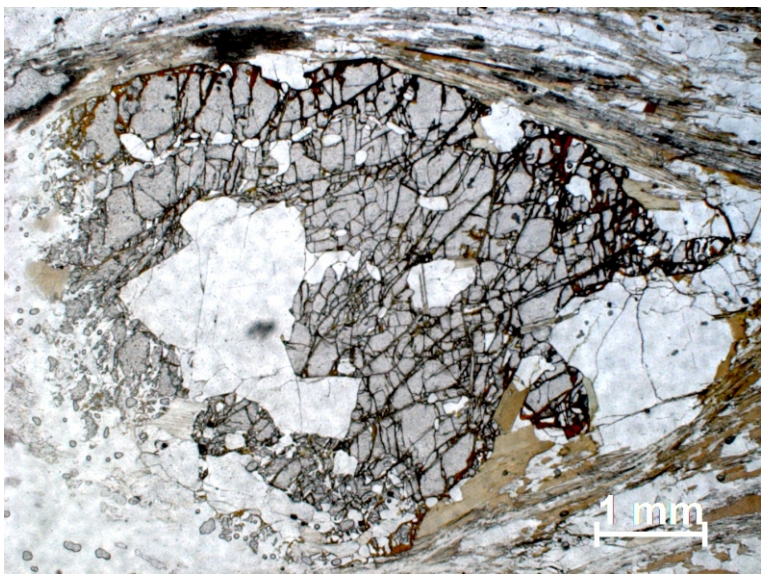

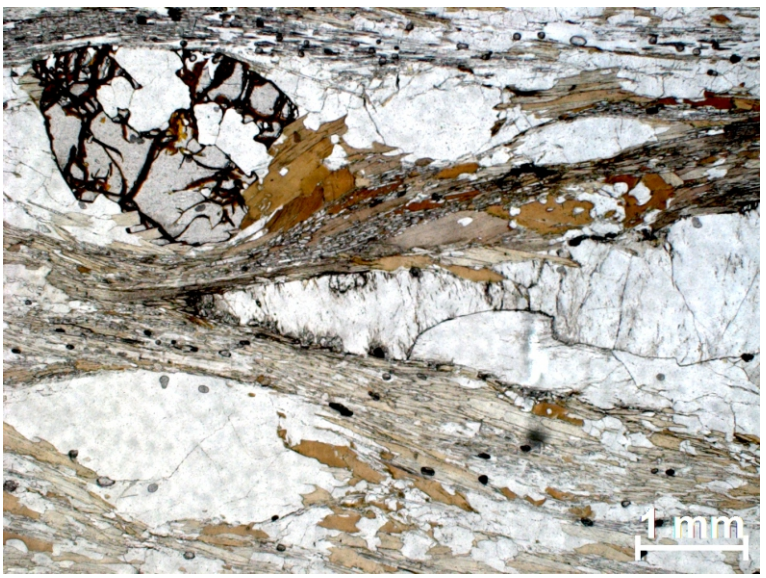

Ricardo et al.(2021)

Supplementary Material

Sample DR298

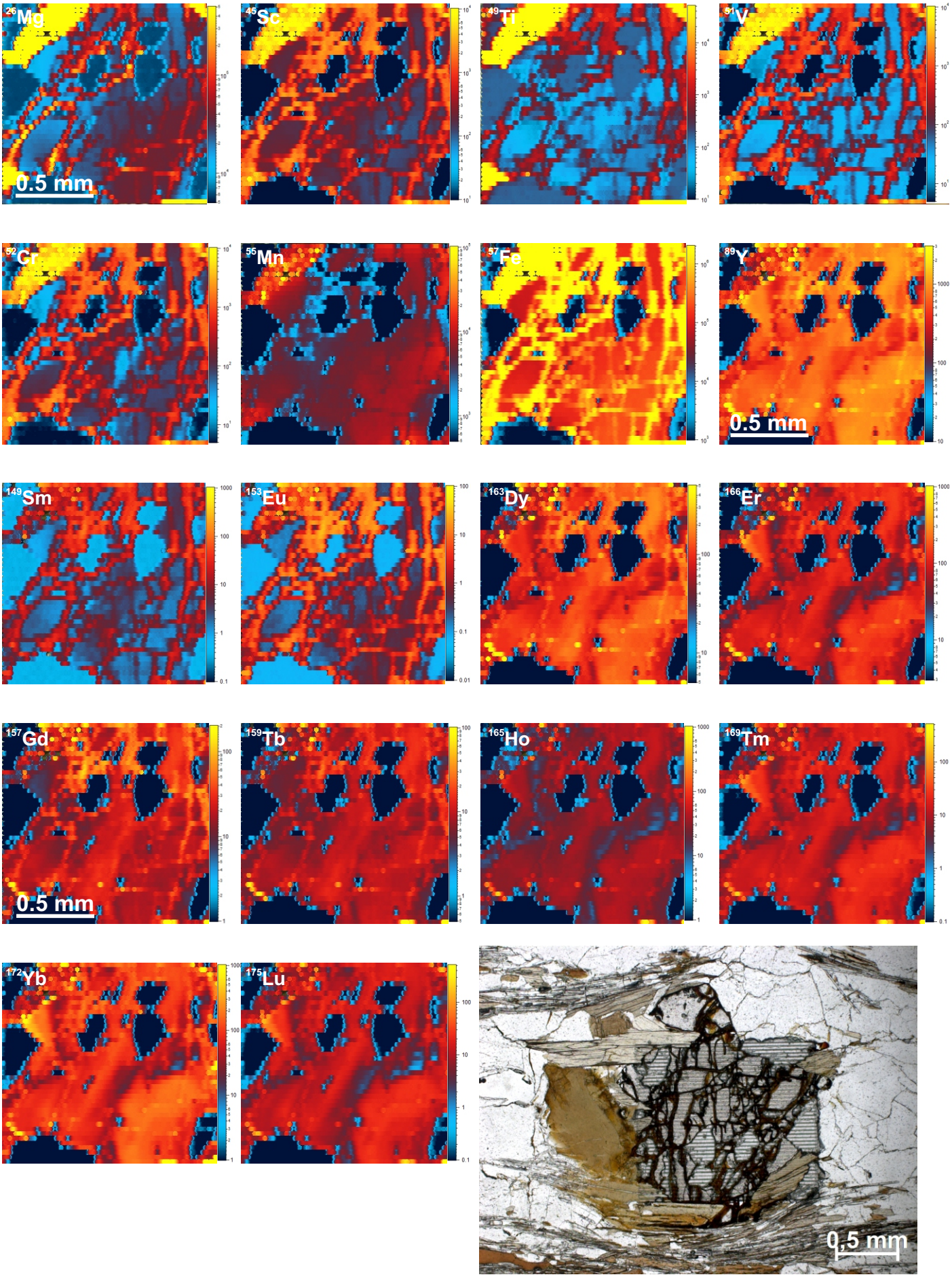

Ricardo et al.(2021)

Supplementary Material

Sample 129

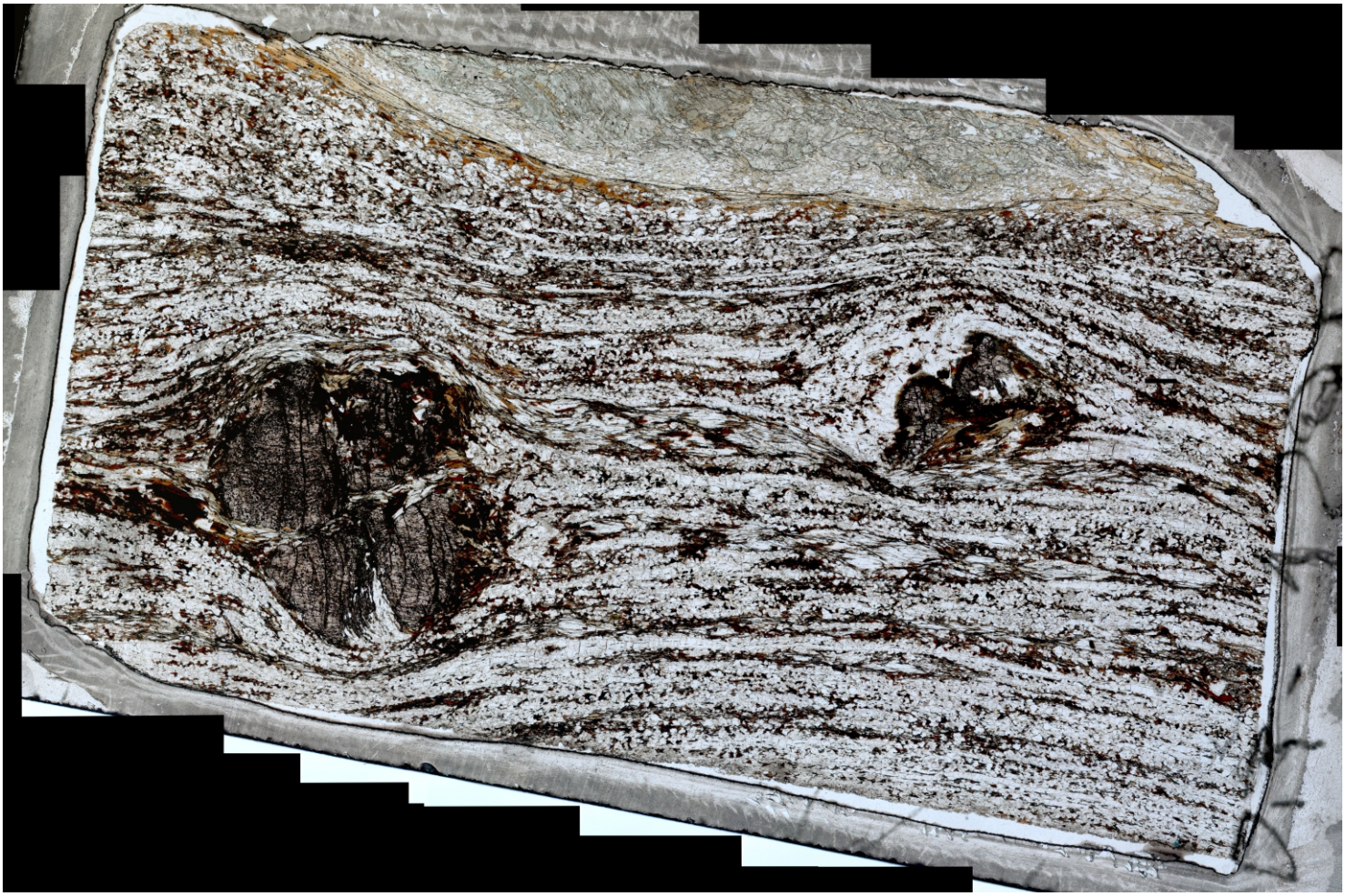

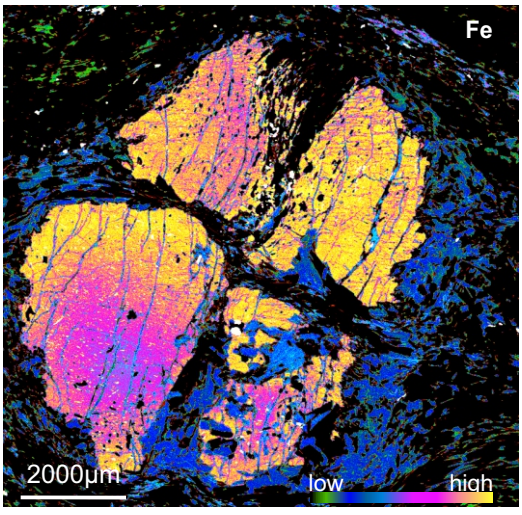

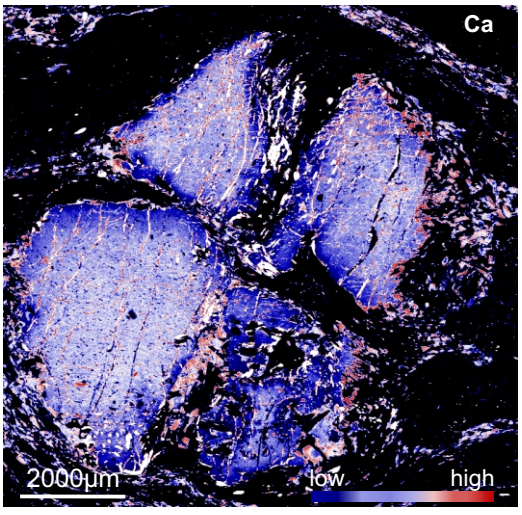

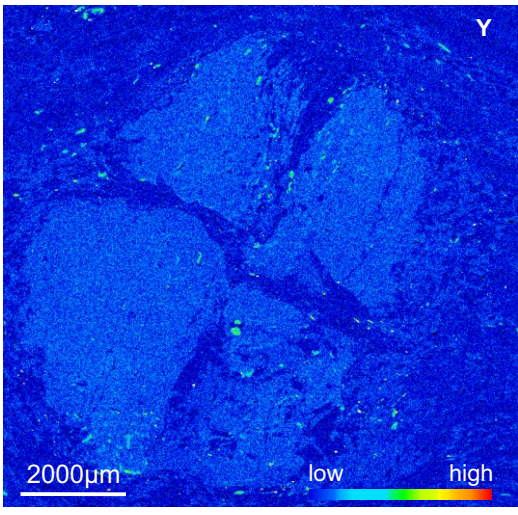

Ricardo et al.(2021)

Supplementary Material

Sample 129

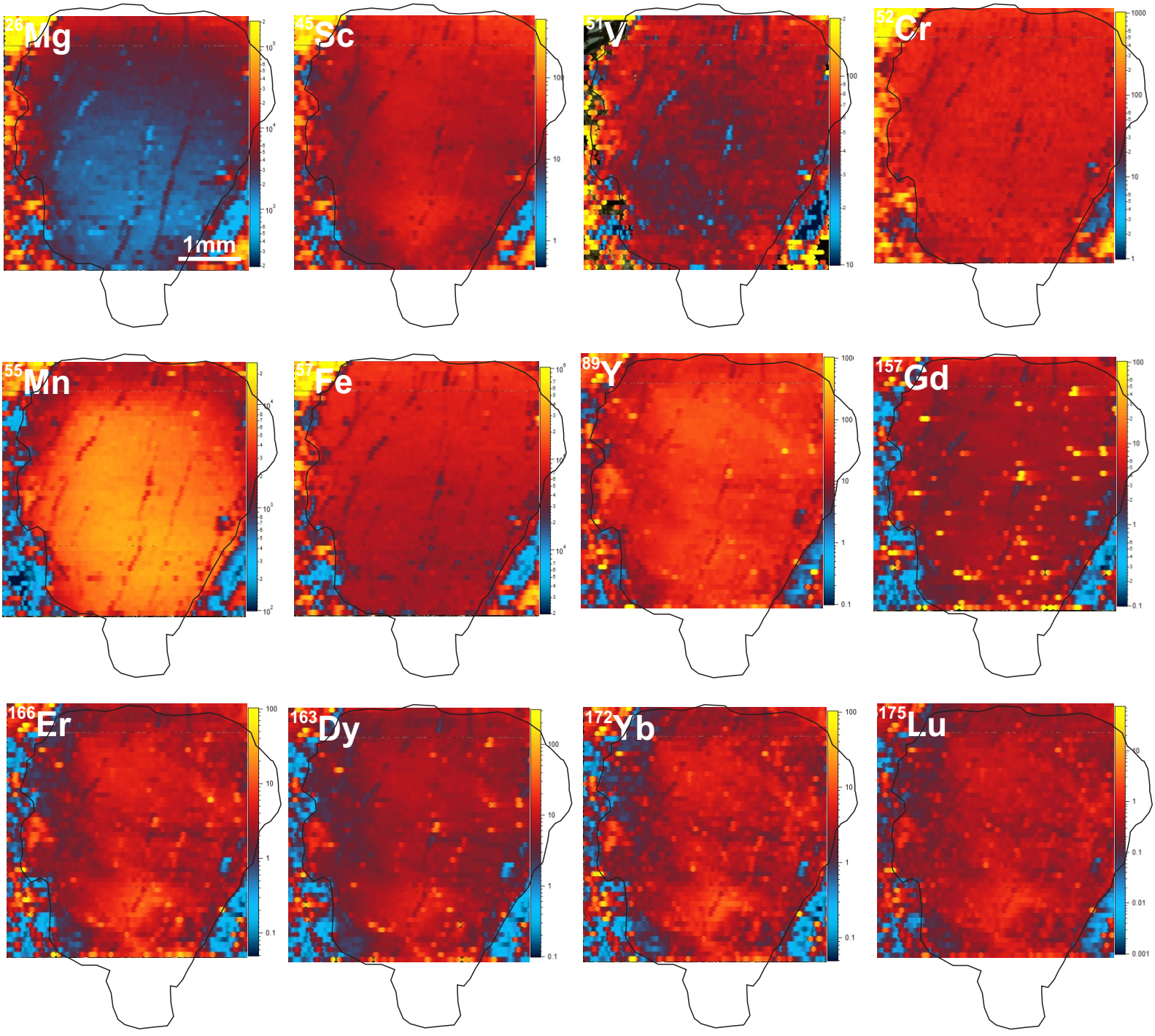

Supplementary Material

Sample DR378

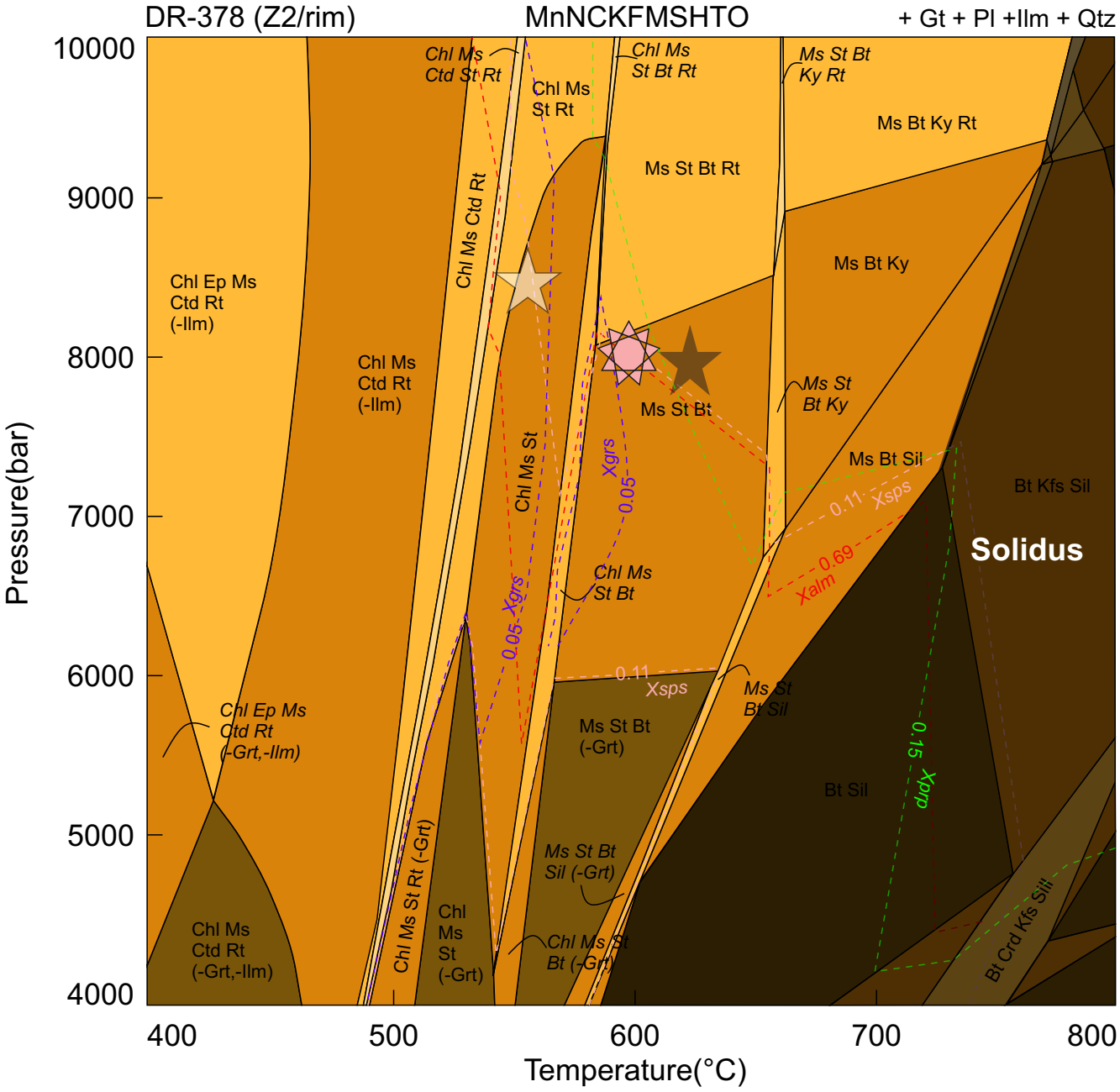

Ricardo et al.(2021)

Supplementary Material

Sample Dr378 - %ilm isopleth modeled with composition from Z2

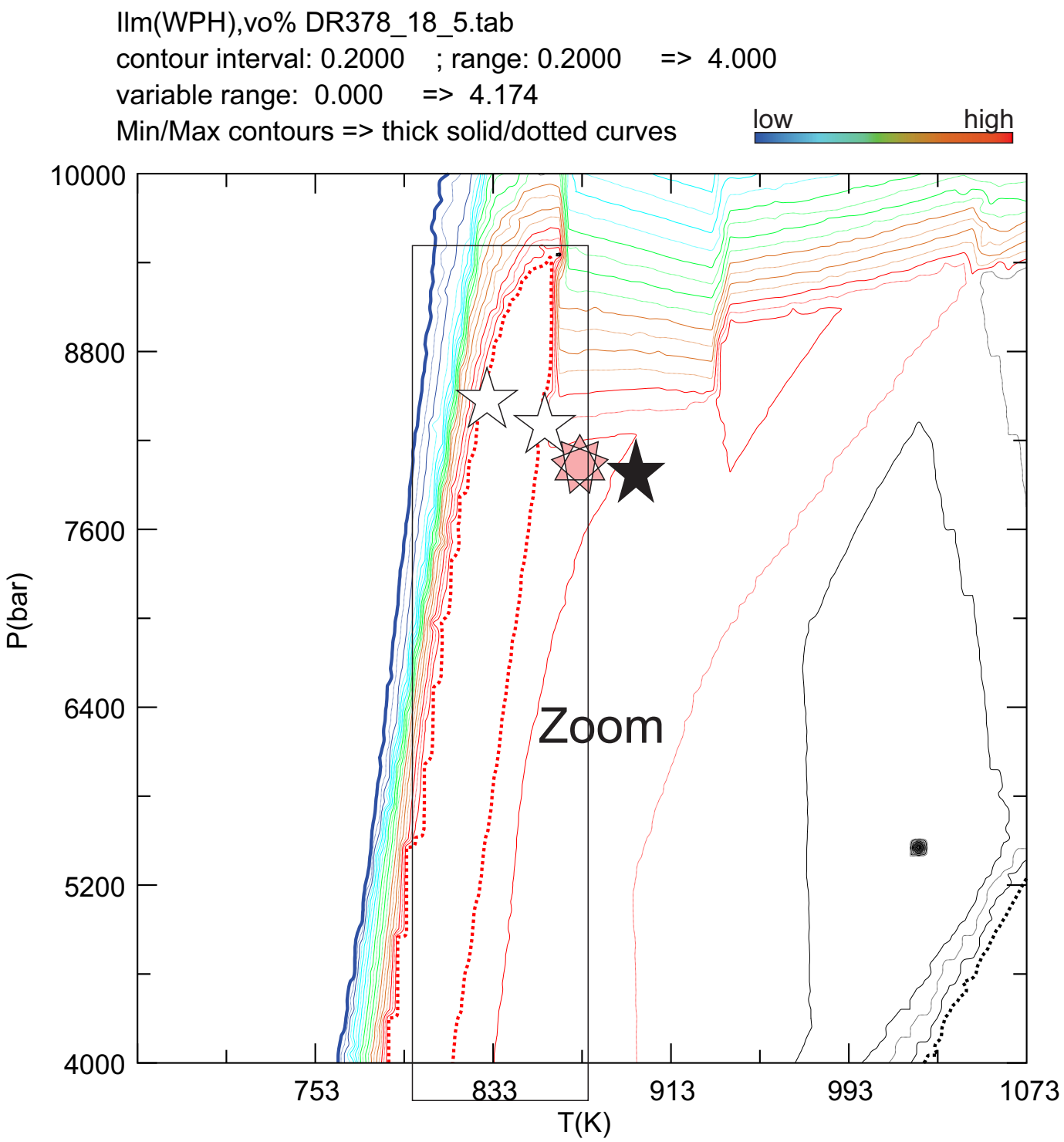

Ricardo et al.(2021)

Supplementary Material

Sample Dr378 - %ilm isopleth modeled with composition from Z2

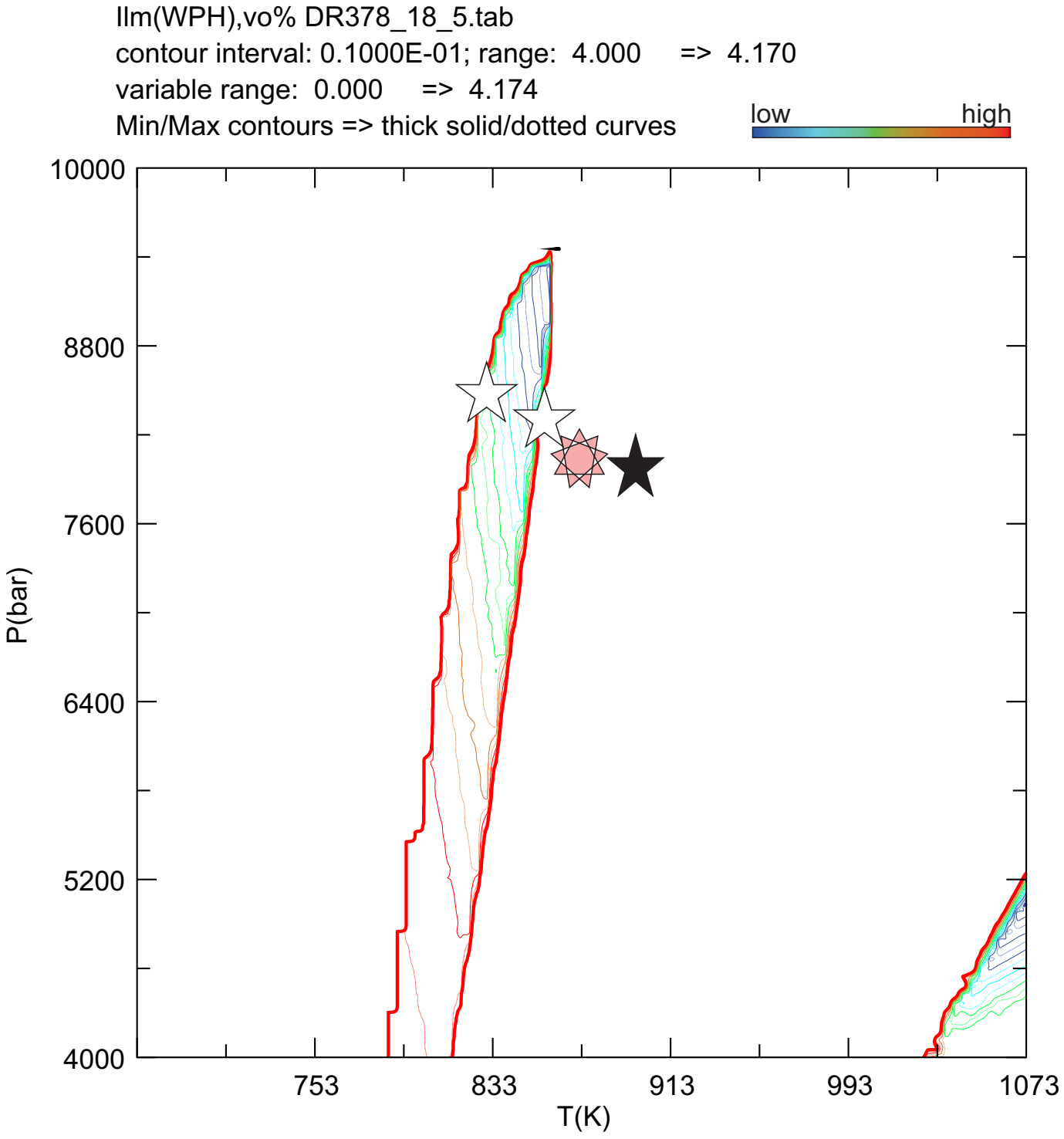

Ricardo et al.(2021)

Supplementary Material

Sample Dr378 - Xsps isopleth modeled with composition from Z2

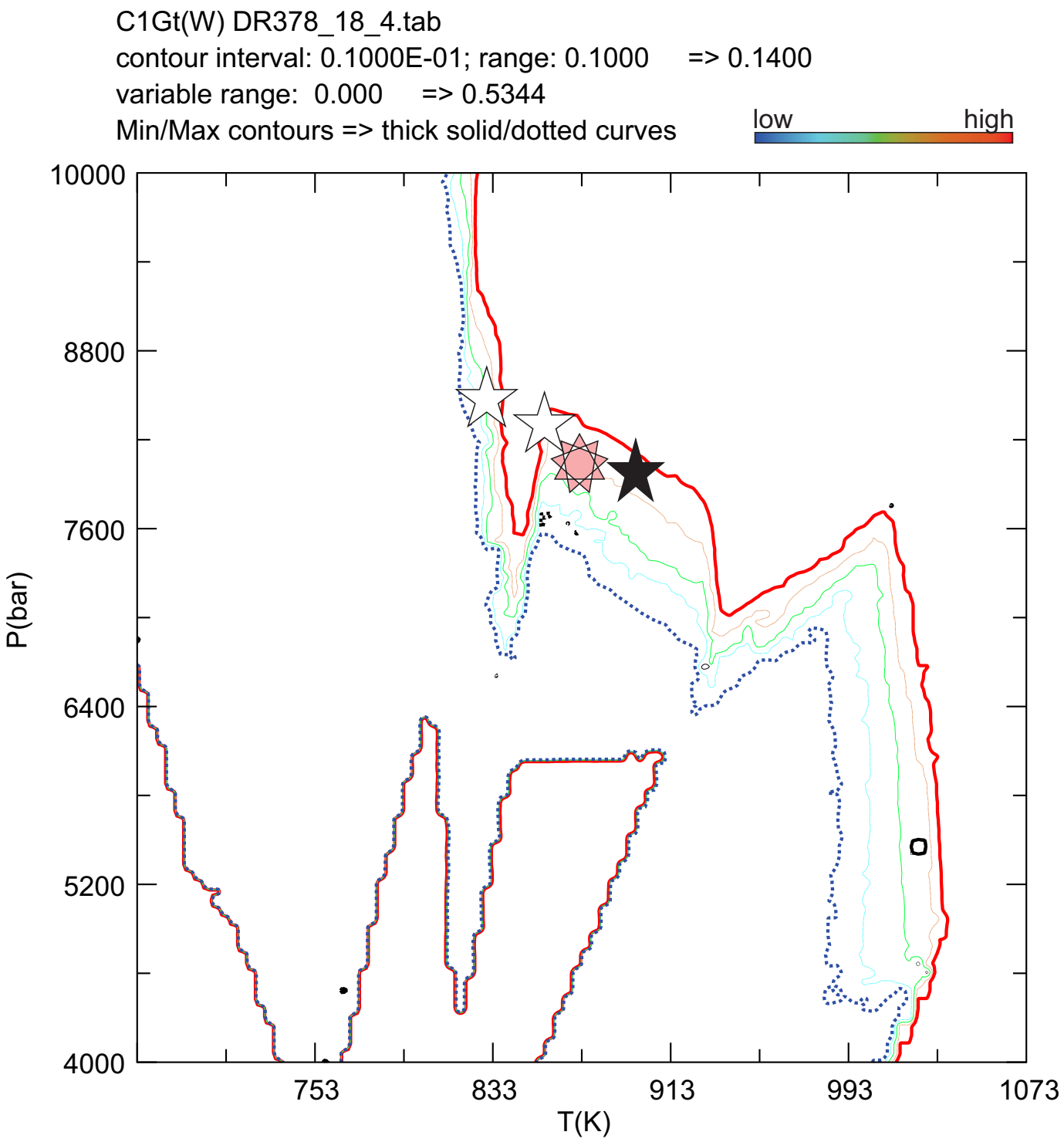

Ricardo et al.(2021)

Supplementary Material

Sample DR352

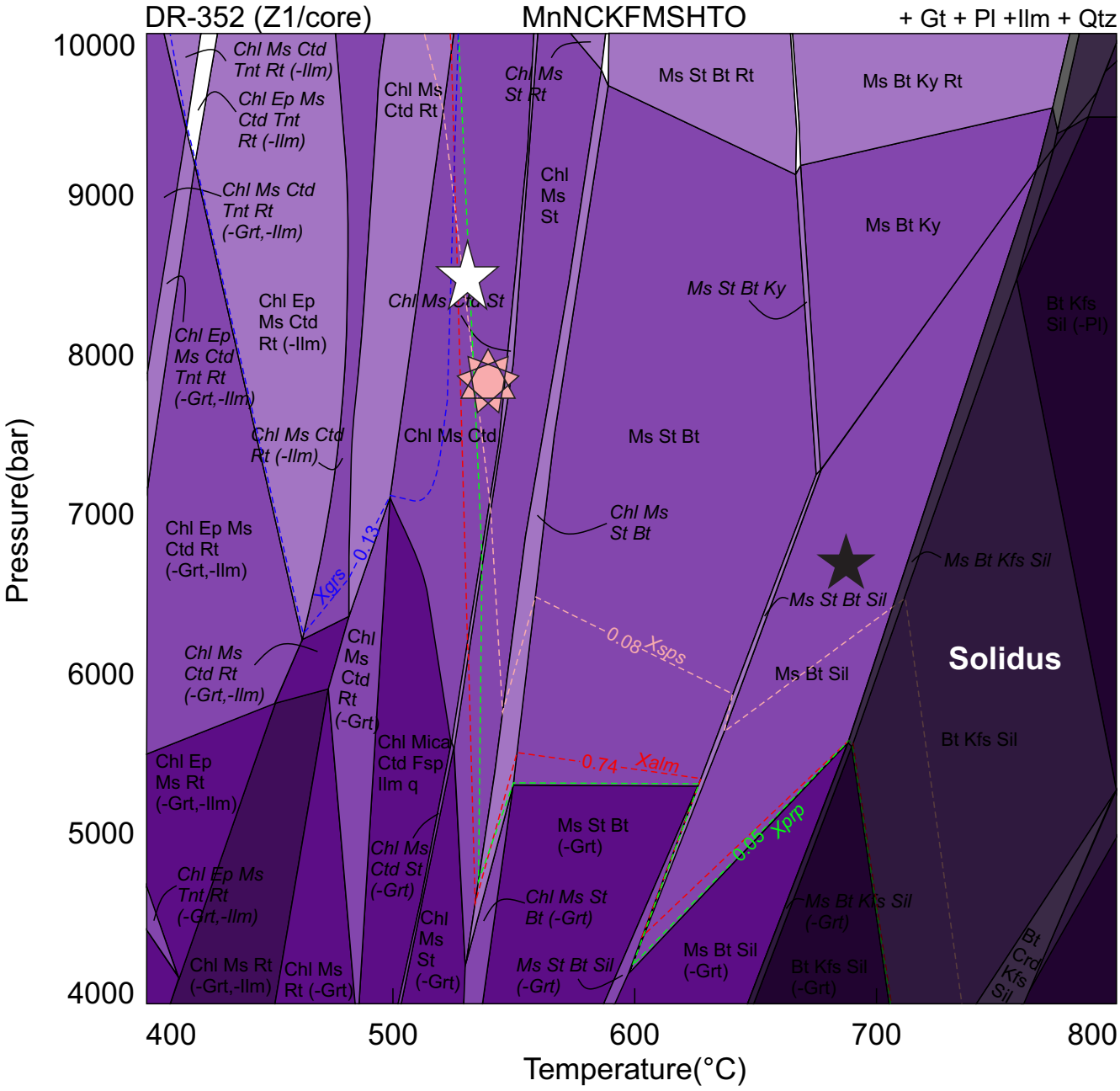

Ricardo et al.(2021)

Supplementary Material

Sample DR378

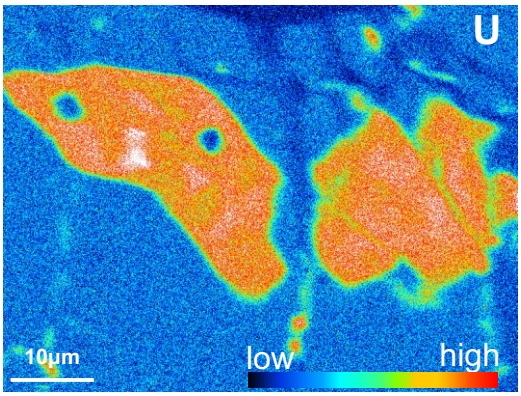

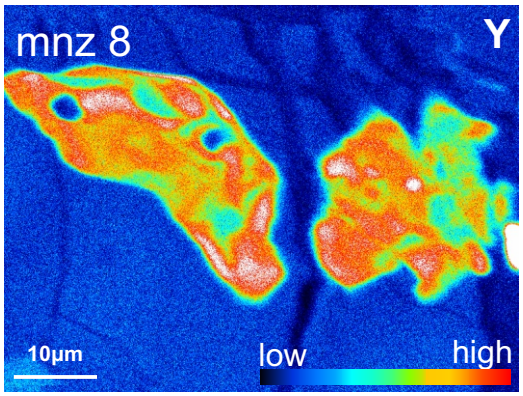

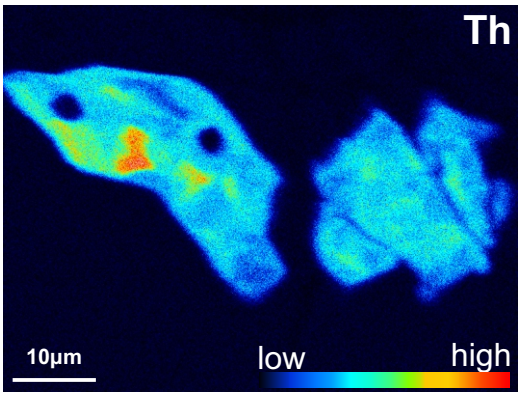

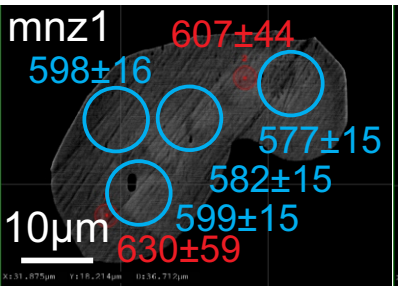

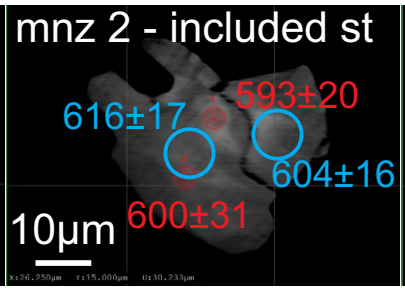

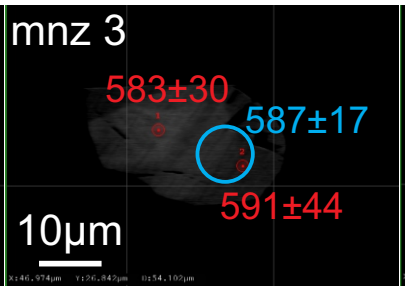

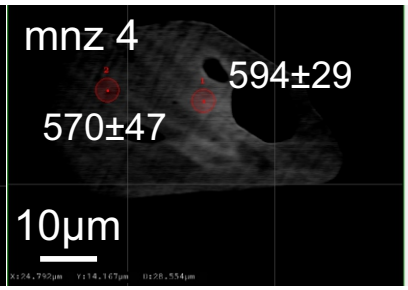

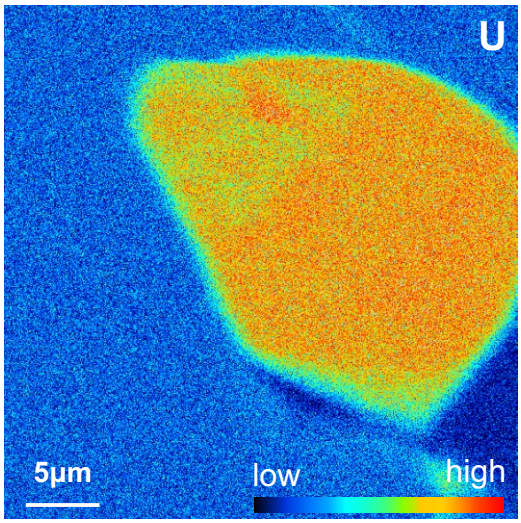

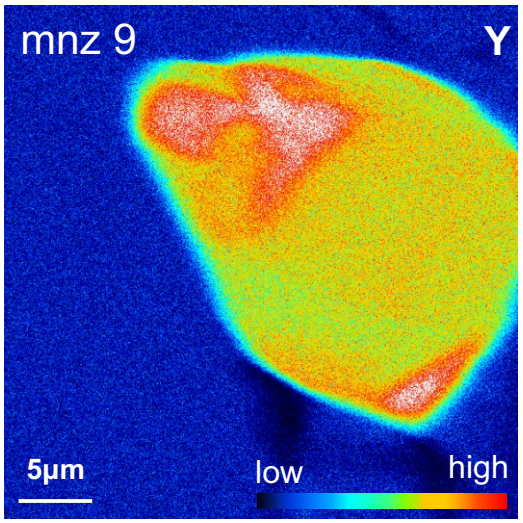

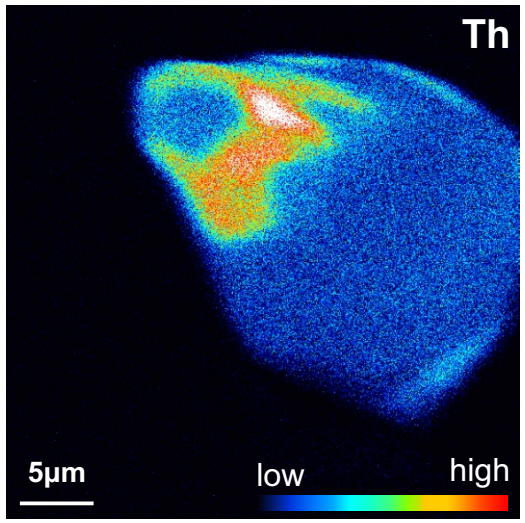

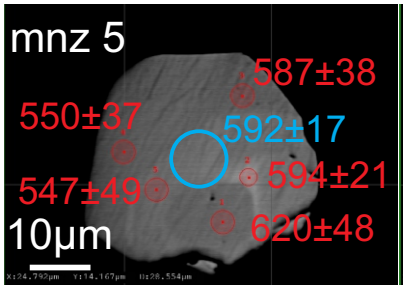

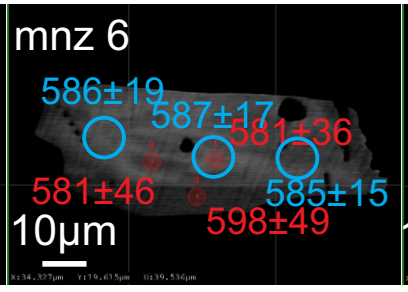

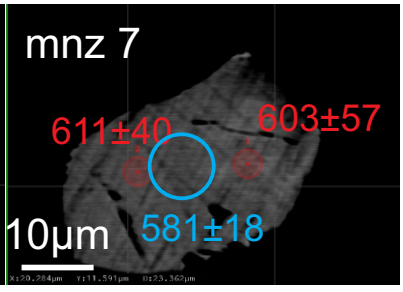

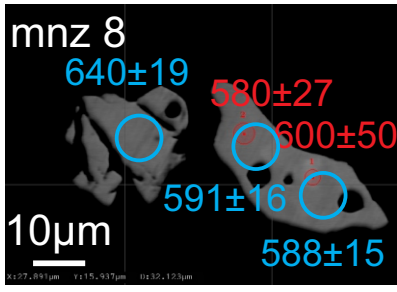

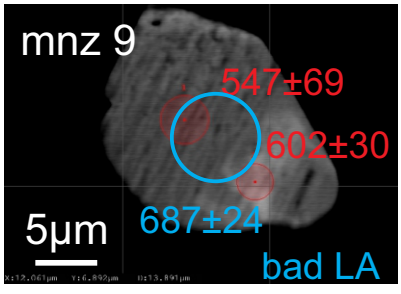

Ricardo et al.(2021)

Supplementary Material

Sample DR378

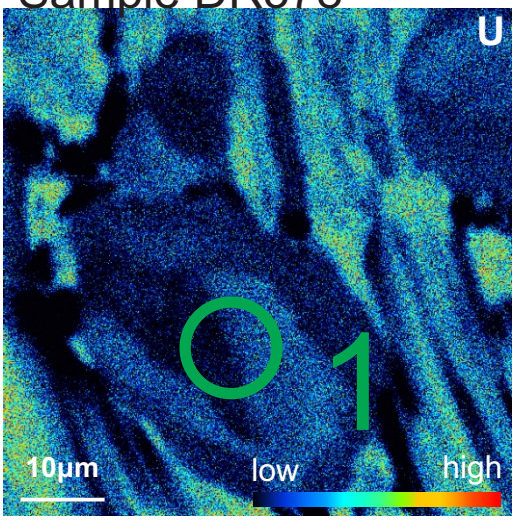

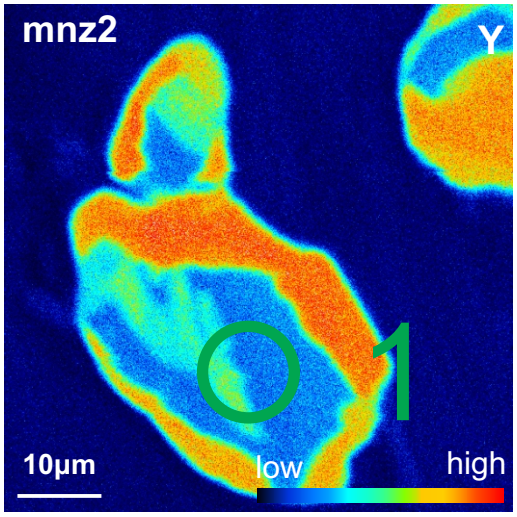

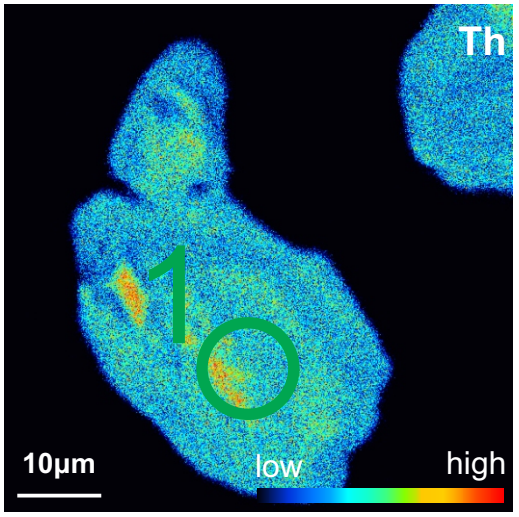

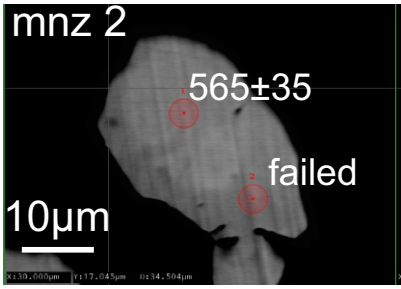

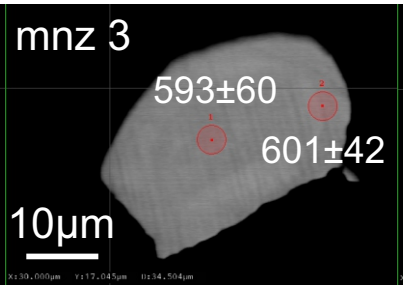

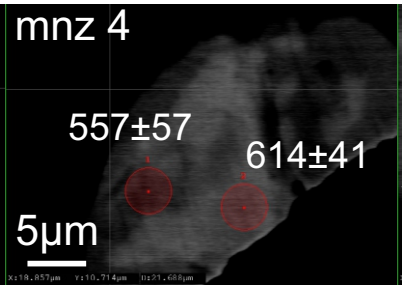

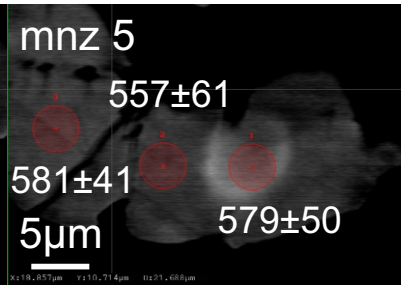

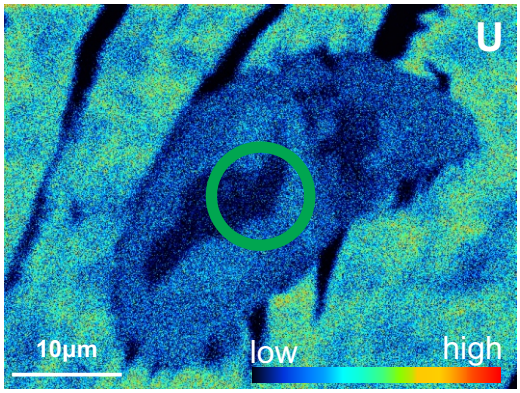

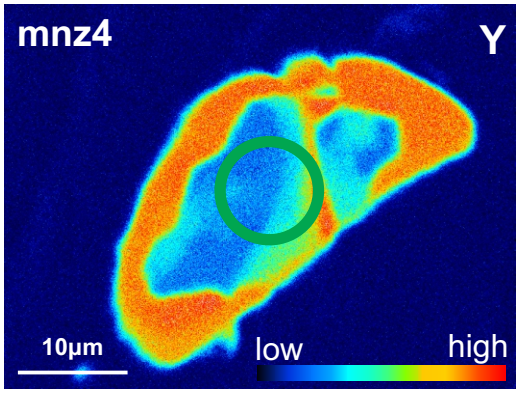

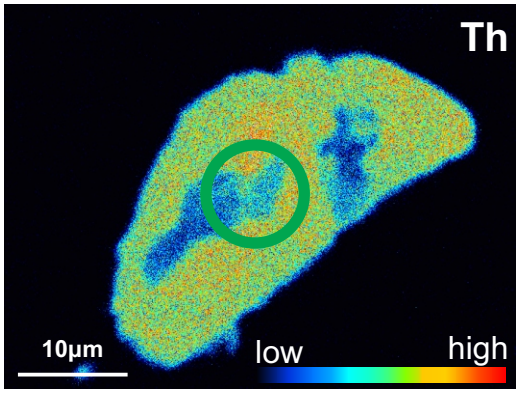

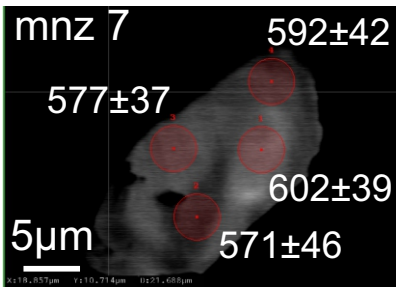

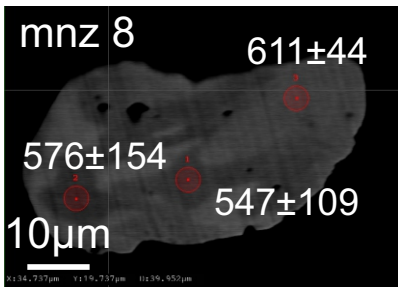

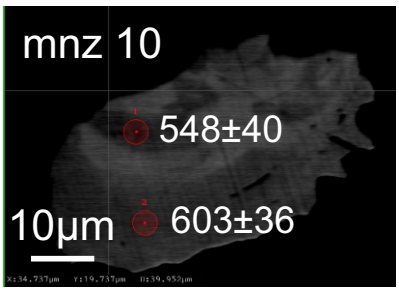

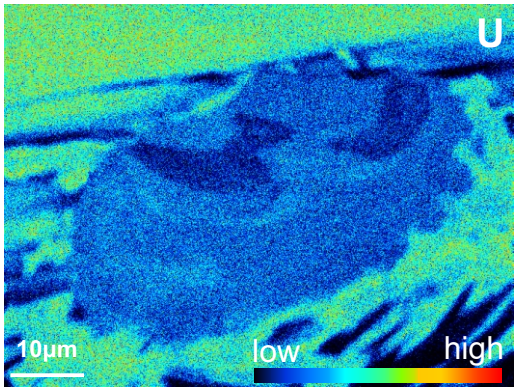

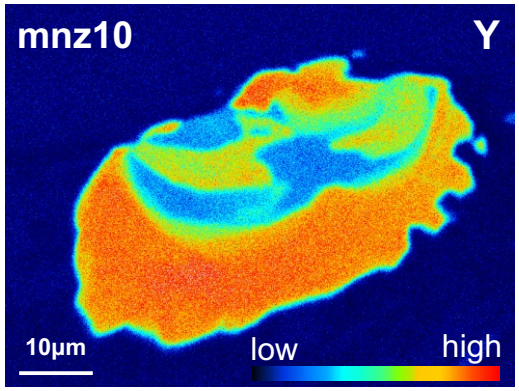

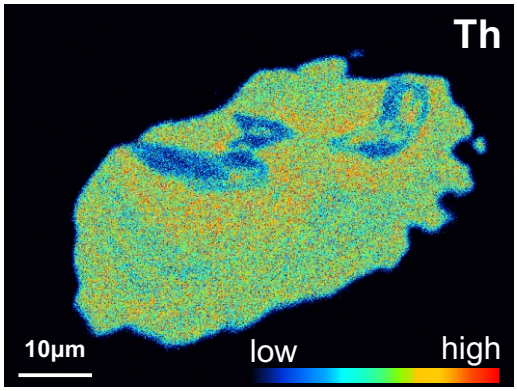

Ricardo et al.(2021)

Supplementary Material

Sample BR04

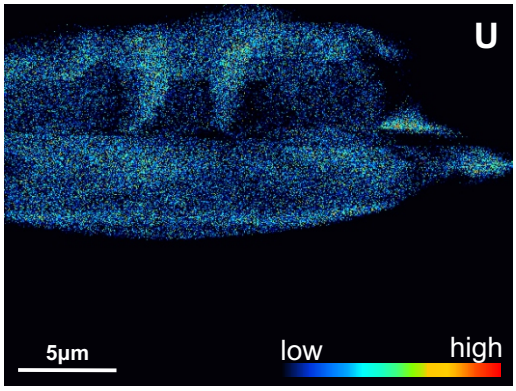

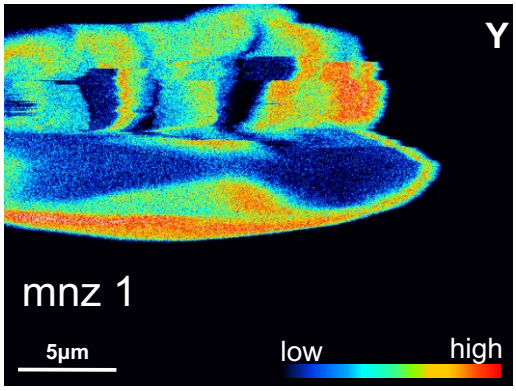

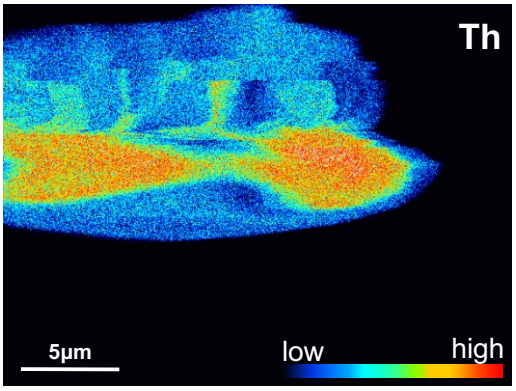

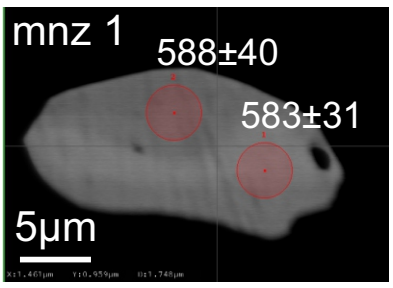

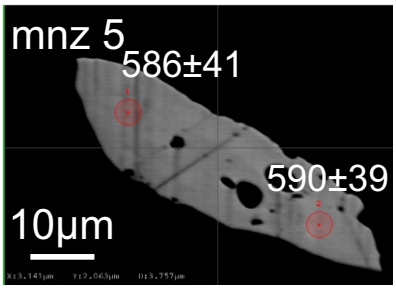

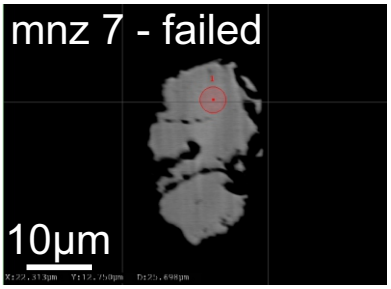

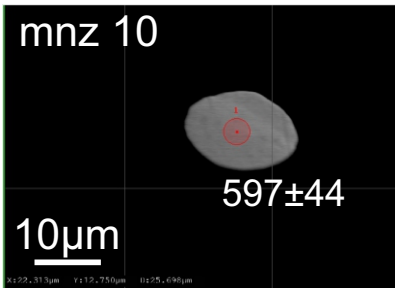

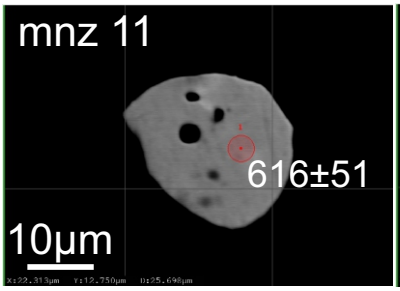

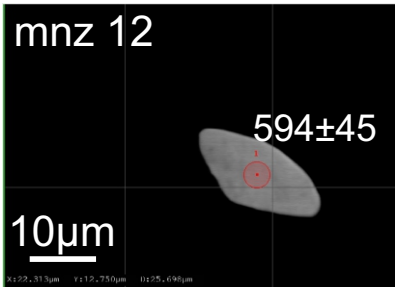

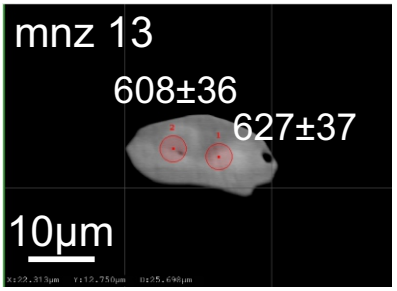

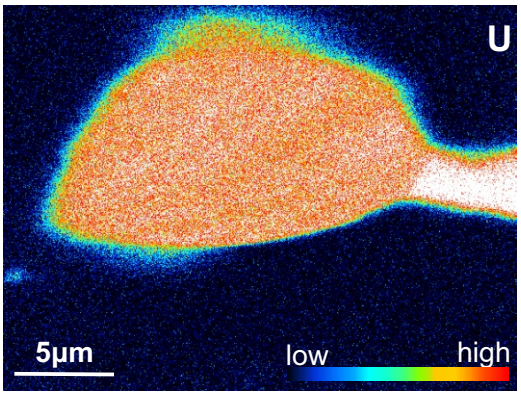

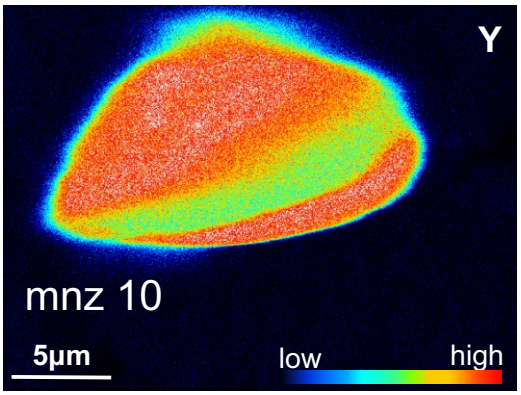

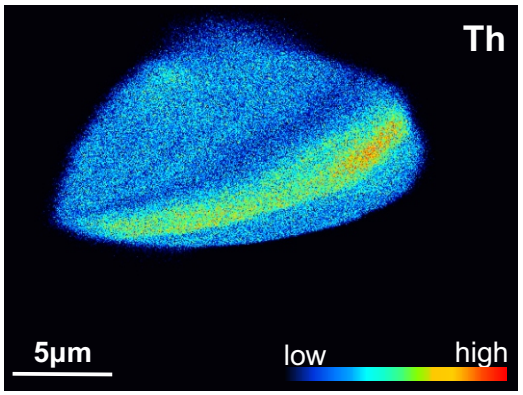

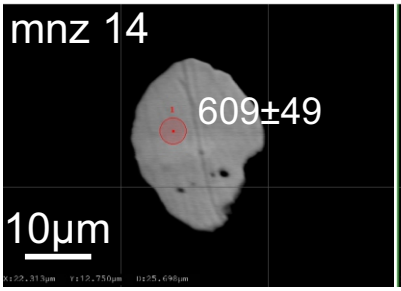

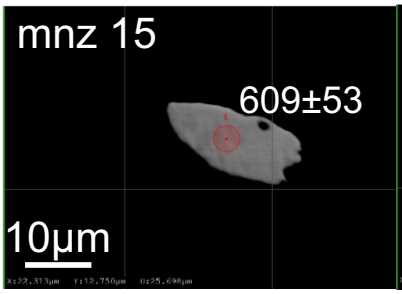

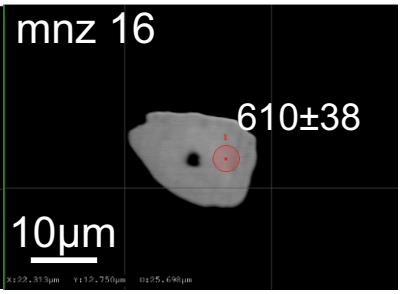

Ricardo et al.(2021)

Supplementary Material

Sample 129

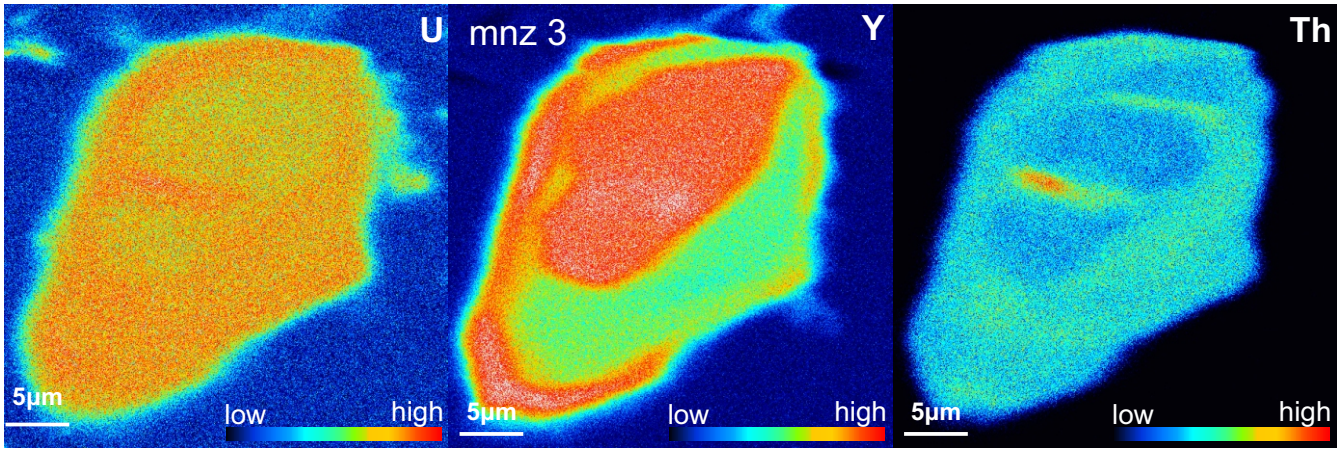

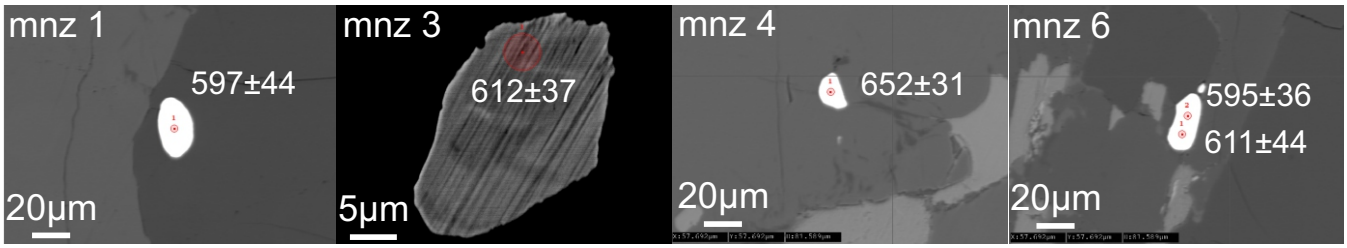

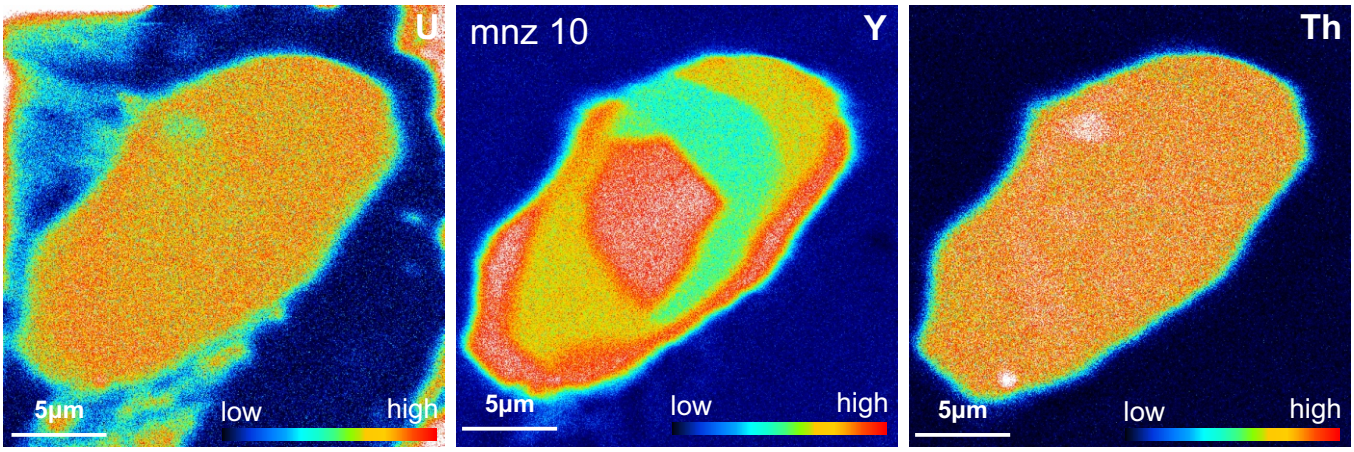

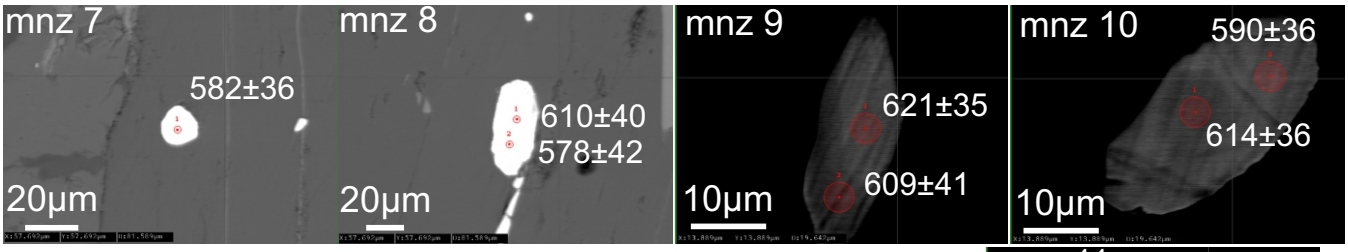

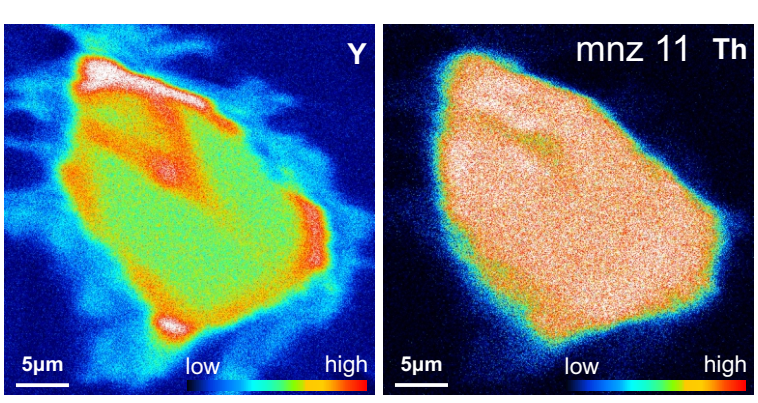

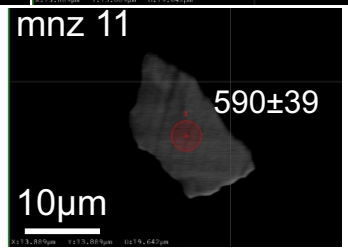

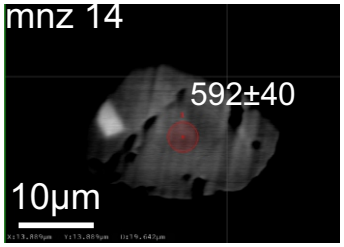

Ricardo et al.(2021)

Supplementary Material

Sample BR18

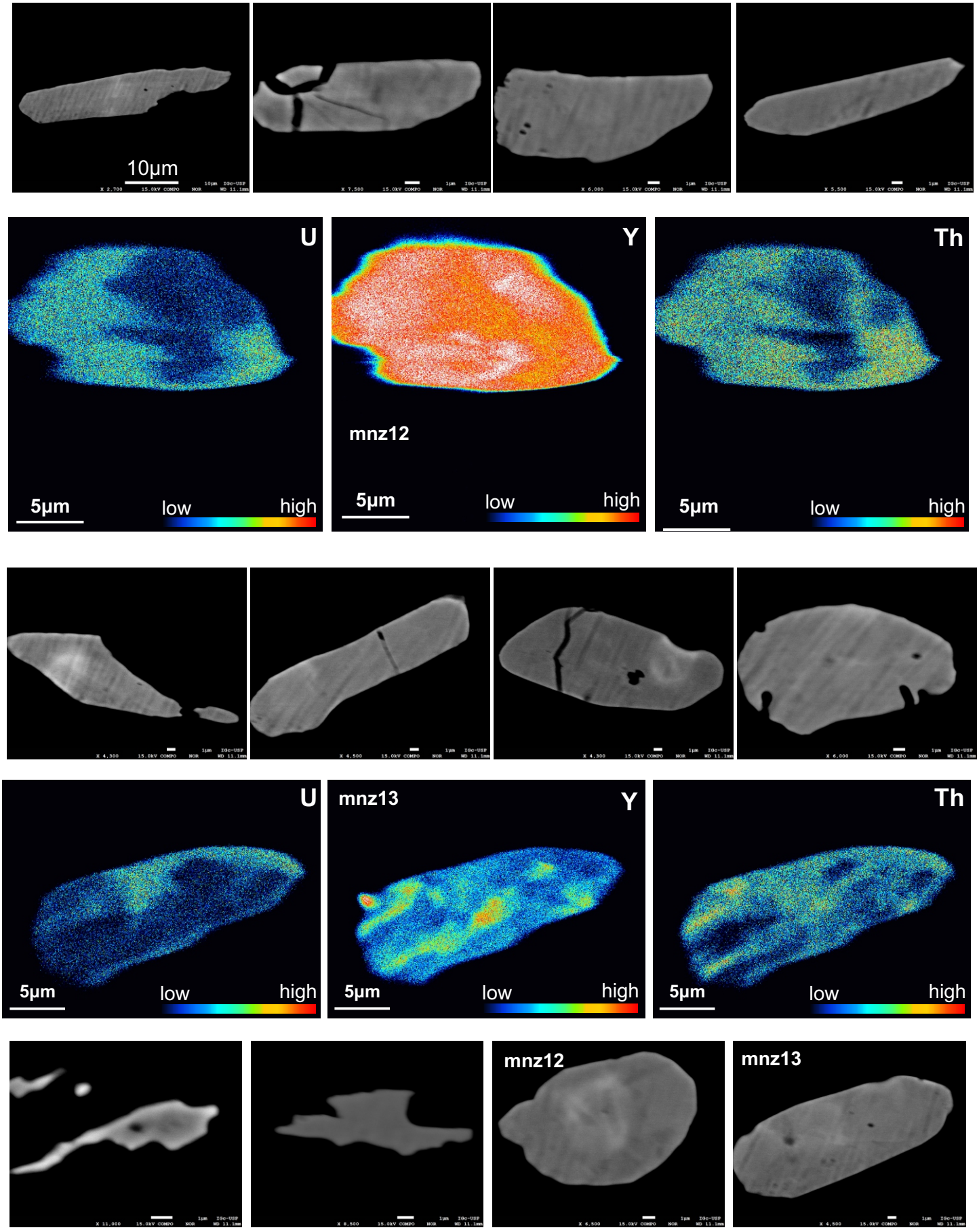

Ricardo et al.(2021)

Supplementary Material

Sample BR07

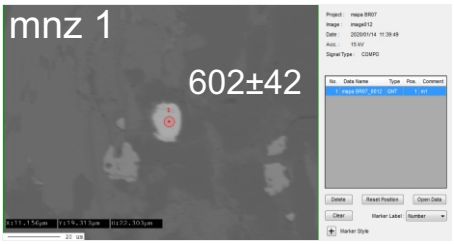

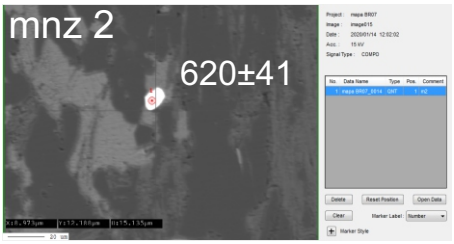

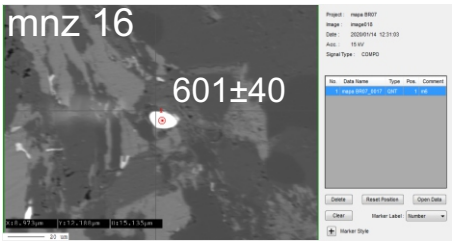

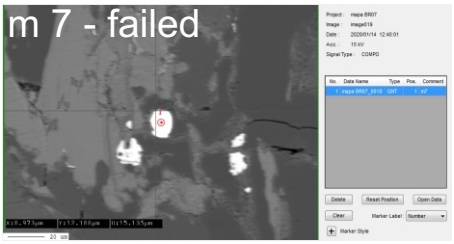

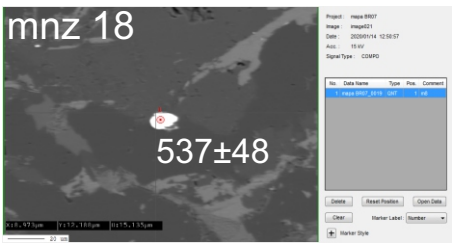

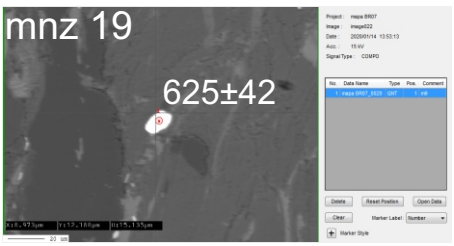

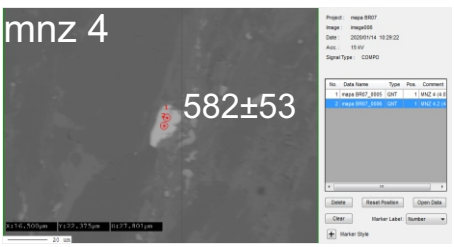

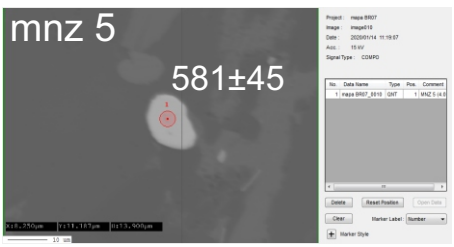

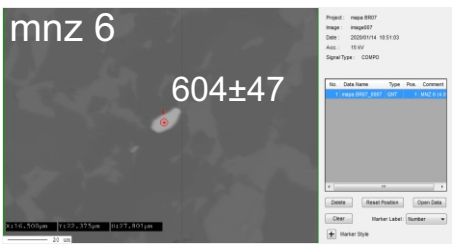

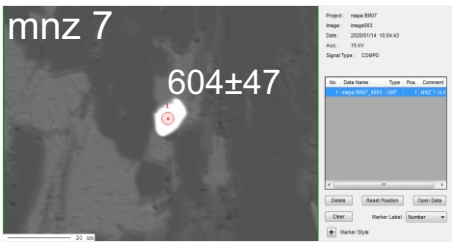

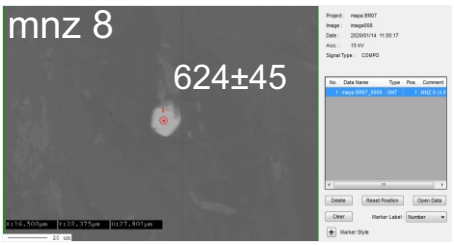

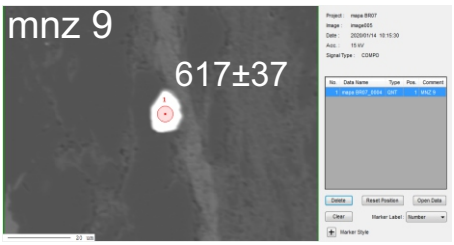

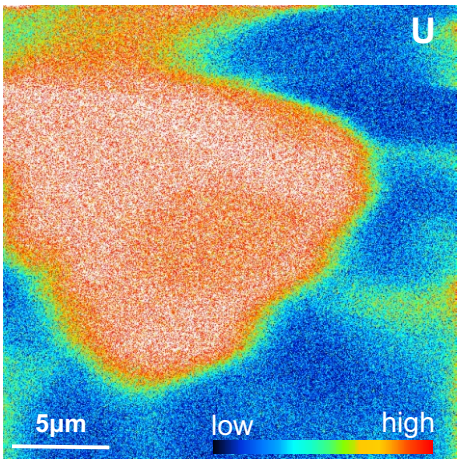

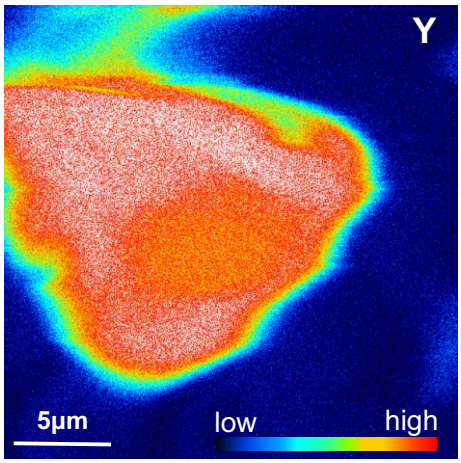

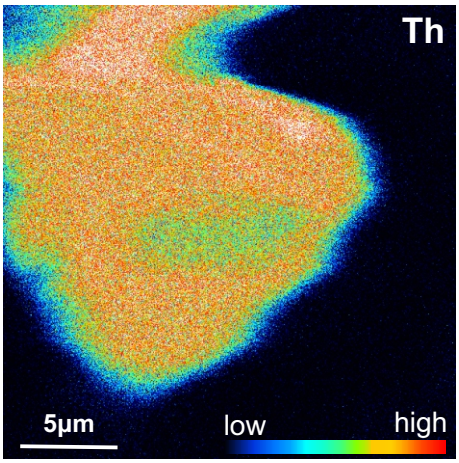

Ricardo et al.(2021)

Supplementary Material

Reference Material

Primary

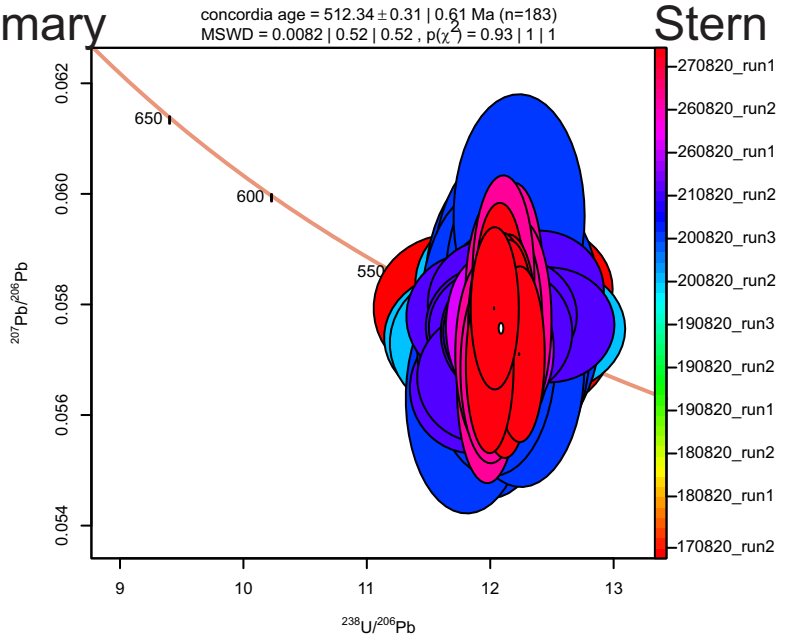

Stern

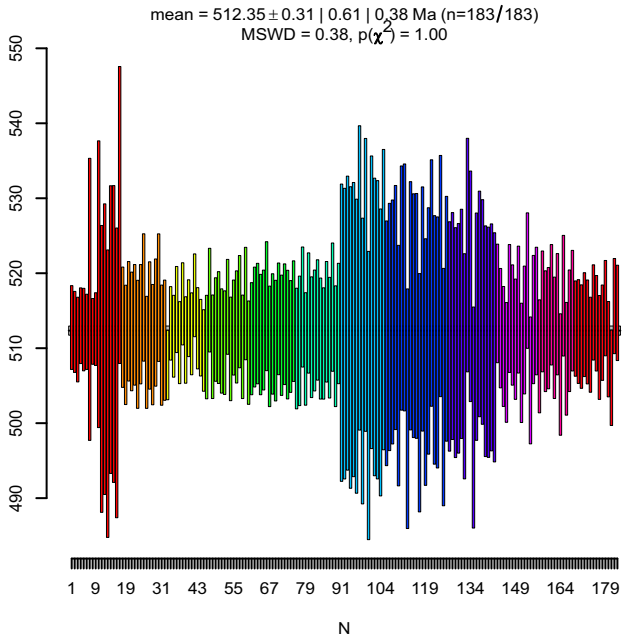

Secondary

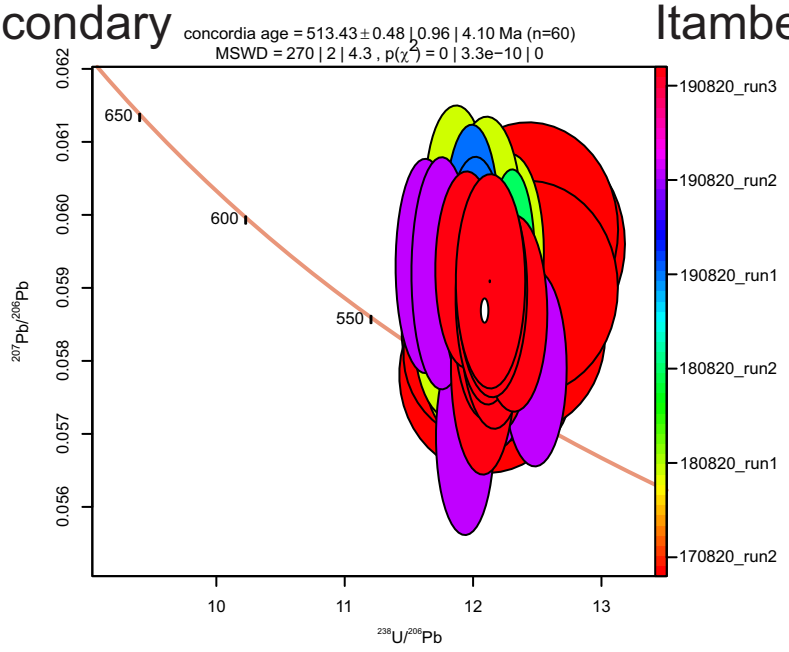

Itambe

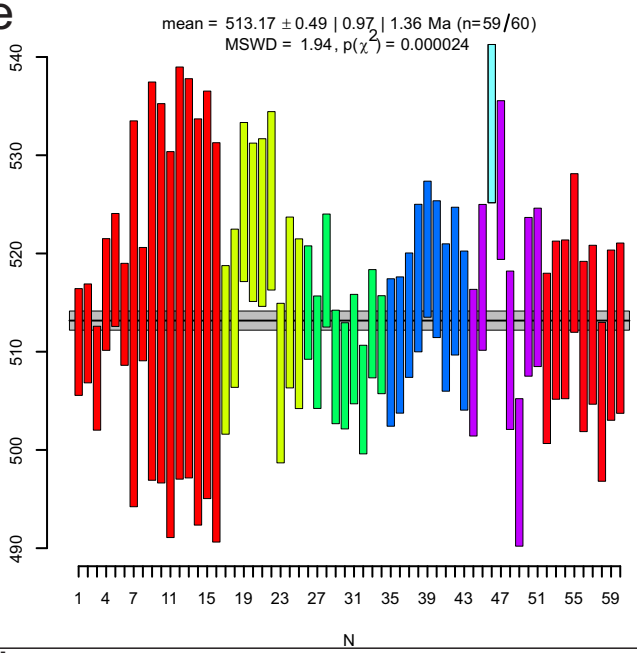

Bananeira

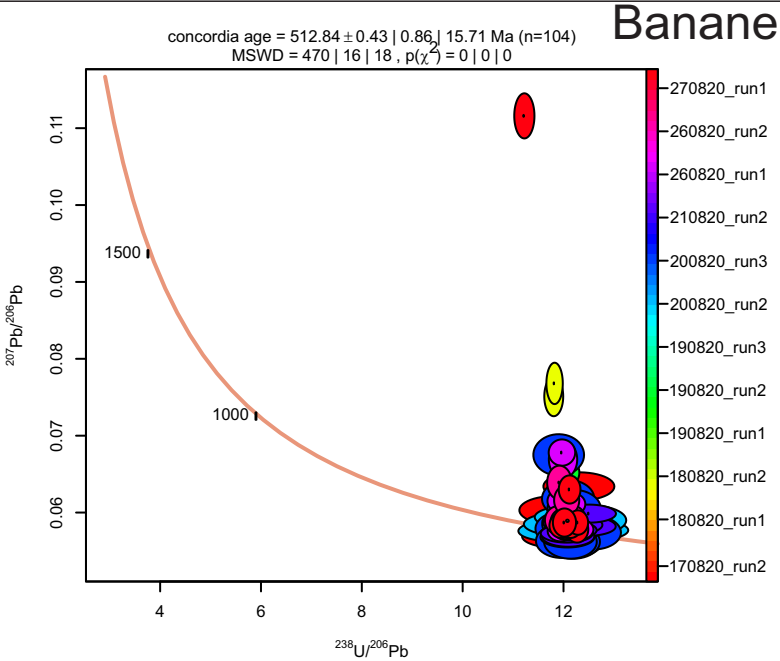

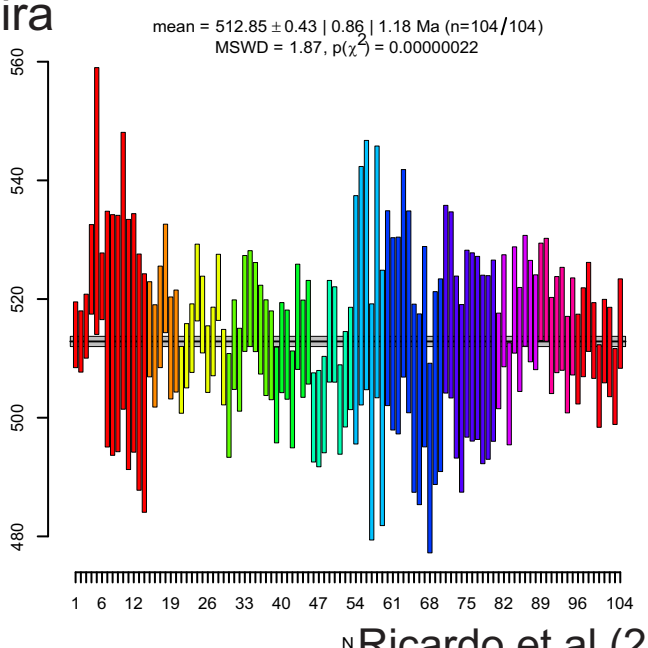

N Ricardo et al.(2021)

Supplementary Material

Secondary Reference Material

Trebilcock

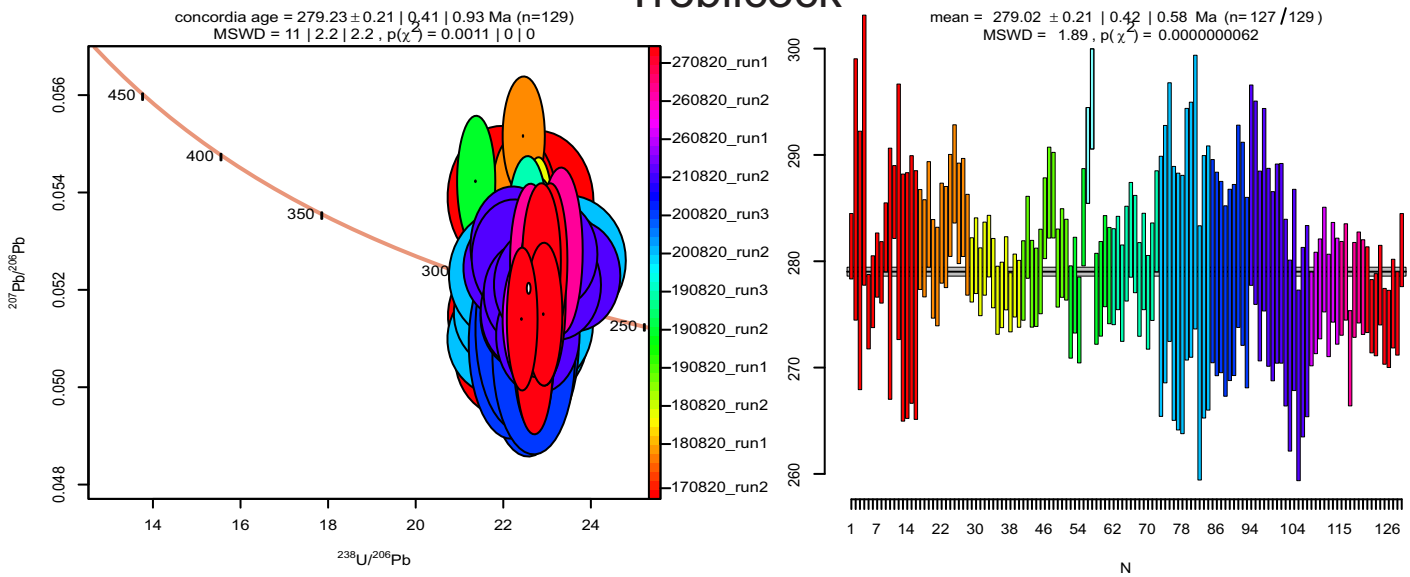

Vermilion

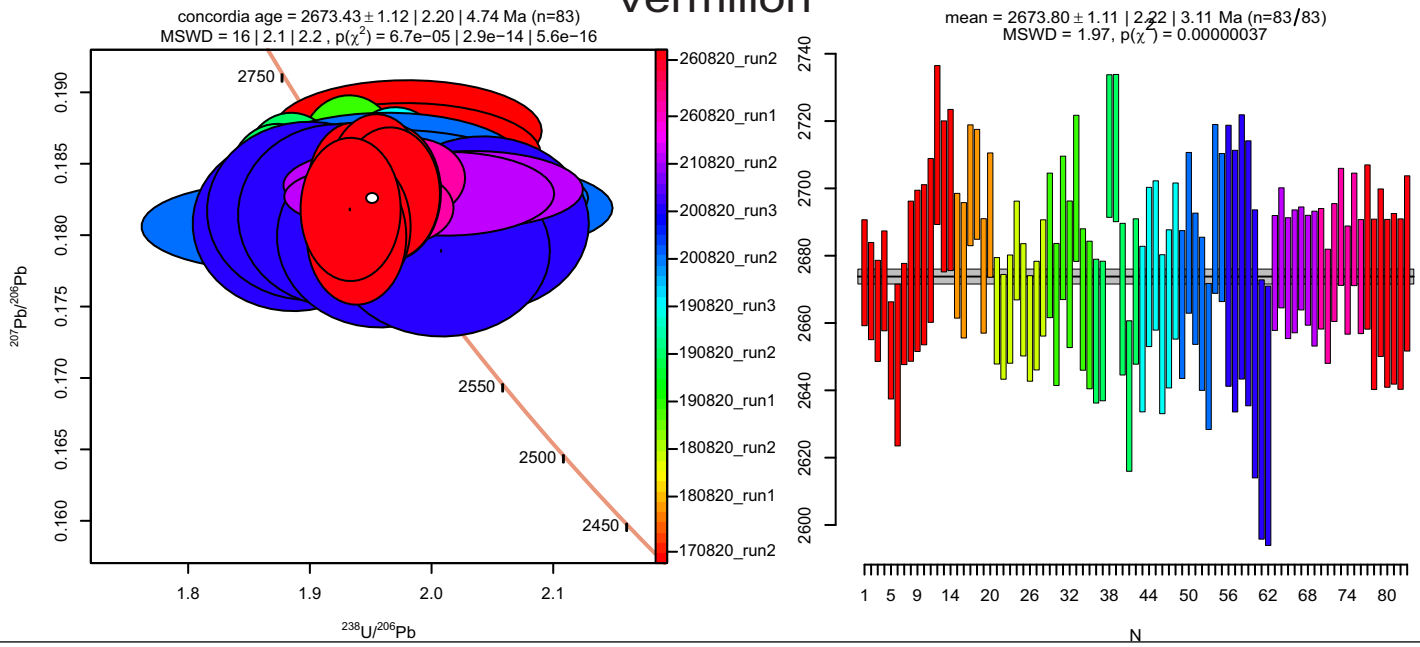

44069

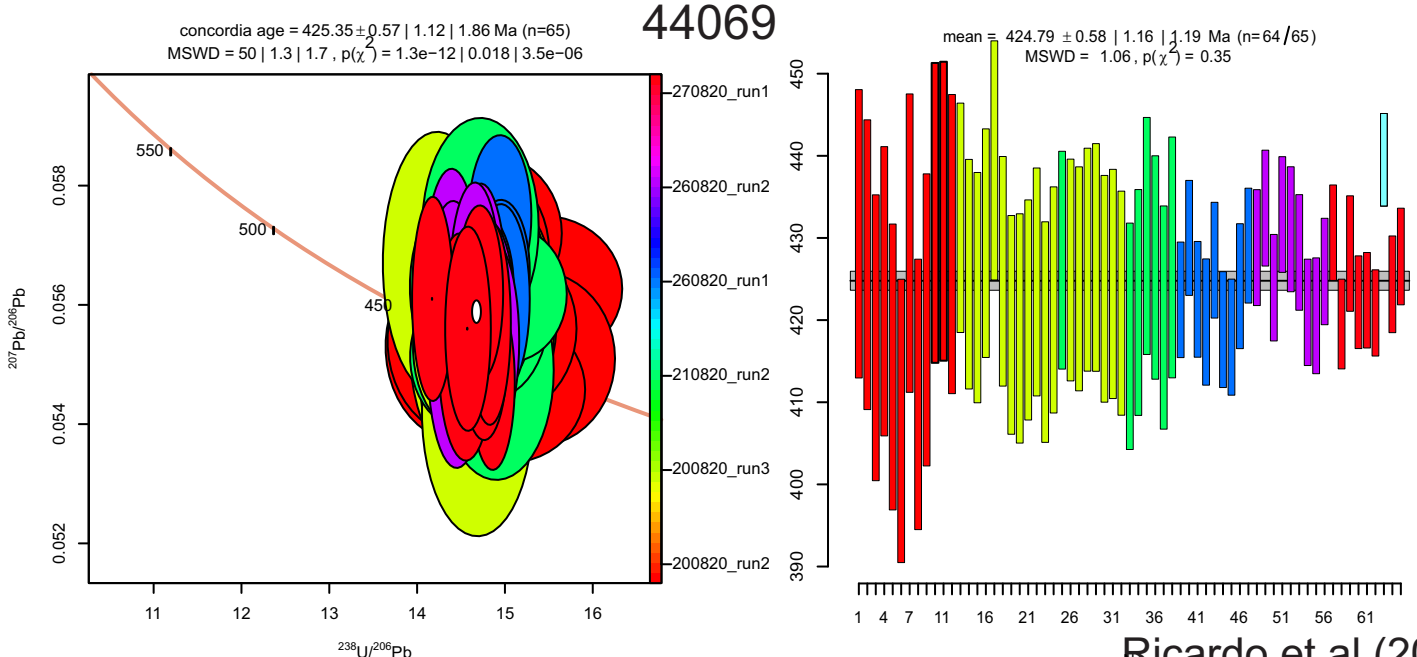

Ricardo et al.(2021)

Supplementary material from CHAPTER 3
Sample:DR378
Mineral:muscovite

Sample	ms1	ms2	ms3
SiO2	44.91	45.51	45.45
TiO2	0.48	0.42	0.50
Al2O3	35.27	35.09	35.48
Cr2O3	0.00	0.00	0.00
Fe2O3	1.51	1.51	1.51
FeO	1.33	3.01	2.81
MnO	0.00	0.01	0.03
MgO	0.66	0.76	0.65
CaO	0.01	0.01	0.00
Na2O	1.40	1.09	1.50
K2O	8.94	9.28	8.84
Totals	94.50	96.70	96.77
Oxygens	11.000	11.000	11.000
Si	3.016	3.015	3.002
Ti	0.024	0.021	0.025
Al	2.793	2.740	2.763
Cr	0.000	0.000	0.000
Fe3	0.076	0.075	0.075
Fe2	0.075	0.167	0.155
Mn	0.000	0.001	0.001
Mg	0.066	0.075	0.063
Ca	0.001	0.001	0.000
Na	0.182	0.141	0.192
K	0.766	0.784	0.745
Sum	7.000	7.020	7.023
XMg	0.47	0.31	0.29
Al/Si	0.93	0.91	0.92

Sample:DR378
Mineral:biotite

Sample	bt1	bt2	bt3	bt4	bt5	bt7
SiO2	35.66	35.53	35.99	35.22	35.74	34.12
TiO2	1.49	1.32	1.56	1.25	1.85	1.31
Al2O3	19.33	19.15	19.59	19.41	19.35	19.20
Cr2O3	0.00	0.00	0.00	0.00	0.00	0.00
Fe2O3	0.61	0.61	0.61	0.61	0.61	0.61
FeO	17.72	19.19	17.82	19.57	18.58	20.79
MnO	0.13	0.14	0.13	0.11	0.16	0.16
MgO	11.20	10.70	11.22	10.72	10.82	10.27
CaO	0.00	0.02	0.03	0.03	0.02	0.02
Na2O	0.21	0.21	0.39	0.19	0.41	0.12
K2O	9.17	9.17	8.97	9.20	8.85	8.86
Totals	95.53	96.05	96.30	96.30	96.38	95.46
Oxygens	11.000	11.000	11.000	11.000	11.000	11.000
Si	2.685	2.681	2.684	2.656	2.674	2.616
Ti	0.084	0.075	0.088	0.071	0.104	0.075
Al	1.716	1.703	1.722	1.726	1.707	1.736
Cr	0.000	0.000	0.000	0.000	0.000	0.000
Fe3	0.035	0.035	0.034	0.035	0.034	0.035
Fe2	1.116	1.211	1.111	1.234	1.163	1.333
Mn	0.008	0.009	0.008	0.007	0.010	0.010
Mg	1.257	1.203	1.247	1.205	1.206	1.174
Ca	0.000	0.002	0.002	0.002	0.001	0.002
Na	0.031	0.031	0.056	0.028	0.059	0.018
K	0.881	0.883	0.853	0.885	0.845	0.867
Sum	7.812	7.833	7.806	7.850	7.804	7.866
XMg	0.53	0.50	0.53	0.49	0.51	0.47

Sample:DR378

Mineral:garnet

													Z3		Z1			Z2	
Sample	grt1.1	grt1.2	grt1.3	grt1.4	grt1.5	grt1.6	grt1.7	grt1.8	grt1.9	grt1.10	grt2.1	grt2.2	grt2.3	grt2.4	grt2.5	grt2.7	grt2.8	grt2.9	grt2.10
SiO2	37.11	36.98	37.05	36.27	36.89	36.79	36.90	36.86	36.66	33.58	36.75	36.62	36.90	36.49	36.55	36.66	36.28	36.83	36.18
TiO2	0.00	0.01	0.03	0.00	0.02	0.01	0.05	0.00	0.00	0.01	0.05	0.01	0.00	0.03	0.01	0.00	0.07	0.00	0.02
Al2O3	21.43	20.96	20.91	20.67	20.97	20.89	20.81	21.24	21.12	20.33	21.04	21.01	21.31	20.86	21.02	21.19	20.84	21.02	20.86
Cr2O3	0.04	0.02	0.03	0.03	0.02	0.00	0.00	0.00	0.00	0.04	0.00	0.00	0.00	0.00	0.02	0.01	0.01	0.00	0.03
Fe2O3	0.55	0.55	0.55	0.55	0.55	0.55	0.55	0.55	0.55	0.55	0.55	0.55	0.55	0.55	0.55	0.55	0.55	0.55	0.55
FeO	29.49	30.78	30.39	30.77	31.37	31.71	31.72	31.11	30.51	30.91	30.36	30.72	31.27	31.23	31.73	31.03	30.87	31.13	30.68
MnO	7.27	6.74	7.11	6.25	5.25	5.25	5.13	4.99	5.32	6.67	6.18	5.19	4.88	5.21	4.69	4.59	5.29	4.49	5.44
MgO	2.86	3.04	2.66	3.28	3.41	3.55	3.50	3.58	3.74	4.08	3.35	3.79	3.83	3.29	3.58	3.90	3.47	4.07	3.72
CaO	1.84	1.71	1.85	1.91	1.88	1.66	1.80	1.85	1.88	0.90	1.40	1.70	1.94	2.22	2.11	2.15	1.77	1.97	1.38
Na2O	0.02	0.00	0.01	0.01	0.01	0.01	0.00	0.00	0.02	0.03	0.01	0.02	0.01	0.03	0.01	0.01	0.02	0.02	0.00
K2O	0.00	0.00	0.00	0.00	0.00	0.00	0.00	0.00	0.00	0.00	0.00	0.00	0.00	0.00	0.00	0.00	0.00	0.00	0.00
Totals	100.60	100.79	100.59	99.74	100.37	100.42	100.46	100.18	99.80	97.10	99.68	99.61	100.69	99.90	100.27	100.09	99.16	100.09	98.86
Oxygens	12.000	12.000	12.000	12.000	12.000	12.000	12.000	12.000	12.000	12.000	12.000	12.000	12.000	12.000	12.000	12.000	12.000	12.000	12.000
Si	2.972	2.968	2.981	2.946	2.964	2.959	2.966	2.959	2.954	2.830	2.969	2.957	2.948	2.951	2.943	2.945	2.951	2.956	2.949
Ti	0.000	0.000	0.002	0.000	0.001	0.001	0.003	0.000	0.000	0.001	0.003	0.001	0.000	0.002	0.001	0.000	0.004	0.000	0.001
Al	2.023	1.983	1.983	1.980	1.987	1.981	1.972	2.010	2.006	2.020	2.004	2.000	2.007	1.989	1.995	2.007	1.999	1.989	2.004
Cr	0.003	0.001	0.002	0.002	0.002	0.000	0.000	0.000	0.000	0.003	0.000	0.000	0.000	0.000	0.001	0.001	0.000	0.000	0.002
Fe3	0.033	0.033	0.033	0.034	0.033	0.033	0.033	0.033	0.033	0.035	0.033	0.033	0.033	0.033	0.033	0.033	0.034	0.033	0.034
Fe2	1.975	2.066	2.045	2.090	2.108	2.133	2.132	2.089	2.056	2.179	2.051	2.075	2.090	2.112	2.137	2.085	2.100	2.090	2.091
Mn	0.493	0.458	0.484	0.430	0.357	0.358	0.349	0.339	0.363	0.476	0.423	0.355	0.330	0.357	0.320	0.312	0.364	0.305	0.376
Mg	0.341	0.364	0.319	0.397	0.408	0.426	0.419	0.428	0.449	0.513	0.403	0.456	0.456	0.397	0.430	0.467	0.421	0.487	0.452
Ca	0.158	0.147	0.159	0.166	0.162	0.143	0.155	0.159	0.162	0.081	0.121	0.147	0.166	0.192	0.182	0.185	0.154	0.169	0.121
Na	0.002	0.000	0.001	0.002	0.001	0.002	0.000	0.000	0.003	0.005	0.002	0.003	0.001	0.004	0.001	0.002	0.003	0.004	0.000
K	0.000	0.000	0.000	0.000	0.000	0.000	0.000	0.000	0.000	0.000	0.000	0.000	0.000	0.000	0.000	0.000	0.000	0.000	0.000
Sum	8.000	8.022	8.009	8.047	8.024	8.035	8.029	8.019	8.027	8.143	8.010	8.027	8.032	8.038	8.042	8.036	8.030	8.034	8.030
Alm	0.67	0.68	0.68	0.68	0.69	0.70	0.70	0.69	0.68	0.67	0.68	0.68	0.69	0.69	0.70	0.68	0.69	0.69	0.69
Grs	0.05	0.05	0.05	0.05	0.05	0.05	0.05	0.05	0.05	0.02	0.04	0.05	0.05	0.06	0.06	0.06	0.05	0.06	0.04
Pyr	0.11	0.12	0.11	0.13	0.13	0.14	0.14	0.14	0.15	0.16	0.13	0.15	0.15	0.13	0.14	0.15	0.14	0.16	0.15
Sps	0.17	0.15	0.16	0.14	0.12	0.12	0.11	0.11	0.12	0.15	0.14	0.12	0.11	0.12	0.10	0.10	0.12	0.10	0.12

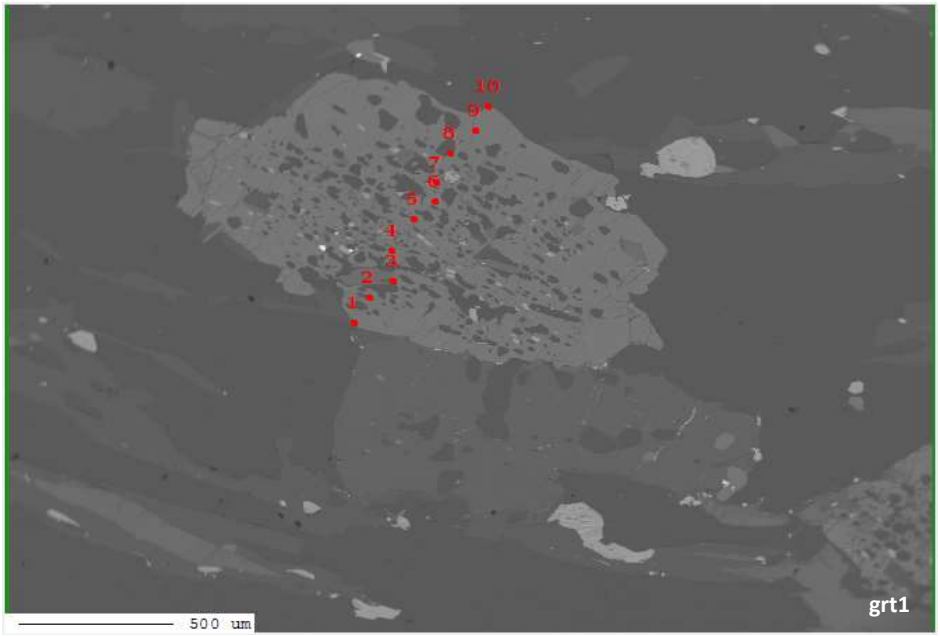
10
9
8
7
6
5
4
3
2
1
500 um
grt1

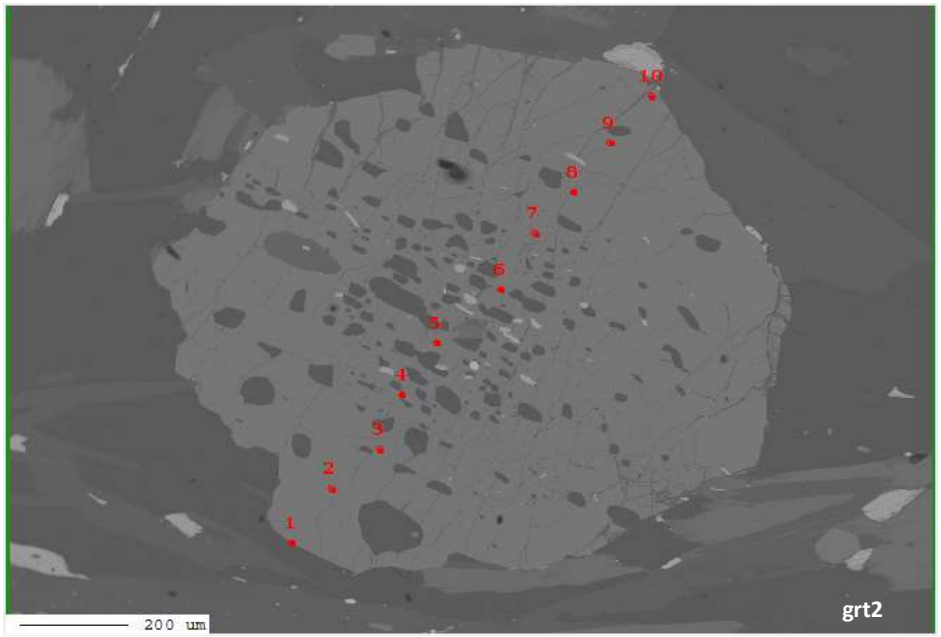
10
9
8
7
6
5
4
3
2
1
200 um
grt2

Sample:DR378
Mineral:staurolite

Sample	st1.1	st1.2	st1.3	st1.4	st1.5	st2.1	st2.2	st2.3	st2.4	st2.5	st2.6	st3.2	st3.4	st3.5	st3.6	st3.8
SiO2	27.16	27.35	27.85	27.84	27.95	28.60	28.37	27.91	27.98	28.19	27.89	26.55	26.17	26.25	27.57	27.57
TiO2	0.53	0.59	0.65	0.63	0.62	0.75	0.63	0.55	0.51	0.70	0.72	0.56	0.59	0.69	0.54	0.57
Al2O3	54.83	54.05	54.32	54.50	54.77	54.29	51.36	51.44	53.54	54.13	54.23	52.36	52.44	52.73	54.29	54.79
Cr2O3	0.00	0.00	0.05	0.04	0.02	0.03	0.04	0.07	0.06	0.02	0.01	0.03	0.06	0.00	0.00	0.02
Fe2O3	0.00	0.00	0.00	0.00	0.00	0.00	0.00	0.00	0.00	0.00	0.00	0.00	0.00	0.00	0.00	0.00
FeO	13.41	13.22	13.12	13.05	13.45	12.97	13.12	13.54	13.62	13.11	13.30	13.07	13.21	12.92	13.37	12.82
MnO	0.55	0.57	0.56	0.47	0.55	0.44	0.39	0.35	0.44	0.48	0.49	0.46	0.50	0.44	0.45	0.56
MgO	1.09	1.39	1.29	1.73	1.15	1.41	2.29	2.30	1.65	1.38	1.26	1.32	1.21	1.39	1.39	1.40
CaO	0.04	0.01	0.01	0.01	0.00	0.01	0.01	0.01	0.00	0.00	0.00	0.03	0.00	0.02	0.00	0.00
Na2O	0.00	0.00	0.02	0.00	0.00	0.01	0.02	0.02	0.00	0.00	0.00	0.00	0.01	0.00	0.00	0.00
K2O	0.02	0.00	0.01	0.02	0.01	0.05	0.14	0.23	0.01	0.01	0.00	0.02	0.01	0.03	0.01	0.01
Totals	97.63	97.18	97.88	98.28	98.52	98.57	96.37	96.40	97.81	98.02	97.90	94.39	94.19	94.46	97.62	97.73
Oxygens	46.000	46.000	46.000	46.000	46.000	46.000	46.000	46.000	46.000	46.000	46.000	46.000	46.000	46.000	46.000	46.000
Si	7.552	7.635	7.708	7.670	7.692	7.843	7.987	7.881	7.767	7.783	7.720	7.638	7.556	7.544	7.658	7.631
Ti	0.110	0.123	0.134	0.130	0.128	0.155	0.134	0.116	0.107	0.145	0.149	0.121	0.129	0.148	0.112	0.119
Al	17.974	17.788	17.725	17.702	17.770	17.551	17.047	17.125	17.521	17.618	17.696	17.759	17.850	17.865	17.779	17.878
Cr	0.000	0.000	0.011	0.009	0.005	0.007	0.008	0.015	0.014	0.005	0.002	0.006	0.013	0.000	0.000	0.005
Fe3	0.000	0.000	0.000	0.000	0.000	0.000	0.000	0.000	0.000	0.000	0.000	0.000	0.000	0.000	0.000	0.000
Fe2	3.118	3.086	3.037	3.007	3.096	2.974	3.089	3.198	3.162	3.027	3.079	3.145	3.190	3.105	3.106	2.968
Mn	0.128	0.135	0.132	0.109	0.128	0.103	0.093	0.083	0.102	0.113	0.115	0.111	0.122	0.107	0.107	0.130
Mg	0.453	0.577	0.533	0.710	0.470	0.575	0.961	0.968	0.683	0.568	0.521	0.567	0.519	0.595	0.575	0.575
Ca	0.012	0.004	0.001	0.003	0.000	0.003	0.004	0.002	0.000	0.000	0.000	0.008	0.000	0.007	0.000	0.000
Na	0.000	0.000	0.010	0.001	0.001	0.007	0.011	0.009	0.001	0.002	0.000	0.000	0.004	0.000	0.001	0.000
K	0.008	0.000	0.005	0.006	0.005	0.018	0.050	0.081	0.003	0.002	0.000	0.007	0.004	0.010	0.002	0.002
Sum	29.355	29.348	29.297	29.347	29.294	29.236	29.382	29.478	29.360	29.262	29.282	29.362	29.388	29.381	29.341	29.309
XMg	0.13	0.16	0.15	0.19	0.13	0.16	0.24	0.23	0.18	0.16	0.14	0.15	0.14	0.16	0.16	0.16

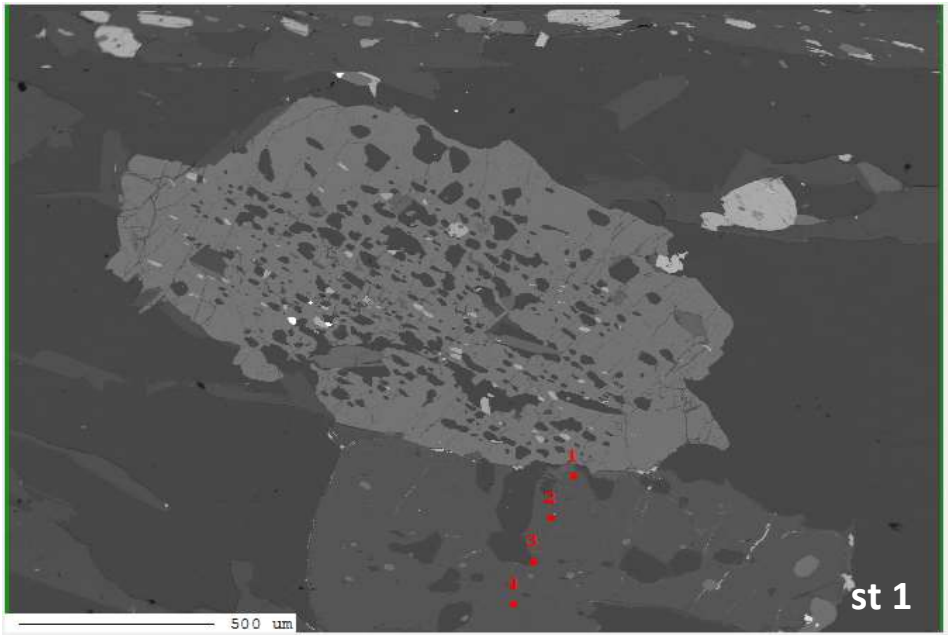

Project : DR378
Image : image004
Date : 2019/12/13 11:09:37
Acc. : 15 kV
Signal Type : COMPO

No.	Data Name	Type	Pos.	Comment
1	DR378_0005	QNT	1	st1 Line 00
2	DR378_0005	QNT	2	st1 Line 00
3	DR378_0005	QNT	3	st1 Line 00
4	DR378_0005	QNT	4	st1 Line 00

Delete | Reset Position | Open Data
Clear | Marker Label : Number
Marker Style

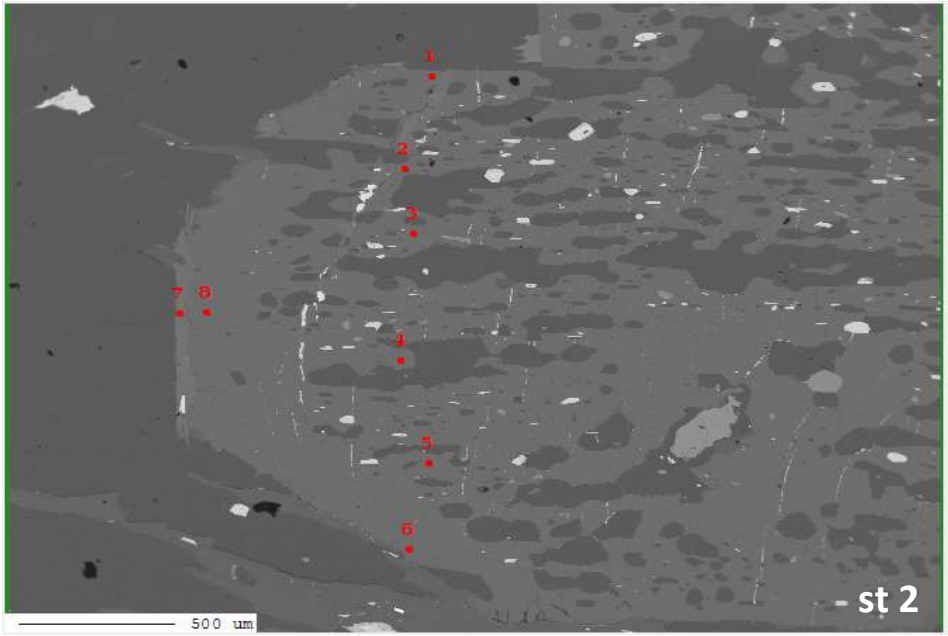

Project : DR378
Image : image008
Date : 2019/12/13 11:30:27
Acc. : 15 kV
Signal Type : COMPO

No.	Data Name	Type	Pos.	Comment
1	DR378_0005	QNT	14	st3 Line 00
2	DR378_0005	QNT	15	st3 Line 00
3	DR378_0005	QNT	16	st3 Line 00
4	DR378_0005	QNT	17	st3 Line 00
5	DR378_0005	QNT	18	st3 Line 00
6	DR378_0005	QNT	19	st3 Line 00
7	DR378_0005	QNT	20	st3 Line 00
8	DR378_0005	QNT	21	st3 Line 00

Delete | Reset Position | Open Data
Clear | Marker Label : Number
Marker Style

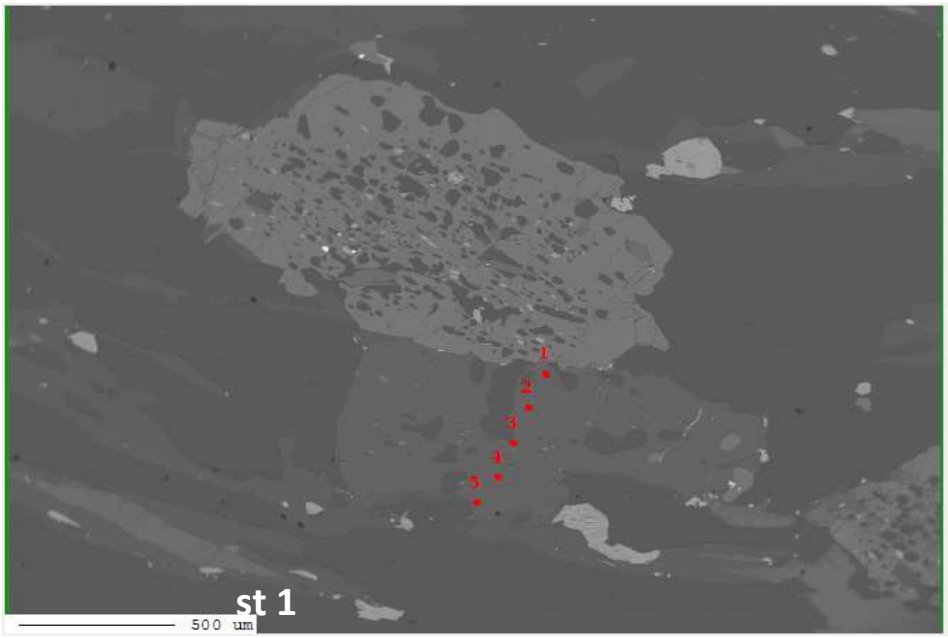

Project : DR378
Image : image001
Date : 2019/12/12 19:53:32
Acc. : 15 kV
Signal Type : COMPO

No.	Data Name	Type	Pos.	Comment
1	DR378_0005	QNT	1	st1 Line 00
2	DR378_0005	QNT	2	st1 Line 00
3	DR378_0005	QNT	3	st1 Line 00
4	DR378_0005	QNT	4	st1 Line 00
5	DR378_0005	QNT	5	st1 Line 00

Delete | Reset Position | Open Data

Clear | Marker Label : Number

Marker Style

Sample:DR352

Mineral:plagioclase

Sample	pl1	pl2	pl3	pl4	pl5
SiO2	68.27	64.47	64.99	66.22	66.93
TiO2	0.00	0.02	0.00	0.00	0.01
Al2O3	20.15	22.53	22.97	21.09	21.12
Cr2O3	0.00	0.00	0.00	0.00	0.00
Fe2O3	0.04	0.04	0.04	0.04	0.04
FeO	0.00	0.07	0.01	0.07	0.00
MnO	0.00	0.00	0.02	0.01	0.00
MgO	0.00	0.00	0.00	0.00	0.00
CaO	0.23	2.40	1.37	0.97	1.25
Na2O	11.49	9.84	9.70	10.78	10.87
K2O	0.04	0.55	1.06	0.32	0.06
Totals	100.21	99.91	100.16	99.50	100.28
Oxygens	8.000	8.000	8.000	8.000	8.000
Si	2.974	2.844	2.853	2.918	2.923
Ti	0.000	0.000	0.000	0.000	0.000
Al	1.035	1.172	1.189	1.096	1.087
Cr	0.000	0.000	0.000	0.000	0.000
Fe3	0.001	0.001	0.001	0.001	0.001
Fe2	0.000	0.003	0.000	0.002	0.000
Mn	0.000	0.000	0.001	0.000	0.000
Mg	0.000	0.000	0.000	0.000	0.000
Ca	0.011	0.113	0.065	0.046	0.059
Na	0.971	0.842	0.826	0.921	0.920
K	0.002	0.031	0.059	0.018	0.003
Sum	4.994	5.006	4.994	5.003	4.994
Anorthite	0.01	0.11	0.07	0.05	0.06

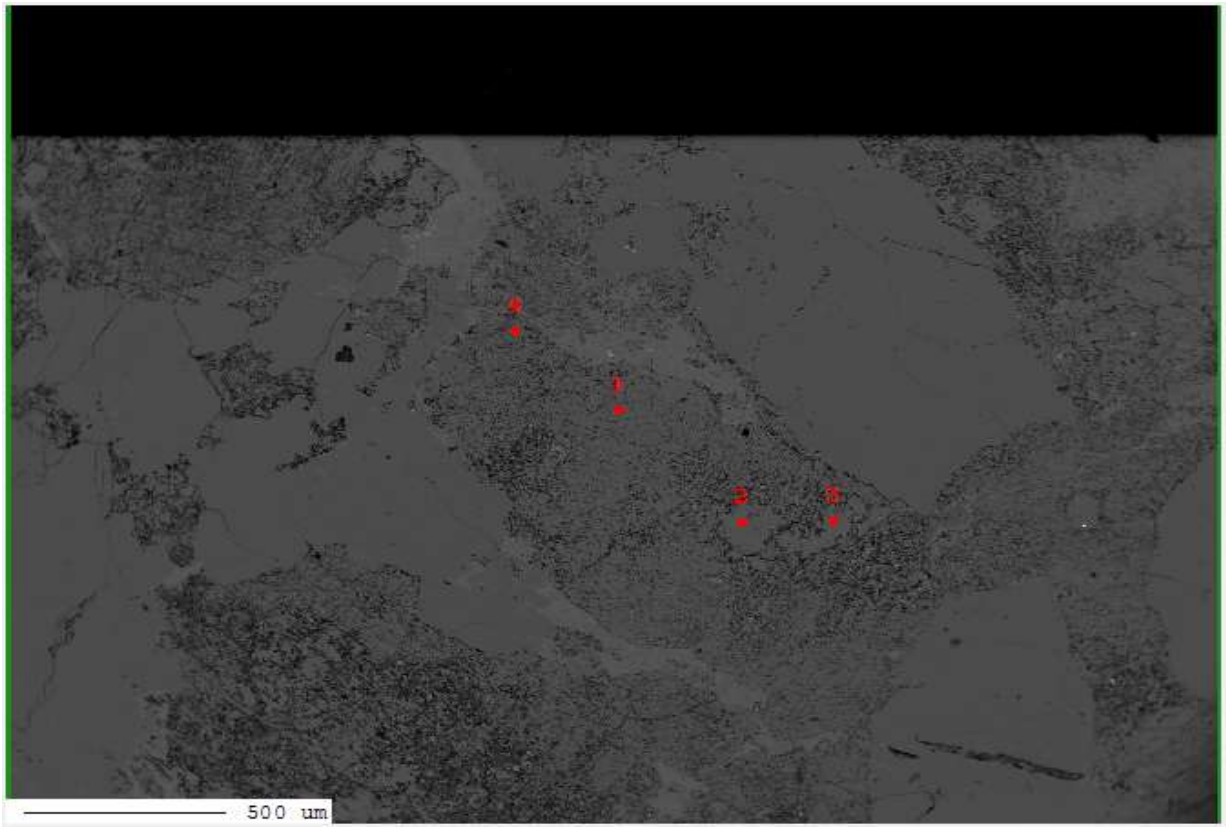

Project : DR352
Image : image008
Date : 2019/12/12 17:50:57
Acc. : 15 kV
Signal Type : COMPO

No.	Data Name	Type	Pos.	Comment
1	DR352_0005	QNT	1	pl1
2	DR352_0005	QNT	2	pl2
3	DR352_0005	QNT	3	pl3
4	DR352_0005	QNT	4	pl4

Delete | Reset Position | Open Data

Clear | Marker Label : Number

Marker Style

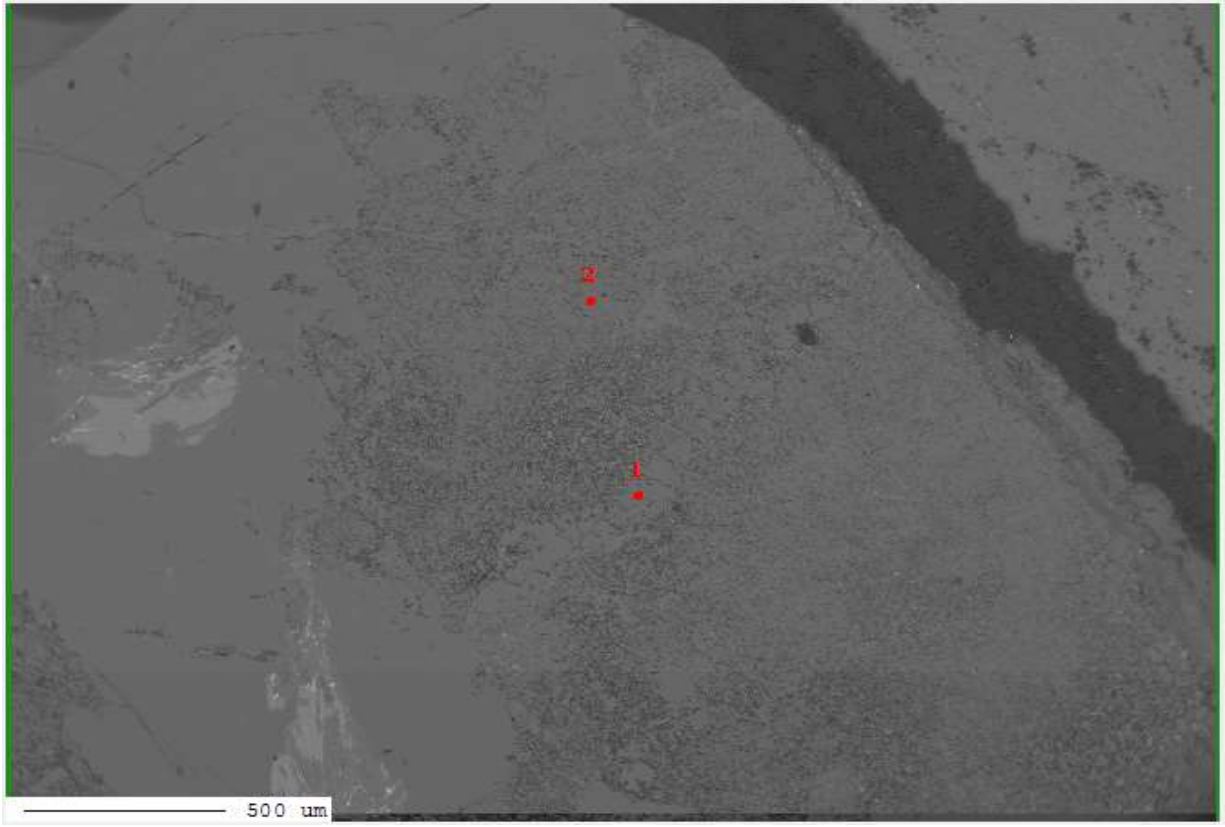

Project : DR352
Image : image009
Date : 2019/12/12 17:53:31
Acc. : 15 kV
Signal Type : COMPO

No.	Data Name	Type	Pos.	Comment
1	DR352_0005	QNT	5	pl5
2	DR352_0005	QNT	6	pl6

Delete | Reset Position | Open Data

Clear | Marker Label : Number

Marker Style

Sample:DR352
Mineral:biotite

Sample	bt1	bt2	bt3	bt4	bt5	bt6	bt7	bt8
SiO2	33.80	33.79	33.60	33.99	33.69	33.14	33.90	33.12
TiO2	2.91	2.85	2.84	3.00	2.85	2.83	2.88	2.87
Al2O3	19.31	19.64	19.86	19.52	19.97	19.19	19.52	19.33
Cr2O3	0.00	0.00	0.00	0.00	0.00	0.00	0.00	0.00
Fe2O3	0.00	0.00	0.36	0.36	0.36	0.36	0.36	0.36
FeO	25.35	24.56	24.78	24.55	24.91	25.67	24.57	26.25
MnO	0.18	0.17	0.16	0.13	0.16	0.14	0.14	0.14
MgO	5.84	5.87	6.20	6.16	5.63	6.30	6.08	5.78
CaO	0.00	0.00	0.01	0.02	0.02	0.00	0.00	0.02
Na2O	0.08	0.10	0.13	0.14	0.09	0.08	0.06	0.10
K2O	8.73	8.84	8.58	8.95	8.92	8.30	8.85	8.43
Totals	96.20	95.81	96.51	96.82	96.59	96.01	96.35	96.39
Oxygens	11.000	11.000	11.000	11.000	11.000	11.000	11.000	11.000
Si	2.621	2.622	2.590	2.613	2.600	2.581	2.617	2.578
Ti	0.170	0.166	0.165	0.173	0.165	0.166	0.167	0.168
Al	1.766	1.797	1.805	1.769	1.817	1.762	1.777	1.774
Cr	0.000	0.000	0.000	0.000	0.000	0.000	0.000	0.000
Fe3	0.000	0.000	0.021	0.021	0.021	0.021	0.021	0.021
Fe2	1.644	1.594	1.597	1.578	1.608	1.672	1.586	1.709
Mn	0.012	0.011	0.010	0.009	0.010	0.009	0.009	0.009
Mg	0.675	0.679	0.712	0.706	0.648	0.731	0.700	0.671
Ca	0.000	0.000	0.001	0.001	0.001	0.000	0.000	0.001
Na	0.012	0.014	0.019	0.021	0.014	0.012	0.009	0.015
K	0.864	0.875	0.844	0.878	0.878	0.825	0.872	0.837
Sum	7.764	7.759	7.765	7.769	7.762	7.780	7.758	7.783
XMg	0.29	0.30	0.31	0.31	0.29	0.30	0.31	0.28

Sample:DR352

Mineral:muscovite

Sample	ms1	ms2	ms3	ms4
SiO2	46.74	46.87	46.37	48.65
TiO2	0.70	0.55	0.82	0.83
Al2O3	39.42	38.74	39.16	39.41
Cr2O3	0.00	0.00	0.00	0.00
Fe2O3	1.06	1.06	1.06	1.06
FeO	0.41	1.23	1.23	1.53
MnO	0.01	0.00	0.00	0.01
MgO	0.54	0.60	0.55	0.47
CaO	0.02	0.00	0.00	0.01
Na2O	0.51	0.50	0.55	0.41
K2O	6.21	6.49	6.29	5.42
Totals	95.61	96.03	96.02	97.80
Oxygens	11.000	11.000	11.000	11.000
Si	3.005	3.018	2.986	3.053
Ti	0.034	0.026	0.039	0.039
Al	2.988	2.941	2.973	2.916
Cr	0.000	0.000	0.000	0.000
Fe3	0.051	0.051	0.051	0.050
Fe2	0.022	0.066	0.066	0.080
Mn	0.000	0.000	0.000	0.000
Mg	0.051	0.058	0.053	0.044
Ca	0.002	0.000	0.000	0.000
Na	0.064	0.062	0.068	0.050
K	0.509	0.533	0.517	0.434
Sum	6.728	6.757	6.755	6.667
XMg	0.70	0.47	0.45	0.35
Al/Si	0.99	0.97	1.00	0.96

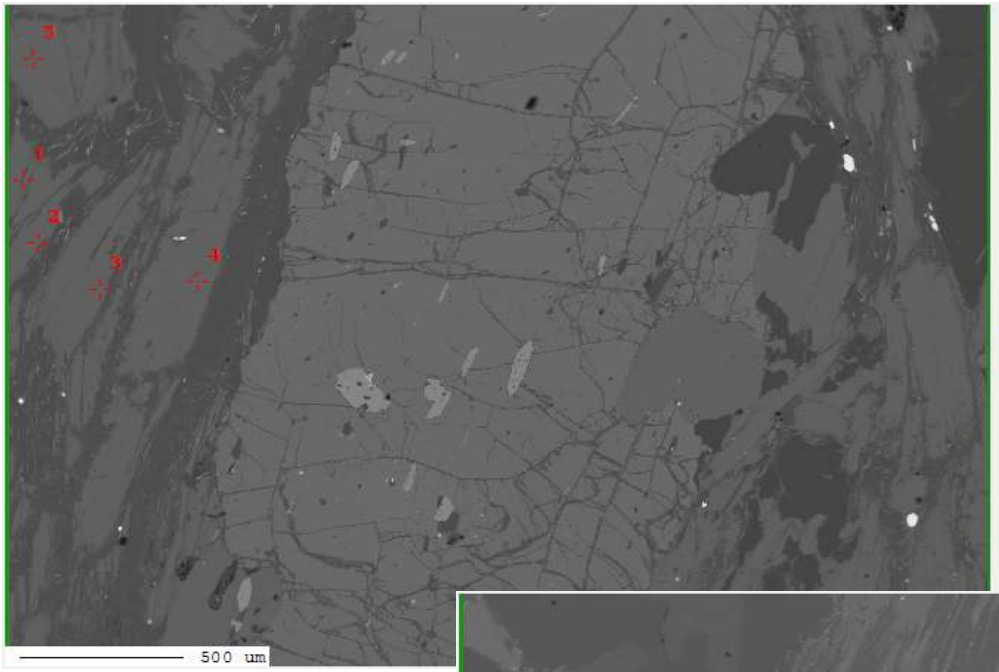

Project : DR352
Image : image004
Date : 2019/12/11 10:24:52
Acc. : 15 kV
Signal Type : COMPO

No.	Data Name	Type	Pos.	Comment
1	DR352_0003	QNT	2	bt2
2	DR352_0003	QNT	3	bt3
3	DR352_0003	QNT	4	bt4
4	DR352_0003	QNT	5	bt5
5	DR352_0003	QNT	6	bt6

Delete | Reset Position | Open Data

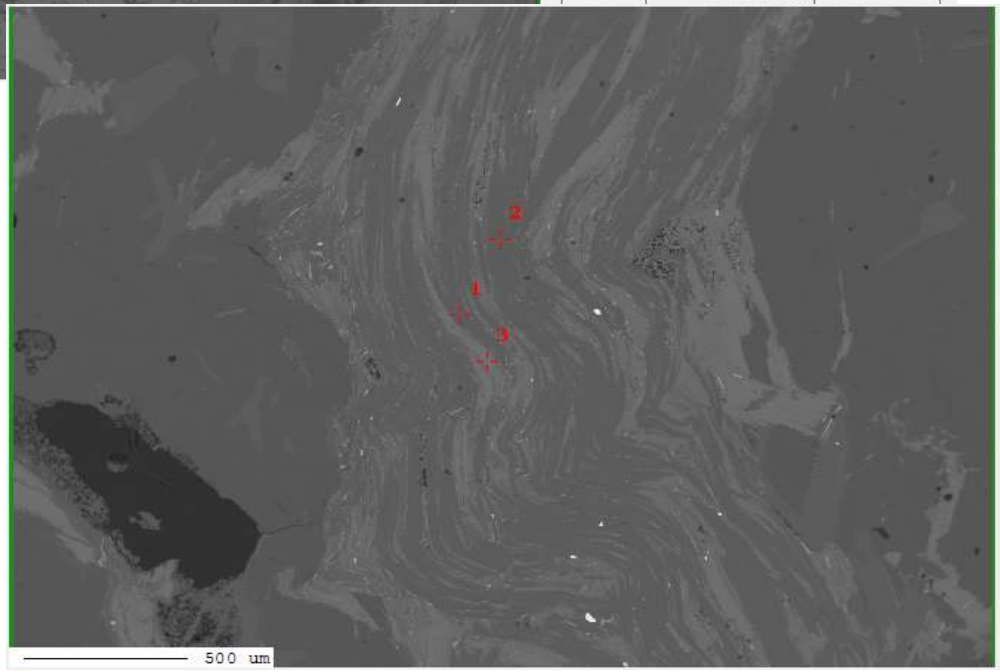

Project : DR352
Image : image007
Date : 2019/12/11 10:36:03
Acc. : 15 kV
Signal Type : COMPO

No.	Data Name	Type	Pos.	Comment
1	DR352_0003	QNT	11	ms4
2	DR352_0003	QNT	12	ms5
3	DR352_0003	QNT	13	bt8

Delete | Reset Position | Open Data

Clear | Marker Label : Number

Marker Style

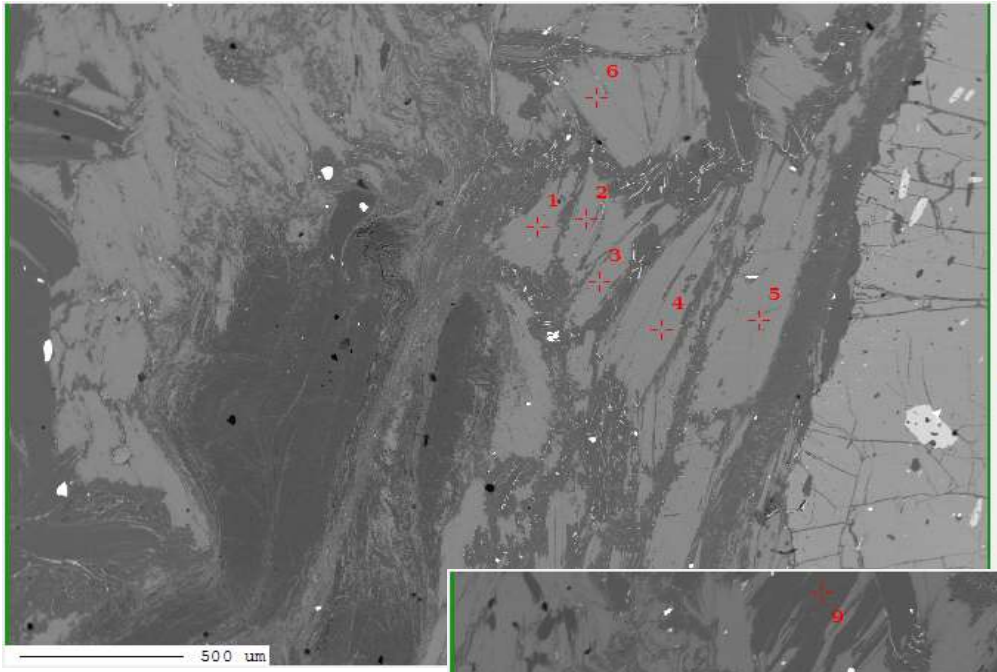

Project : DR352
Image : image005
Date : 2019/12/11 10:29:44
Acc. : 15 kV
Signal Type : COMPO

No.	Data Name	Type	Pos.	Comment
1	DR352_0003	QNT	1	bt1
2	DR352_0003	QNT	2	bt2
3	DR352_0003	QNT	3	bt3
4	DR352_0003	QNT	4	bt4
5	DR352_0003	QNT	5	bt5
6	DR352_0003	QNT	6	bt6

Delete | Reset Position | Open Data

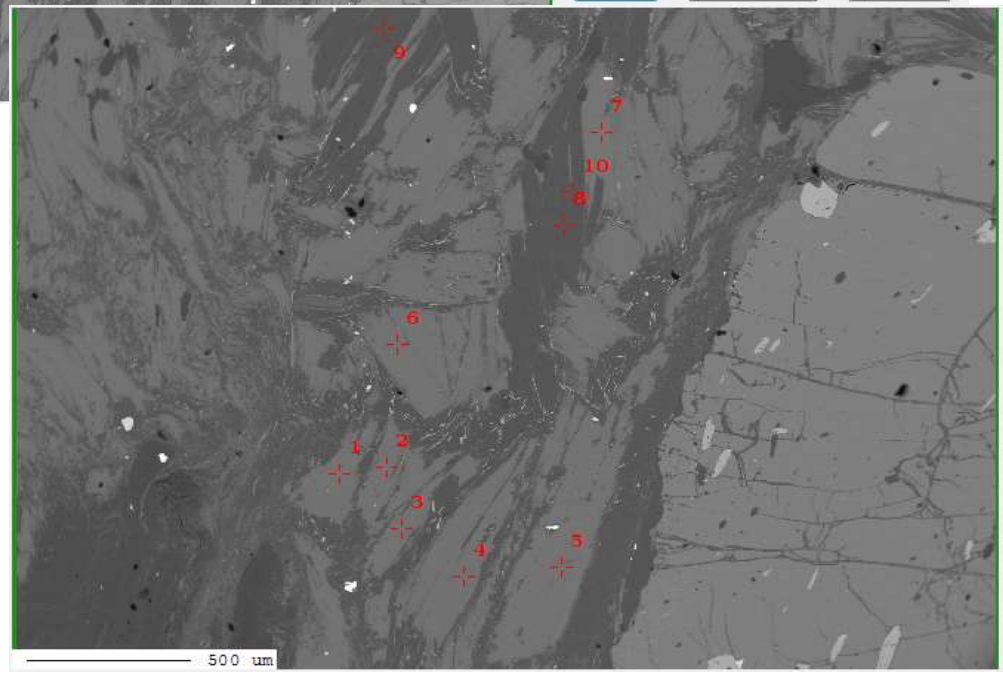

Project : DR352
Image : image006
Date : 2019/12/11 10:32:22
Acc. : 15 kV
Signal Type : COMPO

No.	Data Name	Type	Pos.	Comment
1	DR352_0003	QNT	1	bt1
2	DR352_0003	QNT	2	bt2
3	DR352_0003	QNT	3	bt3
4	DR352_0003	QNT	4	bt4
5	DR352_0003	QNT	5	bt5
6	DR352_0003	QNT	6	bt6
7	DR352_0003	QNT	7	bt7
8	DR352_0003	QNT	8	ms1
9	DR352_0003	QNT	9	ms2
10	DR352_0003	QNT	10	ms3

Delete | Reset Position | Open Data

Clear | Marker Label : Number

Marker Style

Sample:DR352

Mineral:garnet

				Z3			Z2						Z1						
Sample	grt1.1	grt1.2	grt1.3	grt1.4	grt1.5	grt1.6	grt1.7	grt1.8	grt1.9	grt1.10	grt1.11	grt1.12	grt1.13	grt1.14	grt1.15	grt1.16.3	grt1.16.4	grt1.16.5	grt1.16.6
SiO2	36.15	36.44	36.42	36.18	36.62	36.66	36.61	36.50	36.61	36.15	36.17	35.93	36.33	36.21	36.17	35.82	36.07	36.45	36.41
TiO2	0.02	0.04	0.01	0.05	0.01	0.12	0.02	0.06	0.09	0.03	0.03	0.04	0.01	0.13	0.02	0.04	0.03	0.03	0.04
Al2O3	20.82	20.90	21.03	20.81	20.92	20.77	20.81	20.71	20.74	20.89	20.59	20.80	20.78	20.64	20.71	20.83	20.79	20.93	20.81
Cr2O3	0.02	0.01	0.02	0.05	0.02	0.00	0.03	0.01	0.01	0.01	0.02	0.04	0.02	0.04	0.00	0.02	0.05	0.00	0.04
Fe2O3	2.17	2.17	2.17	2.17	2.17	2.17	2.17	2.17	2.17	2.17	2.17	2.17	2.17	2.17	2.17	2.17	2.17	2.17	2.17
FeO	34.64	38.27	38.66	38.00	38.35	35.55	36.03	35.30	34.69	34.71	33.89	33.69	32.75	33.86	35.10	36.32	36.48	35.57	35.73
MnO	2.73	0.40	0.39	0.53	0.82	1.42	1.80	2.34	2.84	3.12	3.55	3.75	3.68	3.58	2.99	3.68	2.63	3.15	3.98
MgO	2.13	2.31	2.22	2.15	1.96	1.73	1.64	1.51	1.38	1.53	1.23	1.15	1.14	1.23	1.52	1.95	2.00	1.98	2.00
CaO	1.59	1.83	1.95	1.97	2.06	3.04	3.36	3.46	3.74	3.34	3.61	4.09	4.52	4.01	2.98	1.38	1.73	1.65	1.33
Na2O	0.00	0.00	0.00	0.00	0.01	0.02	0.02	0.02	0.03	0.00	0.02	0.02	0.03	0.01	0.00	0.01	0.01	0.00	0.02
K2O	0.00	0.00	0.00	0.00	0.00	0.00	0.00	0.00	0.00	0.00	0.00	0.00	0.00	0.00	0.00	0.00	0.00	0.00	0.00
Totals	100.26	102.37	102.87	101.92	102.94	101.48	102.49	102.08	102.29	101.95	101.27	101.68	101.44	101.88	101.67	102.22	101.96	101.93	102.52
Oxygens	12.000	12.000	12.000	12.000	12.000	12.000	12.000	12.000	12.000	12.000	12.000	12.000	12.000	12.000	12.000	12.000	12.000	12.000	12.000
Si	2.936	2.913	2.902	2.908	2.917	2.943	2.924	2.927	2.929	2.906	2.926	2.900	2.926	2.914	2.917	2.887	2.904	2.925	2.916
Ti	0.001	0.002	0.001	0.003	0.000	0.007	0.001	0.004	0.005	0.002	0.002	0.002	0.001	0.008	0.001	0.002	0.002	0.002	0.003
Al	1.993	1.970	1.976	1.972	1.965	1.966	1.959	1.958	1.956	1.980	1.964	1.979	1.973	1.958	1.969	1.979	1.973	1.980	1.965
Cr	0.001	0.001	0.001	0.003	0.001	0.000	0.002	0.001	0.001	0.001	0.001	0.002	0.001	0.003	0.000	0.001	0.003	0.000	0.002
Fe3	0.133	0.131	0.130	0.131	0.130	0.131	0.131	0.131	0.131	0.131	0.132	0.132	0.132	0.132	0.132	0.132	0.132	0.131	0.131
Fe2	2.352	2.559	2.577	2.554	2.555	2.387	2.406	2.367	2.321	2.334	2.293	2.274	2.206	2.279	2.367	2.448	2.456	2.387	2.393
Mn	0.188	0.027	0.026	0.036	0.055	0.097	0.122	0.159	0.192	0.212	0.243	0.256	0.251	0.244	0.204	0.251	0.179	0.214	0.270
Mg	0.258	0.275	0.264	0.258	0.233	0.207	0.195	0.181	0.164	0.183	0.148	0.138	0.137	0.148	0.183	0.234	0.240	0.237	0.239
Ca	0.138	0.157	0.167	0.170	0.176	0.262	0.288	0.297	0.321	0.288	0.313	0.354	0.390	0.346	0.258	0.119	0.149	0.142	0.114
Na	0.000	0.000	0.000	0.001	0.002	0.003	0.003	0.002	0.004	0.000	0.002	0.004	0.005	0.001	0.000	0.001	0.002	0.000	0.002
K	0.000	0.000	0.000	0.000	0.000	0.000	0.000	0.000	0.000	0.000	0.000	0.000	0.000	0.000	0.000	0.000	0.000	0.000	0.000
Sum	8.000	8.034	8.044	8.036	8.035	8.002	8.030	8.026	8.024	8.037	8.025	8.042	8.022	8.032	8.031	8.055	8.041	8.018	8.034
Alm	0.80	0.85	0.85	0.85	0.85	0.81	0.80	0.79	0.77	0.77	0.77	0.75	0.74	0.76	0.79	0.80	0.81	0.80	0.79
Grs	0.05	0.05	0.06	0.06	0.06	0.09	0.10	0.10	0.11	0.10	0.10	0.12	0.13	0.11	0.09	0.04	0.05	0.05	0.04
Pyr	0.09	0.09	0.09	0.09	0.08	0.07	0.06	0.06	0.05	0.06	0.05	0.05	0.05	0.05	0.06	0.08	0.08	0.08	0.08
Sps	0.06	0.01	0.01	0.01	0.02	0.03	0.04	0.05	0.06	0.07	0.08	0.08	0.08	0.08	0.07	0.08	0.06	0.07	0.09

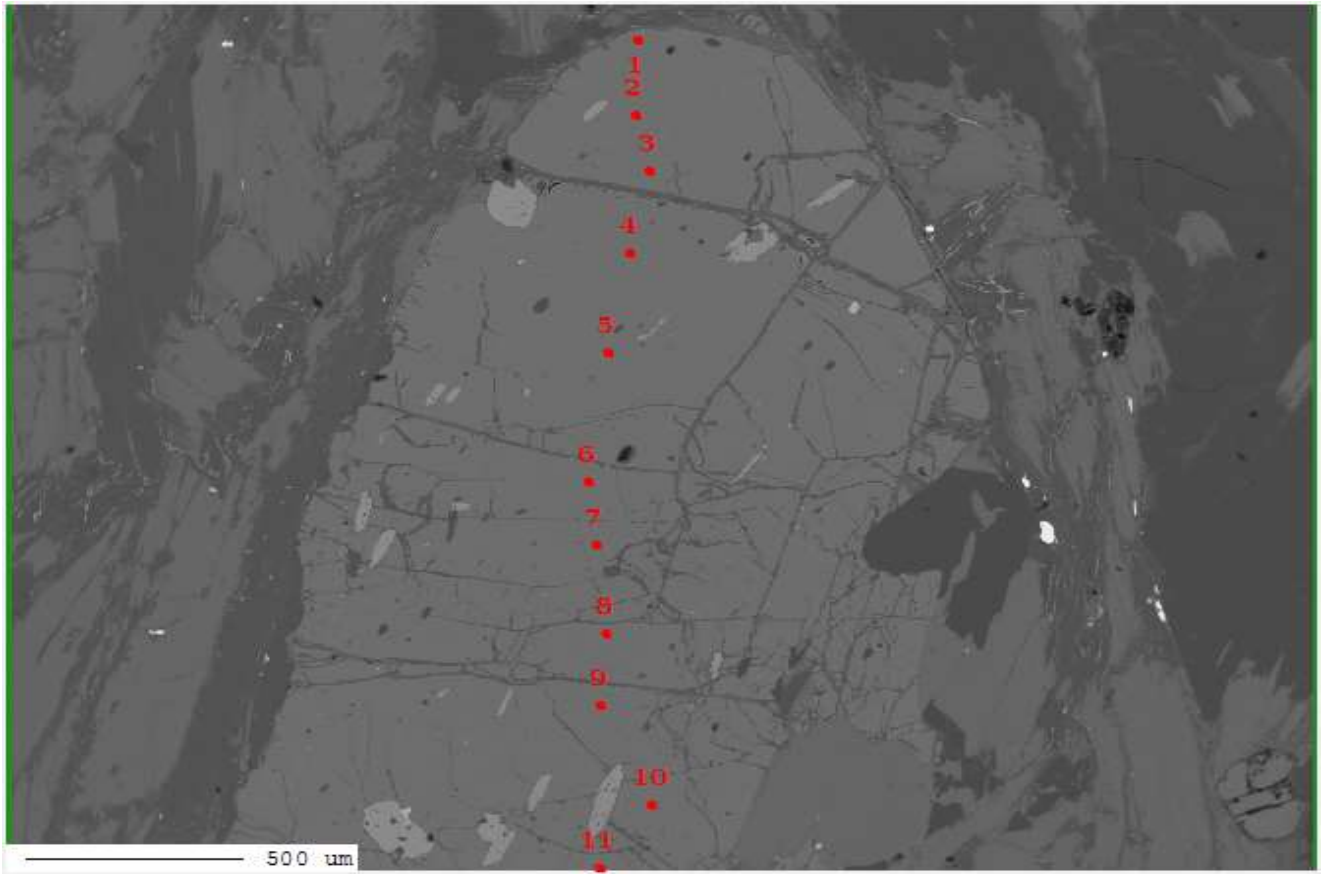
1
2
3
4
5
6
7
8
9
10
11
500 um

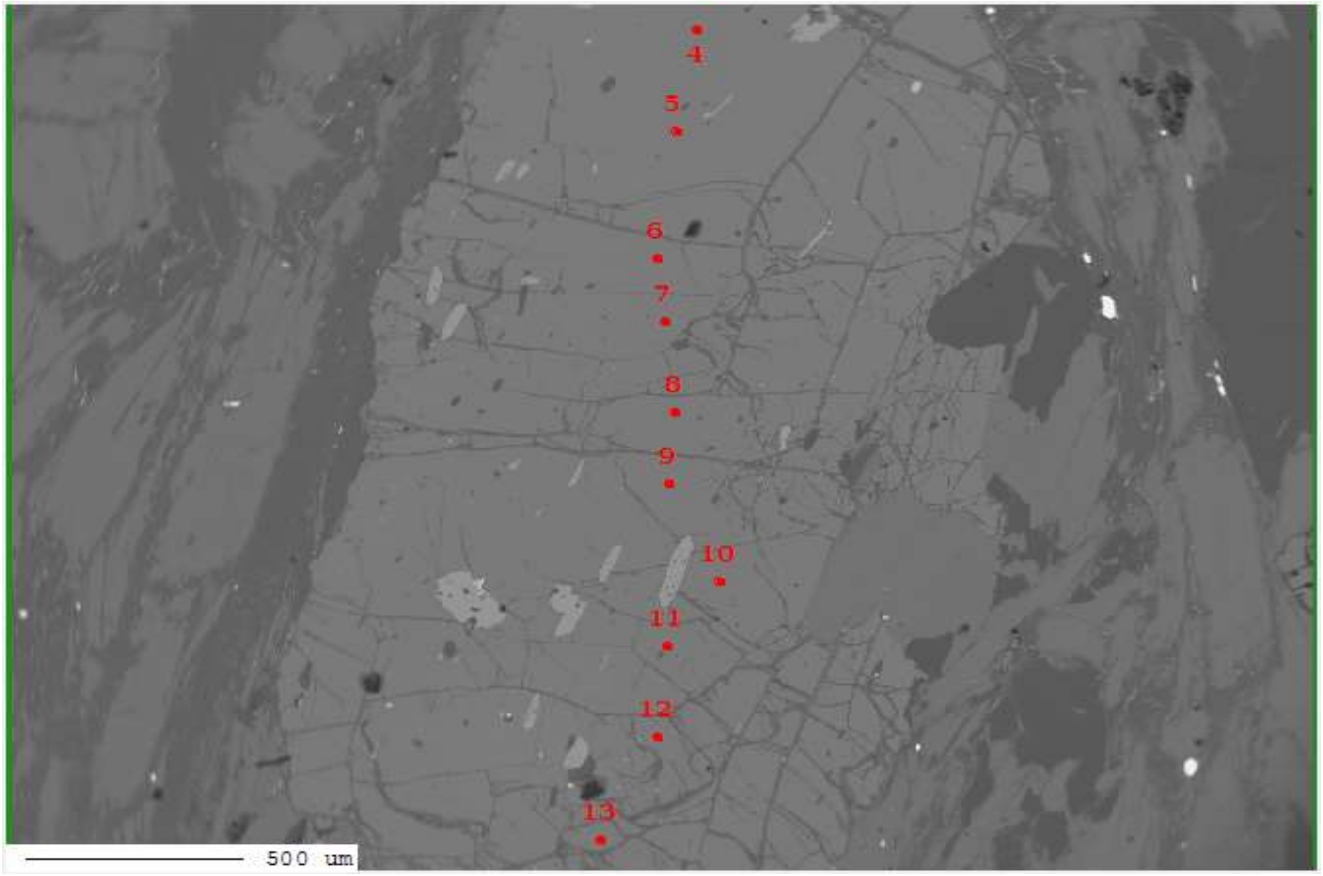
4
5
6
7
8
9
10
11
12
13
500 um

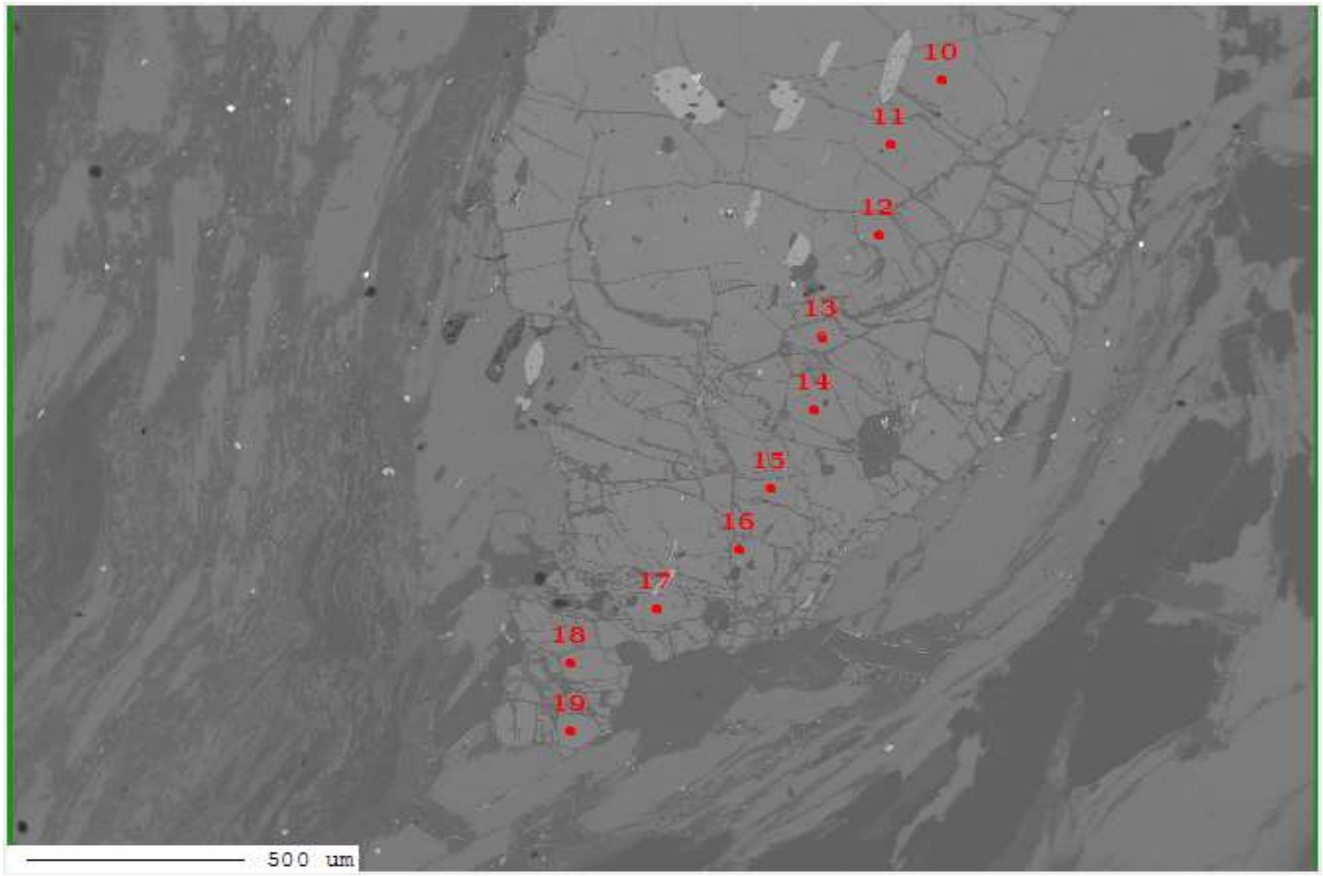
10
11
12
13
14
15
16
17
18
19
500 um

Sample:BR04A
Mineral:plagioclase

Sample	pl4.1	pl4.2	pl4.3	pl5.1	pl5.2	pl5.4	pl5.5	pl5.1	pl5.2	pl5.3	pl5.4	pl5.5	pl6.3	pl6.4	pl6.5	pl6.6
SiO2	62.67	62.92	63.19	62.02	63.34	62.78	62.98	63.06	62.41	62.75	63.00	62.53	62.77	71.79	63.50	63.01
TiO2	0.02	0.01	0.00	0.00	0.00	0.02	0.00	0.00	0.00	0.00	0.00	0.00	0.03	0.03	0.02	0.00
Al2O3	24.27	24.47	24.51	24.18	24.22	24.32	24.13	24.17	23.91	24.06	24.06	24.21	24.19	17.58	23.78	24.08
Cr2O3	0.00	0.00	0.00	0.00	0.00	0.00	0.00	0.00	0.00	0.00	0.00	0.00	0.00	0.00	0.00	0.00
Fe2O3	0.18	0.18	0.18	0.18	0.18	0.18	0.18	0.18	0.18	0.18	0.18	0.18	0.18	0.18	0.18	0.18
FeO	0.00	0.18	0.15	0.15	0.11	0.11	0.11	0.11	0.10	0.16	0.18	0.36	0.21	0.20	0.14	0.11
MnO	0.01	0.01	0.00	0.00	0.00	0.00	0.01	0.01	0.01	0.00	0.00	0.00	0.00	0.00	0.01	0.01
MgO	0.00	0.00	0.00	0.00	0.00	0.00	0.00	0.00	0.00	0.00	0.00	0.00	0.00	0.00	0.00	0.00
CaO	4.79	4.95	4.89	4.84	4.69	4.92	4.46	4.57	4.67	4.56	4.64	4.80	4.86	2.63	4.22	4.84
Na2O	8.93	8.84	8.69	8.93	8.87	8.75	8.86	8.97	8.99	8.99	8.84	8.95	8.94	7.65	9.18	8.94
K2O	0.06	0.08	0.05	0.11	0.07	0.10	0.20	0.08	0.10	0.09	0.09	0.09	0.11	0.08	0.06	0.08
Totals	100.93	101.63	101.66	100.41	101.47	101.17	100.93	101.14	100.37	100.78	100.98	101.11	101.29	100.15	101.08	101.24
Oxygens	8.000	8.000	8.000	8.000	8.000	8.000	8.000	8.000	8.000	8.000	8.000	8.000	8.000	8.000	8.000	8.000
Si	2.750	2.745	2.751	2.741	2.762	2.749	2.762	2.760	2.756	2.758	2.762	2.745	2.749	3.098	2.778	2.758
Ti	0.000	0.000	0.000	0.000	0.000	0.001	0.000	0.000	0.000	0.000	0.000	0.000	0.001	0.001	0.001	0.000
Al	1.255	1.258	1.258	1.260	1.245	1.255	1.248	1.247	1.245	1.247	1.243	1.253	1.249	0.894	1.227	1.242
Cr	0.000	0.000	0.000	0.000	0.000	0.000	0.000	0.000	0.000	0.000	0.000	0.000	0.000	0.000	0.000	0.000
Fe3	0.006	0.006	0.006	0.006	0.006	0.006	0.006	0.006	0.006	0.006	0.006	0.006	0.006	0.006	0.006	0.006
Fe2	0.000	0.006	0.006	0.005	0.004	0.004	0.004	0.004	0.004	0.006	0.006	0.013	0.008	0.007	0.005	0.004
Mn	0.000	0.000	0.000	0.000	0.000	0.000	0.000	0.000	0.000	0.000	0.000	0.000	0.000	0.000	0.000	0.000
Mg	0.000	0.000	0.000	0.000	0.000	0.000	0.000	0.000	0.000	0.000	0.000	0.000	0.000	0.000	0.000	0.000
Ca	0.225	0.231	0.228	0.229	0.219	0.231	0.210	0.214	0.221	0.215	0.218	0.226	0.228	0.122	0.198	0.227
Na	0.760	0.748	0.734	0.765	0.750	0.743	0.753	0.761	0.770	0.766	0.751	0.762	0.759	0.640	0.779	0.759
K	0.004	0.004	0.003	0.006	0.004	0.005	0.011	0.004	0.005	0.005	0.005	0.005	0.006	0.004	0.003	0.004
Sum	5.001	4.999	4.985	5.012	4.990	4.994	4.994	4.997	5.007	5.002	4.992	5.009	5.006	4.773	4.996	5.000
Anortite	0.23	0.23	0.24	0.23	0.23	0.24	0.22	0.22	0.22	0.22	0.22	0.23	0.23	0.16	0.20	0.23
			avPT													

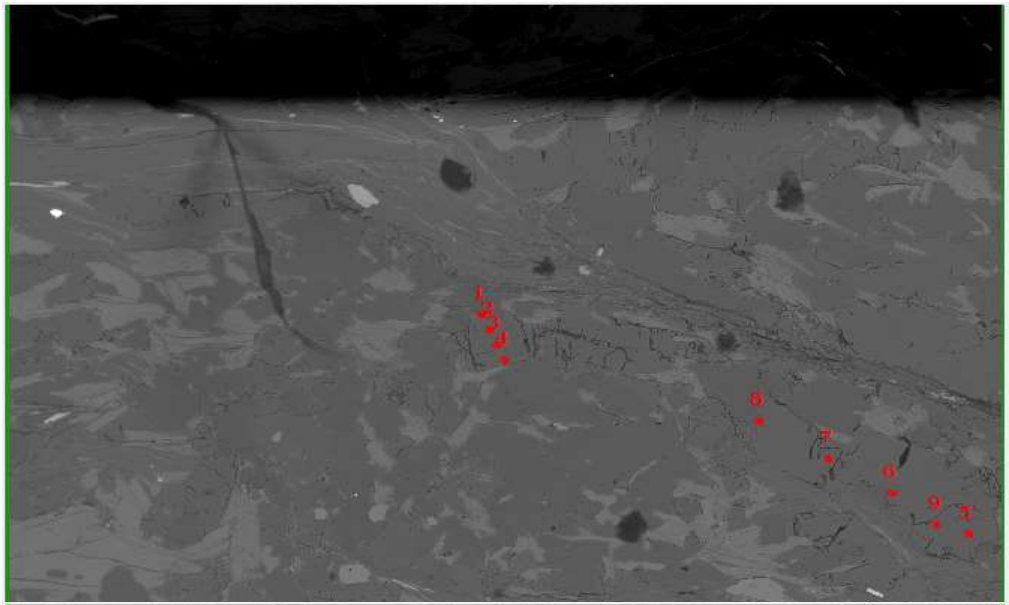

Project : BR04A
Image : image013
Date : 2019/12/10 16:26:18
Acc. : 15 kV
Signal Type : COMPO

No.	Data Name	Type	Pos.	Comment
1	BR04A_0009	QNT	1	pl4 Line 00
2	BR04A_0009	QNT	2	pl4 Line 00
3	BR04A_0009	QNT	3	pl4 Line 00
4	BR04A_0009	QNT	4	pl4 Line 00
5	BR04A_0009	QNT	5	pl4 Line 00
6	BR04A_0009	QNT	6	pl4 Line 00
7	BR04A_0009	QNT	7	pl4 Line 00
8	BR04A_0009	QNT	8	pl4 Line 00
9	BR04A_0009	QNT	9	pl4 Line 00

Delete | Reset Position | Open Data

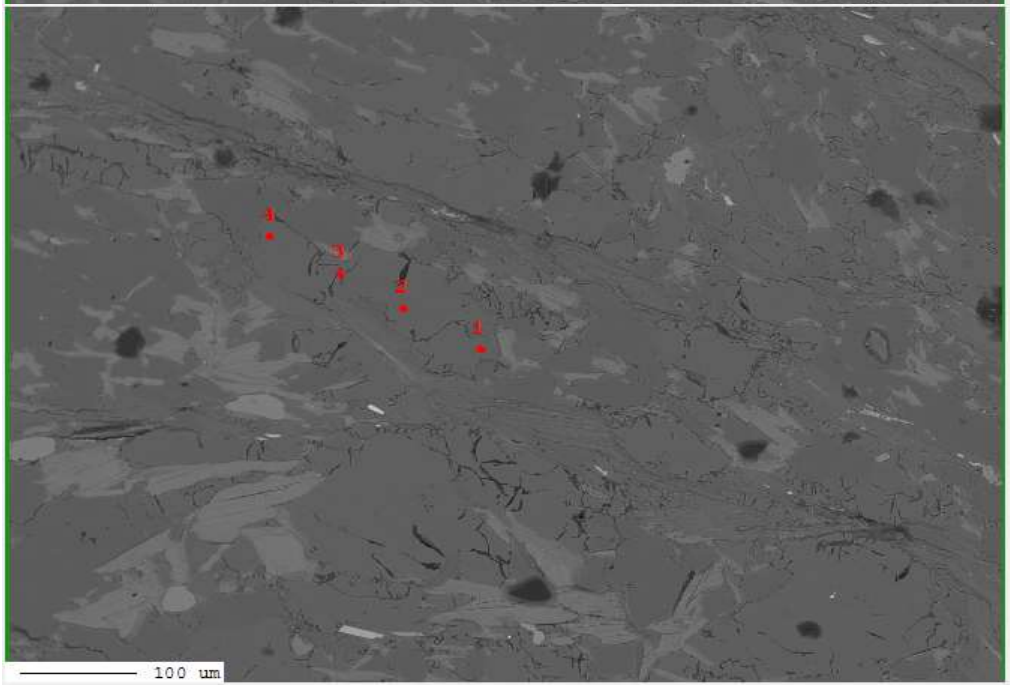

Project : BR04A
Image : image015
Date : 2019/12/10 16:28:43
Acc. : 15 kV
Signal Type : COMPO

No.	Data Name	Type	Pos.	Comment
1	BR04A_0009	QNT	5	pl4 Line 00
2	BR04A_0009	QNT	6	pl4 Line 00
3	BR04A_0009	QNT	7	pl4 Line 00
4	BR04A_0009	QNT	8	pl4 Line 00

Delete | Reset Position | Open Data

Clear | Marker Label : Number

Marker Style

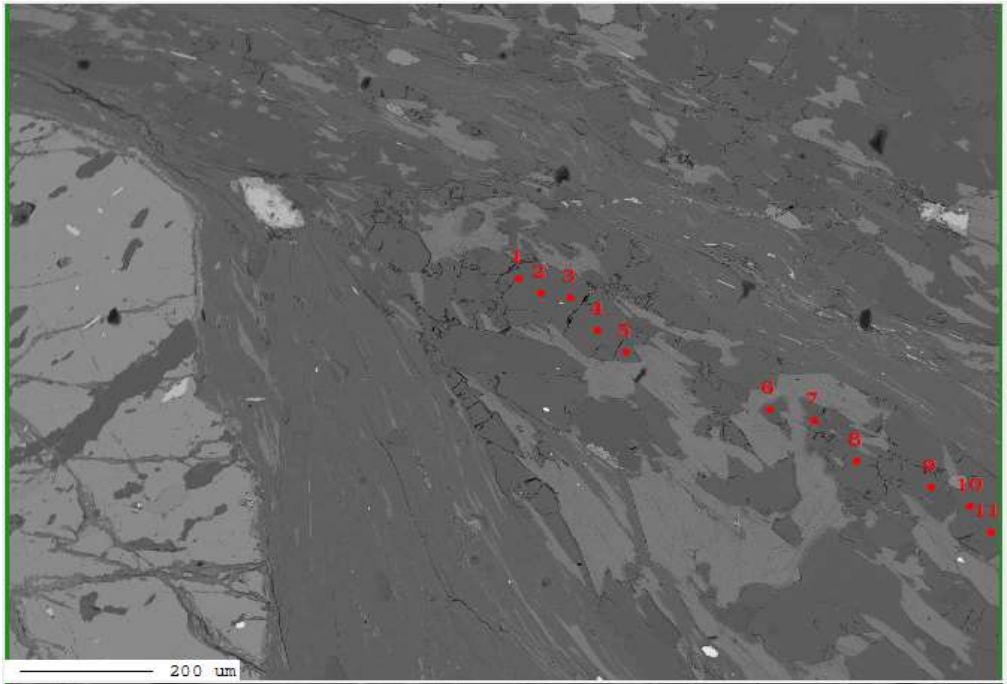

Project : BR04A
Image : image016
Date : 2019/12/10 16:33:39
Acc. : 15 kV
Signal Type : COMPO

No.	Data Name	Type	Pos.	Comme
3	BR04A_0010	QNT	3	pl5 Line
4	BR04A_0010	QNT	4	pl5 Line
5	BR04A_0010	QNT	5	pl5 Line
6	BR04A_0010	QNT	6	pl5 Line
7	BR04A_0010	QNT	7	pl5 Line
8	BR04A_0010	QNT	8	pl5 Line
9	BR04A_0010	QNT	9	pl5 Line
10	BR04A_0010	QNT	10	pl5 Line
11	BR04A_0010	QNT	11	pl5 Line

Delete | Reset Position | Open Data

Clear | Marker Label : Number

Marker Style

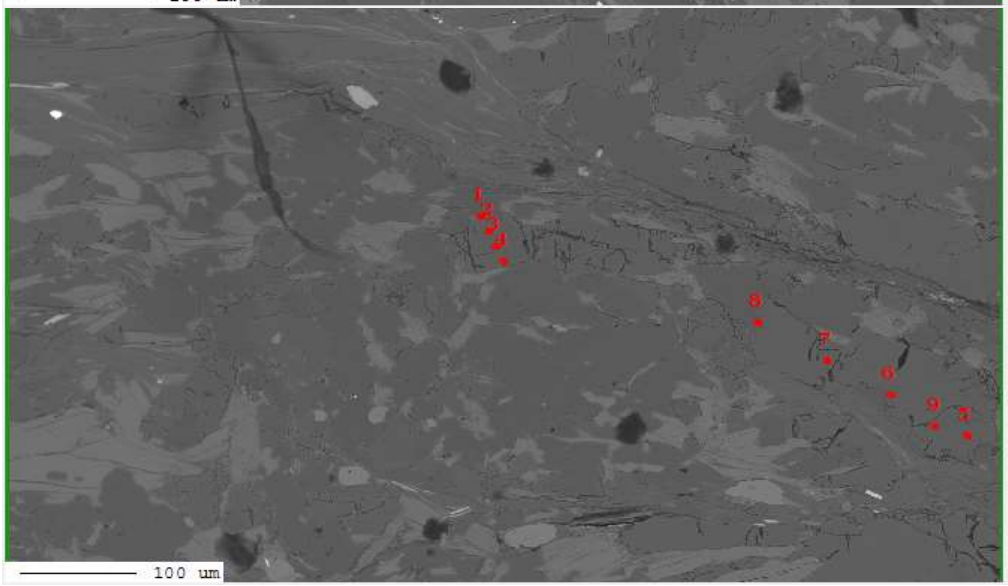

Acc. : 15 kV
Signal Type : COMPO

No.	Data Name	Type	Pos.	Comment
1	BR04A_0009	QNT	1	pl4 Line 00
2	BR04A_0009	QNT	2	pl4 Line 00
3	BR04A_0009	QNT	3	pl4 Line 00
4	BR04A_0009	QNT	4	pl4 Line 00
5	BR04A_0009	QNT	5	pl4 Line 00
6	BR04A_0009	QNT	6	pl4 Line 00
7	BR04A_0009	QNT	7	pl4 Line 00
8	BR04A_0009	QNT	8	pl4 Line 00
9	BR04A_0009	QNT	9	pl4 Line 00

Delete | Reset Position | Open Data

Clear | Marker Label : Number

Marker Style

Sample:BR04A

Mineral:muscovite

Sample	ms1	ms2	ms3	ms5	ms6	ms8	ms9	bt10	bt6
SiO2	45.920	45.970	45.670	44.900	45.430	45.260	46.120	46.260	45.880
TiO2	0.530	0.610	0.510	0.570	0.840	0.640	0.590	0.640	0.510
Al2O3	36.940	36.680	36.890	37.510	36.820	37.410	37.680	37.750	36.490
Cr2O3	0.000	0.000	0.000	0.000	0.000	0.000	0.000	0.000	0.000
Fe2O3	0.470	0.470	0.470	0.470	0.470	0.470	0.470	0.470	0.470
FeO	0.690	1.040	0.970	0.820	1.590	1.040	0.860	0.860	1.680
MnO	0.000	0.000	0.000	0.030	0.010	0.000	0.000	0.030	0.040
MgO	0.640	0.800	0.700	0.520	0.660	0.480	0.510	0.520	0.780
CaO	0.020	0.000	0.010	0.030	0.030	0.020	0.020	0.020	0.090
Na2O	0.720	0.900	1.020	1.140	0.990	1.090	1.120	0.910	0.660
K2O	9.540	9.380	9.330	9.360	9.330	9.470	9.430	9.060	9.040
Totals	95.470	95.850	95.570	95.350	96.170	95.880	96.800	96.520	95.640
Oxygens	11.000	11.000	11.000	11.000	11.000	11.000	11.000	11.000	11.000
Si	3.028	3.025	3.014	2.973	2.992	2.983	3.004	3.012	3.028
Ti	0.026	0.030	0.025	0.028	0.042	0.032	0.029	0.031	0.025
Al	2.871	2.845	2.870	2.928	2.859	2.907	2.893	2.897	2.839
Cr	0.000	0.000	0.000	0.000	0.000	0.000	0.000	0.000	0.000
Fe3	0.023	0.023	0.023	0.024	0.023	0.023	0.023	0.023	0.023
Fe2	0.038	0.058	0.053	0.046	0.088	0.057	0.047	0.047	0.093
Mn	0.000	0.000	0.000	0.002	0.000	0.000	0.000	0.002	0.002
Mg	0.063	0.078	0.069	0.051	0.065	0.047	0.050	0.050	0.077
Ca	0.001	0.000	0.000	0.002	0.002	0.001	0.001	0.001	0.007
Na	0.092	0.115	0.131	0.146	0.127	0.140	0.141	0.115	0.085
K	0.803	0.787	0.786	0.791	0.784	0.796	0.784	0.752	0.761
Sum	6.946	6.962	6.973	6.991	6.981	6.988	6.972	6.931	6.940
XMg	0.62	0.57	0.57	0.53	0.42	0.45	0.52	0.52	0.45
Al/SI	0.95	0.94	0.95	0.98	0.96	0.97	0.96	0.96	0.94

Sample:BR04A
Mineral:biotite

Sample	bt1	bt2	bt4	bt5	bt6	bt11	bt12
SiO2	35.26	35.00	48.46	34.38	35.27	35.97	35.71
TiO2	1.84	1.56	0.84	1.37	1.70	2.11	1.73
Al2O3	20.11	19.50	21.49	19.27	20.08	19.30	20.05
Cr2O3	0.00	0.00	0.00	0.00	0.00	0.00	0.00
Fe2O3	0.00	0.05	0.00	1.08	0.00	0.00	0.00
FeO	20.71	19.91	11.61	18.93	20.09	19.92	19.39
MnO	0.14	0.16	0.07	0.17	0.16	0.12	0.15
MgO	8.91	9.51	5.30	9.31	9.03	9.11	9.23
CaO	0.10	0.08	1.35	0.15	0.10	0.08	0.09
Na2O	0.05	0.08	4.28	0.06	0.06	0.08	0.06
K2O	8.97	8.97	5.03	8.41	8.32	8.88	8.83
Totals	96.09	94.81	98.43	93.13	94.81	95.57	95.24
Oxygens	11.000	11.000	11.000	11.000	11.000	11.000	11.000
Si	2.667	2.679	3.277	2.672	2.685	2.721	2.702
Ti	0.105	0.090	0.043	0.080	0.097	0.120	0.098
Al	1.793	1.759	1.713	1.765	1.802	1.721	1.789
Cr	0.000	0.000	0.000	0.000	0.000	0.000	0.000
Fe3	0.000	0.003	0.000	0.063	0.000	0.000	0.000
Fe2	1.310	1.274	0.657	1.230	1.279	1.260	1.227
Mn	0.009	0.010	0.004	0.011	0.010	0.008	0.010
Mg	1.004	1.085	0.534	1.078	1.025	1.027	1.041
Ca	0.008	0.007	0.098	0.012	0.008	0.006	0.007
Na	0.007	0.012	0.561	0.009	0.009	0.012	0.009
K	0.865	0.876	0.434	0.834	0.808	0.857	0.852
Sum	7.768	7.795	7.321	7.754	7.723	7.732	7.735
XMg	0.43	0.46	0.45	0.47	0.44	0.45	0.46

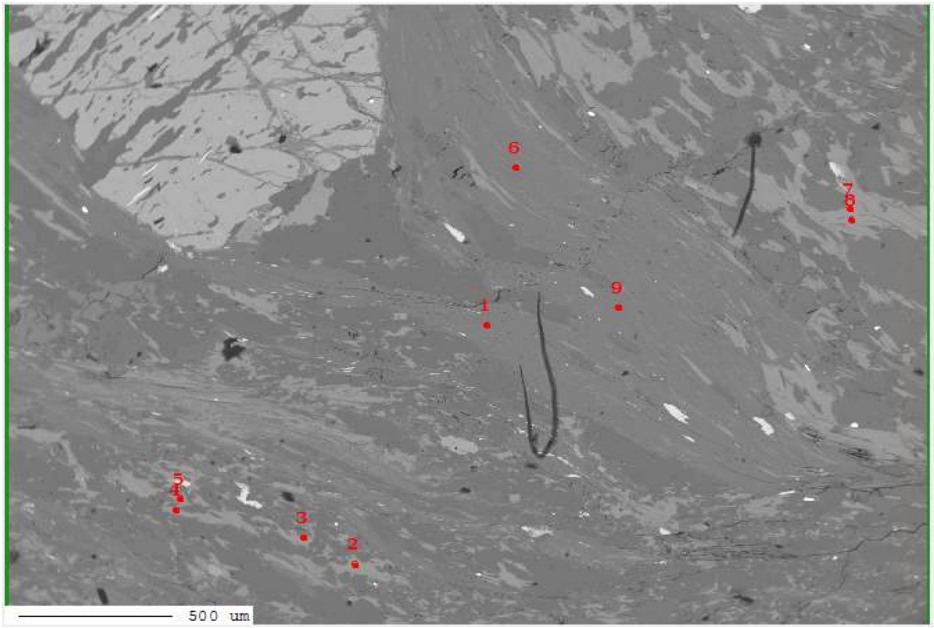

Project : BR04A
Image : image009
Date : 2019/12/10 15:26:10
Acc. : 15 kV
Signal Type : COMPO

No.	Data Name	Type	Pos.	Comment
1	BR04A_0006	QNT	1	ms1
2	BR04A_0006	QNT	2	bt1
3	BR04A_0007	QNT	1	bt2
4	BR04A_0007	QNT	2	bt3
5	BR04A_0007	QNT	3	bt4
6	BR04A_0007	QNT	4	ms2
7	BR04A_0007	QNT	5	bt5
8	BR04A_0007	QNT	6	bt6
9	BR04A_0007	QNT	7	ms3

Delete | Reset Position | Open Data

Clear | Marker Label : Number

Marker Style

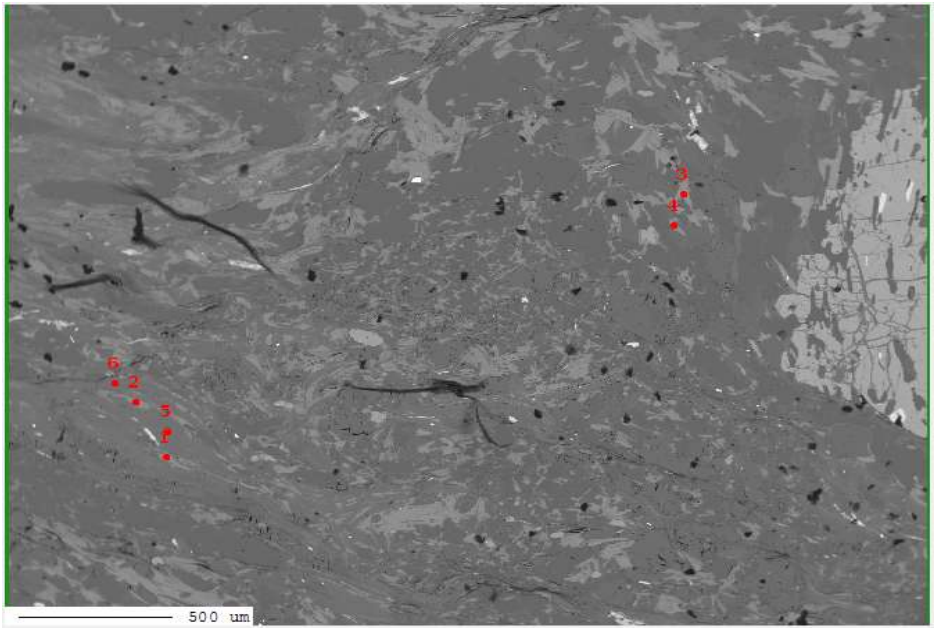

Project : BR04A
Image : image010
Date : 2019/12/10 15:43:27
Acc. : 15 kV
Signal Type : COMPO

No.	Data Name	Type	Pos.	Comment
1	BR04A_0008	QNT	1	bt6
2	BR04A_0008	QNT	2	bt7
3	BR04A_0008	QNT	3	bt8
4	BR04A_0008	QNT	4	bt9
5	BR04A_0008	QNT	5	ms5
6	BR04A_0008	QNT	6	ms6

Delete | Reset Position | Open Data

Clear | Marker Label : Number

Marker Style

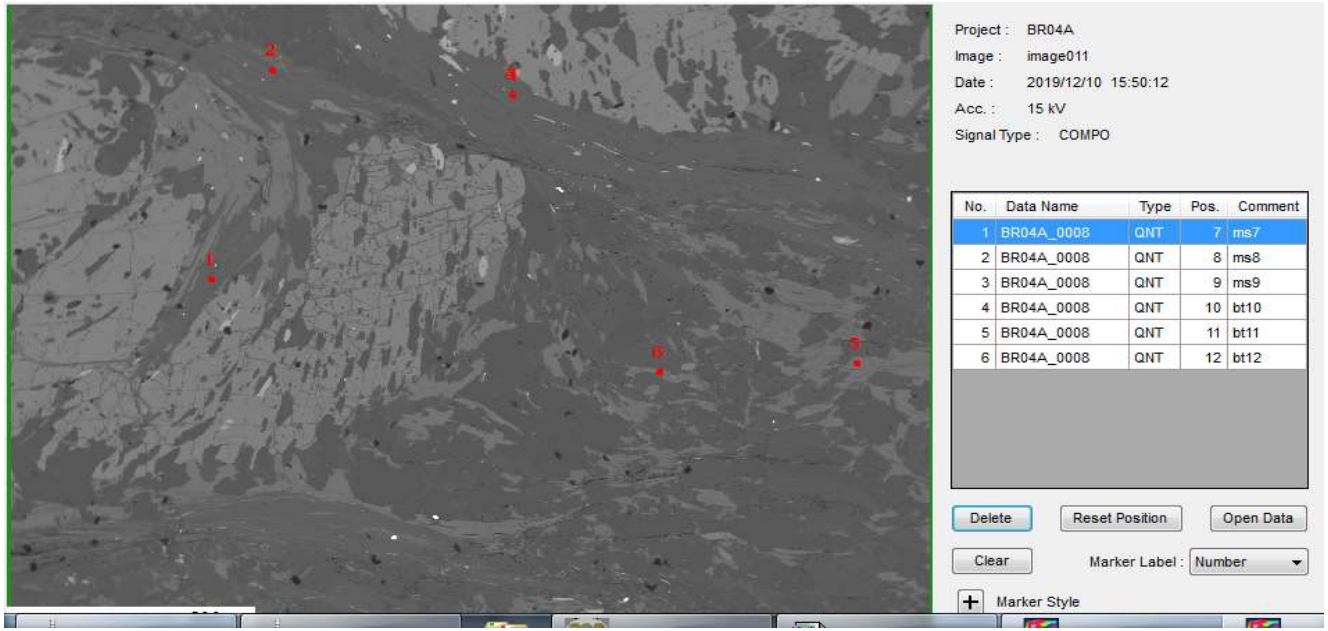

Project : BR04A
Image : image011
Date : 2019/12/10 15:50:12
Acc. : 15 kV
Signal Type : COMPO

No.	Data Name	Type	Pos.	Comment
1	BR04A_0008	QNT	7	ms7
2	BR04A_0008	QNT	8	ms8
3	BR04A_0008	QNT	9	ms9
4	BR04A_0008	QNT	10	bt10
5	BR04A_0008	QNT	11	bt11
6	BR04A_0008	QNT	12	bt12

Delete | Reset Position | Open Data

Clear | Marker Label : Number

Marker Style

Sample:BR04A

Mineral:garnet

							Z1		Z2			Z3	
Sample	grt1.1	grt1.3	grt1.4	grt1.5	grt1.6	grt1.8	grt1.9	grt1.10	grt1.11	grt1.12	grt1.13	grt1.14	grt1.15
SiO2	36.21	36.58	36.27	36.65	36.85	36.38	36.70	36.57	36.60	36.64	37.03	36.69	36.21
TiO2	0.08	0.14	0.06	0.04	0.03	0.09	0.15	0.23	0.11	0.10	0.00	0.02	0.03
Al2O3	20.97	21.06	20.72	20.73	20.51	20.97	20.70	20.75	20.71	20.89	21.08	21.01	21.05
Cr2O3	0.04	0.02	0.02	0.01	0.00	0.02	0.04	0.00	0.04	0.05	0.00	0.04	0.04
Fe2O3	1.38	1.38	1.38	1.38	1.38	1.38	1.38	1.38	1.38	1.38	1.38	1.38	1.38
FeO	30.80	32.40	32.56	31.78	32.04	29.44	29.84	29.96	29.25	29.86	32.38	34.00	33.72
MnO	3.66	3.56	4.01	5.05	5.37	6.45	6.10	6.05	5.27	4.83	3.47	3.09	2.91
MgO	3.01	2.26	2.02	1.56	1.91	1.42	1.53	1.49	1.29	1.33	2.01	2.28	2.87
CaO	2.67	3.99	3.94	4.23	2.84	4.68	4.31	4.73	5.57	5.72	4.28	3.28	2.65
Na2O	0.02	0.00	0.02	0.01	0.01	0.04	0.04	0.02	0.02	0.01	0.01	0.01	0.00
K2O	0.00	0.00	0.00	0.00	0.00	0.00	0.00	0.00	0.00	0.00	0.00	0.00	0.00
Totals	98.84	101.39	101.00	101.43	100.94	100.87	100.79	101.17	100.23	100.80	101.64	101.79	100.86
Oxygens	12.000	12.000	12.000	12.000	12.000	12.000	12.000	12.000	12.000	12.000	12.000	12.000	12.000
Si	2.947	2.927	2.926	2.946	2.972	2.934	2.958	2.941	2.959	2.948	2.952	2.933	2.915
Ti	0.005	0.008	0.004	0.002	0.002	0.006	0.009	0.014	0.007	0.006	0.000	0.001	0.002
Al	2.012	1.987	1.971	1.964	1.950	1.993	1.967	1.967	1.974	1.981	1.981	1.980	1.998
Cr	0.003	0.001	0.001	0.001	0.000	0.001	0.002	0.000	0.003	0.003	0.000	0.002	0.003
Fe3	0.084	0.083	0.084	0.083	0.084	0.084	0.083	0.083	0.084	0.083	0.083	0.083	0.083
Fe2	2.096	2.169	2.197	2.136	2.161	1.985	2.011	2.015	1.978	2.009	2.159	2.273	2.270
Mn	0.252	0.241	0.274	0.344	0.367	0.441	0.416	0.412	0.361	0.329	0.234	0.209	0.198
Mg	0.365	0.270	0.243	0.187	0.230	0.171	0.184	0.179	0.155	0.159	0.239	0.272	0.344
Ca	0.233	0.342	0.341	0.364	0.245	0.404	0.372	0.408	0.483	0.493	0.366	0.281	0.229
Na	0.003	0.000	0.003	0.001	0.002	0.006	0.006	0.002	0.003	0.001	0.002	0.002	0.000
K	0.000	0.000	0.000	0.000	0.000	0.000	0.000	0.000	0.000	0.000	0.000	0.000	0.000
Sum	8.000	8.029	8.044	8.029	8.011	8.024	8.010	8.021	8.005	8.013	8.017	8.035	8.042
Alm	0.71	0.72	0.72	0.70	0.72	0.66	0.67	0.67	0.66	0.67	0.72	0.75	0.75
Pyr	0.12	0.09	0.08	0.06	0.08	0.06	0.06	0.06	0.05	0.05	0.08	0.09	0.11
Grs	0.08	0.11	0.11	0.12	0.08	0.13	0.12	0.14	0.16	0.16	0.12	0.09	0.08
Sps	0.09	0.08	0.09	0.11	0.12	0.15	0.14	0.14	0.12	0.11	0.08	0.07	0.07

Sample	grt2.1	grt2.2	grt2.3	grt2.4	grt2.5	grt2.6	grt2.7	grt2.8	grt2.9	grt2.10	grt2.11	grt2.12
SiO2	39.31	37.17	36.21	36.56	36.66	36.74	36.78	36.39	36.34	36.67	37.59	34.06
TiO2	0.06	0.06	0.07	0.06	0.05	0.05	0.07	0.15	0.07	0.08	0.06	0.13
Al2O3	22.68	21.06	20.74	21.13	21.06	21.04	21.10	20.89	21.03	20.94	21.05	17.44
Cr2O3	0.01	0.02	0.00	0.02	0.04	0.04	0.01	0.04	0.04	0.06	0.00	0.03
Fe2O3	0.00	0.64	2.04	1.69	0.70	1.54	1.16	1.61	1.46	1.01	0.00	0.13
FeO	31.45	32.03	30.71	30.96	32.34	32.12	31.84	31.04	30.43	31.73	30.15	27.18
MnO	5.49	4.11	2.93	2.93	2.81	2.67	2.93	3.31	3.64	3.15	4.23	2.65
MgO	1.61	2.71	2.86	2.10	2.67	2.88	2.70	2.37	2.28	2.74	2.66	5.49
CaO	2.76	2.71	3.58	4.69	3.07	3.14	3.38	3.89	4.13	3.21	2.52	0.75
Na2O	0.00	0.00	0.00	0.02	0.00	0.00	0.02	0.01	0.01	0.00	0.01	0.05
K2O	0.00	0.00	0.00	0.00	0.00	0.00	0.00	0.00	0.00	0.00	0.00	0.00
Totals	103.37	100.51	99.13	100.16	99.40	100.21	99.99	99.70	99.43	99.59	98.27	87.91
Oxygens	12.000	12.000	12.000	12.000	12.000	12.000	12.000	12.000	12.000	12.000	12.000	12.000
Si	3.041	2.981	2.941	2.943	2.969	2.953	2.961	2.945	2.946	2.965	3.049	3.065
Ti	0.003	0.004	0.004	0.004	0.003	0.003	0.004	0.009	0.004	0.005	0.004	0.009
Al	2.068	1.991	1.986	2.005	2.011	1.993	2.002	1.993	2.010	1.996	2.013	1.850
Cr	0.001	0.001	0.000	0.001	0.003	0.003	0.001	0.003	0.003	0.004	0.000	0.002
Fe3	0.000	0.039	0.124	0.103	0.043	0.093	0.070	0.098	0.089	0.061	0.000	0.009
Fe2	2.034	2.149	2.086	2.084	2.191	2.158	2.143	2.101	2.063	2.146	2.045	2.046
Mn	0.360	0.279	0.202	0.200	0.193	0.182	0.200	0.227	0.250	0.216	0.291	0.202
Mg	0.186	0.324	0.346	0.252	0.322	0.345	0.324	0.286	0.275	0.330	0.321	0.736
Ca	0.229	0.233	0.312	0.405	0.266	0.270	0.292	0.337	0.359	0.278	0.219	0.072
Na	0.000	0.000	0.000	0.003	0.000	0.000	0.003	0.002	0.002	0.000	0.002	0.009
K	0.000	0.000	0.000	0.000	0.000	0.000	0.000	0.000	0.000	0.000	0.000	0.000
Sum	7.922	8.000	8.000	8.000	8.000	8.000	8.000	8.000	8.000	8.000	7.942	8.000
Alm	0.72	0.72	0.71	0.71	0.74	0.73	0.72	0.71	0.70	0.72	0.71	0.67
Pyr	0.07	0.11	0.12	0.09	0.11	0.12	0.11	0.10	0.09	0.11	0.11	0.24
Grs	0.08	0.08	0.11	0.14	0.09	0.09	0.10	0.11	0.12	0.09	0.08	0.02
Sps	0.13	0.09	0.07	0.07	0.06	0.06	0.07	0.08	0.08	0.07	0.10	0.07

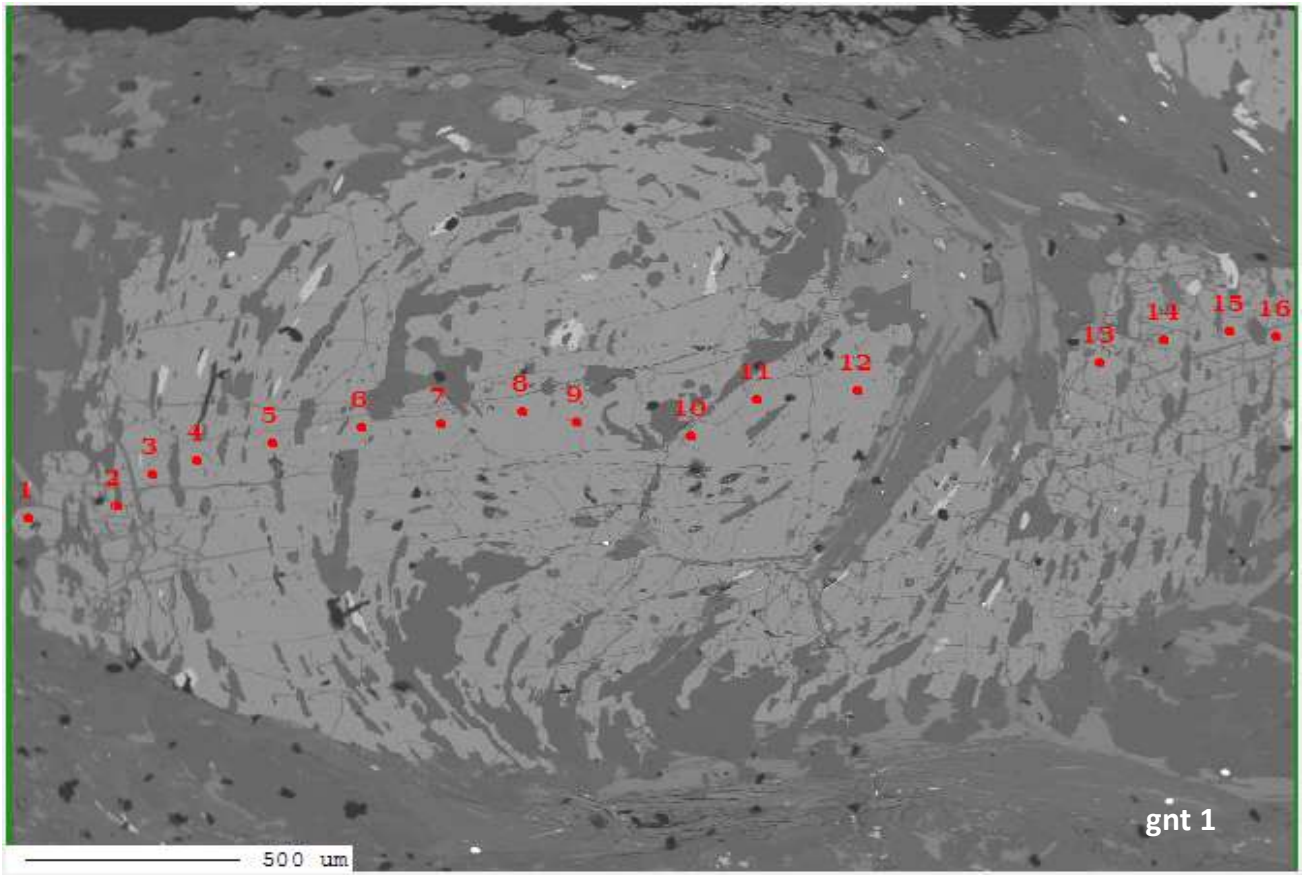
1
2
3
4
5
6
7
8
9
10
11
12
13
14
15
16
gnt 1
500 um

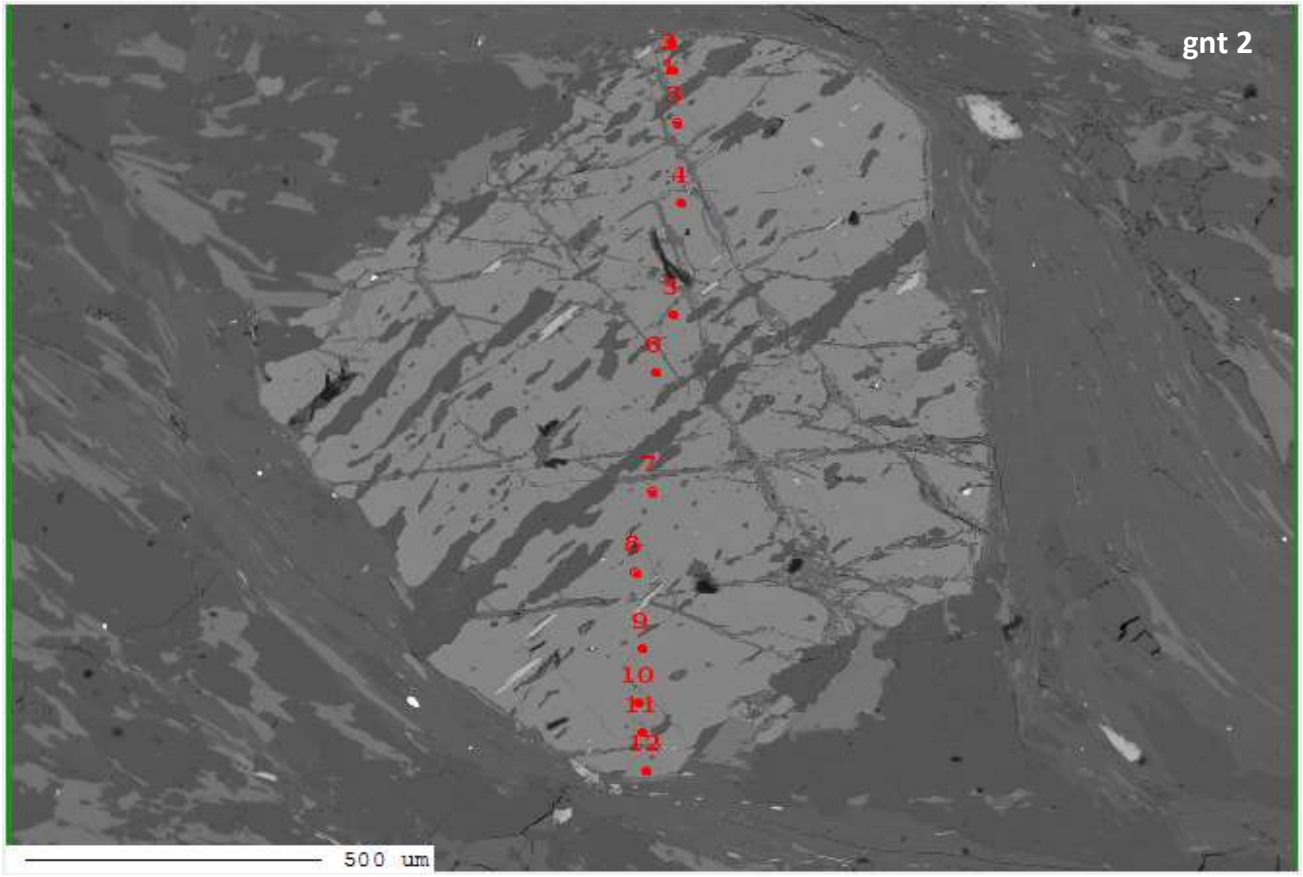
gnt 2
1
2
3
4
5
6
7
8
9
10
11
12
500 um

Sample:BR07

Mineral:plagioclase

Sample	pl1	pl2	pl3_1	pl3_2	pl3_3	pl3_4	pl5	pl6
SiO2	60.08	60.72	60.67	60.23	59.56	61.41	60.48	60.19
TiO2	0.00	0.00	0.00	0.04	0.00	0.00	0.00	0.00
Al2O3	25.59	24.20	25.24	25.15	24.61	24.58	25.11	25.33
Cr2O3	0.00	0.00	0.00	0.00	0.00	0.00	0.00	0.00
Fe2O3	0.11	0.11	0.11	0.11	0.11	0.11	0.11	0.11
FeO	0.00	0.29	0.17	0.12	0.35	0.49	0.23	0.33
MnO	0.00	0.02	0.01	0.01	0.04	0.00	0.00	0.02
MgO	0.00	0.06	0.00	0.00	0.05	0.10	0.00	0.06
CaO	6.42	4.49	5.95	6.10	5.69	3.95	5.75	5.21
Na2O	7.87	8.45	8.09	8.12	7.70	7.83	7.80	7.70
K2O	0.16	0.61	0.29	0.37	0.90	1.48	0.40	0.92
Totals	100.23	98.96	100.55	100.25	99.02	99.95	99.88	99.87
Oxygens	8.00	8.00	8.00	8.00	8.00	8.00	8.00	8.00
Si	2.668	2.727	2.687	2.679	2.687	2.733	2.693	2.685
Ti	0.000	0.000	0.000	0.001	0.000	0.000	0.000	0.000
Al	1.340	1.281	1.318	1.319	1.309	1.290	1.318	1.332
Cr	0.000	0.000	0.000	0.000	0.000	0.000	0.000	0.000
Fe3	0.004	0.004	0.004	0.004	0.004	0.004	0.004	0.004
Fe2	0.000	0.011	0.006	0.004	0.013	0.018	0.009	0.012
Mn	0.000	0.001	0.000	0.000	0.002	0.000	0.000	0.001
Mg	0.000	0.004	0.000	0.000	0.003	0.006	0.000	0.004
Ca	0.305	0.216	0.282	0.291	0.275	0.188	0.274	0.249
Na	0.678	0.736	0.695	0.700	0.674	0.676	0.673	0.666
K	0.009	0.035	0.017	0.021	0.052	0.084	0.023	0.052
Sum	5.004	5.016	5.008	5.019	5.019	5.000	4.994	5.006
Anortite	0.31	0.22	0.28	0.29	0.27	0.20	0.28	0.26

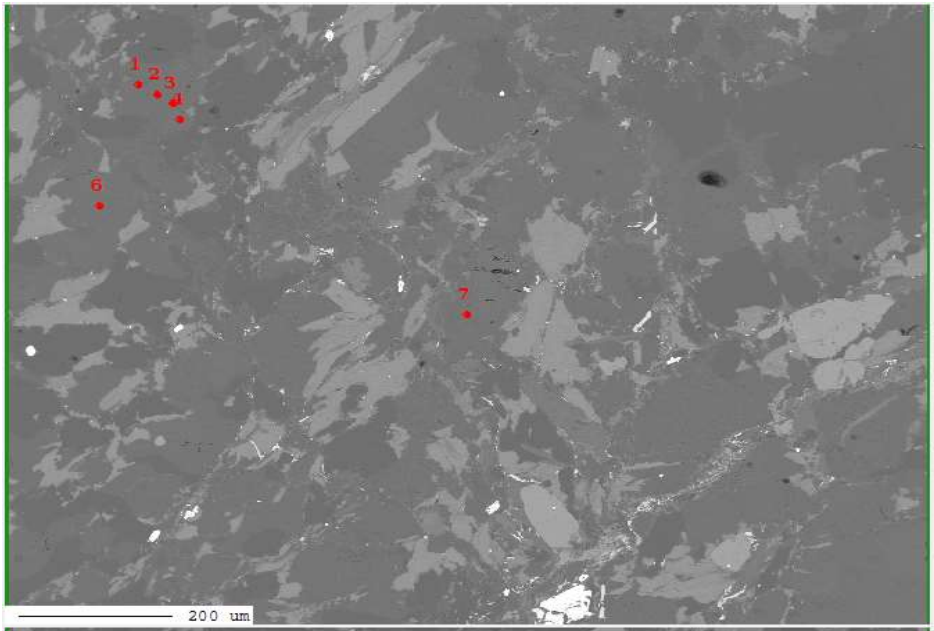

Project : BR07
Image : image006
Date : 2019/12/11 12:11:55
Acc. : 15 kV
Signal Type : COMPO

No.	Data Name	Type	Pos.	Comment
1	BR07_0003	QNT	1	pl3
2	BR07_0003	QNT	2	pl3_2
3	BR07_0003	QNT	3	pl3_3
4	BR07_0003	QNT	4	pl3_4
5	BR07_0003	QNT	5	pl4
6	BR07_0003	QNT	6	pl5
7	BR07_0003	QNT	7	pl6

Delete | Reset Position | Open Data

Clear | Marker Label : Number

Marker Style

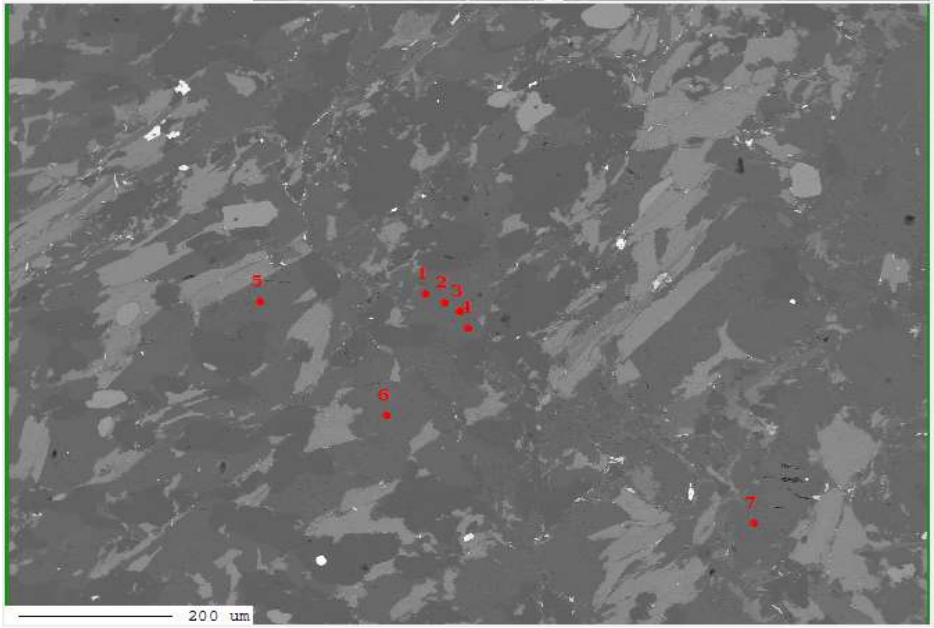

Project : BR07
Image : image005
Date : 2019/12/11 12:08:56
Acc. : 15 kV
Signal Type : COMPO

No.	Data Name	Type	Pos.	Comment
1	BR07_0003	QNT	1	pl3
2	BR07_0003	QNT	2	pl3_2
3	BR07_0003	QNT	3	pl3_3
4	BR07_0003	QNT	4	pl3_4
5	BR07_0003	QNT	5	pl4
6	BR07_0003	QNT	6	pl5
7	BR07_0003	QNT	7	pl6

Delete | Reset Position | Open Data

Clear | Marker Label : Number

Marker Style

Sample:BR07

Mineral:muscovite

Sample	ms1	ms2	chl4	chl5
SiO2	44.74	44.70	44.98	45.48
TiO2	0.86	1.09	0.48	2.23
Al2O3	34.64	34.28	33.16	32.40
Cr2O3	0.00	0.00	0.00	0.00
Fe2O3	2.54	2.54	0.16	0.16
FeO	1.19	3.43	4.38	3.50
MnO	0.03	0.00	0.04	0.06
MgO	0.64	0.69	1.38	0.95
CaO	0.01	0.00	0.03	0.04
Na2O	0.46	0.44	0.32	0.22
K2O	10.19	10.21	10.37	10.02
Totals	95.29	97.37	95.31	95.07
Oxygens	11.000	11.000	11.000	11.000
Si	3.004	2.974	3.882	3.910
Ti	0.044	0.054	0.031	0.144
Al	2.742	2.689	3.374	3.284
Cr	0.000	0.000	0.000	0.000
Fe3	0.128	0.127	0.011	0.011
Fe2	0.067	0.191	0.316	0.252
Mn	0.001	0.000	0.003	0.004
Mg	0.064	0.068	0.177	0.122
Ca	0.001	0.000	0.003	0.004
Na	0.059	0.057	0.053	0.037
K	0.873	0.867	1.142	1.099
Sum	6.984	7.026	8.993	8.867
XMg	0.49	0.26	0.36	0.33
Al/Si	0.91	0.90	0.87	0.84

ps: wrongly named as chlorite grains

Sample:BR07

Mineral:chlorite

Sample	chl7	chl8
SiO2	25.04	26.21
TiO2	0.09	0.00
Al2O3	20.37	21.04
Cr2O3	0.00	0.00
Fe2O3	0.16	0.16
FeO	25.15	24.09
MnO	0.68	0.65
MgO	15.96	15.39
CaO	0.04	0.00
Na2O	0.04	0.01
K2O	0.03	0.04
Totals	87.56	87.59
Oxygens	14.000	14.000
Si	2.658	2.749
Ti	0.007	0.000
Al	2.549	2.602
Cr	0.000	0.000
Fe3	0.013	0.013
Fe2	2.232	2.113
Mn	0.061	0.057
Mg	2.524	2.406
Ca	0.005	0.000
Na	0.008	0.002
K	0.004	0.005
Sum	10.061	9.948
XMg	0.53	0.53
Al/Si	0.96	0.95

Sample:BR07
Mineral:biotite

Sample	bt1	bt2	bt3	bt4	bt5	bt7	bt9	bt10	chl1	chl2
SiO2	34.35	35.44	35.22	34.59	34.78	35.26	34.67	34.32	34.65	34.75
TiO2	2.03	1.95	1.56	2.71	2.24	2.12	1.96	2.26	2.47	2.15
Al2O3	18.21	18.81	19.10	18.04	18.46	18.46	18.46	18.33	18.54	17.96
Cr2O3	0.00	0.00	0.00	0.00	0.00	0.00	0.00	0.00	0.00	0.00
Fe2O3	1.11	1.11	1.11	1.11	1.11	1.11	1.11	1.11	0.00	0.16
FeO	20.08	19.99	19.87	21.23	20.10	20.61	20.85	20.80	20.42	21.04
MnO	0.44	0.41	0.38	0.35	0.43	0.39	0.38	0.40	0.44	0.41
MgO	9.46	9.47	9.93	9.42	9.52	9.63	10.12	9.47	9.49	9.75
CaO	0.04	0.02	0.07	0.00	0.03	0.04	0.08	0.04	0.00	0.01
Na2O	0.06	0.09	0.09	0.06	0.07	0.08	0.06	0.06	0.09	0.04
K2O	9.43	9.44	8.50	9.65	9.51	9.56	9.09	9.00	9.40	9.48
Totals	95.21	96.74	95.83	97.16	96.25	97.25	96.79	95.79	95.49	95.75
Oxygens	11.000	11.000	11.000	11.000	11.000	11.000	11.000	11.000	11.000	11.000
Si	2.650	2.677	2.669	2.629	2.650	2.661	2.630	2.633	3.381	3.396
Ti	0.118	0.111	0.089	0.155	0.128	0.120	0.112	0.130	0.181	0.158
Al	1.656	1.675	1.707	1.617	1.658	1.643	1.651	1.658	2.133	2.069
Cr	0.000	0.000	0.000	0.000	0.000	0.000	0.000	0.000	0.000	0.000
Fe3	0.065	0.063	0.063	0.064	0.064	0.063	0.064	0.064	0.000	0.012
Fe2	1.295	1.263	1.259	1.350	1.281	1.301	1.323	1.334	1.666	1.720
Mn	0.028	0.026	0.024	0.022	0.028	0.025	0.025	0.026	0.036	0.034
Mg	1.088	1.066	1.122	1.067	1.081	1.083	1.144	1.083	1.380	1.420
Ca	0.004	0.002	0.005	0.000	0.002	0.003	0.007	0.003	0.000	0.001
Na	0.009	0.013	0.014	0.009	0.010	0.011	0.009	0.009	0.016	0.008
K	0.928	0.910	0.822	0.936	0.925	0.921	0.880	0.881	1.170	1.182
Sum	7.841	7.806	7.775	7.849	7.828	7.832	7.845	7.821	9.965	10.001
XMg	0.46	0.46	0.47	0.44	0.46	0.45	0.46	0.45	0.45	0.45
Al/Si	0.62	0.63	0.64	0.62	0.63	0.62	0.63	0.63	0.63	0.61

ps: wrongly named as chlorite grains

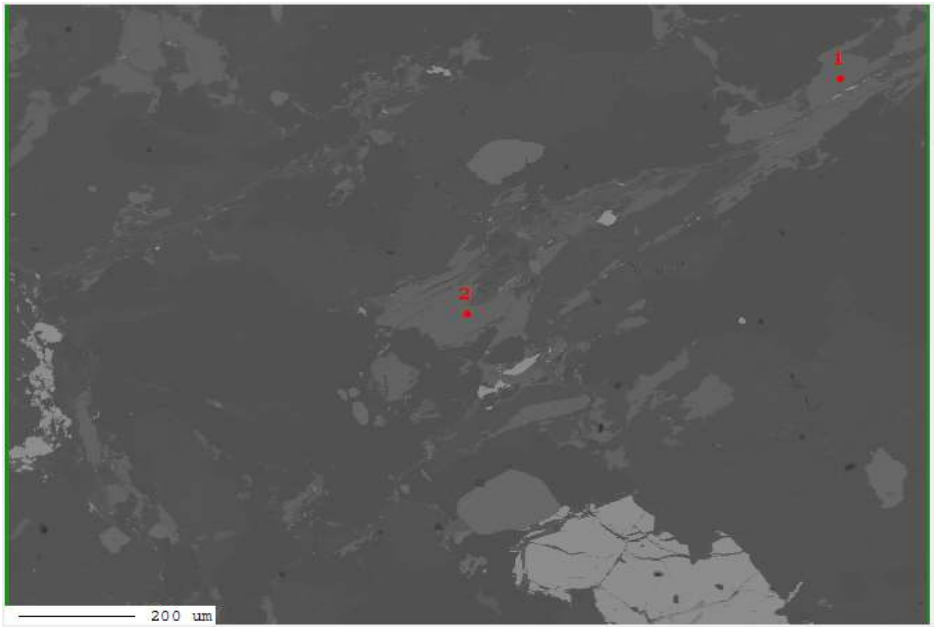

Project : BR07
Image : image004
Date : 2019/12/11 11:28:35
Acc. : 15 kV
Signal Type : COMPO

No.	Data Name	Type	Pos.	Comment
1	BR07_0001	QNT	8	chl1
2	BR07_0001	QNT	9	chl2

Delete | Reset Position | Open Data

Clear | Marker Label : Number

Marker Style

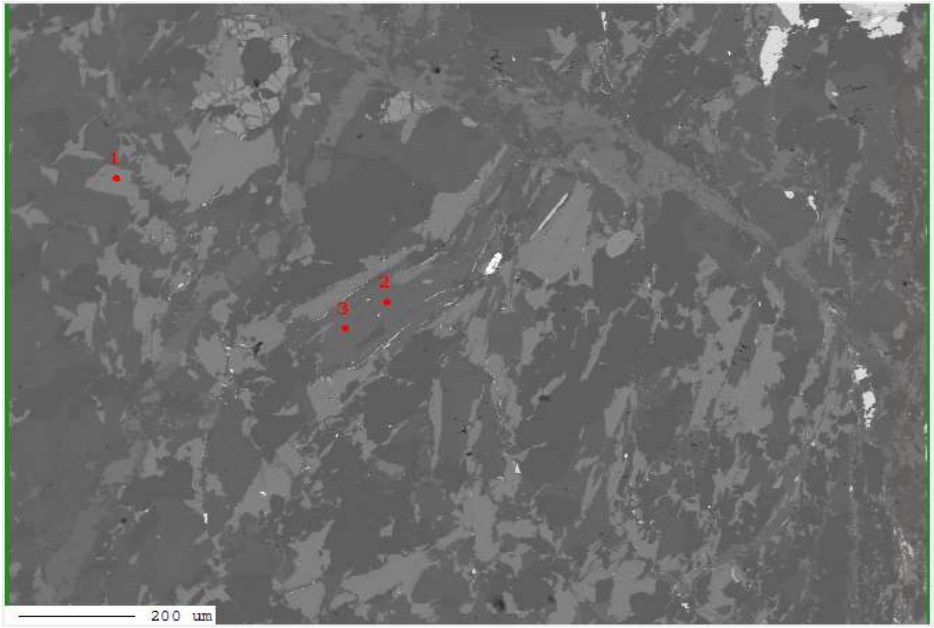

Project : BR07
Image : image002
Date : 2019/12/11 11:21:12
Acc. : 15 kV
Signal Type : COMPO

No.	Data Name	Type	Pos.	Comment
1	BR07_0001	QNT	5	bt5
2	BR07_0001	QNT	6	ms1
3	BR07_0001	QNT	7	ms2

Delete | Reset Position | Open Data

Clear | Marker Label : Number

Marker Style

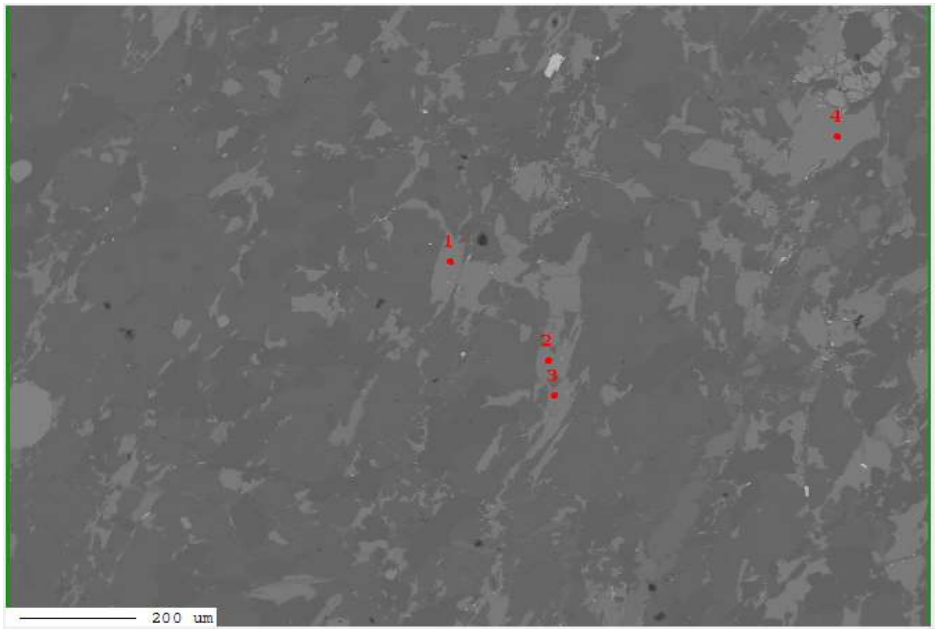

Project : BR07
Image : image001
Date : 2019/12/11 11:17:20
Acc. : 15 kV
Signal Type : COMPO

No.	Data Name	Type	Pos.	Comment
1	BR07_0001	QNT	1	bt1
2	BR07_0001	QNT	2	bt2
3	BR07_0001	QNT	3	bt3
4	BR07_0001	QNT	4	bt4

Delete | Reset Position | Open Data

Clear | Marker Label : Number

Marker Style

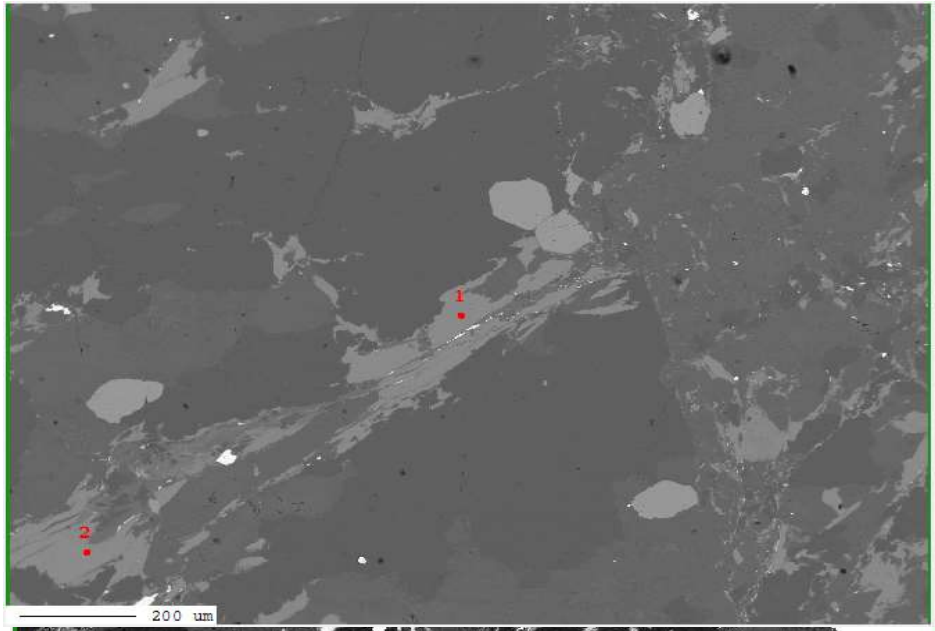

Project : BR07
Image : image003
Date : 2019/12/11 11:27:07
Acc. : 15 kV
Signal Type : COMPO

No.	Data Name	Type	Pos.	Comment
1	BR07_0001	QNT	8	chl1
2	BR07_0001	QNT	9	chl2

Delete | Reset Position | Open Data

Clear | Marker Label : Number

Marker Style

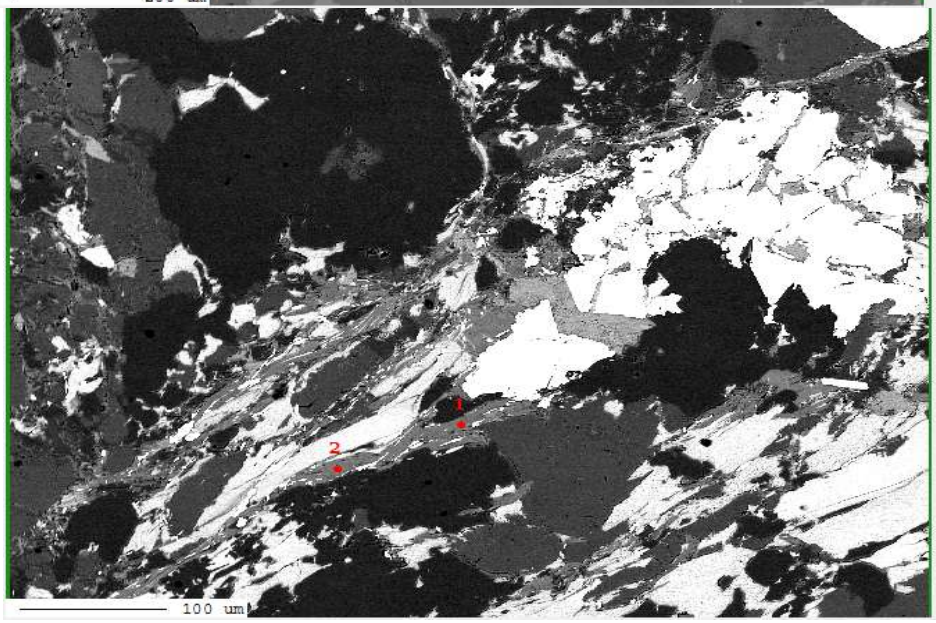

Project : BR07
Image : image007
Date : 2019/12/11 15:21:17
Acc. : 15 kV
Signal Type : COMPO

No.	Data Name	Type	Pos.	Comment
1	BR07_0005	QNT	1	chl4
2	BR07_0005	QNT	2	chl5

Delete | Reset Position | Open Data

Clear | Marker Label : Number

Marker Style

Sample:BR18

Mineral:plagioclase

Sample	pl1	pl2	pl3	pl6	pl7	pl8	pl9
SiO2	62.91	62.73	64.12	63.04	62.72	63.34	62.59
TiO2	0.05	0.01	0.03	0.01	0.00	0.00	0.00
Al2O3	24.19	24.25	24.25	24.44	24.02	24.06	24.24
Cr2O3	0.00	0.00	0.00	0.00	0.00	0.00	0.00
Fe2O3	0.24	0.24	0.24	0.24	0.24	0.24	0.24
FeO	0.00	0.18	0.31	0.29	0.26	0.22	0.29
MnO	0.02	0.01	0.00	0.00	0.00	0.02	0.01
MgO	0.00	0.00	0.00	0.01	0.00	0.00	0.00
CaO	3.94	4.62	4.29	4.60	4.60	4.45	4.81
Na2O	8.97	8.84	8.64	8.76	8.94	8.96	8.82
K2O	0.08	0.10	0.11	0.13	0.12	0.11	0.13
Totals	100.40	100.97	101.99	101.51	100.90	101.40	101.13
Oxygens	8.000	8.000	8.000	8.000	8.000	8.000	8.000
Si	2.766	2.752	2.777	2.751	2.756	2.766	2.746
Ti	0.002	0.000	0.001	0.000	0.000	0.000	0.000
Al	1.254	1.254	1.238	1.257	1.244	1.238	1.254
Cr	0.000	0.000	0.000	0.000	0.000	0.000	0.000
Fe3	0.008	0.008	0.008	0.008	0.008	0.008	0.008
Fe2	0.000	0.006	0.011	0.011	0.009	0.008	0.011
Mn	0.001	0.000	0.000	0.000	0.000	0.001	0.000
Mg	0.000	0.000	0.000	0.001	0.000	0.000	0.000
Ca	0.186	0.217	0.199	0.215	0.217	0.208	0.226
Na	0.765	0.752	0.725	0.741	0.762	0.759	0.750
K	0.005	0.005	0.006	0.007	0.007	0.006	0.007
Sum	4.986	4.995	4.965	4.990	5.002	4.994	5.002
Anorthite	0.19	0.22	0.21	0.22	0.22	0.21	0.23

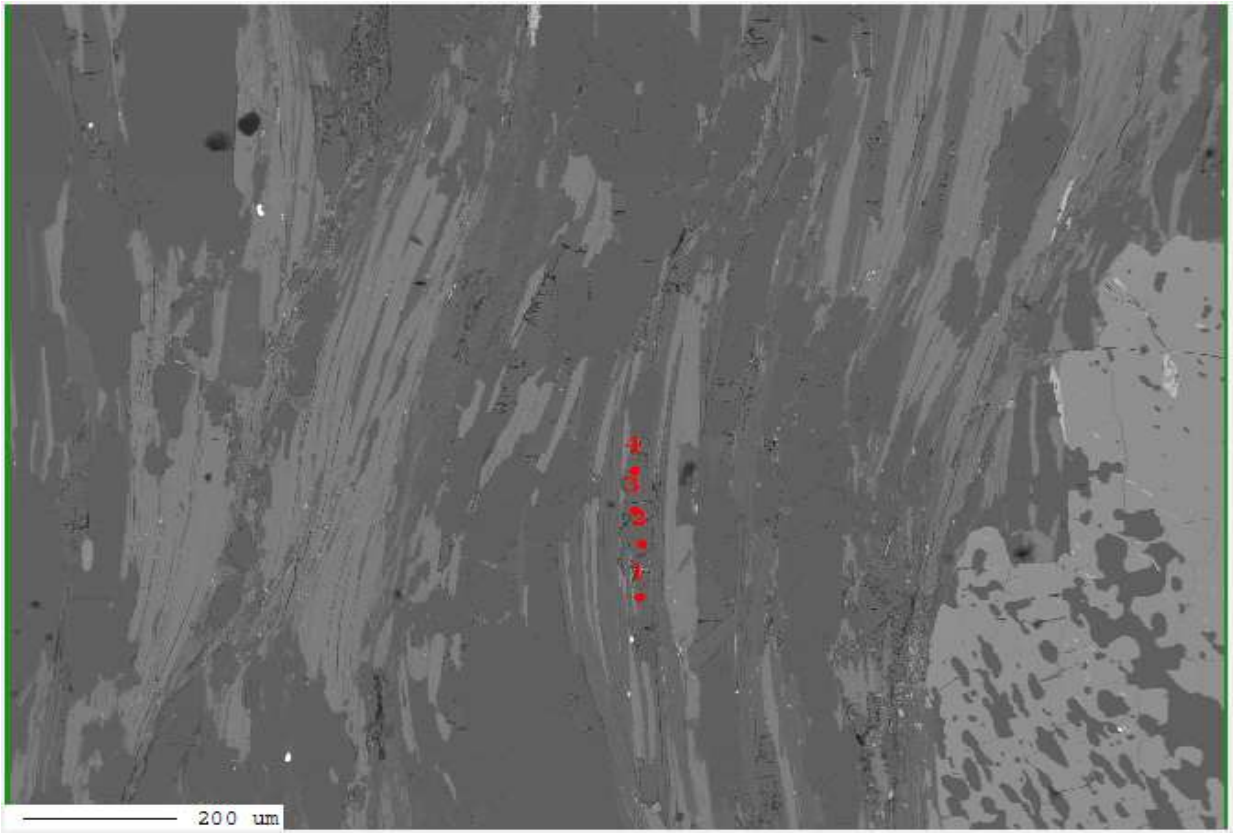

Project : BR18
Image : image017
Date : 2019/12/12 18:03:16
Acc. : 15 kV
Signal Type : COMPO

No.	Data Name	Type	Pos.	Comment
1	BR18_0008	QNT	1	pl6
2	BR18_0008	QNT	2	pl7
3	BR18_0008	QNT	3	pl8
4	BR18_0008	QNT	4	pl9

Delete | Reset Position | Open Data

Clear | Marker Label : Number

Marker Style

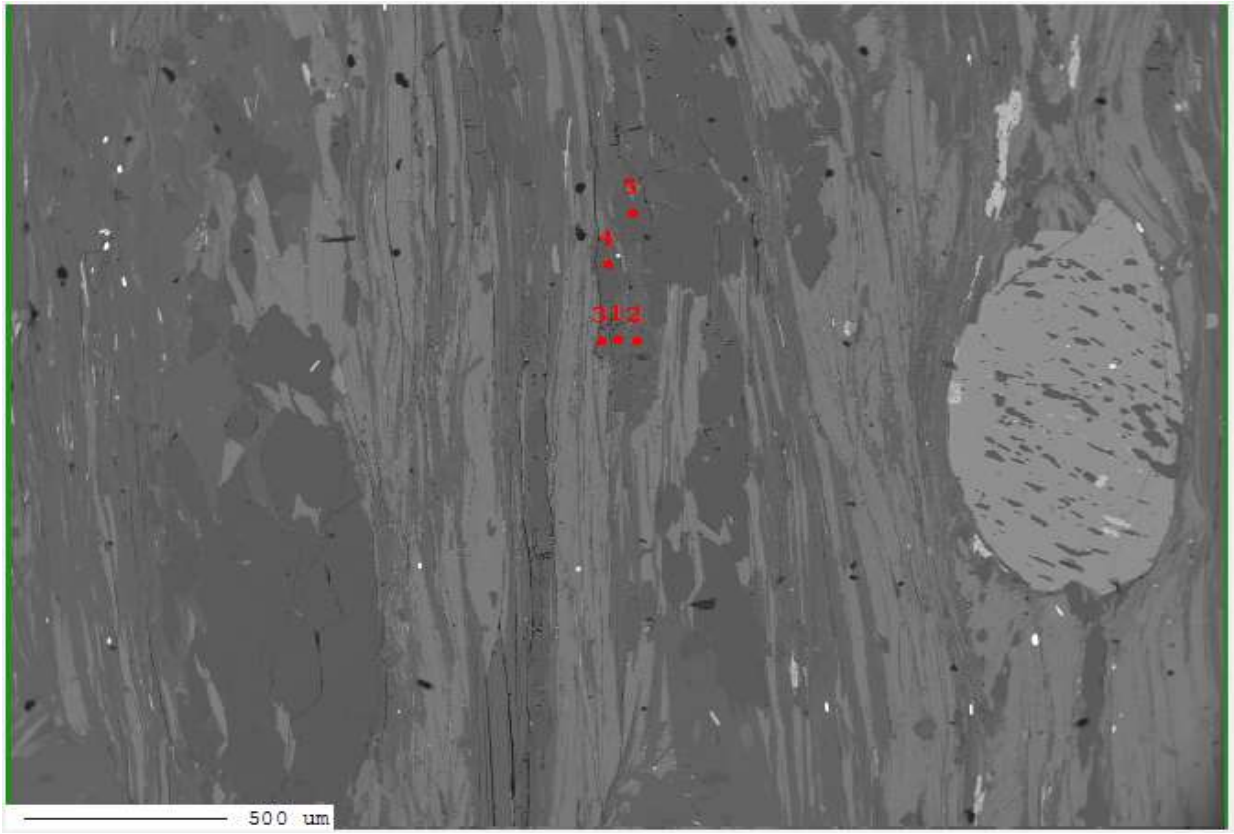

Project : BR18
Image : image016
Date : 2019/12/12 17:59:44
Acc. : 15 kV
Signal Type : COMPO

No.	Data Name	Type	Pos.	Comment
1	BR18_0007	QNT	1	pl1
2	BR18_0007	QNT	2	pl2
3	BR18_0007	QNT	3	pl3
4	BR18_0007	QNT	4	pl4
5	BR18_0007	QNT	5	pl5

Delete | Reset Position | Open Data

Clear | Marker Label : Number

Marker Style

Sample:BR18
Mineral:garnet

Sample	grt1.2	grt1.3	grt1.4	grt1.5	grt1.6	grt1.7	grt1.8	grt1.9	grt1.10	grt1.11	grt1.12
SiO2	37.27	36.89	36.30	36.58	36.66	36.74	36.74	36.69	36.73	36.60	36.29
TiO2	0.04	0.06	0.05	0.05	0.03	0.12	0.12	0.08	0.05	0.03	0.08
Al2O3	21.17	20.98	20.96	20.80	20.90	20.62	20.74	20.89	20.58	20.88	21.01
Cr2O3	0.00	0.00	0.00	0.00	0.02	0.00	0.01	0.02	0.00	0.00	0.00
Fe2O3	0.00	0.25	0.25	0.25	0.25	0.25	0.25	0.25	0.25	0.25	0.25
FeO	31.13	31.21	31.28	30.86	31.24	31.30	30.40	30.98	31.43	31.83	31.42
MnO	6.31	5.96	6.25	6.14	6.50	6.50	6.74	6.61	6.52	6.37	6.16
MgO	2.30	2.47	2.57	2.63	2.58	2.55	2.48	2.51	2.53	2.55	2.48
CaO	2.12	1.88	1.79	1.87	1.80	1.73	2.14	1.97	1.71	1.75	2.05
Na2O	0.01	0.02	0.01	0.01	0.02	0.02	0.01	0.03	0.01	0.01	0.01
K2O	0.00	0.00	0.00	0.00	0.00	0.00	0.00	0.00	0.00	0.00	0.00
Totals	100.35	99.73	99.46	99.19	100.00	99.84	99.63	100.04	99.81	100.27	99.76
Oxygens	12.000	12.000	12.000	12.000	12.000	12.000	12.000	12.000	12.000	12.000	12.000
Si	2.999	2.988	2.958	2.981	2.971	2.983	2.984	2.972	2.985	2.964	2.952
Ti	0.003	0.004	0.003	0.003	0.002	0.008	0.007	0.005	0.003	0.002	0.005
Al	2.008	2.004	2.014	1.999	1.997	1.974	1.986	1.995	1.972	1.994	2.015
Cr	0.000	0.000	0.000	0.000	0.001	0.000	0.001	0.001	0.000	0.000	0.000
Fe3	0.000	0.016	0.016	0.016	0.016	0.016	0.016	0.016	0.016	0.016	0.016
Fe2	2.095	2.115	2.132	2.103	2.117	2.126	2.065	2.099	2.137	2.156	2.137
Mn	0.430	0.409	0.431	0.424	0.446	0.447	0.464	0.454	0.449	0.437	0.424
Mg	0.276	0.298	0.312	0.319	0.312	0.309	0.300	0.303	0.306	0.308	0.301
Ca	0.183	0.163	0.156	0.163	0.156	0.151	0.186	0.171	0.149	0.152	0.179
Na	0.001	0.004	0.001	0.001	0.002	0.003	0.002	0.005	0.002	0.001	0.001
K	0.000	0.000	0.000	0.000	0.000	0.000	0.000	0.000	0.000	0.000	0.000
Sum	7.995	8.000	8.024	8.009	8.021	8.016	8.009	8.020	8.019	8.029	8.029
Alm	70.2%	70.9%	70.3%	69.9%	69.8%	70.1%	68.5%	69.3%	70.3%	70.6%	70.3%
Grs	6.1%	5.5%	5.1%	5.4%	5.1%	5.0%	6.2%	5.6%	4.9%	5.0%	5.9%
Pyr	9.2%	10.0%	10.3%	10.6%	10.3%	10.2%	10.0%	10.0%	10.1%	10.1%	9.9%
Sps	14.4%	13.7%	14.2%	14.1%	14.7%	14.7%	15.4%	15.0%	14.8%	14.3%	13.9%

Sample	grt2.1	grt2.2	grt2.3	grt2.4	grt2.5	grt2.6	grt2.7	grt2.8	grt2.9	grt2.10	grt2.11	grt2.12	grt2.13	grt2.14
SiO2	36.52	36.19	36.60	36.46	36.53	36.21	36.11	36.23	35.55	35.96	36.31	36.16	36.49	36.03
TiO2	0.03	0.06	0.06	0.08	0.08	0.14	0.32	0.12	1.62	0.13	0.10	0.10	0.02	0.27
Al2O3	21.15	20.92	20.95	20.90	20.97	20.89	20.77	20.79	20.31	20.80	20.83	20.85	20.87	20.88
Cr2O3	0.03	0.03	0.03	0.04	0.00	0.04	0.00	0.02	0.04	0.01	0.01	0.00	0.00	0.01
Fe2O3	0.25	0.25	0.25	0.25	0.25	0.25	0.25	0.25	0.25	0.25	0.25	0.25	0.25	0.25
FeO	30.55	30.89	31.13	31.11	31.58	30.89	30.97	30.48	31.93	30.98	31.66	30.77	31.66	30.77
MnO	8.30	6.39	6.23	6.14	6.25	6.34	6.94	7.29	6.76	6.72	6.31	6.73	7.11	7.97
MgO	1.75	2.30	2.43	2.47	2.48	2.44	2.19	2.10	2.26	2.40	2.50	2.43	2.33	1.87
CaO	1.67	1.95	2.09	1.97	2.02	2.04	2.03	2.02	1.63	1.81	1.82	1.77	1.64	1.73
Na2O	0.01	0.01	0.01	0.01	0.02	0.01	0.01	0.01	0.01	0.01	0.00	0.02	0.01	0.01
K2O	0.00	0.00	0.00	0.00	0.00	0.00	0.00	0.00	0.00	0.00	0.00	0.00	0.00	0.00
Totals	100.26	98.99	99.79	99.43	100.18	99.25	99.60	99.32	100.36	99.07	99.80	99.08	100.38	99.80
Oxygens	12.000	12.000	12.000	12.000	12.000	12.000	12.000	12.000	12.000	12.000	12.000	12.000	12.000	12.000
Si	2.965	2.963	2.971	2.969	2.959	2.957	2.949	2.964	2.895	2.949	2.956	2.960	2.960	2.945
Ti	0.002	0.003	0.004	0.005	0.005	0.008	0.020	0.008	0.099	0.008	0.006	0.006	0.001	0.017
Al	2.025	2.019	2.005	2.007	2.003	2.011	2.000	2.005	1.950	2.011	1.999	2.012	1.996	2.012
Cr	0.002	0.002	0.002	0.002	0.000	0.003	0.000	0.001	0.002	0.001	0.001	0.000	0.000	0.001
Fe3	0.016	0.016	0.016	0.016	0.016	0.016	0.016	0.016	0.016	0.016	0.016	0.016	0.016	0.016
Fe2	2.075	2.115	2.113	2.119	2.139	2.110	2.115	2.085	2.175	2.125	2.155	2.107	2.148	2.103
Mn	0.571	0.443	0.428	0.424	0.429	0.439	0.480	0.505	0.466	0.467	0.435	0.467	0.489	0.552
Mg	0.212	0.281	0.294	0.300	0.299	0.297	0.267	0.256	0.274	0.293	0.303	0.296	0.282	0.228
Ca	0.145	0.171	0.182	0.172	0.175	0.179	0.178	0.177	0.142	0.159	0.159	0.155	0.143	0.152
Na	0.002	0.001	0.002	0.002	0.003	0.001	0.002	0.002	0.001	0.001	0.000	0.003	0.001	0.002
K	0.000	0.000	0.000	0.000	0.000	0.000	0.000	0.000	0.000	0.000	0.000	0.000	0.000	0.000
Sum	8.013	8.015	8.016	8.015	8.028	8.020	8.025	8.019	8.022	8.030	8.030	8.022	8.034	8.025
Alm	69.1%	70.3%	70.0%	70.3%	70.3%	69.8%	69.6%	69.0%	71.1%	69.8%	70.6%	69.7%	70.2%	69.3%
Grs	4.8%	5.7%	6.0%	5.7%	5.8%	5.9%	5.9%	5.9%	4.6%	5.2%	5.2%	5.1%	4.7%	5.0%
Pyr	7.1%	9.3%	9.7%	10.0%	9.8%	9.8%	8.8%	8.5%	9.0%	9.6%	9.9%	9.8%	9.2%	7.5%
Sps	19.0%	14.7%	14.2%	14.1%	14.1%	14.5%	15.8%	16.7%	15.2%	15.3%	14.3%	15.4%	16.0%	18.2%

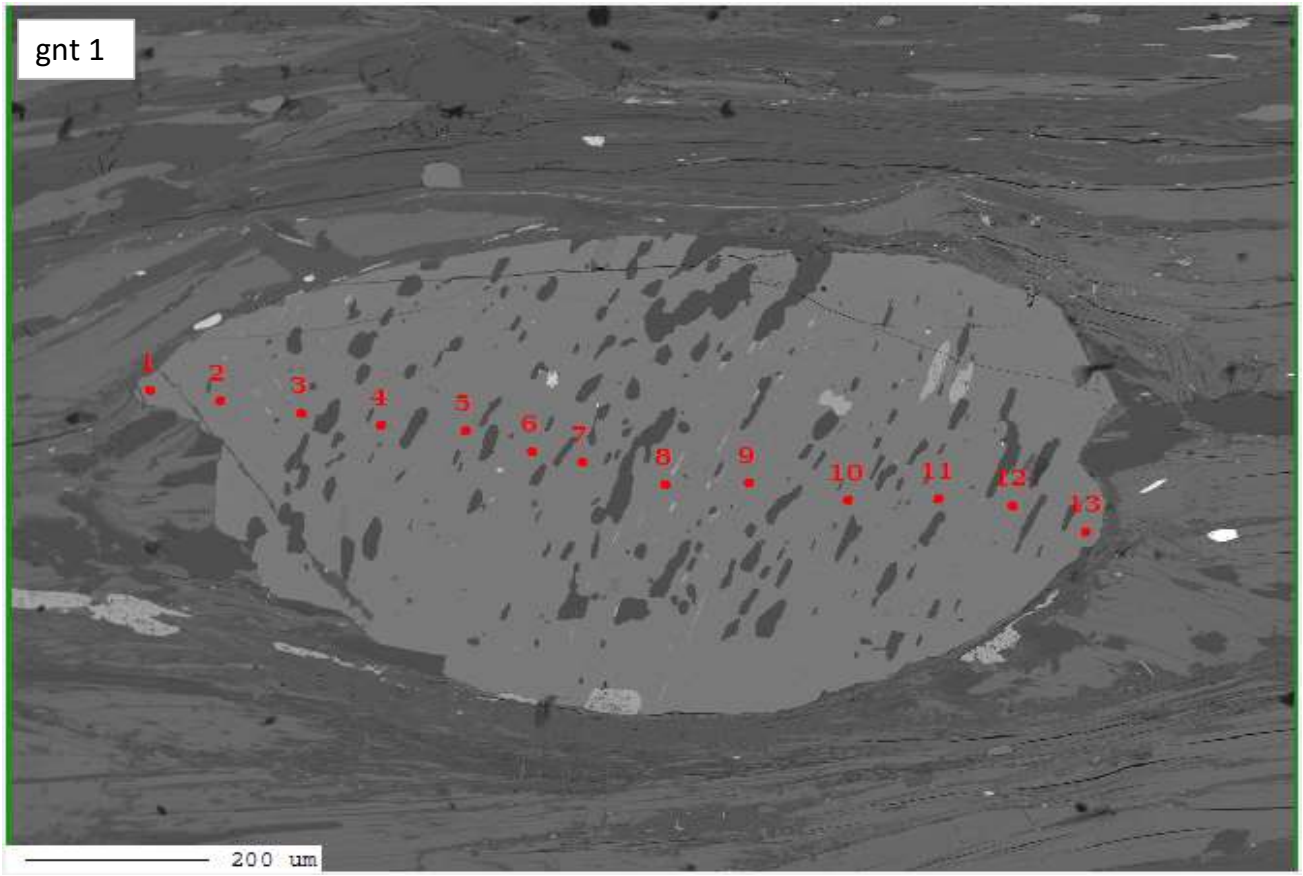
gnt 1
1
2
3
4
5
6
7
8
9
10
11
12
13
200 um

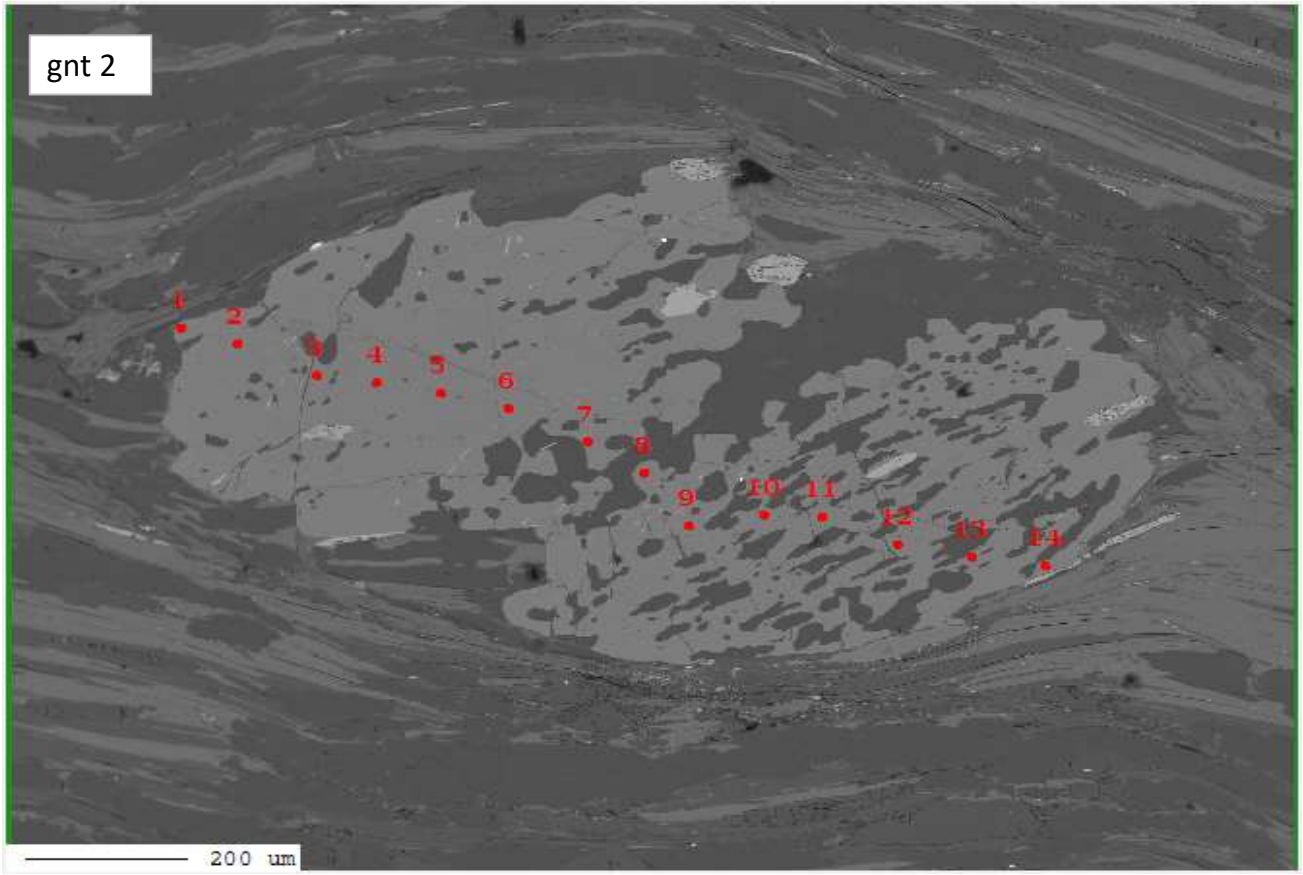
gnt 2
1
2
3
4
5
6
7
8
9
10
11
12
13
14
200 um

Sample:BR18

Mineral:Muscovite

Sample	ms1	ms2	ms4
SiO2	45.73	45.17	45.55
TiO2	0.57	0.46	0.48
Al2O3	37.14	36.92	37.24
Cr2O3	0.00	0.00	0.00
Fe2O3	0.00	0.07	0.07
FeO	0.89	1.15	1.10
MnO	0.01	0.00	0.02
MgO	0.44	0.47	0.51
CaO	0.01	0.03	0.01
Na2O	1.02	0.97	0.90
K2O	9.60	9.36	9.52
Totals	95.41	94.60	95.39
Oxygens	11.000	11.000	11.000
Si	3.021	3.011	3.011
Ti	0.028	0.023	0.024
Al	2.892	2.902	2.902
Cr	0.000	0.000	0.000
Fe3	0.000	0.003	0.003
Fe2	0.049	0.064	0.061
Mn	0.001	0.000	0.001
Mg	0.043	0.046	0.050
Ca	0.000	0.002	0.001
Na	0.131	0.126	0.115
K	0.809	0.796	0.803
Sum	6.975	6.975	6.971
XMg	0.47	0.42	0.45

Sample:BR18

Mineral:biotite

Sample	bt1	bt2	bt4	bt6	bt7	bt8	bt9
SiO2	36.27	43.18	34.72	35.47	35.10	34.52	35.04
TiO2	2.04	0.88	2.27	1.68	2.22	2.40	2.46
Al2O3	21.11	20.34	19.39	19.78	19.92	20.10	20.01
Cr2O3	0.00	0.00	0.00	0.00	0.00	0.00	0.00
Fe2O3	0.00	0.00	0.00	0.00	0.00	0.00	0.00
FeO	20.28	15.83	20.39	20.11	21.34	19.94	20.87
MnO	0.14	0.09	0.16	0.18	0.22	0.15	0.18
MgO	7.66	4.99	8.53	8.37	8.48	8.27	8.44
CaO	0.07	1.57	0.10	0.01	0.04	0.04	0.01
Na2O	0.20	3.90	0.13	0.19	0.22	0.23	0.21
K2O	8.14	5.02	8.60	8.56	8.78	8.31	8.66
Totals	95.91	95.80	94.28	94.35	96.31	93.95	95.88
Oxygens	11.000	11.000	11.000	11.000	11.000	11.000	11.000
Si	2.716	3.103	2.675	2.718	2.658	2.658	2.657
Ti	0.115	0.048	0.132	0.097	0.126	0.139	0.140
Al	1.864	1.723	1.761	1.787	1.778	1.824	1.788
Cr	0.000	0.000	0.000	0.000	0.000	0.000	0.000
Fe3	0.000	0.000	0.000	0.000	0.000	0.000	0.000
Fe2	1.270	0.951	1.314	1.289	1.351	1.284	1.323
Mn	0.009	0.005	0.011	0.012	0.014	0.009	0.012
Mg	0.855	0.534	0.980	0.956	0.957	0.949	0.954
Ca	0.005	0.121	0.008	0.001	0.003	0.003	0.001
Na	0.029	0.543	0.019	0.028	0.032	0.034	0.031
K	0.778	0.460	0.845	0.837	0.848	0.816	0.838
Sum	7.641	7.490	7.745	7.725	7.767	7.717	7.744
XMg	0.40	0.36	0.43	0.43	0.41	0.42	0.42

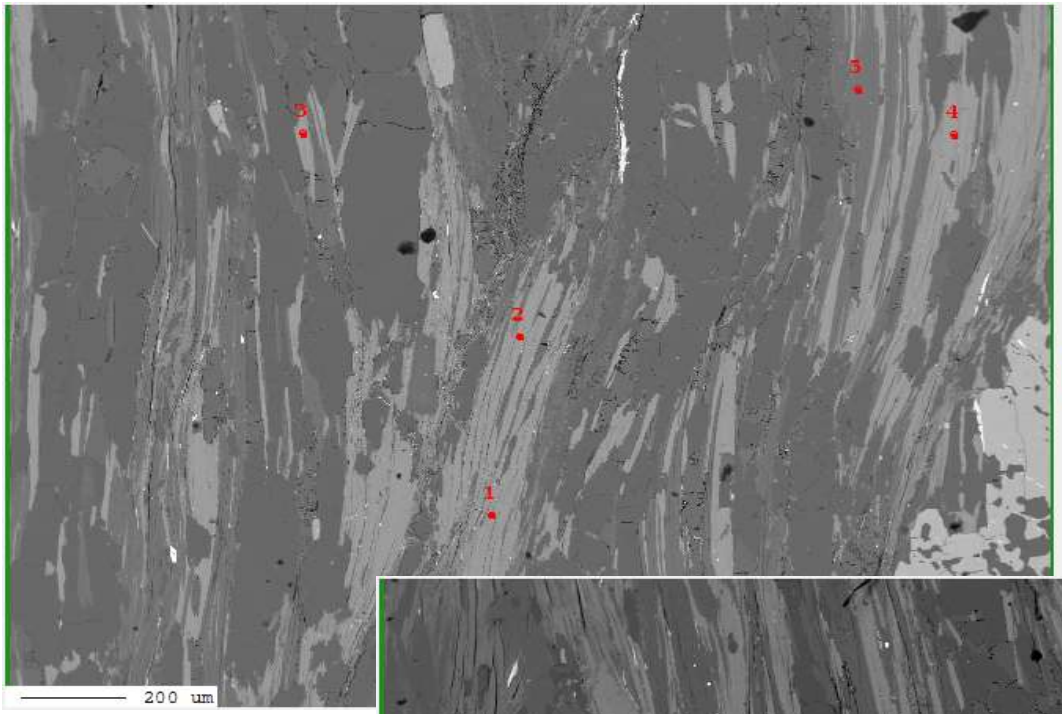

Project : BR18
Image : image018
Date : 2019/12/12 18:06:34
Acc. : 15 kV
Signal Type : COMPO

No.	Data Name	Type	Pos.	Comment
1	BR18_0009	QNT	1	bt6
2	BR18_0009	QNT	2	bt7
3	BR18_0009	QNT	3	bt8
4	BR18_0009	QNT	4	bt9
5	BR18_0009	QNT	5	ms4

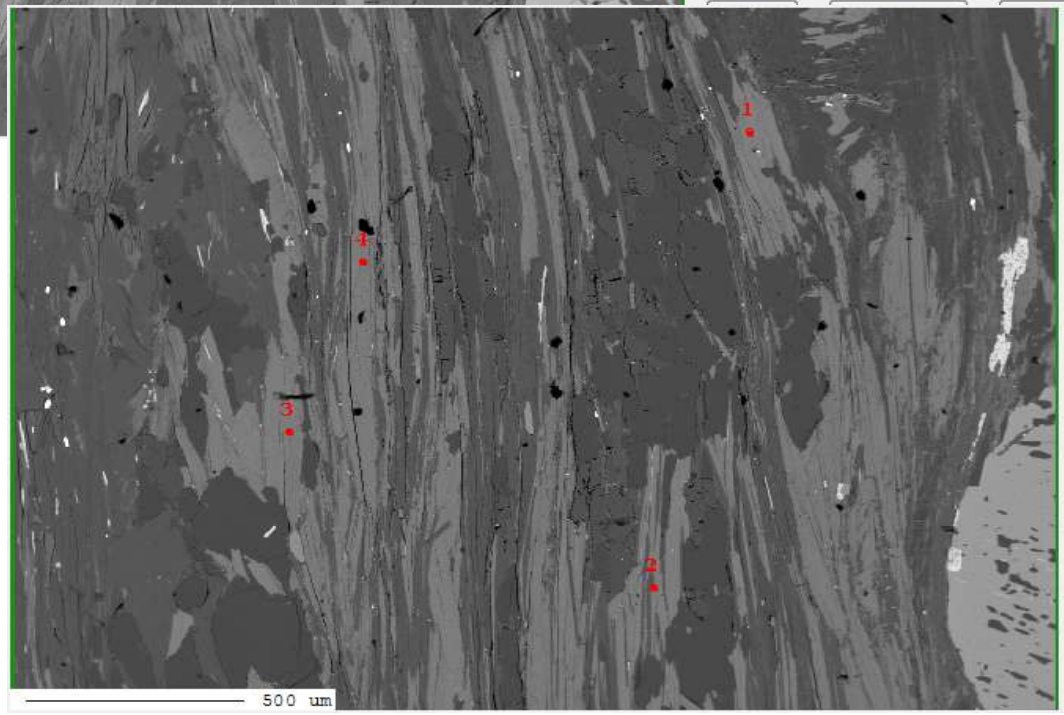

Project : BR18
Image : image019
Date : 2019/12/12 18:09:54
Acc. : 15 kV
Signal Type : COMPO

No.	Data Name	Type	Pos.	Comment
1	BR18_0010	QNT	1	bt1
2	BR18_0010	QNT	2	bt2
3	BR18_0010	QNT	3	bt3
4	BR18_0010	QNT	4	bt4

Delete | Reset Position | Open Data

Clear | Marker Label : Number

Marker Style

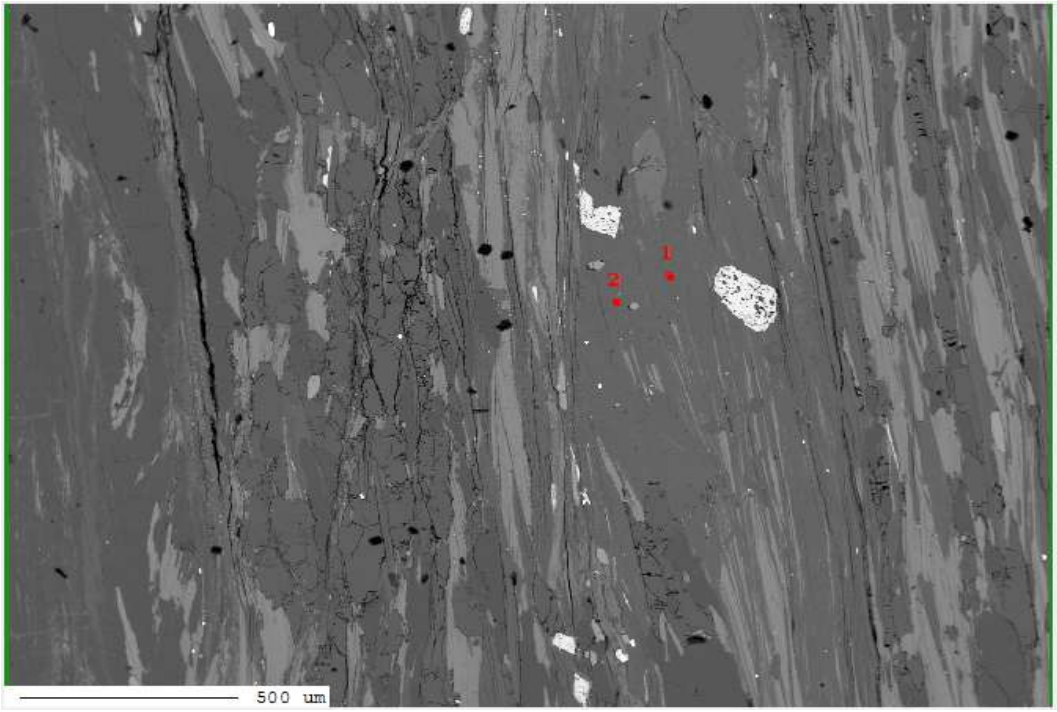

Project : BR18
Image : image020
Date : 2019/12/12 18:11:56
Acc. : 15 kV
Signal Type : COMPO

No.	Data Name	Type	Pos.	Comment
1	BR18_0010	QNT	5	ms1
2	BR18_0010	QNT	6	ms2

Delete | Reset Position | Open Data

Clear | Marker Label : Number

Marker Style

Sample:BR18
Mineral:staurolite

Sample	st1.2	st1.3	st1.4	st1.5	st1.6	st1.7	st1.8	st1.9	st2.1	st2.2	st2.3	st2.4	st2.5	st2.6	st2.7	st2.8	st2.9	st2.10	st2.11
SiO2	27.25	27.21	27.24	27.20	27.25	27.09	27.37	27.90	27.90	27.53	27.37	26.84	26.93	26.72	27.00	26.81	27.13	27.48	26.94
TiO2	0.65	0.56	0.42	0.49	0.46	0.62	0.56	0.41	0.49	0.29	0.51	0.51	0.56	0.57	0.62	0.63	0.51	0.52	0.67
Al2O3	53.39	53.29	53.41	53.09	53.11	53.87	53.37	54.52	54.89	54.19	54.30	54.48	53.99	54.04	53.76	53.40	53.76	54.76	54.00
Cr2O3	0.09	0.02	0.00	0.00	0.01	0.02	0.05	0.02	0.06	0.02	0.03	0.06	0.03	0.10	0.01	0.02	0.03	0.09	0.05
Fe2O3	0.00	0.00	0.00	0.00	0.00	0.00	0.00	0.00	0.00	0.00	0.00	0.00	0.00	0.00	0.00	0.00	0.00	0.00	0.00
FeO	12.71	12.60	12.96	12.67	12.44	12.45	12.46	12.52	12.17	12.05	12.42	12.29	12.35	12.58	12.53	12.57	12.52	12.30	12.71
MnO	0.45	0.44	0.42	0.40	0.41	0.39	0.42	0.42	0.45	0.43	0.42	0.44	0.46	0.44	0.46	0.45	0.47	0.49	0.49
MgO	1.32	1.35	1.35	1.36	1.31	1.25	1.30	1.30	1.25	1.32	1.23	1.29	1.34	1.34	1.28	1.35	1.39	1.34	1.34
CaO	0.00	0.01	0.00	0.00	0.02	0.00	0.00	0.03	0.04	0.01	0.03	0.02	0.01	0.01	0.02	0.04	0.02	0.02	0.02
Na2O	0.03	0.02	0.02	0.03	0.00	0.02	0.01	0.03	0.02	0.01	0.00	0.02	0.00	0.02	0.03	0.00	0.02	0.00	0.02
K2O	0.02	0.02	0.00	0.01	0.01	0.04	0.00	0.03	0.05	0.02	0.03	0.01	0.01	0.00	0.02	0.01	0.01	0.04	0.04
Totals	95.91	95.52	95.82	95.25	95.03	95.75	95.53	97.18	97.31	95.87	96.34	95.95	95.68	95.83	95.73	95.28	95.86	97.05	96.29
Oxygens	46.000	46.000	46.000	46.000	46.000	46.000	46.000	46.000	46.000	46.000	46.000	46.000	46.000	46.000	46.000	46.000	46.000	46.000	46.000
Si	7.689	7.703	7.697	7.723	7.744	7.643	7.737	7.745	7.722	7.732	7.668	7.553	7.602	7.545	7.626	7.614	7.650	7.641	7.577
Ti	0.138	0.118	0.089	0.104	0.099	0.132	0.119	0.086	0.102	0.061	0.107	0.108	0.118	0.121	0.131	0.135	0.108	0.109	0.142
Al	17.761	17.786	17.793	17.770	17.794	17.917	17.785	17.844	17.912	17.942	17.935	18.073	17.969	17.990	17.902	17.878	17.872	17.950	17.905
Cr	0.020	0.004	0.000	0.001	0.002	0.004	0.011	0.004	0.014	0.004	0.008	0.014	0.007	0.022	0.002	0.005	0.008	0.020	0.012
Fe3	0.000	0.000	0.000	0.000	0.000	0.000	0.000	0.000	0.000	0.000	0.000	0.000	0.000	0.000	0.000	0.000	0.000	0.000	0.000
Fe2	2.999	2.983	3.063	3.008	2.957	2.937	2.946	2.907	2.817	2.830	2.910	2.892	2.916	2.971	2.960	2.985	2.953	2.860	2.990
Mn	0.108	0.106	0.101	0.097	0.099	0.093	0.099	0.099	0.104	0.103	0.101	0.104	0.110	0.106	0.111	0.108	0.112	0.116	0.116
Mg	0.556	0.571	0.567	0.573	0.556	0.527	0.549	0.539	0.517	0.552	0.513	0.540	0.565	0.563	0.541	0.572	0.585	0.557	0.562
Ca	0.001	0.002	0.000	0.001	0.007	0.000	0.000	0.008	0.012	0.003	0.008	0.005	0.004	0.004	0.006	0.011	0.007	0.007	0.006
Na	0.016	0.009	0.012	0.019	0.000	0.011	0.003	0.014	0.010	0.007	0.002	0.009	0.000	0.013	0.017	0.000	0.009	0.000	0.013
K	0.008	0.008	0.000	0.003	0.003	0.013	0.000	0.012	0.016	0.007	0.010	0.003	0.002	0.000	0.007	0.004	0.002	0.013	0.013
Sum	29.295	29.292	29.323	29.299	29.260	29.278	29.248	29.258	29.226	29.241	29.260	29.302	29.293	29.334	29.303	29.312	29.307	29.273	29.335
XMg	0.16	0.16	0.16	0.16	0.16	0.15	0.16	0.16	0.16	0.16	0.15	0.16	0.16	0.16	0.15	0.16	0.17	0.16	0.16

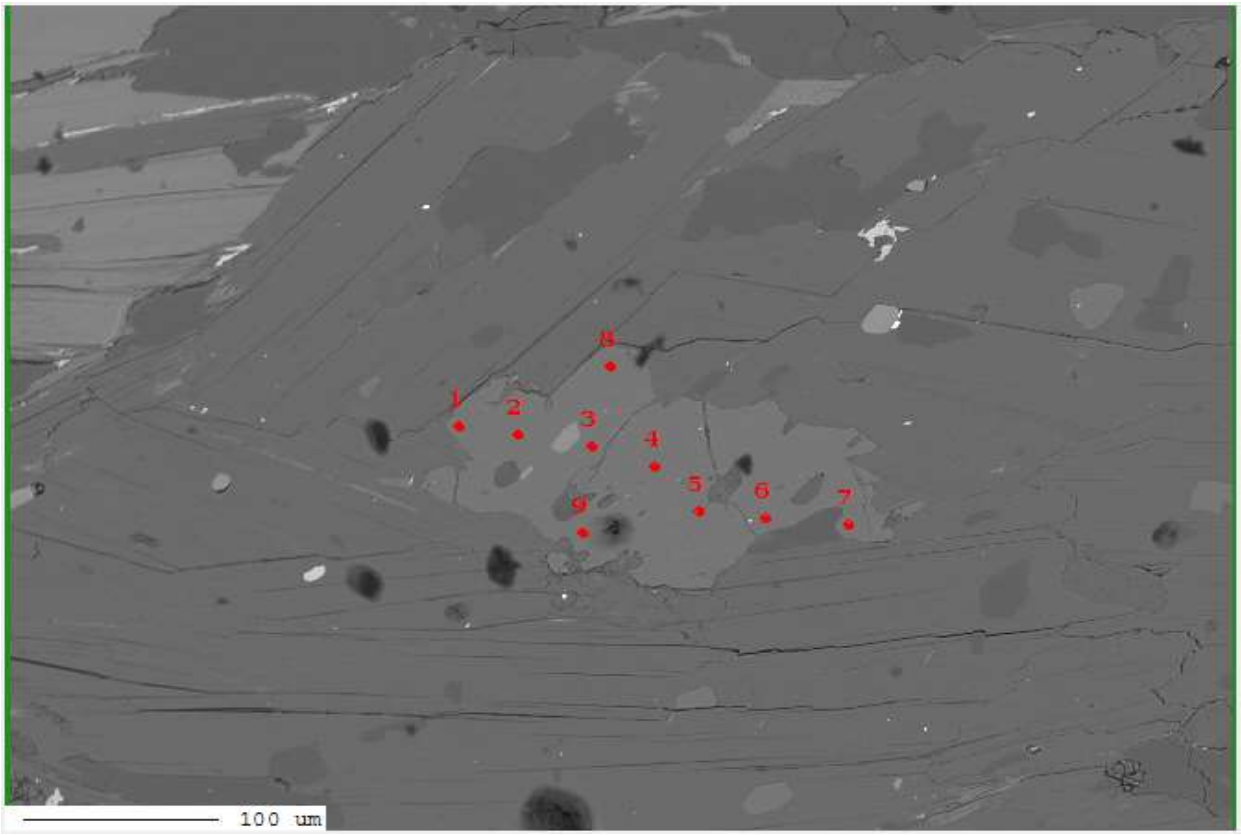

Project : BR18
Image : image005
Date : 2019/12/10 11:44:34
Acc. : 15 kV
Signal Type : COMPO

No.	Data Name	Type	Pos.	Comment
1	BR18_0004	QNT	1	st1 Line 00
2	BR18_0004	QNT	2	st1 Line 00
3	BR18_0004	QNT	3	st1 Line 00
4	BR18_0004	QNT	4	st1 Line 00
5	BR18_0004	QNT	5	st1 Line 00
6	BR18_0004	QNT	6	st1 Line 00
7	BR18_0004	QNT	7	st1 Line 00
8	BR18_0004	QNT	8	st1 Line 00
9	BR18_0004	QNT	9	st1 Line 00

Delete | Reset Position | Open Data

Clear | Marker Label : Number

Marker Style

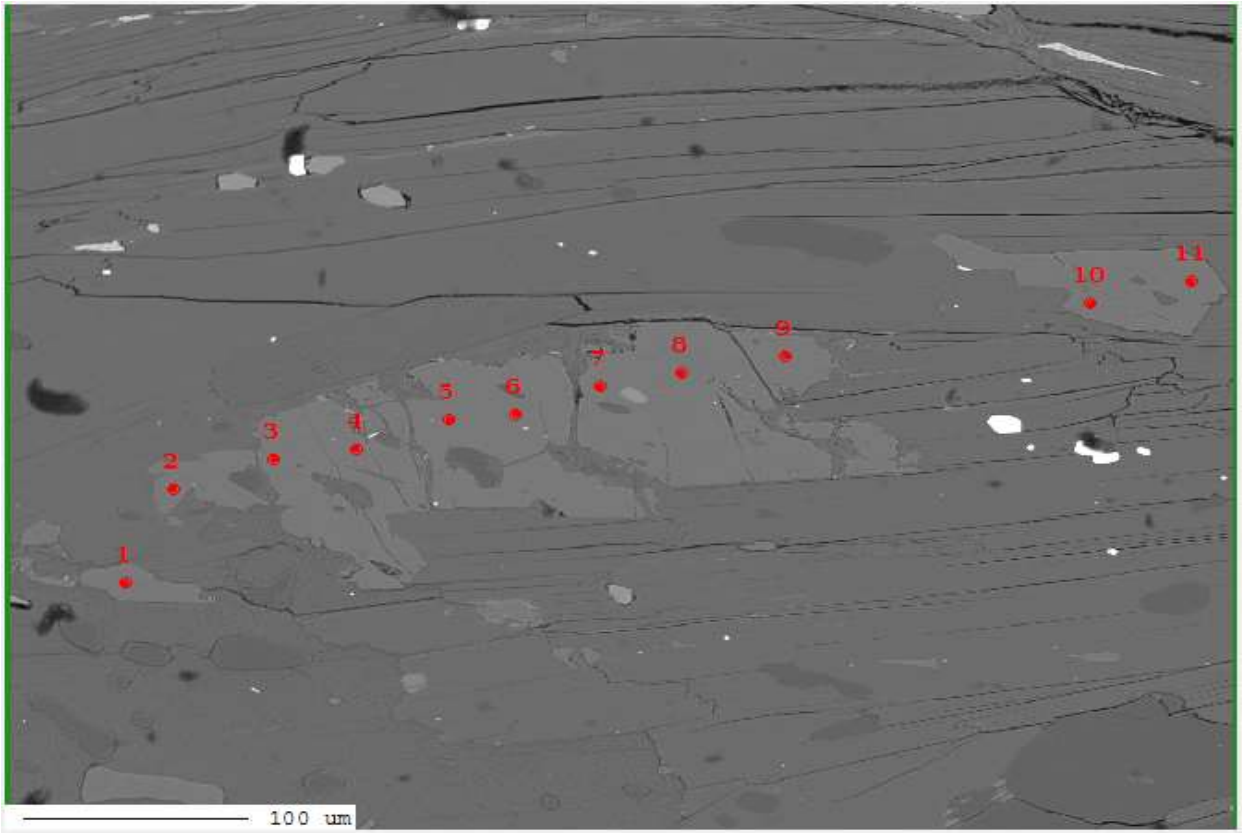

Project : BR18
Image : image007
Date : 2019/12/10 11:59:31
Acc. : 15 kV
Signal Type : COMPO

No.	Data Name	Type	Pos.	Comme
3	BR18_0005	QNT	3	st2 Line
4	BR18_0005	QNT	4	st2 Line
5	BR18_0005	QNT	5	st2 Line
6	BR18_0005	QNT	6	st2 Line
7	BR18_0005	QNT	7	st2 Line
8	BR18_0005	QNT	8	st2 Line
9	BR18_0005	QNT	9	st2 Line
10	BR18_0005	QNT	10	st2 Line
11	BR18_0005	QNT	11	st2 Line

Delete | Reset Position | Open Data

Clear | Marker Label : Number

Marker Style

Sample:BR35A
Mineral:plagioclase

Sample	pl1.1	pl1.2	pl1.3	pl1.4	pl2.1	pl2.2	pl2.3	pl2.4	pl3.1	pl3.2	pl3.3	pl3.4	pl4	pl5	pl6	pl7
SiO2	62.97	62.73	63.22	62.94	62.78	61.73	62.45	63.41	61.92	62.95	62.00	61.98	61.80	62.54	62.04	62.53
TiO2	0.01	0.02	0.00	0.00	0.02	0.01	0.05	0.02	0.00	0.00	0.01	0.00	0.08	0.00	0.00	0.00
Al2O3	23.60	23.66	23.60	23.59	24.08	24.20	24.43	23.68	24.11	23.65	24.30	24.36	24.40	23.99	24.01	23.91
Cr2O3	0.00	0.00	0.00	0.00	0.00	0.00	0.00	0.00	0.00	0.00	0.00	0.00	0.00	0.00	0.00	0.00
Fe2O3	0.12	0.12	0.12	0.12	0.12	0.12	0.12	0.12	0.12	0.12	0.12	0.12	0.12	0.12	0.12	0.12
FeO	0.00	0.12	0.09	0.06	0.54	0.37	0.38	0.33	0.10	0.11	0.07	0.05	0.03	0.08	0.06	0.13
MnO	0.00	0.00	0.00	0.00	0.01	0.00	0.00	0.01	0.00	0.01	0.00	0.01	0.00	0.00	0.01	0.01
MgO	0.00	0.00	0.00	0.00	0.01	0.00	0.00	0.00	0.00	0.00	0.00	0.00	0.00	0.00	0.00	0.00
CaO	4.26	4.16	3.95	4.04	4.23	5.35	4.85	4.05	4.98	4.01	5.12	5.11	5.14	4.63	4.55	4.41
Na2O	9.19	9.23	9.23	9.19	8.67	8.56	8.60	9.08	8.72	9.17	8.77	8.82	8.50	8.95	8.80	8.90
K2O	0.11	0.12	0.08	0.10	0.37	0.11	0.08	0.09	0.09	0.11	0.08	0.07	0.05	0.07	0.13	0.05
Totals	100.26	100.15	100.28	100.04	100.82	100.44	100.96	100.78	100.03	100.12	100.46	100.52	100.11	100.38	99.71	100.06
Oxygens	8.000	8.000	8.000	8.000	8.000	8.000	8.000	8.000	8.000	8.000	8.000	8.000	8.000	8.000	8.000	8.000
Si	2.778	2.772	2.785	2.781	2.760	2.731	2.742	2.782	2.744	2.779	2.737	2.735	2.735	2.758	2.754	2.764
Ti	0.000	0.001	0.000	0.000	0.001	0.000	0.002	0.000	0.000	0.000	0.000	0.000	0.003	0.000	0.000	0.000
Al	1.227	1.233	1.226	1.229	1.248	1.262	1.264	1.225	1.260	1.231	1.265	1.267	1.273	1.247	1.257	1.246
Cr	0.000	0.000	0.000	0.000	0.000	0.000	0.000	0.000	0.000	0.000	0.000	0.000	0.000	0.000	0.000	0.000
Fe3	0.004	0.004	0.004	0.004	0.004	0.004	0.004	0.004	0.004	0.004	0.004	0.004	0.004	0.004	0.004	0.004
Fe2	0.000	0.004	0.003	0.002	0.020	0.014	0.014	0.012	0.004	0.004	0.003	0.002	0.001	0.003	0.002	0.005
Mn	0.000	0.000	0.000	0.000	0.000	0.000	0.000	0.000	0.000	0.000	0.000	0.000	0.000	0.000	0.000	0.000
Mg	0.000	0.000	0.000	0.000	0.001	0.000	0.000	0.000	0.000	0.000	0.000	0.000	0.000	0.000	0.000	0.000
Ca	0.201	0.197	0.186	0.191	0.199	0.254	0.228	0.190	0.236	0.190	0.242	0.242	0.244	0.219	0.216	0.209
Na	0.786	0.791	0.788	0.787	0.739	0.734	0.732	0.772	0.749	0.785	0.751	0.755	0.729	0.765	0.757	0.763
K	0.006	0.007	0.004	0.006	0.020	0.006	0.005	0.005	0.005	0.006	0.004	0.004	0.003	0.004	0.008	0.003
Sum	5.003	5.008	4.997	5.000	4.993	5.006	4.991	4.992	5.002	4.999	5.006	5.009	4.991	5.001	4.998	4.994
Anorthite	0.20	0.20	0.19	0.19	0.21	0.26	0.24	0.20	0.24	0.19	0.24	0.24	0.25	0.22	0.22	0.21

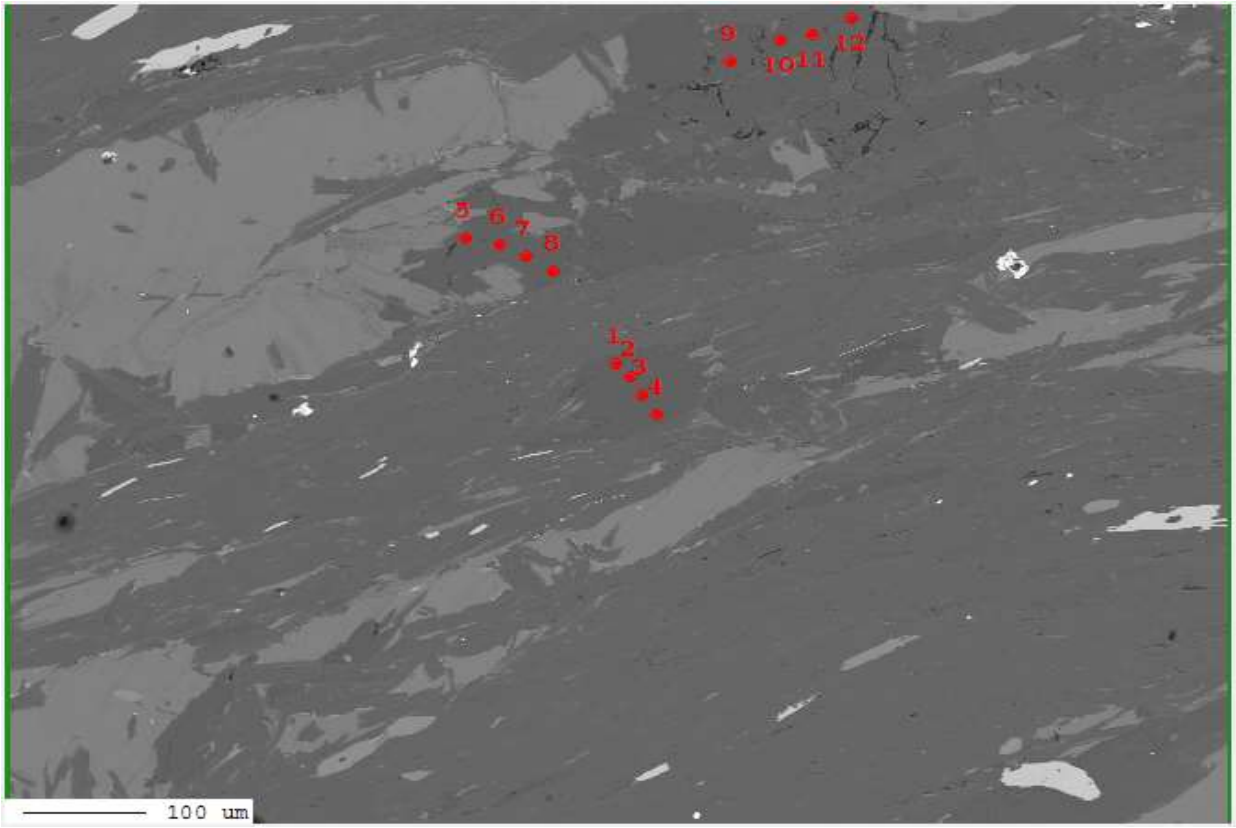

Project : BR35B
Image : image006
Date : 2019/12/12 11:57:06
Acc. : 15 kV
Signal Type : COMPO

No.	Data Name	Type	Pos.	Comme
4	BR35B_0006	QNT	4	pl1 Line
5	BR35B_0006	QNT	5	pl2 Line
6	BR35B_0006	QNT	6	pl2 Line
7	BR35B_0006	QNT	7	pl2 Line
8	BR35B_0006	QNT	8	pl2 Line
9	BR35B_0006	QNT	9	pl3 Line
10	BR35B_0006	QNT	10	pl3 Line
11	BR35B_0006	QNT	11	pl3 Line
12	BR35B_0006	QNT	12	pl3 Line

Delete | Reset Position | Open Data

Clear | Marker Label : Number

Marker Style

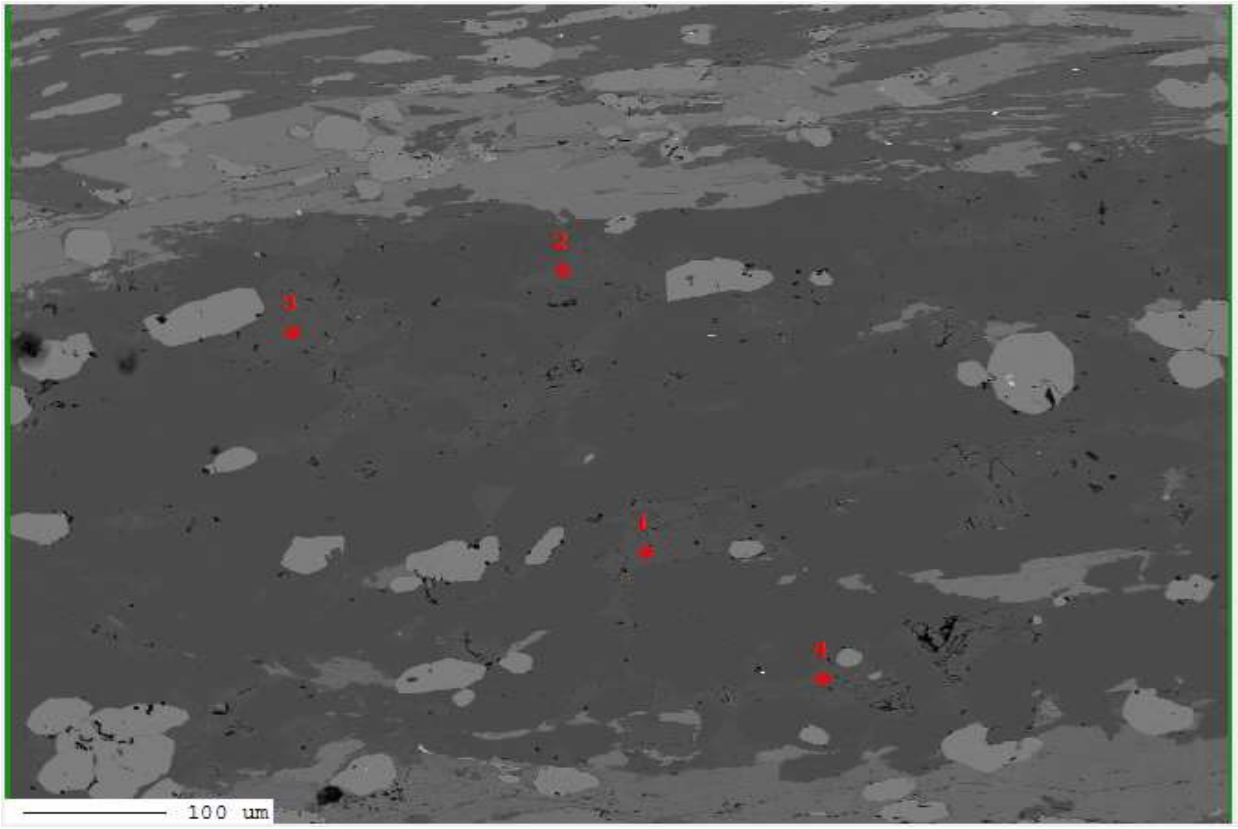

Project : BR35B
Image : image007
Date : 2019/12/12 12:08:40
Acc. : 15 kV
Signal Type : COMPO

No.	Data Name	Type	Pos.	Comment
1	BR35B_0007	QNT	1	pl4
2	BR35B_0007	QNT	2	pl5
3	BR35B_0007	QNT	3	pl6
4	BR35B_0007	QNT	4	pl7

Delete | Reset Position | Open Data

Clear | Marker Label : Number

Marker Style

Sample:BR35A
Mineral:muscovite

Sample	ms1	ms2	ms3	ms4	ms6	ms7
SiO2	45.89	45.99	45.98	47.09	46.51	46.52
TiO2	0.29	0.26	0.24	0.42	0.25	0.35
Al2O3	35.45	36.67	35.10	33.05	35.87	34.26
Cr2O3	0.00	0.00	0.00	0.00	0.00	0.00
Fe2O3	0.21	0.21	0.21	0.21	0.21	0.21
FeO	1.11	1.05	1.85	2.33	1.14	2.26
MnO	0.00	0.00	0.00	0.03	0.02	0.01
MgO	0.96	0.74	1.28	1.88	0.92	1.48
CaO	0.00	0.00	0.00	0.01	0.03	0.04
Na2O	0.41	0.85	0.43	0.27	0.85	0.27
K2O	10.18	9.99	10.21	10.44	9.66	10.33
Totals	94.50	95.77	95.30	95.73	95.45	95.74
Oxygens	11.000	11.000	11.000	11.000	11.000	11.000
Si	3.071	3.036	3.065	3.136	3.074	3.094
Ti	0.014	0.013	0.012	0.021	0.012	0.017
Al	2.796	2.854	2.758	2.594	2.795	2.686
Cr	0.000	0.000	0.000	0.000	0.000	0.000
Fe3	0.011	0.011	0.011	0.011	0.011	0.011
Fe2	0.062	0.058	0.103	0.130	0.063	0.126
Mn	0.000	0.000	0.000	0.001	0.001	0.000
Mg	0.096	0.073	0.127	0.187	0.090	0.147
Ca	0.000	0.000	0.000	0.001	0.002	0.003
Na	0.054	0.109	0.055	0.034	0.109	0.035
K	0.869	0.841	0.868	0.887	0.815	0.876
Sum	6.973	6.995	7.001	7.002	6.973	6.997
XMg	0.61	0.56	0.55	0.59	0.59	0.54

Sample:BR35A
Mineral:chlorite

Sample	chl1	chl2	chl5	chl5	chl6	chl7	chl8	chl9	chl10	chl11	chl12
SiO2	23.89	24.09	24.75	26.82	25.83	27.00	26.20	23.93	23.90	23.70	23.91
TiO2	0.00	0.01	0.09	0.22	0.20	0.23	0.07	0.07	0.06	0.12	0.06
Al2O3	23.33	22.41	23.15	20.87	22.13	20.34	21.04	23.23	23.35	23.78	23.61
Cr2O3	0.00	0.00	0.00	0.00	0.00	0.00	0.00	0.00	0.00	0.00	0.00
Fe2O3	1.12	1.12	1.12	1.12	1.12	1.12	1.12	1.12	1.12	1.12	1.12
FeO	25.36	25.83	26.02	26.41	26.83	26.58	26.88	26.47	28.08	26.13	26.61
MnO	0.23	0.23	0.20	0.26	0.25	0.22	0.23	0.19	0.27	0.16	0.17
MgO	14.35	13.88	14.21	13.00	12.94	13.59	14.37	13.81	12.69	13.90	13.57
CaO	0.01	0.02	0.01	0.14	0.07	0.01	0.03	0.04	0.03	0.03	0.01
Na2O	0.02	0.03	0.01	0.04	0.02	0.02	0.01	0.01	0.00	0.02	0.02
K2O	0.01	0.01	0.03	1.29	0.69	1.10	0.03	0.03	0.01	0.02	0.02
Totals	88.32	87.63	89.58	90.15	90.08	90.19	89.99	88.91	89.51	88.97	89.10
Oxygens	14.000	14.000	14.000	14.000	14.000	14.000	14.000	14.000	14.000	14.000	14.000
Si	2.512	2.562	2.567	2.785	2.682	2.801	2.714	2.514	2.514	2.483	2.506
Ti	0.000	0.001	0.007	0.017	0.016	0.018	0.006	0.006	0.005	0.009	0.004
Al	2.892	2.810	2.831	2.555	2.709	2.487	2.570	2.877	2.895	2.937	2.917
Cr	0.000	0.000	0.000	0.000	0.000	0.000	0.000	0.000	0.000	0.000	0.000
Fe3	0.089	0.090	0.087	0.088	0.088	0.087	0.087	0.089	0.089	0.088	0.088
Fe2	2.231	2.298	2.257	2.294	2.330	2.306	2.329	2.326	2.470	2.289	2.332
Mn	0.020	0.021	0.017	0.023	0.022	0.019	0.020	0.017	0.024	0.014	0.015
Mg	2.249	2.200	2.197	2.012	2.002	2.101	2.219	2.162	1.989	2.170	2.119
Ca	0.001	0.002	0.001	0.015	0.008	0.001	0.003	0.005	0.003	0.003	0.002
Na	0.004	0.005	0.001	0.007	0.004	0.003	0.002	0.001	0.000	0.003	0.003
K	0.002	0.002	0.004	0.171	0.091	0.146	0.004	0.004	0.002	0.002	0.003
Sum	10.000	9.991	9.970	9.966	9.951	9.969	9.954	10.000	9.991	9.998	9.990
XMg	0.50	0.49	0.49	0.47	0.46	0.48	0.49	0.48	0.45	0.49	0.48

Sample:BR35A
Mineral:biotite

Sample	bt1	bt2	bt4	bt5	bt6	bt6	bt7	bt8	bt9	bt10	bt11	bt22	chl3	bt20	bt21
SiO2	34.03	33.52	33.69	35.23	35.47	34.76	35.14	35.20	34.99	34.98	34.78	34.66	34.61	33.61	35.38
TiO2	1.41	1.42	1.38	1.38	1.47	1.32	1.41	1.40	1.44	1.28	1.51	1.27	1.25	1.23	1.38
Al2O3	19.15	18.98	19.33	18.99	19.21	19.12	19.00	19.12	18.78	18.72	18.97	18.64	18.64	19.66	18.74
Cr2O3	0.00	0.00	0.00	0.00	0.00	0.00	0.00	0.00	0.00	0.00	0.00	0.00	0.00	0.00	0.00
Fe2O3	3.69	3.69	3.69	3.69	3.69	3.69	3.69	3.69	3.69	3.69	3.69	3.69	3.69	3.69	3.69
FeO	18.79	22.36	22.26	20.90	21.07	21.92	21.25	21.50	22.10	21.86	21.52	22.34	21.32	22.11	21.15
MnO	0.14	0.13	0.11	0.13	0.12	0.15	0.14	0.16	0.10	0.10	0.12	0.11	0.14	0.14	0.14
MgO	9.48	9.96	9.65	9.36	9.18	9.31	9.36	9.25	9.19	9.50	9.48	9.42	9.54	9.96	9.57
CaO	0.02	0.04	0.02	0.04	0.04	0.04	0.03	0.03	0.03	0.01	0.00	0.04	0.05	0.04	0.01
Na2O	0.05	0.05	0.03	0.05	0.08	0.06	0.10	0.06	0.06	0.07	0.07	0.04	0.09	0.08	0.07
K2O	8.04	7.86	7.85	8.43	9.12	8.82	8.68	8.73	8.81	8.75	8.89	8.35	8.56	7.57	8.61
Totals	94.80	97.99	98.00	98.19	99.44	99.18	98.79	99.14	99.20	98.96	99.03	98.56	97.88	98.09	98.73
Oxygens	11.00	11.00	11.00	11.00	11.00	11.00	11.00	11.00	11.00	11.00	11.00	11.00	11.00	11.00	11.00
Si	2.61	2.53	2.54	2.63	2.63	2.59	2.62	2.62	2.61	2.61	2.59	2.60	2.61	2.53	2.63
Ti	0.08	0.08	0.08	0.08	0.08	0.07	0.08	0.08	0.08	0.07	0.09	0.07	0.07	0.07	0.08
Al	1.73	1.69	1.72	1.67	1.68	1.68	1.67	1.68	1.65	1.65	1.67	1.65	1.66	1.74	1.65
Cr	0.00	0.00	0.00	0.00	0.00	0.00	0.00	0.00	0.00	0.00	0.00	0.00	0.00	0.00	0.00
Fe3	0.21	0.21	0.21	0.21	0.21	0.21	0.21	0.21	0.21	0.21	0.21	0.21	0.21	0.21	0.21
Fe2	1.21	1.41	1.40	1.31	1.30	1.37	1.32	1.34	1.38	1.37	1.34	1.40	1.34	1.39	1.32
Mn	0.01	0.01	0.01	0.01	0.01	0.01	0.01	0.01	0.01	0.01	0.01	0.01	0.01	0.01	0.01
Mg	1.08	1.12	1.08	1.04	1.01	1.03	1.04	1.02	1.02	1.06	1.05	1.05	1.07	1.12	1.06
Ca	0.00	0.00	0.00	0.00	0.00	0.00	0.00	0.00	0.00	0.00	0.00	0.00	0.00	0.00	0.00
Na	0.01	0.01	0.00	0.01	0.01	0.01	0.01	0.01	0.01	0.01	0.01	0.01	0.01	0.01	0.01
K	0.79	0.76	0.76	0.80	0.86	0.84	0.83	0.83	0.84	0.83	0.85	0.80	0.82	0.73	0.82
Sum	7.73	7.82	7.80	7.76	7.79	7.82	7.79	7.79	7.81	7.81	7.81	7.80	7.81	7.80	7.78
XMg	0.47	0.44	0.44	0.44	0.44	0.43	0.44	0.43	0.43	0.44	0.44	0.43	0.44	0.45	0.45

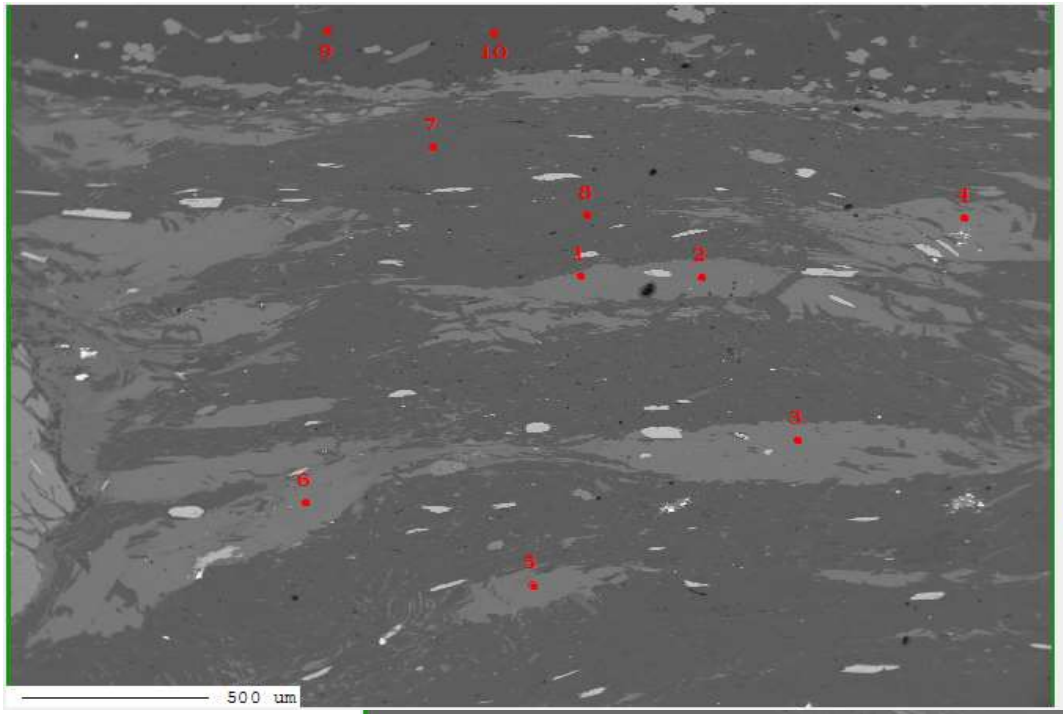

Project : BR35B
Image : image005
Date : 2019/12/12 11:47:40
Acc. : 15 kV
Signal Type : COMPO

No.	Data Name	Type	Pos.	Comment
1	BR35B_0005	QNT	1	bt6
2	BR35B_0005	QNT	2	bt7
3	BR35B_0005	QNT	3	bt8
4	BR35B_0005	QNT	4	bt9
5	BR35B_0005	QNT	5	bt10
6	BR35B_0005	QNT	6	bt11
7	BR35B_0005	QNT	7	ms6
8	BR35B_0005	QNT	8	ms7
9	BR35B_0005	QNT	9	ms8
10	BR35B_0005	QNT	10	ms9

Delete | Reset Position | Open Data

Clear | Marker Label : Number

Marker Style

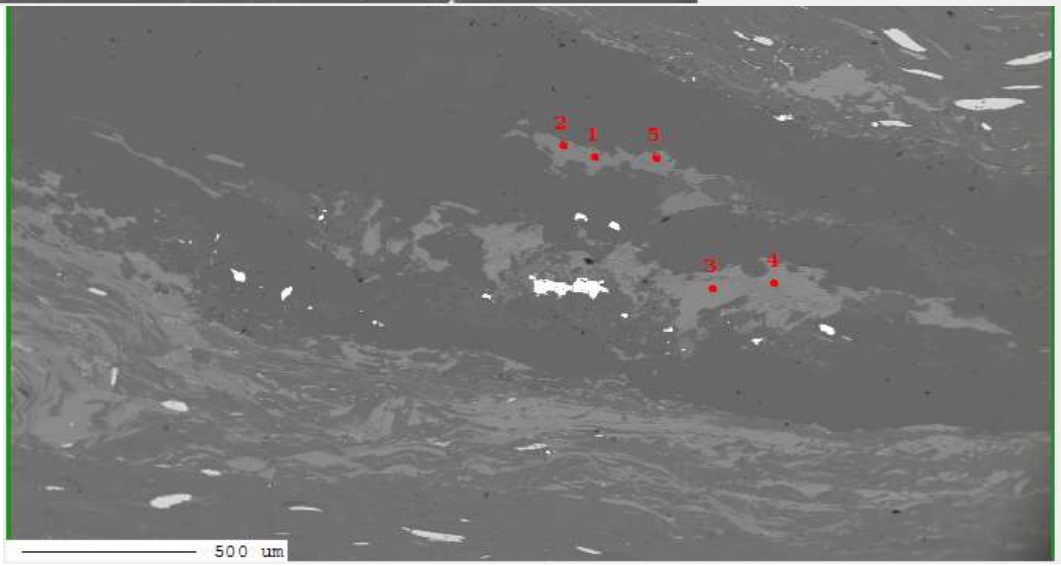

BR35B
image008
2019/12/12 12:17:04
15 kV
Signal Type : COMPO

No.	Data Name	Type	Pos.	Comment
1	BR35B_0008	QNT	1	chl1
2	BR35B_0008	QNT	2	chl2
3	BR35B_0008	QNT	3	chl3
4	BR35B_0008	QNT	4	chl4
5	BR35B_0008	QNT	5	chl5

Delete | Reset Position | Open Data

Clear | Marker Label : Number

Marker Style

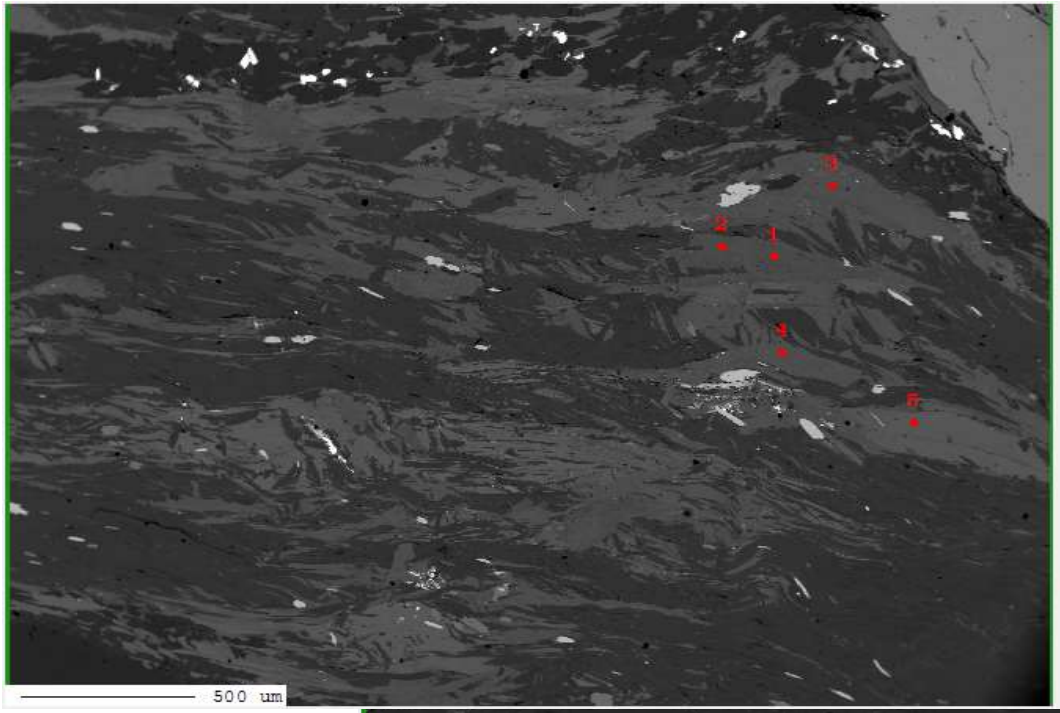

Project : BR35B
Image : image011
Date : 2019/12/12 15:37:04
Acc. : 15 kV
Signal Type : COMPO

No.	Data Name	Type	Pos.	Comment
1	BR35B_0009	QNT	7	chl9
2	BR35B_0009	QNT	8	chl10
3	BR35B_0009	QNT	9	chl11
4	BR35B_0009	QNT	10	chl12
5	BR35B_0009	QNT	11	bt22

Delete | Reset Position | Open Data

Clear | Marker Label : Number

Marker Style

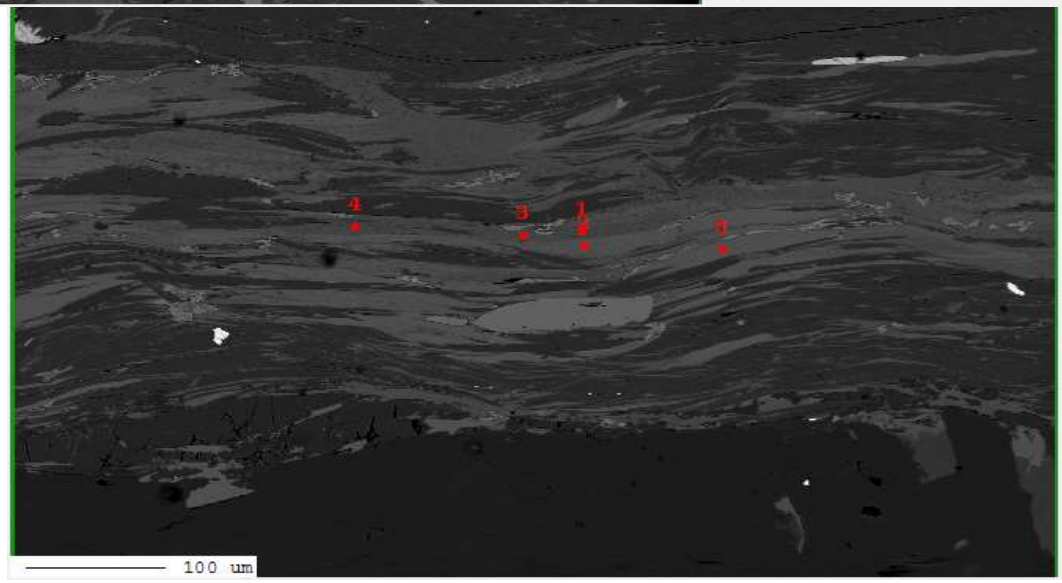

BR35B
image010
2019/12/12 15:31:22
15 kV
Signal Type : COMPO

No.	Data Name	Type	Pos.	Comment
1	BR35B_0009	QNT	1	chl5
2	BR35B_0009	QNT	2	bt20
3	BR35B_0009	QNT	3	chl6
4	BR35B_0009	QNT	4	chl7
5	BR35B_0009	QNT	5	bt21

Delete | Reset Position | Open Data

Clear | Marker Label : Number

Marker Style

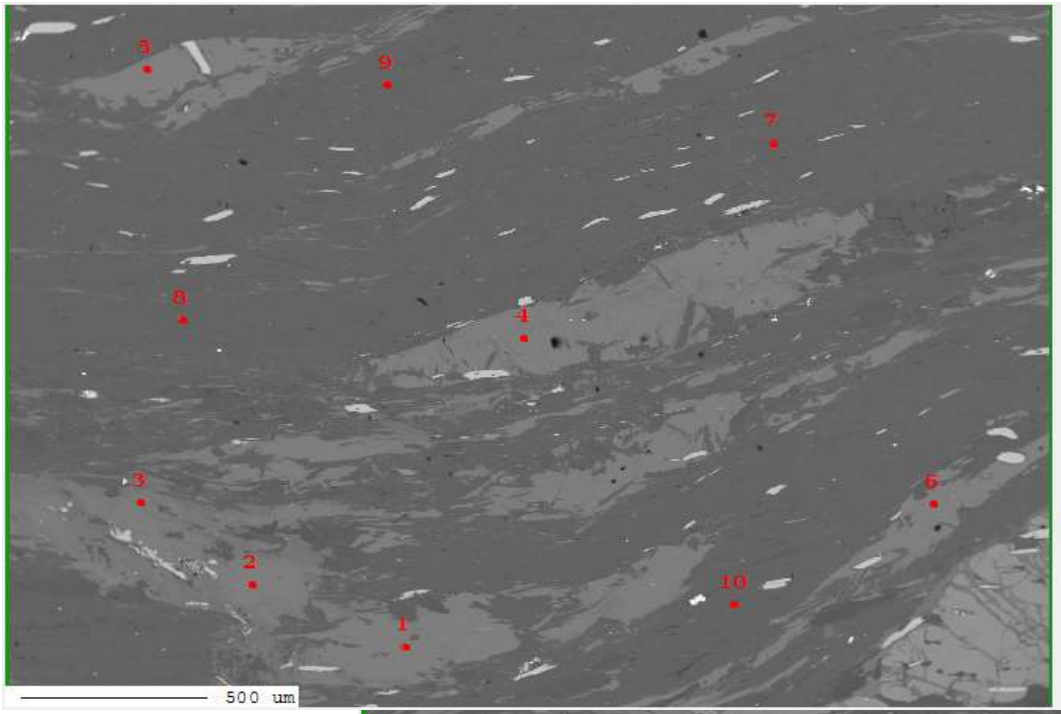

Project : BR35B
Image : image004
Date : 2019/12/12 11:42:45
Acc. : 15 kV
Signal Type : COMPO

No.	Data Name	Type	Pos.	Comment
1	BR35B_0004	QNT	1	bt1
2	BR35B_0004	QNT	2	bt2
3	BR35B_0004	QNT	3	bt3
4	BR35B_0004	QNT	4	bt4
5	BR35B_0004	QNT	5	bt5
6	BR35B_0004	QNT	6	bt6
7	BR35B_0004	QNT	7	ms1
8	BR35B_0004	QNT	8	ms2
9	BR35B_0004	QNT	9	ms3
10	BR35B_0004	QNT	10	ms4

Delete | Reset Position | Open Data

Clear | Marker Label : Number

Marker Style

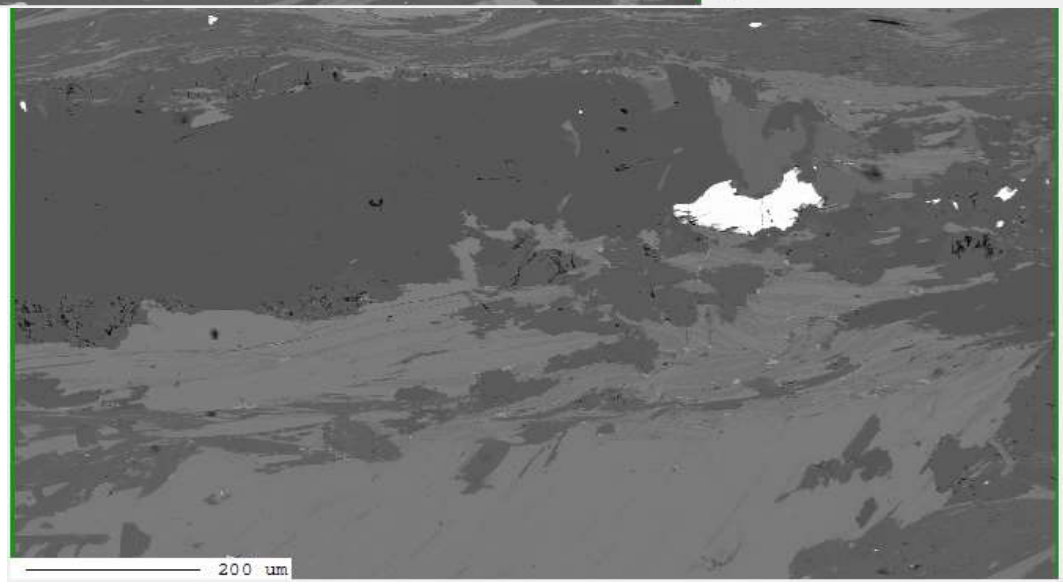

BR35B
image009
2019/12/12 15:27:20
15 kV
Signal Type : COMPO

No.	Data Name	Type	Pos.	Comment
1	BR35B_0009	QNT	1	chl5
2	BR35B_0009	QNT	2	bt20
3	BR35B_0009	QNT	3	chl6
4	BR35B_0009	QNT	4	chl7
5	BR35B_0009	QNT	5	bt21

Delete | Reset Position | Open Data

Clear | Marker Label : Number

Marker Style

Sample:BR35A
Mineral:garnet

				Z1						Z2		
Sample	grt1.1	grt1.2	grt1.3	grt1.4	grt1.5	grt1.6	grt1.7	grt1.8	grt1.9	grt1.10	grt1.11	grt1.12
SiO2	36.46	36.13	36.56	35.25	36.51	36.37	36.45	36.48	36.16	36.42	36.57	35.84
TiO2	0.07	0.08	0.04	0.12	0.08	0.14	0.07	0.14	0.12	0.14	0.10	0.09
Al2O3	20.94	21.04	20.97	20.76	20.75	20.76	21.05	20.77	20.77	20.91	21.05	20.73
Cr2O3	0.05	0.00	0.02	0.02	0.02	0.00	0.01	0.04	0.00	0.02	0.00	0.03
Fe2O3	1.52	1.52	1.52	1.52	1.52	1.52	1.52	1.52	1.52	1.52	1.52	1.52
FeO	30.91	31.39	30.97	30.36	30.02	29.42	29.20	28.41	27.97	28.03	28.17	28.37
MnO	3.92	4.57	5.09	5.28	5.80	6.36	6.39	7.12	7.19	6.95	7.17	7.04
MgO	1.84	1.60	1.47	2.14	1.29	1.02	1.19	1.13	1.08	1.05	1.07	1.29
CaO	4.22	4.44	4.39	4.34	4.92	5.33	5.64	5.73	5.78	6.12	5.70	5.20
Na2O	0.02	0.02	0.01	0.01	0.01	0.01	0.00	0.00	0.01	0.00	0.00	0.02
K2O	0.00	0.00	0.00	0.00	0.00	0.00	0.00	0.00	0.00	0.00	0.00	0.00
Totals	99.95	100.79	101.04	99.80	100.92	100.93	101.51	101.34	100.60	101.16	101.35	100.13
Oxygens	12.000	12.000	12.000	12.000	12.000	12.000	12.000	12.000	12.000	12.000	12.000	12.000
Si	2.950	2.918	2.942	2.881	2.944	2.937	2.924	2.933	2.927	2.929	2.934	2.917
Ti	0.004	0.005	0.002	0.008	0.005	0.008	0.004	0.008	0.007	0.009	0.006	0.005
Al	1.998	2.003	1.989	2.000	1.973	1.976	1.991	1.968	1.982	1.982	1.991	1.989
Cr	0.003	0.000	0.001	0.001	0.001	0.000	0.000	0.003	0.000	0.001	0.000	0.002
Fe3	0.092	0.092	0.092	0.093	0.092	0.092	0.092	0.092	0.093	0.092	0.092	0.093
Fe2	2.092	2.120	2.084	2.075	2.025	1.987	1.959	1.910	1.894	1.885	1.890	1.931
Mn	0.269	0.313	0.347	0.365	0.396	0.435	0.434	0.485	0.493	0.473	0.487	0.485
Mg	0.222	0.193	0.177	0.261	0.156	0.123	0.142	0.135	0.130	0.126	0.128	0.157
Ca	0.366	0.384	0.379	0.380	0.425	0.461	0.485	0.494	0.501	0.527	0.490	0.454
Na	0.003	0.003	0.002	0.002	0.001	0.002	0.000	0.000	0.001	0.000	0.001	0.004
K	0.000	0.000	0.000	0.000	0.000	0.000	0.000	0.000	0.000	0.000	0.000	0.000
Sum	8.000	8.031	8.015	8.066	8.018	8.022	8.031	8.028	8.029	8.025	8.019	8.037
Alm	0.71	0.70	0.70	0.67	0.67	0.66	0.65	0.63	0.63	0.63	0.63	0.64
Pyr	0.08	0.06	0.06	0.08	0.05	0.04	0.05	0.04	0.04	0.04	0.04	0.05
Grs	0.12	0.13	0.13	0.12	0.14	0.15	0.16	0.16	0.17	0.18	0.16	0.15
Sps	0.09	0.10	0.12	0.12	0.13	0.14	0.14	0.16	0.16	0.16	0.16	0.16

Sample	grt2.1	grt2.2	grt2.3	grt2.4	grt2.5	grt2.6	grt2.7	grt2.8	grt2.9	grt2.10	grt2.11	grt2.12
SiO2	35.89	36.63	36.36	36.34	36.56	36.45	36.38	36.47	36.50	36.79	36.67	37.05
TiO2	0.07	0.06	0.10	0.11	0.14	0.12	0.13	0.19	0.09	0.06	0.06	0.09
Al2O3	20.80	21.01	20.97	20.90	20.94	20.93	21.00	20.93	21.10	21.09	20.99	21.17
Cr2O3	0.00	0.01	0.05	0.04	0.03	0.00	0.01	0.00	0.03	0.00	0.02	0.03
Fe2O3	1.52	1.52	1.52	1.52	1.52	1.52	1.52	1.52	1.52	1.52	1.52	1.52
FeO	33.07	32.50	31.11	31.62	30.82	31.30	30.94	30.81	31.63	31.48	31.92	32.65
MnO	3.73	4.13	4.64	4.81	4.79	4.88	4.77	4.54	4.75	4.78	4.16	3.62
MgO	1.95	1.82	1.69	1.64	1.58	1.59	1.59	1.60	1.67	1.70	1.79	1.87
CaO	3.35	4.06	4.45	4.43	4.60	4.66	5.34	5.16	4.43	4.51	4.43	3.83
Na2O	0.01	0.01	0.00	0.01	0.01	0.02	0.02	0.01	0.02	0.00	0.01	0.01
K2O	0.00	0.00	0.00	0.00	0.00	0.00	0.00	0.00	0.00	0.00	0.00	0.00
Totals	100.39	101.76	100.89	101.40	100.99	101.47	101.69	101.23	101.74	101.93	101.57	101.83
Oxygens	12.000	12.000	12.000	12.000	12.000	12.000	12.000	12.000	12.000	12.000	12.000	12.000
Si	2.916	2.931	2.929	2.921	2.940	2.926	2.914	2.928	2.921	2.935	2.935	2.950
Ti	0.004	0.004	0.006	0.006	0.008	0.007	0.008	0.011	0.005	0.004	0.004	0.005
Al	1.992	1.982	1.992	1.981	1.985	1.981	1.983	1.981	1.991	1.983	1.981	1.987
Cr	0.000	0.001	0.003	0.002	0.002	0.000	0.001	0.000	0.002	0.000	0.001	0.002
Fe3	0.093	0.091	0.092	0.092	0.092	0.092	0.092	0.092	0.091	0.091	0.091	0.091
Fe2	2.247	2.175	2.096	2.126	2.073	2.101	2.072	2.068	2.117	2.100	2.137	2.174
Mn	0.257	0.280	0.317	0.328	0.326	0.332	0.324	0.309	0.322	0.323	0.282	0.244
Mg	0.236	0.217	0.203	0.196	0.190	0.190	0.189	0.191	0.199	0.202	0.214	0.222
Ca	0.292	0.348	0.384	0.382	0.396	0.401	0.458	0.444	0.380	0.386	0.380	0.327
Na	0.002	0.002	0.000	0.001	0.001	0.003	0.002	0.002	0.002	0.000	0.002	0.001
K	0.000	0.000	0.000	0.000	0.000	0.000	0.000	0.000	0.000	0.000	0.000	0.000
Sum	8.039	8.030	8.022	8.035	8.013	8.032	8.042	8.026	8.032	8.024	8.026	8.005
Alm	0.74	0.72	0.70	0.70	0.69	0.69	0.68	0.69	0.70	0.70	0.71	0.73
Pyr	0.08	0.07	0.07	0.06	0.06	0.06	0.06	0.06	0.07	0.07	0.07	0.07
Grs	0.10	0.12	0.13	0.13	0.13	0.13	0.15	0.15	0.13	0.13	0.13	0.11
Sps	0.08	0.09	0.11	0.11	0.11	0.11	0.11	0.10	0.11	0.11	0.09	0.08

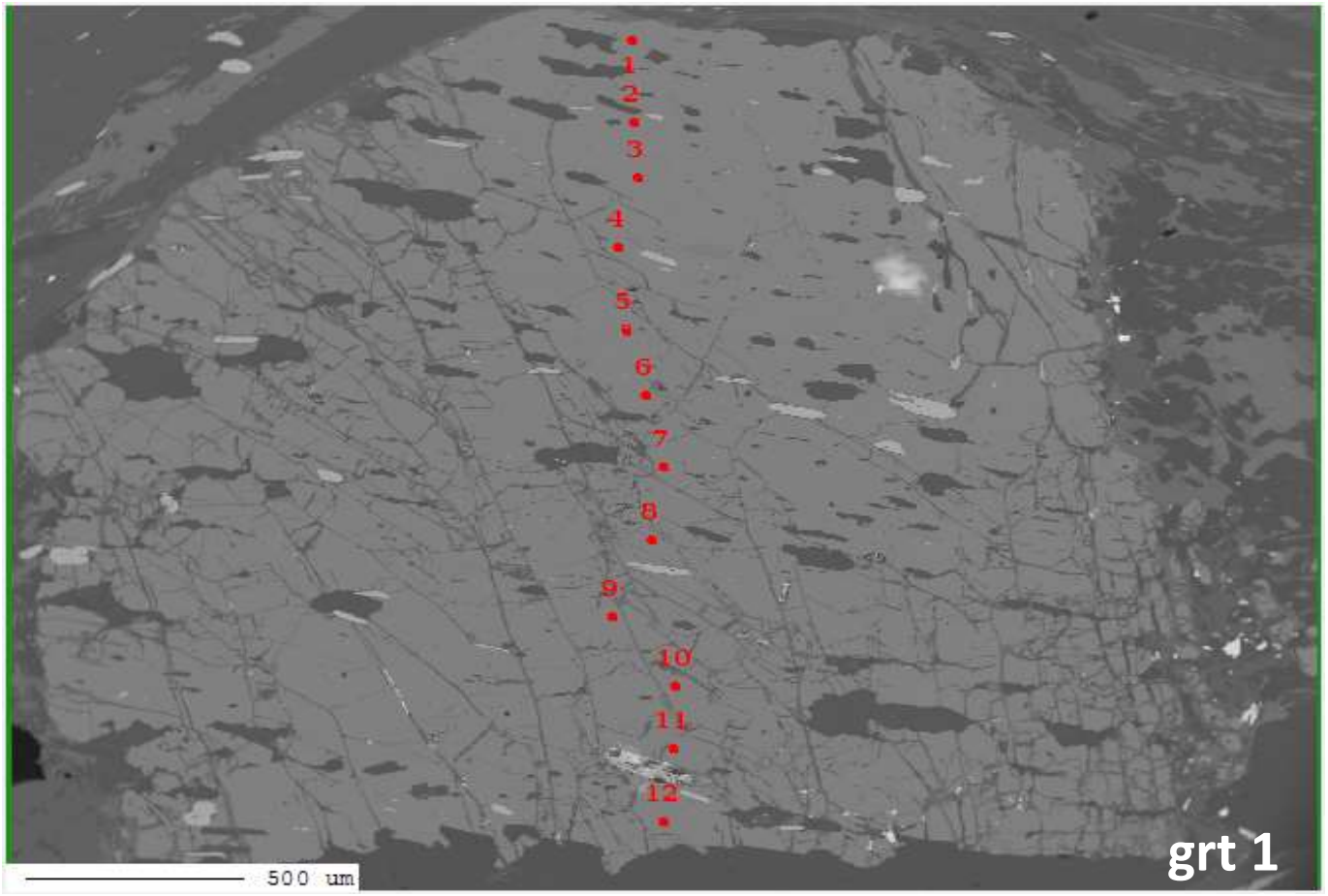
1
2
3
4
5
6
7
8
9
10
11
12
500 um
grt 1

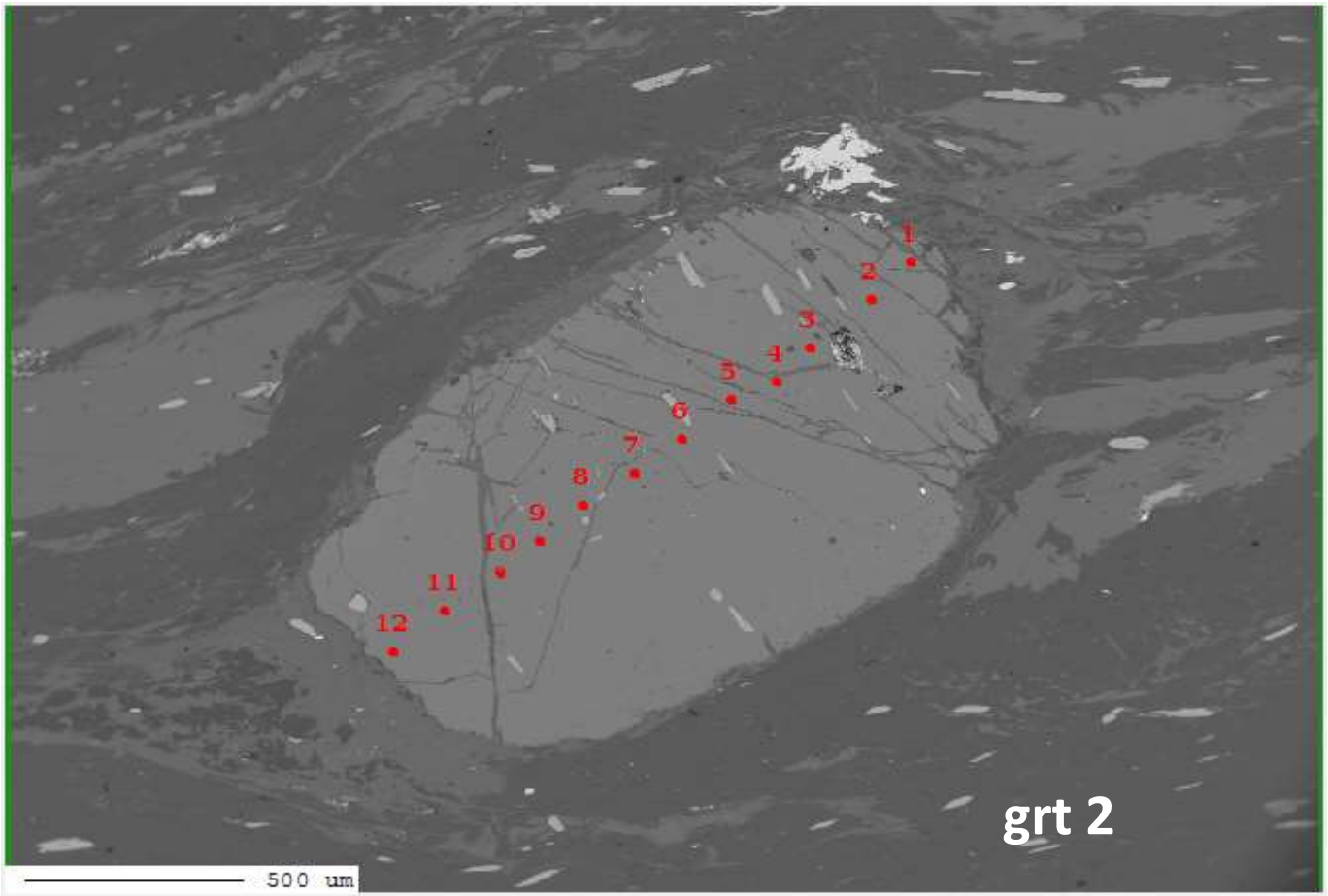
1
2
3
4
5
6
7
8
9
10
11
12
grt 2
500 um